UNIVERSITY OF KENT

Atomistic Simulations of Thermal Effects on Space Materials for Lunar Settlement

by

Adrija Bhowmick

A thesis submitted in partial fulfillment for the
degree of Master of Science

in the
School of Physics and Astronomy

Supervised by Prof Nigel J. Mason & Dr Felipe Fantuzzi

Total number of pages: 194

November 2024

To my beloved grandparents,
Dadaji, Mamoni, Dadun, and Didun,
whose love and blessings shaped my journey.

Though some of you are no longer with me,
your presence lives on in every step I take.

" তুমি রবে নীরবে, হৃদয়ে মম। "

(Tumi robe nirobe hridoye momo.)
“Thou shalt dwell in silence in my heart.”

Declaration of Authorship

I, Adrija Bhowmick, declare that this thesis titled, ‘Atomistic Simulations of Thermal Effects on Space Materials for Lunar Settlement’ and the work presented in it are my own. I confirm that:

- This work was done wholly or mainly while in candidature for a research degree at this University.
- Where any part of this thesis has previously been submitted for a degree or any other qualification at this University or any other institution, this has been clearly stated.
- Where I have consulted the published work of others, this is always clearly attributed.
- Where I have quoted from the work of others, the source is always given. With the exception of such quotations, this thesis is entirely my own work.
- I have acknowledged all main sources of help.
- Where the thesis is based on work done by myself jointly with others, I have made clear exactly what was done by others and what I have contributed myself.

Abstract

The pursuit of sustainable lunar habitats marks a transformative milestone in space exploration, with NASA's Artemis campaign propelling us into a new era dedicated to advancing scientific discovery and supporting extended astronaut missions on the Moon. The lunar surface poses extreme environmental challenges, including temperature fluctuations from 100 K to 400 K and continual exposure to high-energy particles. Developing materials resilient enough to withstand these conditions is crucial for both immediate exploration and longer-term lunar settlement. This study uses molecular dynamics (MD) simulations to evaluate the thermal stability and structural resilience of candidate materials under conditions that mimic lunar thermal cycling. Specifically, it examines the performance of silica (SiO_2)—a major component of lunar regolith and a key material for glassmaking—and polyethylene, a polymer of interest for lunar construction applications. Simulations, conducted using the Meso-Bio-Nano (MBN) Explorer software, focused on temperature variations from 100 K to 400 K, isolating thermal effects to assess structural integrity without the irradiation influences. We find that crystalline SiO_2 exhibits remarkable thermal stability, attributed to its high melting point and ordered atomic structure, while amorphous SiO_2, modelled as glass, shows substantial resilience under extreme temperature shifts. Polyethylene, modelled via CHARMM-GUI and subjected to thermal cycling in MBN Explorer, also maintains structural integrity, highlighting its potential in polymer-based lunar applications. These insights into material performance under lunar-like conditions lay the groundwork for further experimental validation and refinement. Future research will expand on this work by integrating Irradiation Driven Molecular Dynamics (IDMD) into simulations, incorporating experimental data to match engineering requirements, and exploring additional candidate materials for lunar infrastructure—contributing vital knowledge to lunar materials science and supporting the next phase of lunar exploration and settlement.

Acknowledgements

I would like to extend my sincere gratitude to everyone who has contributed to the completion of this thesis. First and foremost, I am immensely thankful to my supervisors, Prof Nigel J. Mason and Dr Felipe Fantuzzi. Their constant support, expert guidance, and deep knowledge have been invaluable throughout this journey. Their encouragement and insightful feedback were instrumental in shaping the direction and depth of this research, and I am profoundly grateful for their mentorship and belief in my potential.

I am also grateful to the faculty at the University of Kent for fostering an inspiring academic environment and providing the resources essential to this research. I acknowledge with thanks the support of the European Commission Horizon 2020 programme through the EU Grant RADON, which enabled several aspects of this project.

A special acknowledgment goes to my colleagues, friends, and the entire KAIROS Team, whose assistance and motivation enriched this journey in both intellectually and personally. I extend particular thanks to Mr. Cauê P. Souza for sharing his expertise and guiding me through much of the computational work, to Mr. Matthew Dickers, whose constant willingness to help was invaluable, and to Mr. Jonathan Cousins, whose provision of experimental data significantly contributed to this thesis.

During a significant part of this work, I was also caring for my grandmother, Mamoni, Mrs. Arati Bhowmick, whose strength, warmth, and patience were a quiet pillar of support throughout. While my parents were away, she was by my side, offering companionship, encouragement, and unwavering understanding. Her presence brought me comfort during some of the most demanding moments of this journey. Although she passed away before I could share this milestone with her, her memory continues to inspire me every day. I am deeply indebted to her for the stability and reassurance she brought during that time.

I would also like to make a special mention of my grandfather, Dadun, Mr. Susil K. Das, whose steadfast faith and quiet encouragement fueled my determination. Although he left us shortly after the thesis submission, his enduring hope to see me succeed has remained a source of inspiration throughout this journey.

Finally, I am extremely grateful to my family, especially my parents, Mr. Arijit Bhowmick and Mrs. Banani Bhowmick, and my brother, Mr. Arpon Bhowmick, for their unwavering belief in me, their love, and encouragement. Their support has been the foundation of this accomplishment, and without them, none of this would have been possible.

My sincere thanks to all of you for making this achievement possible.

Contents

List of Figures

List of Tables

Chapter 1

Introduction

The pursuit of lunar settlements marks a significant milestone in humanity's exploration of space. With NASA's Artemis campaign, we are embarking on a transformative era of lunar exploration aimed at advancing scientific knowledge, developing new technologies, and learning how to live and work on another world.

Scientifically, establishing permanent bases on the Moon offers the potential for groundbreaking discoveries. These include conducting experiments in low gravity, searching for extraterrestrial life, and growing crops in extreme conditions. This renewed focus on lunar exploration heralds a new era, with the potential for humanity's first permanent settlements beyond Earth within the next few decades.

To support astronauts during these extended lunar missions, which are projected to last several months, there is a critical need for habitats that provide large habitable volumes. Ensuring the psychological and physiological well-being of astronauts in the Moon's harsh environment requires innovative habitat designs that address challenges such as lack of gravity and atmosphere, the deleterious effects of radiation, and temperature fluctuations [1].

A sustainable presence on the Moon not only exemplifies human ingenuity but also serves as a crucial stepping stone for deeper space exploration. The Moon's proximity to Earth makes it an ideal candidate for testing and developing space habitation technologies, paving the way for future missions to Mars and beyond.

As we push the boundaries of human exploration, ensuring that we have the right materials to construct and maintain these habitats will be just as critical as the technological innovations themselves. Achieving this goal will depend on significant advancements in materials science to withstand the extreme conditions of space. The materials we choose will play a vital role in shaping the future of space habitation, enabling us to create sustainable, functional, and resilient environments for future generations of explorers.

This thesis aims to address these challenges by discussing the performance of different materials under simulated lunar conditions. By exploring a combination of experimental data and molecular dynamics simulations, this study seeks to provide an understanding of how materials such as SiO_2 and polyethylene—commonly used in space applications—respond to the Moon's extreme environmental factors. The research will focus particularly on the effects of temperature fluctuations on these materials, contributing to the development of more resilient materials for future lunar habitats and infrastructure.

The following sections provide a comprehensive background on the challenges that lunar exploration poses in selection of materials that can be used in developing bases on the lunar surface. The goal is to provide knowledge that will not only advance our understanding of material performance in space but also support the broader vision of sustainable human presence on the Moon and eventually other bodies in the Solar System.

1.1 Background and Motivation

As the nearest celestial body to Earth, the Moon provides a unique platform for scientific discovery, technological advancement, and the development of sustainable space habitats. The exploration of the Moon has been a longstanding goal of human space exploration, driven by both scientific curiosity and the potential for future habitation. It is an object holding many secrets that leaves several unanswered questions since it was formed during Theia Impact. According to the hypothesis proposed by William Hartmann and Donald Davis in 1975 [2], the Moon's formation resulted from a collision between a Mars-sized planetesimal and a proto-Earth during the Hadean Eon, around 4.5 billion years ago (1 Gigaannum, Ga = 1 billion years) [3]. This event is believed to have occurred approximately 20–100 million years (1 Megaannum, Ma = 1 million years) after the Solar System began forming, which began coalescing from interstellar material in the Milky Way Galaxy approximately 4.567 Ga, long after the galaxy itself formed around 13.5 Ga [4].

For millennia, humans observed the Moon with the naked eye, but it was Galileo who first made astronomical observations of the Moon using a telescope, in 1609 AD, marking a new era of lunar exploration [5, 6]. His detailed observations provided significant evidence of the Moon's rocky nature which later published in *Sidereus Nuncius* [7]. As shown in Figure 1.1, Galileo sketched various phases of the Moon and also documented his observations of Jupiter's moons, further advancing our understanding of the celestial bodies.

RECENS HABITAE. 10

Hæc eadem macula ante ſecundam quadraturam nigrioribus quibuſdam terminis circumuallata conſpicitur; qui tanquam altiſſima montium iuga ex parte Soli auerſa obſcuriores apparent, quà verò Solem reſpiciunt lucidiores extant; cuius oppoſitum in cauitatibus accidit, quarum pars Soli auerſa ſplendens apparet, obſcura verò, ac vmbroſa, quæ ex parte Solis ſita eſt. Imminuta deinde luminoſa ſuperficie, cum primum tota fermè dicta macula tenebris eſt obducta, clariora montium dorſa eminenter tenebras ſcandunt. Hanc duplicem apparentiam ſequentes figuræ commonſtrant.

C 2 Vnum

RECENS HABITAE. 10

di medium iam inter Iouem, & orientalem Stellam locum exquiſitè occupantem, ita vt talis fuerit configuratio.

Ori. Occ.

Stella inſuper nouiſſimè conſpecta admodum exigua fuit; veruntamen hora ſexta reliquis magnitudine ferè fuit æqualis.

Die vigeſima hora 1. min: 15. conſtitutio conſimilis viſa eſt. Aderant tres Stellulæ adeo exiguæ, vt vix

Ori. Occ.

percipi poſſent; à Ioue, & inter ſe non magis diſtabant minuto vno: incertus eram nunquid ex occidente duæ, an tres adeſſent Stellulæ. Circa horam ſextam hoc pacto erant diſpoſitæ. Orientalis enim à Ioue

Ori. Occ.

duplo magis aberat quam antea, nempe min: 2. media occidentalis à Ioue diſtabat min: 0. ſec: 40. ab occidentaliori vero min: 0. ſec: 20. Tandem hora ſeptima tres ex occidente viſæ fuerunt Stellulæ. Ioui proxima abe-

Ori. Occ.

rat ab eo min: 0. ſec: 20. inter hanc & occidentaliorem interuallū erat minutorum ſecundorum 40. inter has vero alia ſpectabatur paululum ad meridiem deflectēs;

ab

FIGURE 1.1: Galileo's observations and sketches from *Sidereus Nuncius* (1610). Left: Detailed drawings of different phases of the Moon, with magnification revealing its rocky surface. Right: A sequence of observations of Jupiter's satellites, documenting their movement and disappearance behind the planet (Ref. [7]).

Many astronomical observations and imaging missions took place after Galileo, and numerous fictional stories have revolved around lunar exploration, yet touching the Moon remained a distant dream. The surface of the moon stayed pristine from human contact until the first Apollo Missions [8]. On 20 July 1969, NASA made history with Apollo 11—the first successful manned mission to land on the Moon and return to Earth. Astronauts Neil Armstrong and Edwin "Buzz" Aldrin became the first humans to set foot on the lunar surface (Figure 1.2 [9]), while astronaut Michael Collins remained in lunar orbit aboard the command module Columbia [8]. During their mission, Armstrong and Aldrin conducted experiments on the lunar surface and explored the area around their landing site, including a small cluster of craters and Little West Crater, located approximately 60 meters from the lunar module (Figure 1.3).

These missions unleashed many theories and facts about the Moon. Following the historic success of Apollo 11, six subsequent manned lunar landings expanded our knowledge even further. These missions were not only milestones in space exploration but were also crucial in developing our understanding of the Moon's surface and environment.

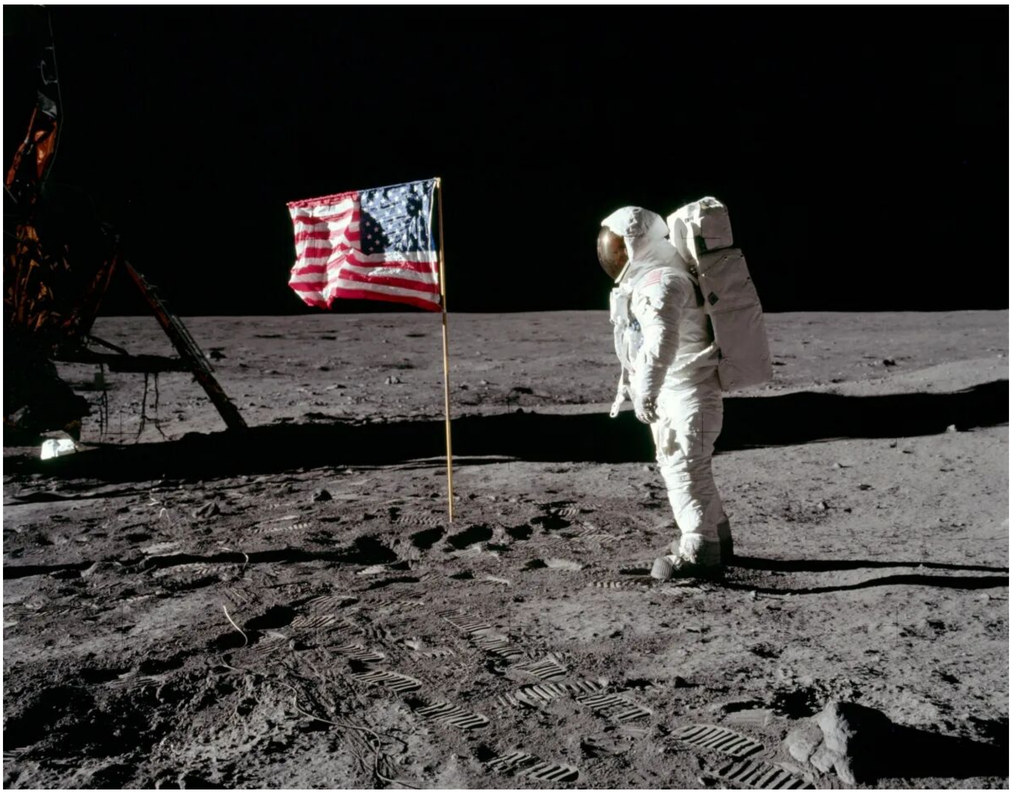

FIGURE 1.2: Astronaut "Buzz" Aldrin standing on the Moon facing a US flag during the Apollo 11 mission in July 1969 (Ref. [9]).

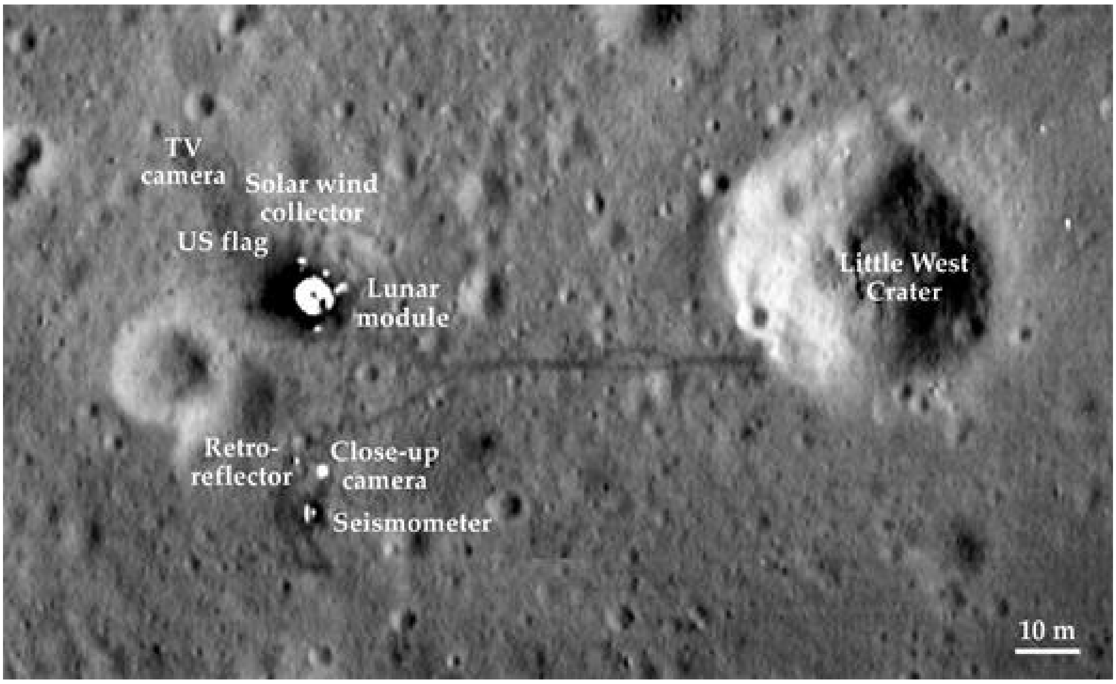

FIGURE 1.3: Apollo 11 landing site. The image depicts the locations where astronauts Neil Armstrong and Edwin "Buzz" Aldrin placed key items, including the US flag, a television camera, and various surface experiments. The footprints and disturbed lunar soil, visible in the image, trace the paths made by the astronauts as they explored and worked around the landing site (Image courtesy of NASA/GSFC/ASU).

The Apollo astronauts' first hand experiences provided valuable observations about the environmental factors influencing the conditions and challenges of working on the lunar surface. For instance, they experienced the extremes of temperature, ranging from blistering heat (390 K) during the lunar day to freezing cold (104 K) during the lunar night [10, 11]. They also had to contend with the Moon's near-total lack of atmosphere, almost 14 orders of magnitude thinner than Earth's [12], which left them exposed to space radiation and micro-meteoroid impacts—both of which poses significant hazards to human life and equipment.

The astronauts also encountered unexpected challenges, such as the abrasive and sticky nature of lunar dust, which clung to their spacesuits and instruments, damaging equipment and reducing visibility [13, 14]. Additionally, the Moon's low gravity—about one-sixth of Earth's [15, 16]—influenced how the crew moved, worked, and handled tools and materials. The lessons learned from the Apollo programme have laid the foundation for advancing space exploration technologies.

However, more than 50 years after the Apollo programme, NASA reignited humanity's quest for lunar exploration by launching the Artemis program in 2017. The programme aims to advance scientific discovery, drive economic benefits, and inspire a new generation of explorers—the Artemis Generation. Its primary goal is to reestablish a human presence on the Moon for the first time since the Apollo 17 mission in 1972. These missions underscore the critical need for habitats capable of supporting astronauts during extended stays, with future lunar surface missions expected to last several months at a time [1]. Unlike the short-term missions of Apollo, Artemis is focused on long-term habitation of the lunar surface, with astronauts expected to conduct missions lasting several months. This underscores the critical need for advanced habitats that can sustain human life in the Moon's harsh environment, providing protection from extreme temperatures, radiation, and other environmental hazards, while supporting both the physical and psychological well-being of astronauts during extended stays [17].

NASA has outlined a two-phased strategy to return humans to the Moon and establish a sustainable presence both in orbit and on the lunar surface. The first phase is focused on administrative groundwork, which includes the development of the Gateway—a lunar orbiting outpost. The initial Gateway configuration marks the foundation of its operational capabilities, designed to support the first human mission to the lunar South Pole. The detailed mission plan is shown in Figure 1.4, while an artistic impression of the mission is depicted in Figure 1.5. This phase is crucial for setting up the infrastructure needed for future exploration. The second phase centers on advancing the technologies necessary for a long-term, sustainable presence on and around the Moon. This includes developing reusable systems, fostering collaborations with a diverse range

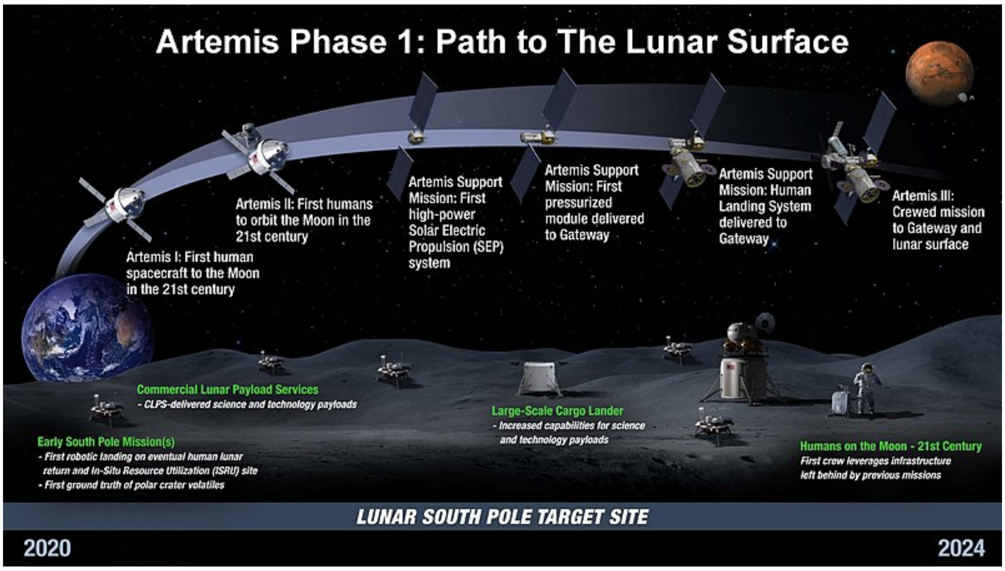

FIGURE 1.4: Mission planning for Artemis programme Phase 1 (Image courtesy of NASA).

FIGURE 1.5: Artistic impression of NASA astronauts performing research on the lunar South Pole. (Image courtesy of NASA).

of international and private sector partners, and enabling regular missions to various locations across the lunar surface. By ensuring that lunar exploration becomes more than a one-off endeavour, NASA's phased approach aims to establish a lasting and productive foothold on the Moon [18].

Following the successful return of humans to the lunar surface, the Artemis programme will transition into Phase 2 as described in Figure 1.6. This phase will prioritise establishing a sustainable human presence both in both in cislunar space—the region between the Earth and the Moon—and on the Moon's surface. NASA will continue utilising the Space Launch System (SLS) and Orion spacecraft for subsequent Artemis missions, while progressively expanding the Gateway into a more advanced platform for science and exploration. This expansion will be supported by contributions from commercial and international partners. A key objective of Phase 2 is to conduct crucial technology demonstrations and scientific experiments, laying the groundwork for future crewed missions to Mars, with the first of these missions anticipated to launch in the 2030s. This phase represents a critical step in advancing space exploration capabilities, not just for lunar operations but as a precursor to deeper space missions [18].

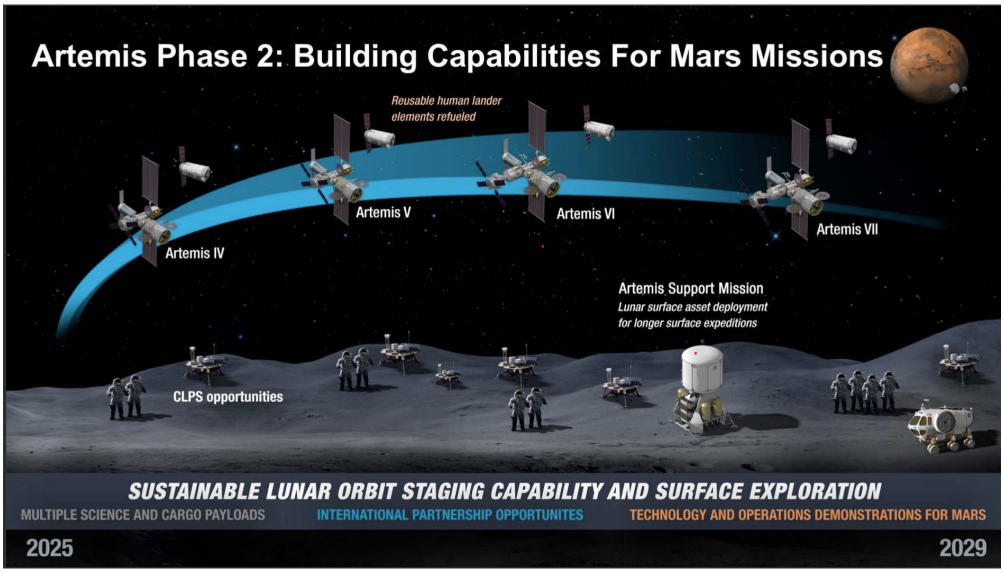

Figure 1.6: Mission planning for Artemis programme Phase 2 (Image courtesy of NASA).

This renewed effort to explore the Moon underscores the importance of addressing the unique challenges of lunar habitation, pushing the boundaries of materials science, engineering, and space technologies in ways not seen since the Apollo era. As we approach Artemis Phase 2, space agencies, in collaboration with industry partners, are working to develop the infrastructure and systems necessary for sustained lunar missions, while also paving the way for future Mars exploration [18].

A major objective in achieving the goals of the Artemis programme and the Space Policy Directive-1 (SPD-1) is to thoroughly understand and utilise the resources available at lunar and other space destinations. Central to this is the concept of In Situ Resource Utilisation (ISRU), which refers to the technology and operations that harness local resources to produce the materials needed for sustained human exploration and space commercialisation. The NASA ISRU programme is specifically focused on generating essential mission consumables and commodities, such as rocket propellant, life support resources, fuel cell reactants, manufacturing and construction materials, and nutrients for food and plant growth. Indeed, it is through the development of ISRU technologies that NASA aims to reduce the reliance on Earth-based supplies and enable a long-term human presence on the Moon and beyond [19].

As we progress into Phase 2 of the Artemis programme, the development of resilient and sustainable materials—both sourced from Earth and derived from in-situ lunar resources—becomes essential in addressing the challenges of long-term lunar habitation. The ability to produce mission-critical consumables and infrastructure directly from the Moon's local resources aligns seamlessly with the overarching objectives of the Artemis programme and Space Policy Directive-1 (SPD-1). This strategy not only facilitates the survival and daily functioning of lunar missions but also paves the way for constructing habitats, energy systems, and other crucial infrastructure using materials harvested directly from the lunar surface. Such advancements will be vital in establishing a self-sustaining lunar base and supporting future missions to Mars and beyond.

The motivation for this thesis arises from the need to better understand how different materials behave under lunar environmental conditions, particularly focusing on the exposure of materials to dramatic temperature extremes and deleterious effects of space radiation. Existing research has provided valuable insights into the effects of space radiation and thermal stress on materials, yet significant gaps remain in our understanding of how these factors interact, especially over extended time periods. The ability to accurately simulate and predict the degradation of materials under such conditions is critical to the design of future lunar habitats, equipment, and spacecraft.

1.2 Objective of the Study

This research is aimed at advancing space exploration by developing materials that are resilient enough to withstand the extreme environmental conditions of the Moon. The ultimate goal is to facilitate the construction of lunar habitats, which are essential for establishing a long-term human presence on the Moon and fostering the sustainable expansion of human settlement beyond Earth. This study focuses on the critical role the choice of materials will play in constructing and maintaining lunar infrastructure, considering both in-situ materials sourced directly from the lunar surface and imported materials from Earth. Each material presents unique advantages and challenges, and understanding their response under lunar conditions is essential for their effective application.

A key motivation behind this research is to explore atomistic perspectives into the behaviour of materials that are suitable for lunar applications. The lunar environment poses unique challenges, significantly different from those experienced on Earth.

Among the most pressing are the extreme temperature fluctuations, which can range from around 100 K (−173 °C) during the lunar night to over 400 K (127 °C) during the day. Such dramatic temperature shifts can lead to thermal fatigue and material degradation, making it imperative to select materials that can endure this constant thermal cycling. This research aims to simulate resilient materials and investigate their performance under thermal stress at the molecular level. Through the use of advanced computational techniques, particularly molecular dynamics simulations using the MBN Explorer software, this study aims to understand how these materials respond to the Moon's harsh conditions at the atomic and molecular level. This knowledge is critical because it will guide the selection and optimisation of materials capable of withstanding lunar extremes, enabling their safe and effective use in building long-term habitats and infrastructure.

By focusing on the investigating resilient materials, this study will contribute to the broader goal of ISRU, a key objective of NASA's Artemis programme and SPD-1. The ability to harness local lunar resources for the production of mission-critical consumables will greatly reduce the cost and complexity of resupplying missions from the Earth. The current research supports the vision of utilising lunar regolith to produce essential materials for construction, energy systems, and other key infrastructure, thereby enabling a self-sustaining lunar presence. The development of materials that can be fabricated directly on the Moon, particularly using silica (SiO_2) and other abundant compounds in lunar regolith, could revolutionise space missions by significantly extending their duration and scope.

Additionally, this study builds on previous research, including experiments conducted at HUN-REN Atomki, to evaluate the effects of proton irradiation and temperature cycling on polymers like polyethylene $(C_2H_4)_n$ and Kevlar $(C_{14}H_{10}N_2O_2)_n$, which are considered for various space applications. Such polymers are being considered for a variety of space applications, from protective layers in space suits to components in lunar habitats [20, 21]. By addressing the fundamental challenges posed by lunar environmental conditions, this research seeks to advance the development of the next generation of space materials, contributing to the success of NASA's Artemis programme and the broader goal of human expansion into space. The findings gained from this study will be crucial for studying materials that can thrive in lunar conditions at atomic level, and ultimately supporting future missions to the Moon, Mars, and beyond.

1.3 Structure of the Thesis

Chapter 1 provides the background and motivation for this research, outlining the current state of research on lunar habitats and the specific objectives of this thesis. It introduces the relevance of material performance in extreme lunar conditions and offers a brief overview of the objectives of the present work and the tools to be used.

Chapter 2 provides a comprehensive review of materials currently considered or used for space applications, focusing particularly on their performance under lunar-like conditions. It examines prior studies and documented research on space materials and delves into the challenges posed by the lunar environment, including thermal extremes, radiation exposure, and material interaction with lunar dust. The chapter also reviews different types of materials—such as in-situ and imported resources—and discusses their suitability for potential use in lunar habitats.

Chapter 3 introduces the computational tools and simulation frameworks used in this research, focusing on multiscale molecular dynamics methods to analyse material performance under lunar conditions. The chapter provides an in-depth overview of the Meso-Bio-Nano (MBN) Explorer software, detailing its capabilities and its specific application to thermal stress simulations in this study. Key simulation parameters are discussed, along with the methodology of irradiation-driven molecular dynamics (IDMD), which models radiation interactions with materials at the molecular level. Although radiation effects are not simulated in this work, the inclusion of IDMD serves to lay the groundwork for future studies. The framework developed here is designed to support both thermal and radiation simulations, ensuring that this thesis can serve as a reference for continued investigations into the combined effects of lunar environmental stressors.

Chapter 4 details the computational methods and modelling approaches used to simulate the performance of selected materials in lunar conditions. This chapter begins by describing the selection criteria for materials, including silicon dioxide (SiO_2) and polyethylene (PE), both of which are critical to lunar construction and radiation shielding. It provides a detailed breakdown of the molecular modelling techniques, including crystal and amorphous simulations for SiO_2 and amorphous models for PE. Each material's unique structural setup is optimised for lunar conditions, followed by targeted simulations that analyse stability under extreme temperatures and radiation exposure. This chapter establishes the methodological foundation for interpreting simulation outcomes and understanding material responses to lunar environmental stresses.

Chapter 5 presents and discusses the computational results for the materials analysed in this study under simulated lunar conditions. The chapter begins with simulations of crystalline silicon dioxide (SiO_2), assessing its stability and response to lunar temperature cycles. It also includes an analysis of amorphous SiO_2 (glass) transition from the crystalline structure and molecular stability of polyethylene (PE) under thermal cycling. For each material, the chapter provides a detailed analysis of temperature response, mechanical resilience, and potential structural adaptations. Comparative analyses are drawn with theoretical predictions highlighting the materials' suitability for lunar infrastructure.

Chapter 6 summarises the main findings of this research - the performance and resilience of various materials, including crystalline and amorphous forms of SiO_2 and polyethylene, under simulated lunar conditions. This chapter provides a comprehensive overview of how these materials respond to thermal cycling. It highlights the present contributions to understanding material characteristics at an atomistic level and assesses the implications of these findings for future lunar infrastructure. Limitations of the study are also acknowledged, with a reflection on how they may impact the broader applicability of the results.

Chapter 7 proposes potential future research directions, emphasising the need for continued investigations into new materials and enhanced computational methodologies for space applications. It suggests expanding material databases to include other polymers, composites, and potential in-situ resources for lunar environments. Additionally, recommendations are made for improving model accuracy by integrating more empirical data and refining molecular dynamics simulations. This chapter underscores the evolving nature of space materials science and its essential role in advancing sustainable lunar exploration.

Chapter 2

Materials for Lunar Environment

This chapter presents a comprehensive overview of current research on space materials, with a specific focus on their behaviour and performance in the harsh conditions of the lunar environment. It examines previous studies on both in-situ materials—sourced directly from the lunar surface—and imported materials, highlighting their responses to various environmental factors such as radiation exposure, extreme temperature fluctuations, and interactions with lunar regolith.

By thoroughly reviewing the key challenges that materials encounter on the Moon, this chapter establishes a solid foundation for the current study and identifies critical gaps in the existing literature. This analysis is intended to guide future research and development efforts in the field. Additionally, the chapter discusses the experiments conducted by Mr. Jonathan Cousins at HUN-REN Atomki, where he investigated the durability of potential materials - polyethylene and Kevlar under simulated lunar conditions. These experiments provide valuable results on the performance of materials in a space environment, further informing the ongoing exploration of suitable resources for lunar missions.

2.1 Challenges in Lunar Environment

The Moon's proximity and unique relationship with Earth—whether through shared origins, composition, or orbital dynamics—plays a crucial role not only in scientific exploration but also in the potential for human habitation and equipment deployment on its surface. However, many processes we take for granted on Earth operate quite differently on the Moon due to its distinct environment.

The most apparent environmental challenges on the Moon include extreme temperature fluctuations, reduced gravity, surface tremors, and the near-complete absence of an atmosphere. These factors pose significant obstacles to both human activity and the operation of equipment. Yet, other environmental hazards, though less visible, are equally important. Chief among these is ionising radiation, which continuously bombards the lunar surface from solar and cosmic sources. [22]

In addition to radiation, several other hazards must be accounted for, including micrometeoroid impacts, which can range in mass from 10^{-12} to 1 g and reach velocities up to 72 km/s [23]. The Moon's abrasive and electrostatically charged dust also presents a significant challenge. Dust particles can become charged by the Sun's light, leading to electrostatic drift toward metal surfaces of opposite potential, causing dust to accumulate upon these surfaces. This dust transport phenomenon, driven by the photoconductive effect, was first observed by the Surveyor 7 mission [24]. Additionally, the unfamiliar lighting conditions (extreme brightness variations and long shadows) on the Moon, which lack the visual cues common on Earth, can further complicate surface operations [22]. These environmental factors underscore the importance of careful study and planning for future lunar missions.

To contextualise these challenges, the experiences of the Apollo missions are instructive. Unlike Earth, the Moon exists in near-total vacuum, with a surface pressure of roughly 3×10^{-15} atm (compared to Earth's surface pressure of 1 atm) and an atmospheric mass of about 25,000 kg (in contrast to Earth's 5.1×10^{18} kg) [25]. Although the Moon's gravity is known to be only one-sixth that of Earth's, Apollo astronauts reported that objects seemed to weigh just one-tenth of their Earth weight, highlighting the complexities of working in the Moon's unique, low-gravity environment. These factors collectively present significant operational challenges that must be addressed for successful future lunar exploration.

Much of this chapter will explore the nature of radiation as well as the extreme temperature fluctuation, and their potential impacts on materials and during lunar missions.

2.1.1 Radiation

Since the giant impact—the collision between the proto-Earth and the planetary embryo Theia (often referred to as the "Mother of the Moon")—which occurred approximately 100 million years after the formation of the Earth [26, 27], the Moon has undergone significant atmospheric changes. One of the most notable outcomes of this event was the Moon's loss of volatile elements, resulting in an extremely thin and tenuous atmosphere

[3]. This thin atmosphere, known as a surface boundary exosphere, offers minimal protection from hazardous ionising radiation, making the Moon's surface highly susceptible to direct exposure.

The primary sources of radiation on the Moon come from three key phenomena: solar flares, the solar wind, and Galactic Cosmic Rays (GCRs) [28]. Solar flares and the solar winds are both generated by the Sun, while GCRs originate from outside our solar system. Each of these radiation types varies in energy, flux, composition, and their interaction depths with the lunar surface and thus have different penetration depths into the lunar surface. Table 2.1 provides a comprehensive summary of the characteristics of these radiation types, derived from data in the Lunar Sourcebook [22], as well as composition data from Feldman et al. (1977) for the solar wind [29], Bame et al. (1983) for magnetospheric plasma [30], McGuire et al. (1986) for solar cosmic rays (SCR) [31], and Simpson (1983) for GCRs [32].

TABLE 2.1: Comparison of Solar Wind, Solar Cosmic Rays, and Galactic Cosmic Rays in the lunar environment.

Type	**Solar Wind**	**Solar Cosmic Rays**	**Galactic Cosmic Rays**
Nuclei energies	$\sim 0.3 - 3$ keV/u*	~ 1 to > 100 MeV/u	~ 0.1 to > 10 GeV/u
Electron energies	$\sim 1 - 100$ eV	< 0.1 to 1 MeV	~ 0.1 to > 10 GeV/u
Fluxes (protons/cm^{2}sec)	$\sim 3 \times 10^8$	$\sim 0 - 10^6$	2-4
Particle ratios			
electron/proton	~ 1	~ 1	~ 0.02
proton/alpha	~ 22	~ 60	~ 7
L $(3 \leq Z \leq 5)$/alpha	n.d.	< 0.0001	~ 0.015
M $(6 \leq Z \leq 9)$/alpha	~ 0.03	~ 0.03	~ 0.06
LH $(10 \leq Z \leq 14)$/alpha	~ 0.005	~ 0.009	~ 0.014
MH $(15 \leq Z \leq 19)$/alpha	~ 0.0005	~ 0.0006	~ 0.002
VH $(20 \leq Z \leq 29)$/alpha	~ 0.0012	~ 0.0014	~ 0.004
VVH $(30 \leq Z)$/alpha	n.d.	n.d.	$\sim 3 \times 10^{-6}$
Lunar Penetration Depths			
protons and alphas	<micrometers	centimeters	meters
heavier nuclei	<micrometers	millimeters	centimeters

The symbols in the particle ratio types L (light), M (medium), H (heavy), VH (very heavy), etc., represent historical groupings of nuclei with charge (Z) values greater than 2 in cosmic rays.
n.d. = not determined (usually because the ratio is too low to measure).

A solar flare is a sudden, rapid, and intense release of energy from the Sun's atmosphere, occurring when magnetic energy stored in the Sun's corona is suddenly unleashed. This release radiates across the entire electromagnetic spectrum, from radio waves to gamma rays, making solar flares a multifaceted phenomenon. These flares originate from active regions, areas with concentrated magnetic fields around the Sun's corona. Solar activity follows an 11-year cycle, during which the frequency and intensity of solar flares increase, especially during periods of maximum solar activity [33].

The solar wind is a continuous stream of charged particles, mainly protons and electrons, that flows outward from the Sun in all directions. These particles can reach speeds of

Figure 2.1: Northern Lights over Tõravere, Estonia, captured by Adrija Bhowmick. The curtain-like structure of the auroras forms as solar wind particles travel along Earth's magnetic field lines, producing vertical sheets of light that resemble drapes. Colors represent different atmospheric gases: green is produced by oxygen at lower altitudes, red by oxygen at higher altitudes, and blue and purple hues by nitrogen. In this image, only the green and purple-blue tones are visible, creating a striking, dynamic display as the auroral curtains ripple with variations in particle flow and magnetic activity.

up to 900 km/s, corresponding to temperatures exceeding one million degrees Celsius [34, 35]. Every object in the Solar System is affected by the solar wind, but the extent of its impact varies depending on whether the object has a magnetic field. Planets with magnetic fields, such as the Earth, deflect the solar winds towards their poles, creating phenomena like auroras. Figure 2.1 shows an image of the auroras, also known as the northern lights, captured in Tõravere, Estonia by the author. However, the Moon lacks a significant or uniform magnetic field, making it more vulnerable to the effects of the solar wind. As the Moon absorbs the solar wind particles, it creates a void region or cavity in the plasma flow near its surface [36].

Galactic Cosmic Rays (GCRs), in contrast, originate from outside the Solar System, likely as a result of violent cosmic events such as supernovae. GCRs consist of highly energetic atomic nuclei stripped of their electrons, traveling at nearly the speed of light. Some GCRs interact with other matter and emit gamma rays during these high-energy collisions [37]. GCRs are composed of nearly every element in the periodic table, with hydrogen making up 89 percent of their content, followed by smaller amounts of heavier elements, including trace amounts of uranium [3].

The energy and composition of GCRs remain relatively stable over time, showing only slow variations. Similar to solar flares, the trajectory of energetic charged particles in GCRs is influenced by local magnetic fields along their path [38]. As the Moon lacks a significant magnetic field, the primary source of deflection for GCRs on the lunar surface comes from the magnetic fields carried by the solar winds. Consequently, the intensity of GCRs impacting the Moon's surface is inversely correlated with the Sun's activity during its eleven-year solar cycle. During periods of high solar activity, the solar winds increase, which enhances magnetic deflection and reduces the GCR flux on the Moon.

However, during periods of low solar activity, such as the unusually prolonged solar minimum in recent years, GCR fluxes on the Moon have reached the highest levels recorded in the space age [39]. At the same time, the power, pressure, and flux of the solar wind, as well as its magnetic influence, have been at historically low levels [40–42]. This heightened GCR exposure during solar minimum presents significant challenges for lunar exploration.

Currently, NASA's Lunar Reconnaissance Orbiter (LRO) is studying lunar radiation to gather essential data for developing protection strategies for future human missions and potential lunar colonisation and research outposts. A key instrument on the LRO, the Cosmic Ray Telescope for the Effects of Radiation (CRaTER, Figure 2.2) has detected a previously unidentified source of hazardous radiation, underscoring the unique challenges such as solar flares, coronal mass ejections, and high-energy charged particles posed by the lunar environment (shown in Figure 2.3) [43–45]. CRaTER's observations have been instrumental in understanding the risks associated with GCRs on the Moon's surface. For instance, at the maximum GCR dose rate observed by CRaTER (11.7 cGy/yr, where 1 Gy = 1 J/kg), GCRs deposit 88 eV per water molecule over 4 billion years, leading to significant alterations in the molecular composition and physical structure of water ice. This prolonged exposure affects density, colour, and crystallinity, causes the loss of molecular hydrogen, and facilitates the formation of more complex molecules by linking carbon and other elements within the irradiated ice [46].

These distinct forms of radiation present on the Moon pose a significant threat to human populations returning for research or extended missions. Some estimated radiation dose rates are presented in Table 2.2, based on data from Nachtwey and Yang (1991) [47]. For context, NASA estimates that the standard radiation dose for a person on Earth is about 0.36 rad [48]. In comparison, Apollo astronauts received an average skin radiation dose of 0.38 rad—equivalent to undergoing two head computed tomography (CT) scans.

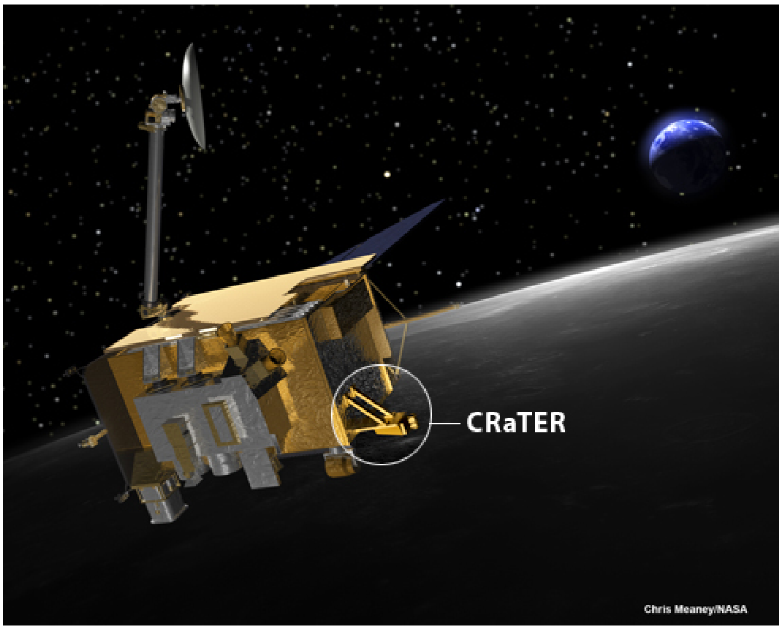

Figure 2.2: The Cosmic Ray Telescope for the Effects of Radiation (CRaTER) aboard NASA's Lunar Reconnaissance Orbiter is equipped with six detectors to monitor energetic charged particles from galactic cosmic rays and solar events. CRaTER performs two vital measurements: one assesses how space radiation interacts with materials similar to human tissue, helping scientists evaluate the potential impact on astronauts and biological organisms. The second examines the radiation striking the lunar surface, revealing the composition of the moon's regolith. (Image courtesy of NASA/GSFC).

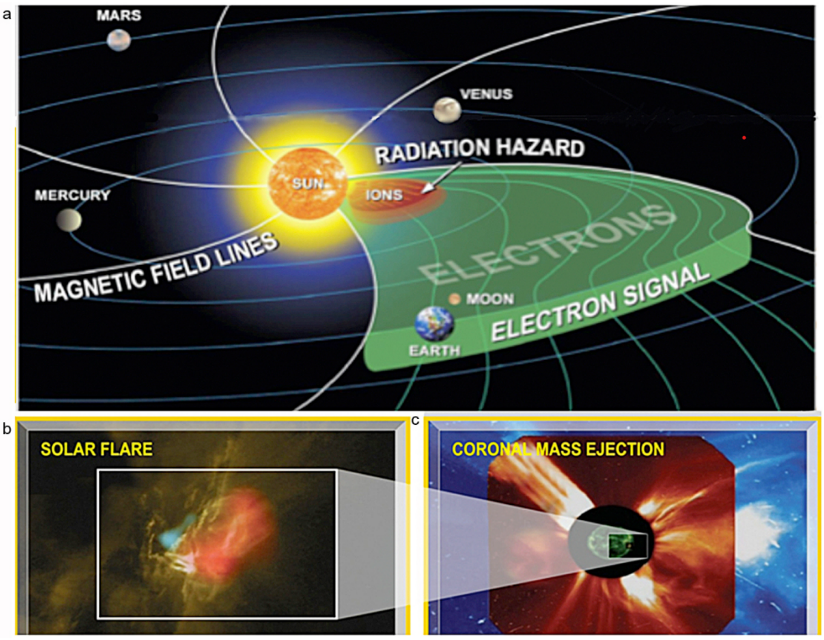

Figure 2.3: Radiation hazards in the solar system. Panel (a) illustrates the Sun's magnetic field lines, ion radiation, and electron signals propagating through the solar system, impacting planetary bodies like Earth and Mars. Panels (b) and (c) highlight solar phenomena critical to radiation hazards: solar flares (b) and coronal mass ejections (c), which are major contributors to high-energy particles affecting space missions (Posner et al. 2006, Ref. [43]).

Table 2.2: Approximate Radiation Doses and Health Risks for an Astronaut on a Mars or Lunar Base Mission During Minimum Solar Activity.

Radiation source	**Representative shielding**	**Skin dose equivalent**	**Deep organ (5 cm) dose equivalent**	**Excess lifetime cancer incidence in a 35-year-old male**
Chronic exposure				
Trapped belts[‡]	2 g/cm^2 Al	< 2 rem*	< 2 rem*	$< 0.1\%$
Free space	4 g/cm^2 Al	75 rem/yr	53 rem/yr	$\sim 1.2\%$/yr of exposure
On lunar surface	4 g/cm^2 Al	38 rem/yr	27 rem/yr	$\sim 0.6\%$/yr of exposure
On martian surface	16 g/cm^2 CO_2 (atm.)	13.2 rem/yr	12 rem/yr	$\sim 0.3\%$/yr of exposure
Acute exposure to large (e.g., Aug. '72) solar particle event				
Free space	2 g/cm^2 Al	1900 rem	254 rem	$\sim 5.7\%$
On lunar surface	4 g/cm^2 Al	440 rem	80 rem	$\sim 1.8\%$
+ shielding	15 g/cm^2 Al	19 rem	6 rem	$\sim 0.2\%$
On martian surface	16 g/cm^2 CO_2 (atm.)	9 rem	4.6 rem	$\sim 0.1\%$
+ shielding	60 g/cm^2 Al	< 1 rem	< 1 rem	$< 0.03\%$

[‡] one-way transit.

* radiation doses are given in rem, a unit representing biological effect. To convert to rad (absorbed dose), a radiation weighting factor (Q) is required. For most space radiation, Q ranges from 2 to 5. Thus, 1 rem typically corresponds to 0.2 – 0.5 rad.

Apollo 14 experienced the highest recorded dose, with 1.14 rad to the skin, all during missions lasting no longer than 12 days [49].

However, the daily radiation exposure on the lunar surface during a longer mission is expected to be substantially higher and cannot be accurately predicted from Earth. To measure these levels directly, the Lunar Lander Neutron and Dosimetry (LND) instrument aboard the Chinese lunar lander Chang'e 4 (Figure 2.4) travelled to the Moon [50]. The LND recorded the first-ever radiation measurements on the lunar surface, revealing an average daily radiation dose significantly higher than on Earth, which poses considerable risks to human health without proper shielding. These findings provide critical information about the radiation risks for future missions [51, 52].

To mitigate radiation exposure, subterranean habitats with enhanced radiological shielding will be crucial for long-term lunar habitation. Even for surface operations, continuous shielding is necessary. As characteristics of the radiations given in Table 2.1, the solar wind has the highest fluence, but the low energy (1 keV/nucleon) of the particles, chiefly protons, means that they are stopped in the outer few micrometers (μm) of surface materials as given in Table 2.3 [53]. While the solar wind is a constant feature of the lunar radiation environment, Solar Energetic Particles (SEPs) occur only in occasional energetic outbursts from the Sun [54, 55]. SEPs are dominated by protons, and energies generally range from 1 to 100 MeV per nucleon [56]. Although the average fluence of SEPs is much lower than that of solar winds, the higher energies allow SEPs to penetrate deeper into materials.

This thesis focuses on the solar wind radiation due to its overwhelming contribution of 95% to the lunar radiation environment, as shown in Table 2.3. Unlike the sporadic

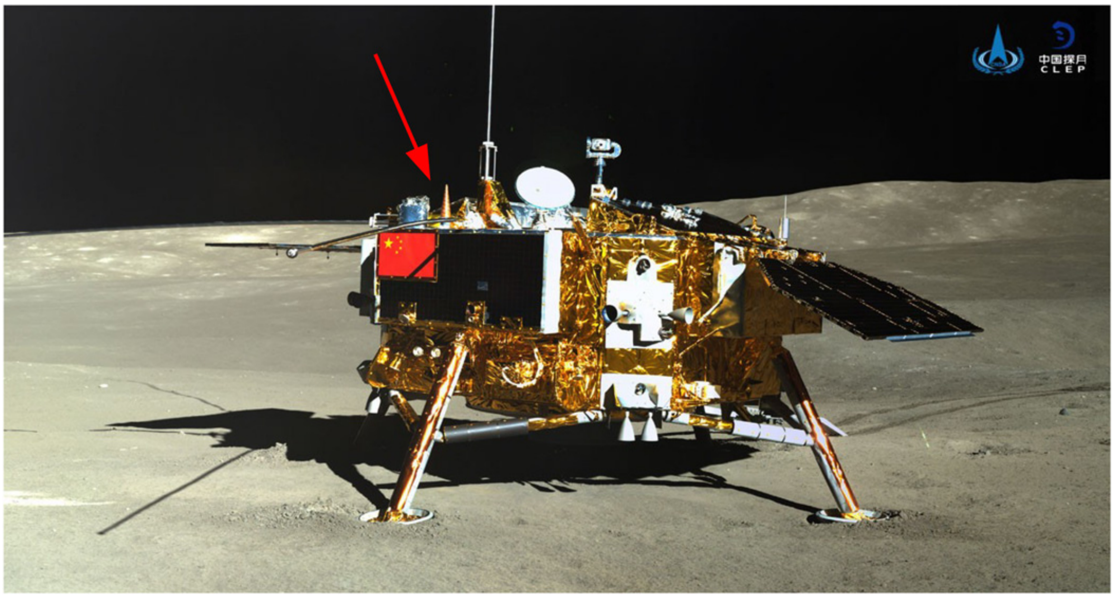

FIGURE 2.4: View of the Chang'e 4 lander, with the LND sensor head location highlighted by a red arrow. The LND is housed within the lander's payload compartment. The red arrow indicates the reclosable door, which shields the LND from the harsh cold of lunar nights and remains open during lunar daytime. Image courtesy of the Chinese National Space Agency (CNSA) and the National Astronomical Observatories of China (NAOC) (Wimmer-Schweingruber et al. 2020, Ref. [50]).

TABLE 2.3: A Summary of the Particle Radiation Types, Compositions, Energy, and Fluxes with depths at the Lunar Surface.

Radiation Type	**Particle Types**	**Energy (MeV nucleon^{-1})**	**Depth of Penetration into Regolith**	**Flux at Lunar Surface (protons cm^{-2} s^{-1})**
Solar wind	Protons ($\sim$ 95%), alpha particles ($\sim$ 4%), heavy ions ($\sim$ 1%)	~ 0.001	A few μm	$\sim 3 \times 10^8$
Solar energetic particles	Protons (98%), alpha particles (2%), small fraction of heavy ions	$\sim 1 - 100$	A few cm	$\sim 0 - 10^6$
Galactic cosmic rays	Protons (87%), alpha particles (12%), heavy ions (1%)	$\sim 100 - 10,000$	Several m	2-4

nature of solar flares or the relatively constant yet lower flux of GCRs, the solar wind is a continuous flow of charged particles emitted by the Sun, impacting the Moon without interruption. Its persistence means lunar habitats and systems will face ongoing exposure, requiring robust shielding and mitigation techniques. By concentrating on the solar wind, this study addresses the most prevalent radiation hazard, allowing for more focused and effective strategies to protect astronauts and infrastructure during extended lunar missions.

2.1.2 Temperature

In addition to hazardous radiation levels and hypervelocity micrometeoroid impacts, the extreme temperature variations on the Moon's surface, particularly near the equator, pose significant challenges for structural integrity. These fluctuations can cause thermal expansion and contraction, which may affect the static, dynamic, and frequency response of lunar structures, potentially leading to material fatigue or failure over time [57]. Being a relatively small planetary body, the Moon has likely lost most of its initial heat during its 4.6-billion-year history. The majority of its current heat flux is thought to be generated by the decay of radioisotopes, such as potassium-40 (^{40}K), thorium-232 (^{232}Th), uranium-235 (^{235}U), and uranium-238 (^{238}U), which are present in the Moon's interior down to a depth of approximately 300 km [11].

The Moon experiences extreme temperature variations due to its lack of a substantial atmosphere, which on Earth acts as an insulator and helps regulate temperature. As a result, lunar surface temperatures fluctuate significantly depending on the location and time of day. During the lunar day, when sunlight directly hits the surface, temperatures can reach scorching highs of around 380 K (107°C). Conversely, during the lunar night, when no sunlight reaches certain areas, temperatures can plunge to a bone-chilling 90 K (−183°C) [3]. The stark contrast between day and night is a direct result of the Moon's inability to trap heat, as there is no atmospheric buffer to hold warmth once the Sun sets.

At the lunar poles, where the axial tilt causes certain regions to remain in permanent shadow, even more extreme conditions exist. NASA's LRO recorded temperatures as low as 35 K (−238°C) at the South Pole and 26 K (−247°C) at the North Pole, marking the coldest places ever measured in the Solar System [58]. These frigid regions could potentially harbour frozen water, making them key areas of interest for future exploration.

Interestingly, human activity during the Apollo missions in the 1970s also impacted the Moon's surface temperatures. When the astronauts walked on the lunar surface, they disturbed the fine layer of dust, revealing darker subsurface material that had likely been untouched for billions of years. This exposed regolith absorbed more heat from the Sun, leading to a measurable increase in surface temperature of nearly 258 K from regular temperatures, as confirmed in 2018 by reanalysis of data from the Apollo Heat Flow Experiment (Figure 2.5, taken from Langseth et al. (1972) [59]) [60].

Despite these surface fluctuations, the Moon's interior remains largely unaffected by external conditions. The core, composed of iron-rich molten mantle, has a temperatures estimated between 1600 K and 1700 K (1327°C to 1427°C), yet this internal heat does not

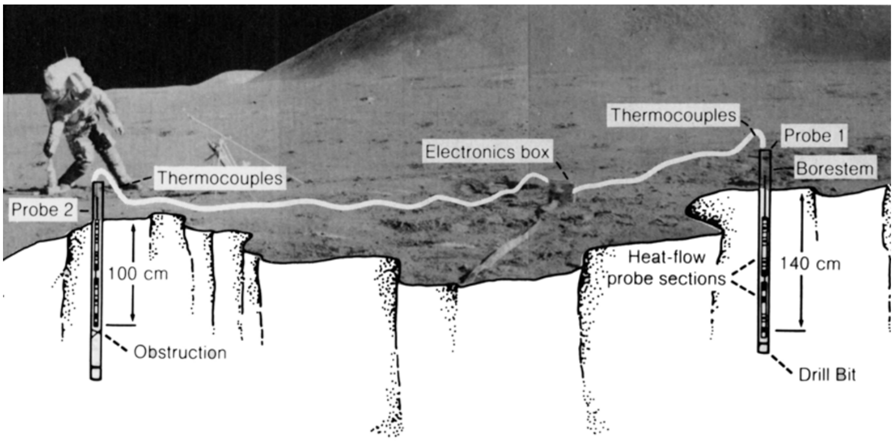

FIGURE 2.5: Diagram showing emplacement of lunar heat-flow probes at the Apollo 15 landing site (angseth et al. 1972, Ref. [59]).

significantly influence surface temperatures [58]. Temperature variations on the surface are primarily driven by solar exposure, with the temperature rising approximately 280 K from just before lunar dawn to lunar noon. These dynamics underscore the Moon's unique thermal environment, where the lack of atmosphere results in rapid heating and cooling cycles depending on solar exposure.

During NASA's Apollo missions in the early 1970s, lunar subsurface heat flow experiments were conducted to determine the temperature profile and thermal conductivity of the Moon's regolith [61]. Heat-flow probes were inserted into the holes created after extracting core samples from the lunar surface. Successful measurements were made at the Apollo 15 and 17 landing sites, while an experiment at the Apollo 16 site was cut short due to a broken cable. Prior to these *in situ* measurements, lunar heat-flow data relied on Earth-based observations of thermal emissions from the Moon in the microwave band. Krotikov and Troitsky (1964) [62] and Tikhonova and Troitsky (1969) [63] identified a brightness temperature gradient of 273.75 K/cm (0.6°C/cm), which they used to estimate a heat flow of approximately 3×10^{-6} W/cm^2 to 4×10^{-6} W/cm^2, closely matching the heat flow measurements later taken on the Moon.

At the Apollo 15 and 17 landing sites, heat flow probes were deployed in drilled holes about 10 meters apart as shown in Figure 2.6, taken from Nagihara et al. (2018) [60]. Dual probes allowed for two independent measurements of heat flow, as well as analysis of lateral heat flow variations within the regolith. Subsurface data from these probes indicated that thermal conductivity increases significantly with depth, reaching values of 1.5×10^{-4} W/cm-K at a depth of 1 meter. This increase in conductivity correlates well with the increasing bulk density of the lunar soil at greater depths [57], offering key knowledge into the Moon's thermal properties.

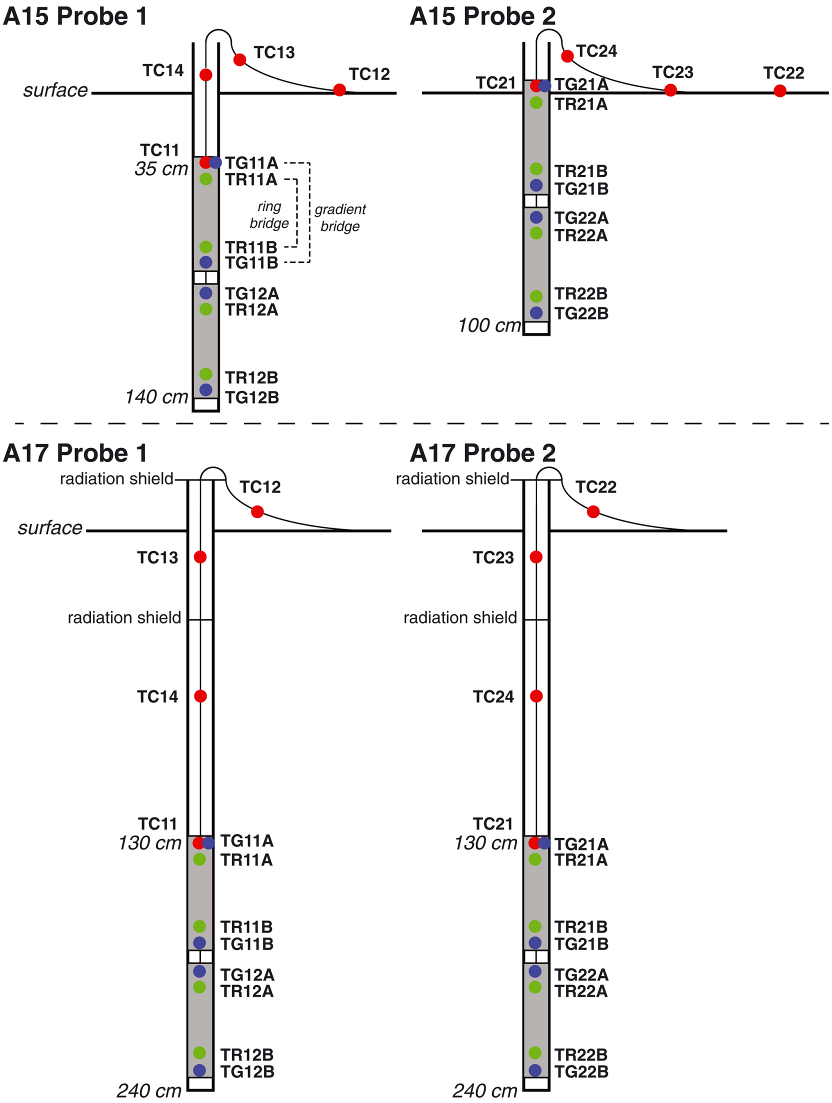

FIGURE 2.6: Schematic drawings describing the emplacement of the heat flow probes at the Apollo 15 and 17 landing sites. The temperature sensors are labeled. The red dots indicate the thermocouples. The blue dots indicate the gradient bridge resistance temperature detectors (RTDs). The green dots indicate the ring bridge RTDs. The probe hardware was almost identical between the two landing sites except that the Apollo 17 probes were equipped with radiation shields (Nagihara et al. 2018, Ref. [60]).

Based on the Apollo mission measurements, it was found that the upper 1–2 cm of lunar regolith exhibits extremely low thermal conductivity (1.5×10^{-5} W/cm-K), with conductivity increasing by a factor of 5 to 7 at a depth of 2 cm. At the Apollo landing sites, temperatures 35 cm below the surface were found to be 40–45 K warmer than those at the surface, primarily due to the temperature-dependent nature of thermal conductivity in the topmost layer of regolith [11]. Thermometers buried at 80 cm depth showed no detectable temperature variation related to the lunar day-night cycle, indicating that temperature profiles are driven by internal lunar heat flow beyond these depths.

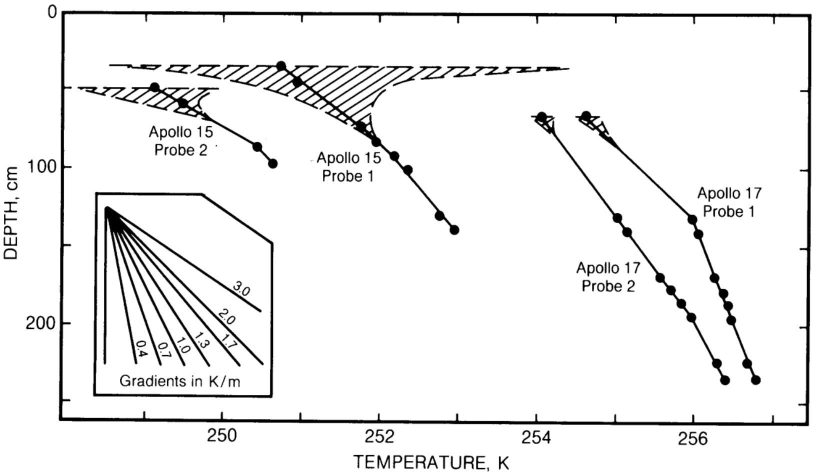

Figure 2.7: Temperature fluctuations in the lunar regolith as a function of depth. The shallow regions of the diagram (less than ~ 30 cm) are left blank due to extreme temperature variations that could not be plotted on the scale provided. The hatched areas represent day-night temperature fluctuations extending from ~ 30 cm to ~ 70 cm depth. Below ~ 50 cm, temperature fluctuations from lunar day-night cycles become negligible, and the steady temperature gradient observed at greater depths is attributed to internal lunar heat flow (adapted from Langseth and Keihm 1977, Ref. [11]).

Figure 2.7 (adapted from Langseth and Keihm (1977) [11]) illustrates the temperature profile in the lunar regolith, showing the near-surface fluctuations superimposed on the steady heat-flow gradient deeper in the soil. Notably, just 30 cm of regolith is sufficient to dampen the surface's extreme temperature fluctuations (ranging about 280 K) to a minimal ±3 K variation. This suggests that a lunar habitat buried beneath a thick regolith radiation shield would be protected from the extreme monthly temperature swings. However, an efficient system for dissipating waste heat would still be essential for maintaining a stable internal environment.

The heat flow measured at two lunar surface points, as well as estimates from microwave emission data, ranges from 2 to 4 $\times$ 10^{-6} W/cm^2, approximately half of Earth's average heat flow (6.3 $\times$ 10^{-6} W/cm^2) [22].

At the Rima Hadley site (25.0° N, 3.0° E) visited during the Apollo 15 mission, the average surface temperature was recorded at 207 K, rising quickly with depth to approximately 252 K at 90 cm. During the lunar night, the surface temperature plummeted to 93 K. The uppermost 2 cm of regolith, which was loosely packed, experienced significant temperature fluctuations with depth. Due to this variability, the regolith profile was divided into two layers for more accurate modelling. The top layer exhibited a thermal conductivity of 1.5 $\times$ 10^{-5} W/cm-K, while the compacted layer beneath had a conductivity of 1.4 $\times$ 10^{-4} W/cm-K [64].

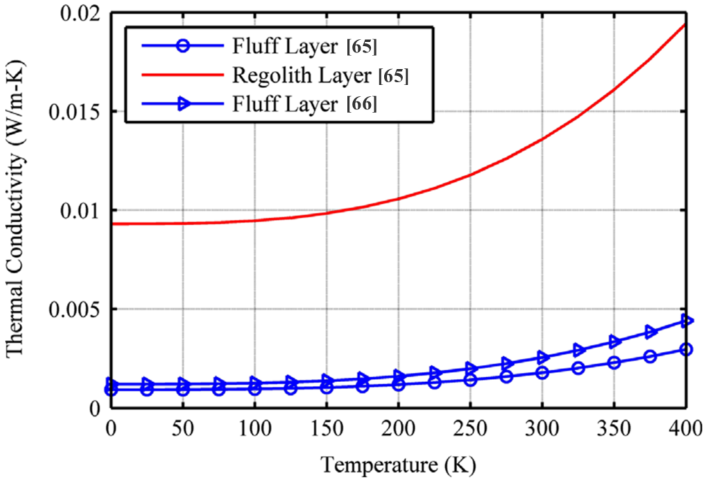

FIGURE 2.8: Comparision between different values of Thermal conductivity of lunar regolith. The first values for the "Fluffy Layer" and "Regolith Layer" were taken from Vasavada et al. 1999 (Ref. [65]) and values for the next "Fluffy Layer" were taken from Marov et al. 2007 (Ref. [66]).

At the Apollo 17 mission's Taurus-Littrow site (20.0° N, 31.0° E), the mean surface temperature was slightly higher at 216 K, rising quickly to 254 K at 67 cm depth. The minimum temperature just before dawn was 103 K, slightly warmer than that of Rima Hadley. As with Rima Hadley, the regolith was modelled with two layers of varying thermal conductivities: the upper 2 cm, the fluffy layer, had a conductivity of 1.5×10^{-5} W/cm-K, while the denser layer below exceeded 1.2×10^{-4} W/cm-K. The density of the compacted regolith ranged between 1.8 to 2.0 g/cm^3 [65].

The thermal conductivity of lunar regolith varies with temperature, and several studies have investigated this relationship to better understand the thermal characteristics of the Moon's surface. Marov et al. (2007) [66] provide a model for the thermal conductivity of the loosely packed lunar surface material ("fluff"), expressed as $k(T) = 1.2 \times 10^{-3}\,\text{W/m-K} + T^3 \times 0.5 \times 10^{-10}\,\text{W/m-K}^4$. A comparative study by Malla et al. (2015) [57], shown in Figure 2.8, illustrates the thermal conductivity of lunar fluff and deeper regolith layers as a function of temperature, using models from both Vasavada et al. (1999) [65] and Marov et al. (2007) [66].

The comparison reveals that the thermal conductivity of the fluff layer varies between the two models by 20–52% , depending on temperature. Despite this considerable difference in conductivity estimates, the resulting temperature profile of the regolith beneath the 2 cm thick fluff layer only differed by about 2%, demonstrating that the bulk thermal properties of the regolith remain largely consistent across different conductivity models.

The Moon is subject to various thermal input sources that significantly impact surface temperatures. The primary source is direct solar radiation, supplemented by internal

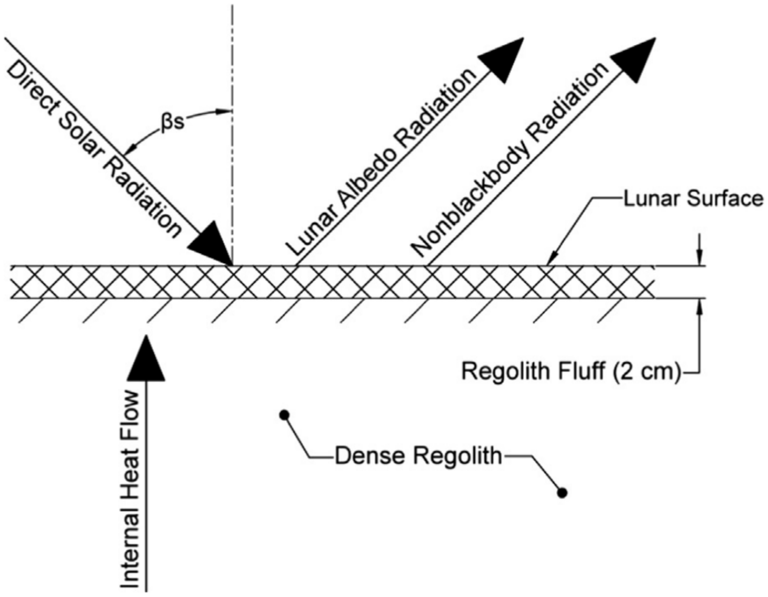

FIGURE 2.9: Illustrative representation of the thermal balance at the lunar surface. The diagram highlights the various heat input and output sources affecting the lunar surface environment. The angle of incidence, denoted as β_s, represents the angle between incoming solar radiation and a plane perpendicular to the lunar surface (Malla et al. 2015, Ref. [57]).

heat flow and a minor thermal contribution from the Earth. Solar radiation is the dominant factor in heating the lunar surface, with its intensity determined by the absorptivity of the lunar regolith and the Sun's radiation power, depending on the Moon's orbital position. The solar radiation power per unit area incident at the lunar surface can vary from a maximum value of 1450 W/m^2 at lunar noon to the minimum value of 0 W/m^2 throughout the night [64]. This variation is influenced by the Moon's rotation and the angle of incidence (β_s), which is the angle between the surface normal and the incoming solar radiation, as depicted in Figure 2.9 [57]. When solar radiation reaches the lunar surface, part of it is absorbed by the regolith, while the rest is reflected back into space as albedo radiation. The amount of absorbed radiation is dependent on the surface material's absorptivity, which is estimated to be 0.87 for lunar regolith [67].

In addition to solar radiation, the lunar regolith generates internal heat flow due to the presence of various minerals within the soil [64]. Measurements of heat flow and microwave emissions indicate that the average internal heating power is approximately 3.1×10^6 W/cm^2, which is, on average, about half that of the Earth (6.3×10^3 W/cm^2) [22].

However, the thermal balance on the lunar surface is not solely determined by heat input. For the Moon to maintain equilibrium, the energy absorbed by the surface must also be released back into space through heat output mechanisms. This balance between incoming and outgoing energy dictates the temperature of the lunar surface at any given moment.

The primary mechanism for heat loss from the lunar surface is thermal radiation, specifically in the form of infrared radiation emitted into space, also known as nonblackbody radiation. A blackbody, by definition, absorbs all incoming radiation and has a surface absorptivity of 1.0. However, because the Moon does not absorb all of the radiation that reaches its surface, it is classified as a nonblackbody. Nonblackbody surfaces are characterised by their emissivity, which is the surface's ability to emit energy as radiation, rather than absorb it completely [68].

The rate at which the Moon radiates heat is governed by several factors, including its surface temperature, emissivity, and the Stefan-Boltzmann law, which quantifies the energy radiated per unit area based on temperature:

$$P = \epsilon \, \sigma \, T^4 \tag{2.1}$$

where P is the power radiated per unit area ($\mathrm{W/m^2}$), ϵ is the emissivity of the object's surface (a dimensionless value between 0 and 1 indicating the efficiency of emission), σ is the Stefan-Boltzmann constant, 5.670×10^{-8} $\mathrm{W/m^{-}2\ K^{-}4}$, and T is the absolute temperature of the surface in K. During the lunar day, the surface absorbs significant heat, reaching high temperatures, but as the Sun sets, this heat is radiated back into space, leading to rapid cooling through the long lunar night.

In addition to the radiation it emits, the Moon also reflects a portion of the incoming solar radiation back into space. This reflected energy, known as albedo radiation, is influenced by the reflectivity of the lunar surface, which, as a nonblackbody, does not absorb all the energy it receives. The Moon's albedo (reflectivity) is approximately 0.13 (13%), which is the complement of its absorptivity (0.87, or 87%). Due to the opacity of the Moon's surface, transmissivity is effectively zero, so all unabsorbed radiation is either reflected or emitted [57, 69].

This interplay between absorption, reflection, and emission defines the thermal balance on the Moon, with nonblackbody radiation playing a key role in the extreme temperature fluctuations experienced across the lunar surface. These processes not only influence surface conditions but also affect the temperature profile as you move deeper into the lunar regolith.

One of the most critical factors is the impact of the topmost 2 cm fluff layer, which has a lower thermal conductivity than the denser, compacted regolith beneath. Due to its insulating properties, this fluff layer provides greater temperature shielding. Within the

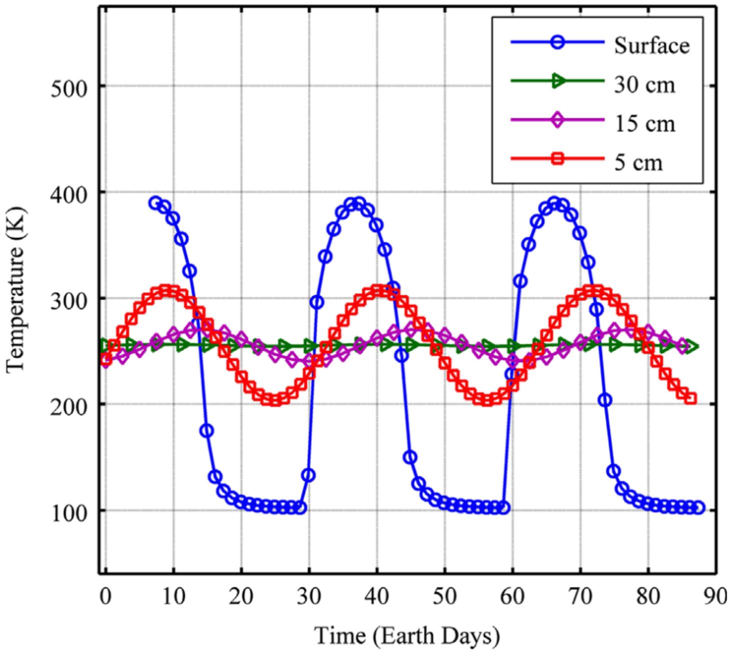

FIGURE 2.10: Subsurface temperature variation throughout lunar cycle (Malla et al. 2015, Ref. [57]).

first 5 cm of depth (including the fluff layer), the temperature drops by nearly 25%, from a peak of 387 K at the surface to 292.1 K—a reduction of 95 K. Below this point, the temperature decreases more gradually, reaching a constant value of 254.8 K at a depth of just 30 cm.

At night, the temperature profile follows a similar pattern. Starting at a low of 102.4 K on the surface, it rapidly increases to 209.4 K at a depth of 5 cm, followed by a slower rise to the same constant value of 254.8 K at 30 cm. Malla et al. [57] studied these temperature variations across the lunar day-night cycle at various depths, and Figure 2.10 presents these findings. Even at a depth of 5 cm, the temperature fluctuations closely follow a sinusoidal pattern, with the extreme highs and lows of the surface cycle significantly dampened, largely due to the insulating fluff layer. As depth increases, temperature variations diminish, leading to a more stable thermal environment.

For the purposes of this study, we will focus on the maximum temperature variation on the lunar surface to test materials under the most extreme conditions. As shown in Figure 2.10, this fluctuation ranges from approximately 400 K during the day to 100 K at night on the lunar surface (0 cm), providing the greatest challenge for material resilience. By understanding how the lunar regolith modulates extreme temperature fluctuations, we can select and design advanced materials and shielding technologies that harness the insulating properties of the lunar surface. The future of lunar exploration may well depend on these adaptive technologies, ensuring that human presence on the Moon is sustainable and resilient to its harsh thermal environment.

While a full lunar day or night spans approximately 14 Earth days, the thermal cycles applied in this study are limited to a few picoseconds due to the need for femtosecond time steps in MD simulations. Although these timescales are significantly shorter than those experienced on the Moon, the applied temperature variations are sufficient to reproduce the thermal stresses that induce atomic rearrangements in the material. The use of such temporally compressed thermal cycles is a common and practical approach in atomistic modelling, despite certain limitations. A more detailed discussion of this methodology and its associated constraints is provided in Section 4.2.1.

2.2 Overview of Space Materials

As we transition from the exploration of the Moon's extreme environment, it becomes clear that the selection and performance of materials are critical to the success of future lunar missions. The Moon's harsh temperature fluctuations, coupled with its vacuum, high energy proton (solar) radiation, and dust-laden surface, present significant challenges for both short-term exploration and long-term habitation. To thrive in such an environment the materials used in lunar structures must not only endure but also efficiently withstand these extreme conditions. This section will provide an overview of the key materials under consideration for use on the Moon and examine how their properties align with the demands of the lunar surface.

In the context of lunar exploration, material selection extends far beyond simply withstanding the physical stresses of launch and landing. As previously discussed, on the Moon, the temperature can swing between highs of over 400 K in direct sunlight to lows of 100 K during the lunar night. Materials must be chosen for their ability to function across this wide temperature range, resisting both thermal expansion and contraction, while maintaining their structural integrity. Additionally, the lunar surface is exposed to high levels of solar radiation, so materials must also possess strong radiation shielding capabilities. Durability, flexibility, and availability are other critical factors that will determine whether a material is viable for use in building lunar habitats or other essential equipment.

This section will introduce various classes of materials—metals, composites, ceramics, and polymers—that are being explored for lunar applications. Each class brings its own advantages and limitations to the table, and we will discuss how these materials can be tailored to meet the unique environmental demands of the Moon. As we move forward with lunar exploration, the understanding and development of such materials will play a pivotal role in ensuring the safety, sustainability, and success of human missions to the Moon.

2.2.1 *In situ* Materials

A natural progression from the development of a fundamental scientific understanding of the Moon's origins is to explore its potential as a resource. Space exploration is an undeniably costly venture, where the return on investment is often measured primarily by scientific discoveries. However, identifying extraterrestrial resources and developing methods to utilise them could dramatically shift this dynamic, reducing reliance on Earth-based resources and paving the way for financially sustainable space exploration programmes [70–73].

One of the most promising and sustainable approaches to achieving this goal is through *in situ* resource utilisation (ISRU), which focuses on sourcing materials directly from the lunar surface. ISRU represents a breakthrough strategy that minimises the need to transport vast quantities of materials from Earth, significantly reducing mission costs, complexity, and environmental impact. Utilising extraterrestrial resources is increasingly recognised as a critical enabling technology, essential for both the exploration and commercial development of space. For extended human presence and operations on other celestial bodies, learning how to harness indigenous resources is fundamental. The advantages of ISRU include its potential to reduce the mass, cost, and risk associated with human and robotic missions, while simultaneously creating new opportunities for the commercial exploitation of space resources [74].

Human exploration missions must also consider ISRU's role in environmental compatibility and sustainability. The cost of delivering payloads to the Moon is currently around $1 million per kilogram, making it imperative to explore alternatives. For long-term missions, a vital first step is the deployment of a lunar base module that can support human presence and operations. Establishing a base will be crucial for colonisation efforts and, importantly, for sustaining life by growing food in semi-permanent habitats. To achieve this it is essential to construct infrastructure on the Moon using locally sourced materials via ISRU [21]. This approach will be key to realising a future where lunar resources support not only exploration but also eventual infrastructure on the Moon.

Lunar exploration mission concepts focus heavily on the potential use of *in situ* materials such as lunar regolith, the solar wind volatiles, and water ice (particularly at the lunar poles) to produce essential resources like propellants, life support consumables, radiation shields, and materials for habitat and infrastructure construction [75]. Lunar regolith, the layer of loose, fragmented material that covers the lunar surface, varies in thickness from about 3 m to 20 m depending on location [76]. This regolith has been formed through billions of years of (micro-)meteoroid impacts, space weathering by thermal cycling, solar wind erosion, and particle comminution caused by impacts, which has led to the formation of a complex mixture of fine particles and rock fragments [56].

Lunar soils generally display log-normal particle size distributions, with typical mean diameters ranging from 45 mm to 100 mm, although the smallest particles can be as fine as 10 nm [77, 78]. These particles exhibit a variety of morphologies, from irregular and angular vesicular agglutinates to spherical glass beads, which are formed through both impact processes and explosive volcanic (pyroclastic) activities [76, 79, 80].

During the Apollo missions, 382 kg of lunar material was collected. The final mission, Apollo 17, brought back 111 kg alone. The regolith, used as filler in the rock box during transit, was separated from the rocks upon return to Earth and analysed in great detail. Among these samples, the fine-grained particles labeled 10084, famously referred to as "Armstrong's packing soil", have become some of the most studied geologic samples in history [8].

The lunar rocks were primarily composed of basalt, a volcanic rock that forms through partial melting in the interior of a planet or moon. These basalts were found to have a higher titanium (Ti) concentration than any basalts known on Earth but otherwise consisted of familiar minerals: the magnesium-iron-calcium silicate (Mg-Fe-Ca) pyroxene, the calcium-aluminium (Ca-Al) silicate plagioclase, with general formula $NaAlSi_3O_8$ – $CaAl_2Si_2O_8$, and the iron-titanium (Fe-Ti) oxide ilmenite, $FeTiO_3$ [8].

Radiometric dating revealed the lunar basalts to be over 3.5 billion years old, and isotopic analysis of both rock and regolith suggested that the Moon itself formed more than 4.4 billion years ago. Despite containing vesicles—evidence of gas release during volcanic eruptions—the basalts showed no signs of significant alteration and were nearly devoid of volatiles like water (H_2O) or carbon dioxide (CO_2) [81]. Unlike Earth's geological samples, lunar rocks were also entirely barren of any traces of life.

The regolith samples proved to be a treasure trove of diverse materials, offering valuable information into lunar history. They contained volcanic and impact glasses, breccias—rock fragments cemented together by the energy released during meteoroid collisions, and agglutinates, which are welded soil particles formed by micrometeorite impacts, as shown in Figure 2.11 (taken from Jolliff and Robinson (2019) [8]). The history of meteoroid and asteroid impacts on the Moon was evident in the way rock fragments had been scattered over distances of tens to hundreds of kilometers.

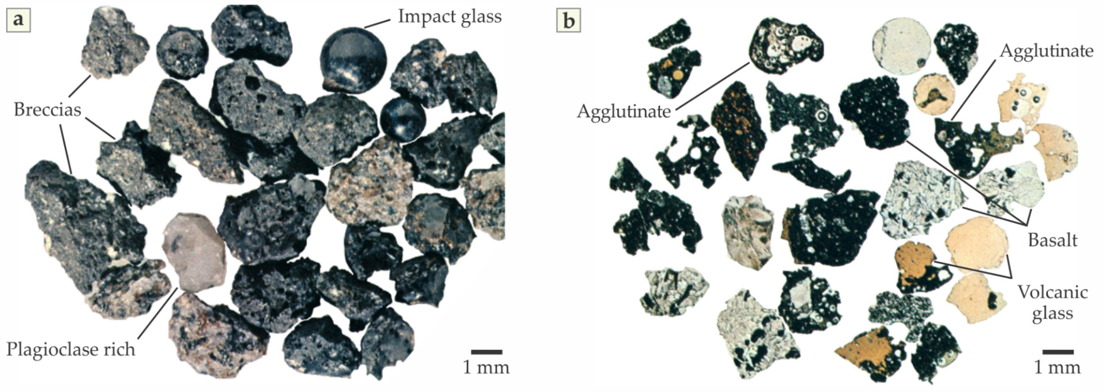

Figure 2.11: Soil particles from the Moon's surface regolith collected during the Apollo 11 mission. (a) The sample includes rock fragments (impact breccias), volcanic and impact glasses, fused particles (agglutinates), a light-colored plagioclase-rich fragment, and pieces of volcanic basalt. (b) The same rock particles have been sectioned into optically thin slices for examination under transmitted-light microscopy. (Images courtesy of John Wood, Smithsonian Astrophysical Observatory, Ref. [8]).

The lunar highlands are predominantly composed of a light-colored rock known as anorthosite, which is rich in Ca and Al. In contrast, the low-lying lunar plains are characterised by mare basalts, which are darker and contain heavier elements such as Fe, Mg, and Ti. It is believed that anorthosite magma floated to the surface of the Moon while it was still molten, solidifying as it cooled. The darker mare basalts, formed subsequently, resulted from lava that erupted from the lunar interior, filling vast mare basins. Lastly, meteoroid impacts give rise not only to impact breccias but also have the potential to melt surrounding rocks, producing volcanic glass [82].

One of the most extraordinary discoveries regarding lunar geochemistry was a clod of green pyroclastic glass beads [83]. These beads are believed to be originated deep within the Moon's mantle, being brought rapidly to the surface during a massive fire fountain eruption, without having enough time to crystallise. Perhaps the most famous sample collected with the aid of the lunar rover was the aptly named ”Seatbelt Rock”, a highly vesicular basalt, shown in Figure 2.12 [8], discovered by mission commander David Scott. With limited time and knowing mission control would not authorise a stop to collect it, Scott cleverly used the pretext of fastening his seatbelt to make a quick stop and pick up the rock—thus, earning it the name ”Seatbelt Rock” [84].

Evidence of lunar regolith wear on Apollo A7L and A7LB spacesuit models provided baseline estimates of regolith mineral composition using scanning electron microscopy (SEM) [85], as shown in Figure 2.13. These analyses reveal that lunar regolith comprises a diverse array of minerals, with the most abundant being plagioclase, pyroxene, olivine, ilmenite, and spinel. Minor minerals such as cristobalite, apatite, sulfides, and native metals like iron (Fe) and nickel (Ni) are also present [86]. The composition of these

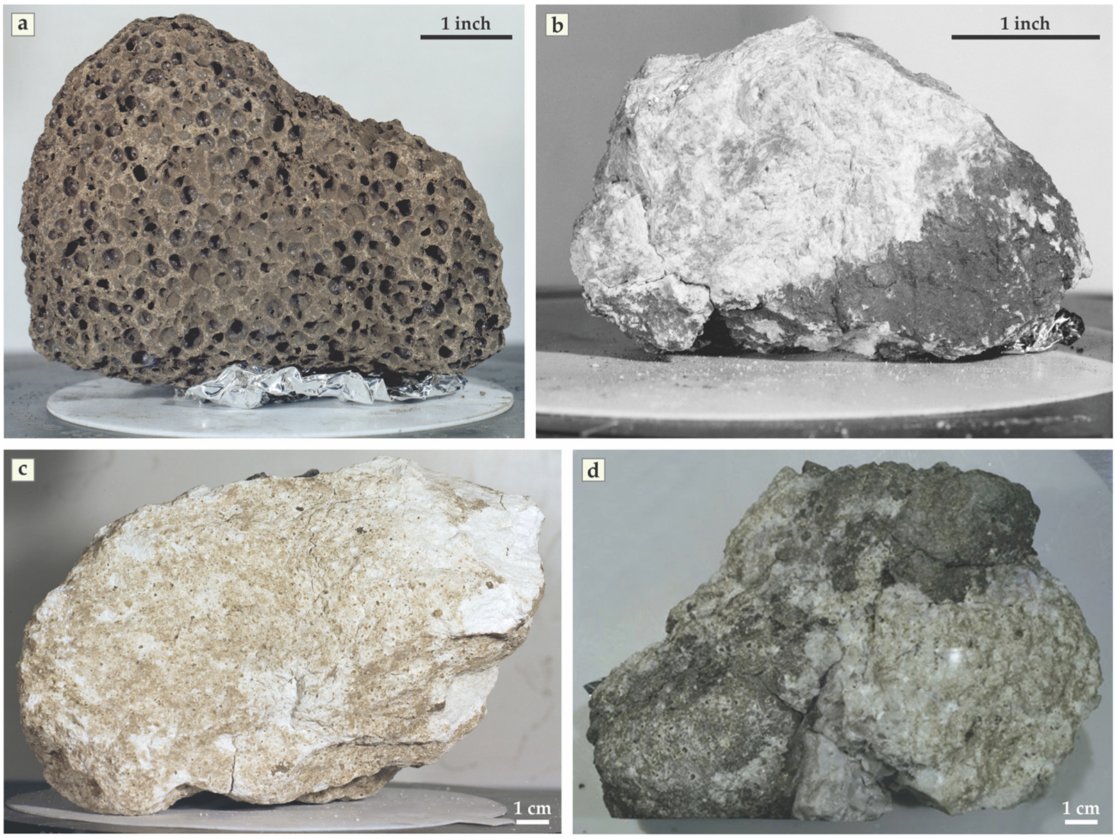

FIGURE 2.12: Rocks collected during the Apollo 15 and Apollo 16 missions. (a) ”Seatbelt Rock” (Sample 15016), a vesicular basalt characterised by its porous structure. (Adapted from NASA photo S71-46632.) (b) ”Genesis Rock” (Sample 15415), composed of ferroan anorthosite, a primary component of the lunar crust. (Adapted from NASA photo S71-44990.) (c) A 1.8 kg anorthosite sample, 60025, showcasing the mineralogy of the lunar highlands. (Adapted from NASA photo S72-42586.) (d) The top surface of ”Big Muley” (Sample 61016), an 11.7 kg breccia, featuring numerous small impact craters, or zap pits, from micrometeorite impacts. (Adapted from NASA photo S98-01215, Ref. [8]).

minerals varies significantly by location. For instance, basaltic terrains in the lunar mare regions are typically richer in ilmenite, olivine, and pyroxene, whereas the more primitive highland regions are dominated by calcium-rich plagioclase [87]. Furthermore, lunar soils exhibit localised compositions, often differing even within a few kilometers, suggesting that lateral mixing of materials is relatively limited [80].

A review on the Apollo Lunar samples reveals that a typical mare soil has a CaO content of nearly 12% by weight, highland soil 17%, basalt rocks 14% and anorthosite rocks, a calcium-rich plagioclase in the feldspar group, almost 19%. The lunar rocks and soils indicate that most lunar materials consist of sufficient amounts of silicate, alumina, and calcium oxide for possible production of cementitious material. Table 2.4, taken from Lin (1985) [88], shows the chemical compositions of some lunar samples studies by Morris et al. (1983) [89], Ryder and Norman (1980) [90], and Fruland (1981) [91].

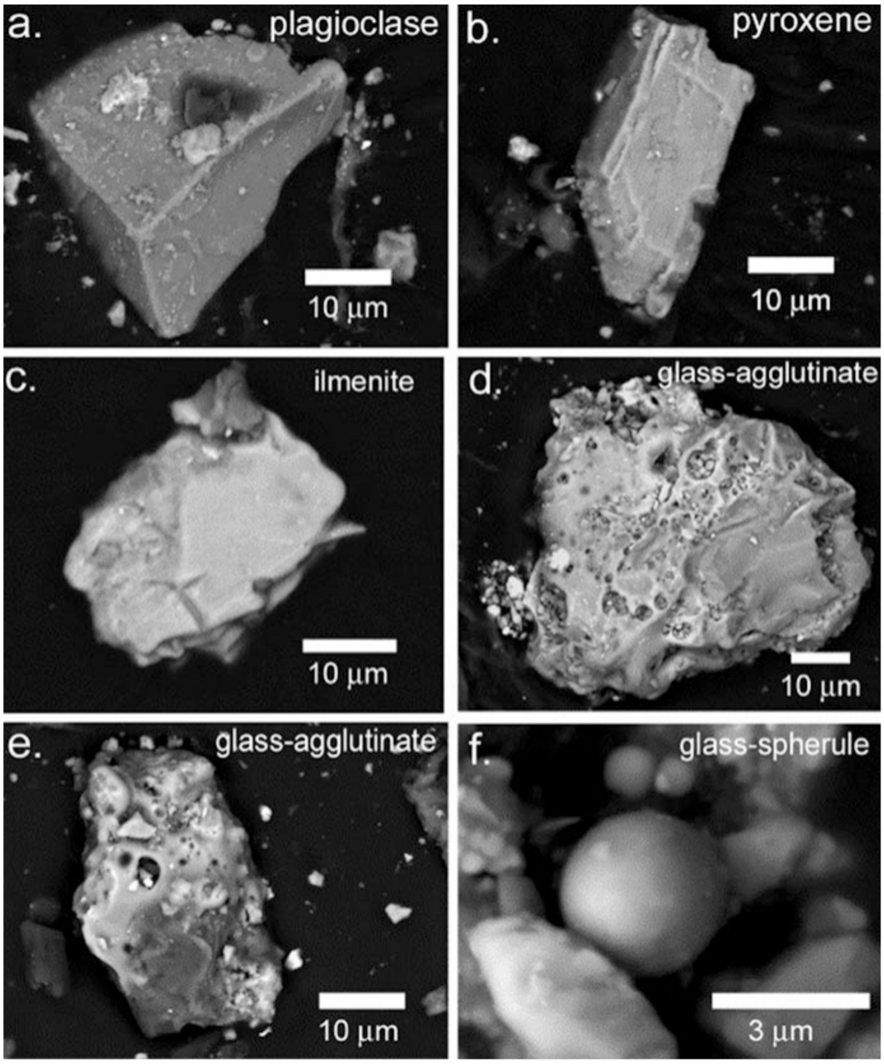

FIGURE 2.13: SEM backscattered images of particles of various mineralogical types from the surface of Apollo 17 spacesuit fabric layers. (a) plagioclase feldspar, (b) pyroxene, (c) ilmenite, (d) agglutinitic glass, and (e) impact glass spherules (Christoffersen et al. 2008, Ref. [85]).

The data presented in the Table 2.4 reveals that oxygen (O) and silicon (Si) are the most abundant elements on the Moon by atomic composition. Oxygen constitutes approximately 60% of the Moon's crust by weight, making it the dominant element. This is followed by significant quantities of Si, Al, Ca, Mg, Fe, and Ti. The concentrations of O, Si, and Al on the Moon are comparable to their proportions in Earth's crust (Kopal, 2020).

Among the compounds formed from these elements, silicon dioxide (SiO_2) accounts for 40-50% of the Moon's crust by weight. Ferrous oxide (FeO) and calcium oxide (CaO) each contribute approximately 10–20% of the crust's composition [92]. A deeper understanding of lunar geomorphology and geochemistry will be crucial for advancing both scientific research and industrial applications.

Table 2.4: Chemical Compositions of Selected Lunar Samples

Elements, wt %	**Mare Soil (10002)**	**Highland Soil (67700)**	**Basalt Rock (60335)**	**Anorthosite Rock (60015)**	**Glass (60095)**
SiO_2	42.16	44.77	46.00	44.00	44.87
Al_2O_3	13.60	28.48	24.90	36.00	25.48
CaO	11.94	16.87	14.30	19.00	14.52
FeO	15.34	4.17	4.70	0.35	5.75
MgO	7.76	4.92	8.10	0.30	8.11
TiO_2	7.75	0.44	0.61	0.02	0.51
Cr_2O_3	0.30	0.00	0.13	0.01	0.14
MnO	0.20	0.06	0.07	0.01	0.07
Na_2O	0.47	0.52	0.57	0.04	0.28

Silicate minerals are the most abundant minerals on the lunar surface, with the primary groups being olivine ($(Mg,Fe)_2SiO_4$), pyroxene ($(Mg,Fe)_2Si_2O_6$ – $(Ca,Mg,Fe)_2Si_2O_6$), and plagioclase ($CaAl_2Si_2O_8$ – $NaAlSi_3O_8$). Plagioclase has a low albite component, and K-feldspar ($KAlSi_3O_8$) is apparently a minor mineral on the Moon when compared with the Earth. Some locations with high abundances of specific minerals have been reported as endmembers of the Lunar Magma Ocean (LMO), which is the theorised molten layer that once enveloped the early Moon, leading to the differentiation and formation of its primary crust. These endmembers include the purest anorthosite (>98 vol% plagioclase) and olivine exposures with a dunite composition, as identified through global remote-sensing data [93, 94].

Oxide minerals are the second most abundant rock constituents. Among them, ilmenite ($FeTiO_3$) occurs most frequently on the Moon, as discussed before. It is commonly distributed in mare basalt, and its abundance varies largely from place to place [95, 96].

Silica (SiO_2) is generally rare in lunar materials when compared with lunar silicate and ilmenite, as mentioned above. However, it remains a significant and promising resource for building materials on the Moon. Although SiO_2 is often cited as a key component of lunar materials, its availability in crystalline or amorphous form is extremely limited on the Moon. While stoichiometrically SiO_2 may constitute 40–50% by mass of lunar rocks and soils, the silicon and oxygen atoms are almost always tightly bound within silicate minerals such as plagioclase and pyroxene [97]. Consequently, if SiO_2 is to be used as a structural material on the Moon, it would likely need to be extracted via energy-intensive processing of these silicate minerals. More detailed discussion in this context will be found in Papike et al. (1998) [97] and Taylor et al. (1993) [98].

Silica found in lunar samples can be traced to three origins: igneous processes, shock metamorphism due to impact events, and hydrothermal fluid activity. The first origin leads to silica polymorphs of cristobalite, tridymite, and quartz; the second to coesite, stishovite, seifertite, baddeleyite-type SiO_2, and high-pressure (HP) silica glass; and the third to moganite. There are many small granular inclusions with a size of 1–10 μm in the silica grains under optical microscope (Figure 2.14 (a) (top right), adapted from Ohtani et al. (2011) [99]). Raman spectroscopy demonstrated that most of the silica grains were amorphous because of missing Raman peaks, and the inclusions were coesite (522 cm^{-1}) (Figure 2.14 (a) (top left)) and quartz (464 cm^{-1}) [100]. The SR-XRD profile of the silica grain can be indexed into a seifertite structure (modified after [101]).

In addition to silicates, oxides of aluminium (Al_2O_3), iron (FeO), magnesium (MgO), calcium (CaO), and titanium (TiO_2). Oxides of sodium (Na_2O), potassium (K_2O), phosphorus (P_2O_3), manganese (MnO), and chromium (Cr_2O_3) occur in trace amounts [102]. Ilmenite is especially important for resource extraction as it contains Fe, Ti, and O. Studies, such as those by Brecher et al. (1975) [103], showed that heating lunar soil containing ilmenite at 1073 K (800°C in the presence of hydrogen led to the formation of metallic iron at the expense of ilmenite [103]. This reaction suggests that ilmenite could be a prime candidate for oxygen extraction on the Moon. Lunar soil, which contains around 45% oxygen by weight, represents a significant resource for oxygen production, critical for sustaining human presence and space travel.

Lunar silica and other materials, such as Al, Ti, Mg, and Fe, are vital for constructing lunar infrastructure. Silica is particularly important for making windows and solar cells, while Ti's strength-to-mass ratio makes it a valuable structural material. Large-scale mining could extract millions of tons of ilmenite annually, supporting lunar operations and broader space exploration [104].

Aluminium on the Moon is found primarily in plagioclase, and Apollo samples showed aluminum content ranging from 4.5 - 14.4%. Although the Apollo missions did not identify rich ore veins, Al can be extracted from lunar anorthosite through methods such as the melt-quench-leach process. This process has successfully recovered over 95% of the alumina from lunar ores, which can then be further refined through electrolysis or other techniques to produce Al metal [104].

Titanium, another essential material, can be obtained through the reduction of ilmenite. As mentioned before, when hydrogen is added to heated ilmenite, the reaction produces iron, titanium oxides, and water. Further refinement can yield pure Ti [105]. Since Ti production on Earth depends heavily on rutile, lunar titanium could enhance terrestrial supply chains and reduce dependence on Earth-based mining.

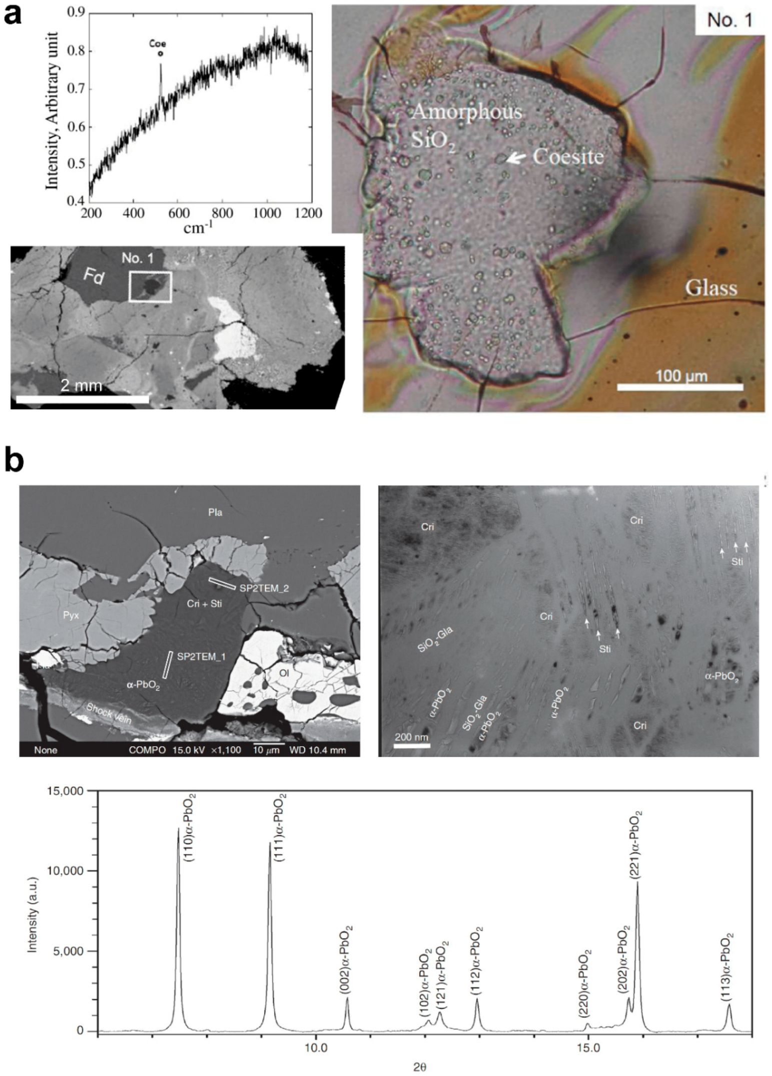

FIGURE 2.14: (a) Raman spectrum (top left), backscattered electron (BSE) image (bottom left), and optical microscopy photograph (right) of a silica grain in Asuka-881757. The amorphous silica grain (No. 1) is encased by glass with radiating cracks, suggesting expansion during pressure release. Numerous coesite (Coe) inclusions, ranging from 1–10 μm in diameter, are visible under optical microscopy, while the BSE image shows the grain surrounded by feldspar (Fd). The Raman spectrum of the inclusion exhibits a characteristic coesite peak at 521 cm^{-1}. (b) BSE image (top left), transmission electron microscopy (TEM) image, and synchrotron angle-dispersive X-ray diffraction (SR-XRD) pattern of a silica grain in NWA 4734. The grain contains seifertite (α-PbO2), cristobalite (Cri), and stishovite (Sti), and is enclosed by olivine (Olv), pyroxene (Pyx), and plagioclase (Plg), adjacent to a shock vein, as seen in the BSE image. TEM reveals nano-fragments of seifertite, cristobalite, and stishovite embedded in an amorphous silica glass (SiO_2–Gla) matrix. The SR-XRD profile is indexed to the seifertite structure. (Adapted from Ohtani et al. 2011, Ref. [99]).

Oxygen extraction from lunar materials has been studied extensively. Several methods, including hydrogen reduction of lunar basalt and mare soil, have shown promise in releasing oxygen. Experiments involving lunar basalt samples demonstrated that weight loss from oxygen release can reach up to 1.92% after reduction at high temperatures

[106, 107]. These techniques could be scaled up for future lunar missions, providing oxygen for life support and spacecraft propulsion.

Lunar glasses also represent a valuable resource. At least 25 distinct types of glass were identified in Apollo samples, with the iron- and titanium-rich varieties, such as Apollo 17's orange glass (22.0% FeO, 8.8% TiO_2), offering particularly high oxygen yields. Experiments by Brecher et al. (1975) [103] demonstrated that reducing lunar orange glass in hydrogen resulted in the conversion of iron oxides to micrometer-sized iron metal particles, along with the release of oxygen [108].

To summarise, the Moon's surface offers a wide range of materials essential for supporting various aspects of lunar exploration, from oxygen extraction to the production of construction materials. These local resources are invaluable in reducing the dependency on Earth for raw materials, significantly cutting down transportation costs and logistical challenges. However, despite the abundance of raw materials available on the Moon, the lunar environment is deficient in certain critical elements that are either scarce or impractical to extract efficiently with current technologies.

To establish a sustainable lunar base and support advanced technological infrastructure, the importation of specific resources becomes important. These imported materials not only bridge the gaps in availability but also ensure the continuity of vital systems for habitation, manufacturing, and scientific operations. The next section will elaborate on that.

2.2.2 Imported Materials

The most critical imported materials include volatile compounds (such as water, nitrogen, and hydrogen), certain metals, and specialised components for technological systems. Importing these materials poses both logistical and financial challenges, but innovative solutions, such as ISRU and advanced space transportation technologies, could mitigate these issues over time.

Findings from the LRO missions have shed light on how radiation alters H_2O chemistry across the Solar System [109]. Water is crucial for human survival, agriculture, and as a source of oxygen and hydrogen for rocket fuel. In 2008, the first signs of water on the Moon were discovered inside volcanic glass beads collected by the Apollo 15 and Apollo 17 missions in the 1970s. These beads formed when magma erupted and crystallised, trapping small amounts of water within. Since then, satellite data has revealed that these volcanic glass deposits are widespread across the lunar surface, hinting at a once water-rich lunar environment [3]. While this discovery does not indicate the presence of

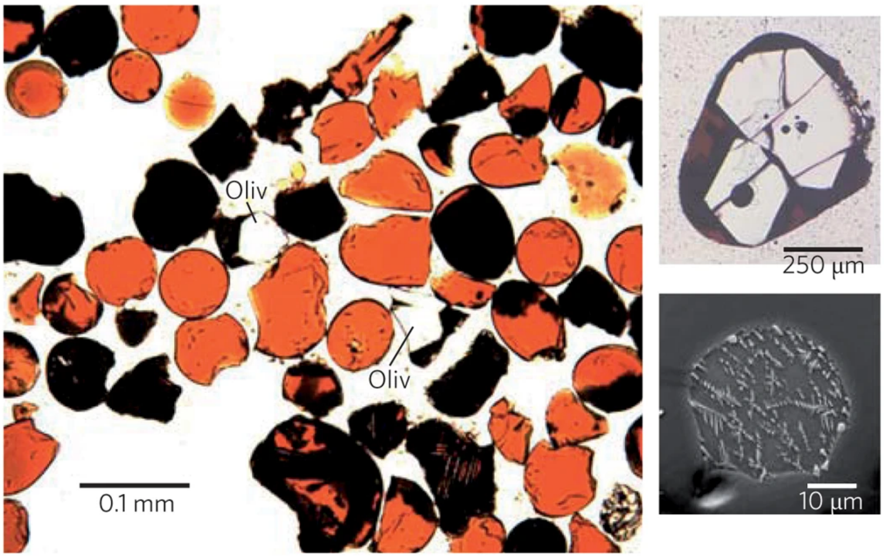

Figure 2.15: Optical micrograph of pyroclastic glass beads containing water from an Apollo sample. Left: Thin section of orange glass beads, showing olivine microphenocrysts (oliv) within some beads, though no melt inclusions are visible in this image. Right: Scanning electron microscope (SEM) images reveal olivine crystals containing trapped melt inclusions (top), many of which are partially crystallised (bottom). These melt inclusions provide insights into the volatile content and crystallisation history of the pyroclastic glass (Robinson et. al. 2014, Ref. [110]).

liquid water, it strongly suggests that the Moon's interior once held significant amounts of water. This is evident from the water trapped in pyroclastic glass during volcanic eruptions, as shown in Figure 2.15 (taken from [110]). Additionally, rocks from some regions of the lunar interior contain much higher water content than those from other areas [110].

The process of converting lunar ice into water and oxygen yields byproducts that can support various life-sustaining and industrial activities. These byproducts can be utilised for life-support systems (water and oxygen), crop fertilisation (carbon and nitrogen), rocket refueling (hydrogen and oxygen), construction materials (aluminium, iron, and silicon), and energy production (silicon solar cells and helium-3 nuclear fusion) [111]. Although water ice exists in permanently shadowed lunar craters, its availability may not be sufficient to meet all lunar resource demands. Hydrogen, while scarce, remains critical for many chemical processes, including water and fuel production.

The Moon is rich in Ti, Al, and Fe, but it lacks certain high-performance alloys and specialised metals required for advanced technologies like spacecraft, solar panels, and electronics. Until local lunar production capabilities advance, these essential materials will need to be imported from Earth.

Carbon, essential for producing plastics, organic compounds, and various industrial processes, is also scarce on the Moon. Importing carbon-based materials will be necessary to manufacture everyday items, from clothing and tools to life-support systems and energy storage technologies. While micrometeorite impacts deliver some organic compounds to the lunar surface, they are often destroyed by physical impacts and radiation [53]. To investigate the effects of solar radiation on the preservation of abiotic and biotic organic compounds in the presence of lunar minerals, Matthewman et al. (2016) [53] exposed various organic materials to proton irradiation simulating solar energetic particles. Table 2 lists the 12 irradiated samples, and Table 2.5 summarises the organic materials used. These materials were categorised into three groups: (1) hydrocarbon biomarkers, (2) polymers, and (3) amino acids. The study found that the presence of lunar regolith simulants promoted the preservation of intermixed organic matter [112].

Table 2.5: Sample Information for Organic Material, Substrate, and Fluence

Sample Number	**Organic Material**	**Substrate**	**Total Mass of Organic Material (mg)**	**Mass of Substrate (mg)**	**Fluence (protons cm^{-2})**
1	PSDVB[†]	Quartz wool	3.74	—	2×10^{14}
2		Quartz wool	2.83	—	3×10^{13}
3		JSC-1	0.97	19.79	
4		MAC 88105 powder	0.99	18.85	
5		H_2O/quartz wool	2.46	—	
6		Serpentinised mafic rock	1.03	19.62	
7	hydrocarbons	Quartz wool	~0.07	—	3×10^{13}
8		JSC-1	~0.07	21.24	
9		MAC 88105 powder	~0.07	20.00	
10	amino acids	Quartz wool	~0.05	—	3×10^{13}
11		JSC-1	~0.05	21.81	
12		MAC 88105 powder	~0.05	19.95	

[†] poly(styrene-co-divinylbenzene)

Carbon compounds, in particular, could play a critical role in construction by serving as a binder for lunar concrete. In experiments conducted by Chen et al. (2016) [113], they explored the use of inorganic–organic hybrid (IOH) lunar ”cements”—building materials created from locally sourced lunar regolith combined with polyethylene (PE). Figure 2.16 presents SEM images of fracture surfaces, which reveal a strong bond between the simulant particles and binder phase, demonstrating the potential of this material for lunar construction.

In addition to structural materials, light-transmitting polymers will be essential for habitat construction on the Moon. These polymers allow natural light to penetrate living spaces while providing protection from the harsh lunar environment, which is crucial for the well-being of inhabitants and reducing energy consumption for lighting. Studies comparing lunar concretes have identified materials that are lightweight, possess high tensile strength, do not require water for processing, and offer effective radiation shielding [114, 115]. Indeed, a recent assessment by Razeto et al. (2024) examined various polymers suitable for creating lunar habitat components that facilitate natural light transmission. The materials evaluated included versatile options such as polyvinyl fluoride (PVF), polytetrafluoroethylene (PTFE, commonly known as Teflon),

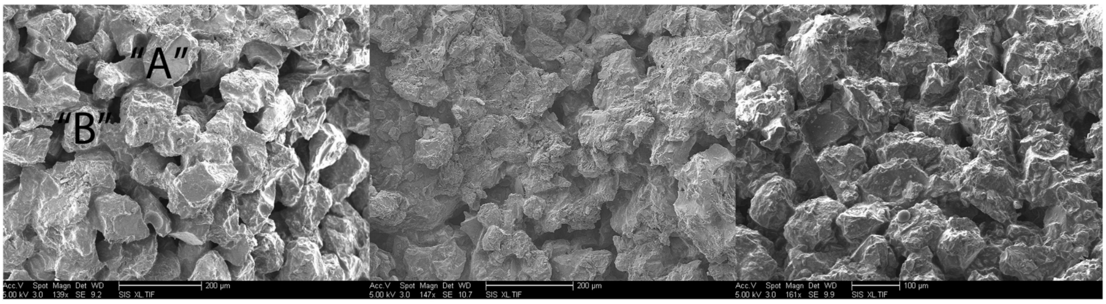

(a) (b) (c)

Figure 2.16: SEM images of three different lunar regolith simulant sample groups: (a) Group A contains only simulant grains sized between 90–112 μm; (b) Group B consists of as-received simulant with a natural, random grain-size distribution; (c) Group C features a two-step grain-size gradation, containing simulant grains of 90–112 μm and 20–25 μm in a weight ratio of 765:235. All samples have a binder content of 9.8% by weight (Chen et al. 2016, Ref. [113]).

polymethyl methacrylate (PMMA), high-density polyethylene (HDPE), silica aerogel, and biaxially oriented polyethylene terephthalate (BoPET). Although these polymers are, as discussed, not available in situ on the Moon, they can be imported for use in the early stages of lunar habitation. Their incorporation into habitat design could contribute significantly to creating liveable environments that are both functional and conducive to human health.

For protection against radiation, especially for astronauts, advanced shielding materials are critical. A study by Ma et al. (2022) [116] focused on Kevlar fiber as a potential protective material in a near-space simulated environment. Kevlar possesses excellent properties such as high strength, high modulus, and high temperature resistance, making it a strong candidate for reinforcing materials used in lunar habitats (Figure 2.17). Additionally, Kevlar's radiation-shielding capabilities were demonstrated in space tests aboard the International Space Station (ISS) during the ALTEA-shield European Space Agency (ESA)-sponsored programme (ALTEA: Anomalous Long-Term Effects in Astronauts Central Nervous System), showing a significant reduction in radiation exposure compared to polyethylene [117].

To further shield habitats from micrometeoroid impacts and direct solar radiation, regolith-based shields are being considered. Technologies like 3D printing could enable the use of lunar regolith to create protective layers for habitats, reducing the surface area exposed to space debris and radiation [115]. Regolith utilisation for additive manufacturing is becoming an intensely studied method for realising sustainable structures on the lunar surface.

While importing these materials from Earth may be costly and logistically complex in the short term, future advances in space transportation and resource extraction from other

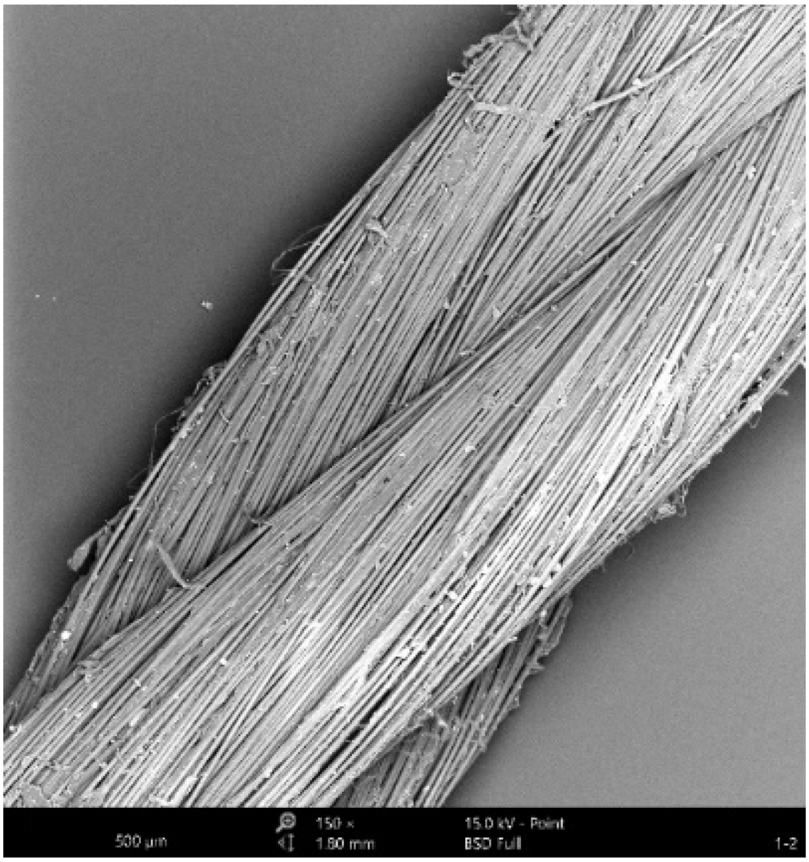

Figure 2.17: SEM image of Kevlar fiber showing a twisted bundle of microfibers. The fibers are closely packed and exhibit fine surface detail. The scale bar indicates 500 μm, and the image was taken at 150× magnification with a 15.0 kV electron beam (Ma et al. 2022, Ref. [116]).

celestial bodies, such as asteroids or Mars, could reduce reliance on Earth. Additionally, improvements in ISRU technologies may eventually enable the production of many of these essential materials directly on the Moon.

Ultimately, the efficient use of both lunar and imported resources will be critical in establishing a sustainable human presence on the Moon. As we look toward the future, developing the necessary infrastructure and technologies will support a continuous flow of materials between Earth, the Moon, and beyond, paving the way for long-term lunar habitation and exploration of other celestial bodies in our solar system.

2.3 Investigations of Thermal and Radiation Effects on Space Materials

Before moving to the next chapter, it is essential to outline recent experiments on space materials closely related to the computational studies conducted in this thesis. In April

2024, Mr. Jonathan Cousins, a PhD student at the University of Kent, conducted preliminary experiments at HUN-REN Atomki on high-density polyethylene (HDPE) $(C_2H_4)_n$, with a density of 0.95 kg/m^3, and Kevlar $(C_{14}H_{14}N_2O_4)_n$ fabric samples. HUN-REN Atomki, the Institute for Nuclear Research in Hungary, is a renowned research institute dedicated to advancing nuclear physics, particle physics, and related scientific fields. Known for its contributions to experimental and theoretical research, Atomki collaborates with many international institutions to explore nuclear reactions, fundamental particles, and applications in medical and environmental sciences. Since 2019, Atomki hosted two specially built beam lines, complete with experiment chambers to simulate space and planetary environments, particularly the solar wind. The HDPE sample measured 15 mm in diameter and 2 mm in thickness, while the Kevlar sample had a diameter of 15 mm and a thickness of 0.47 mm.

2.3.1 Polyethylene Experiments

The polyethylene experiments were conducted in three phases. The first phase involved irradiating a sample with a fluence of 2×10^{16} ions/cm^2 at 10 keV protons at 300 K, simulating approximately 42 years of solar wind proton exposure. This irradiation was performed in a vacuum chamber, as illustrated in Figure 2.18, with a pressure of 4.2×10^{-8} mbar.

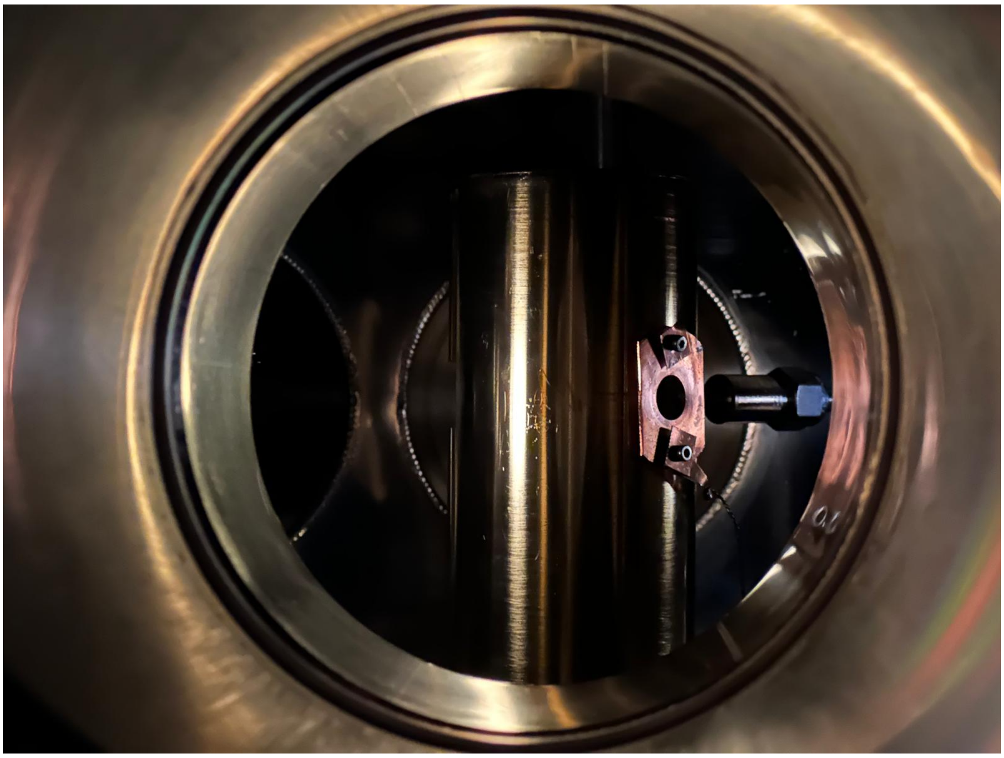

FIGURE 2.18: Vacuum chamber with a pressure of 4.2x10^{-8} mbar, holding a polyethylene sample for proton irradiation.

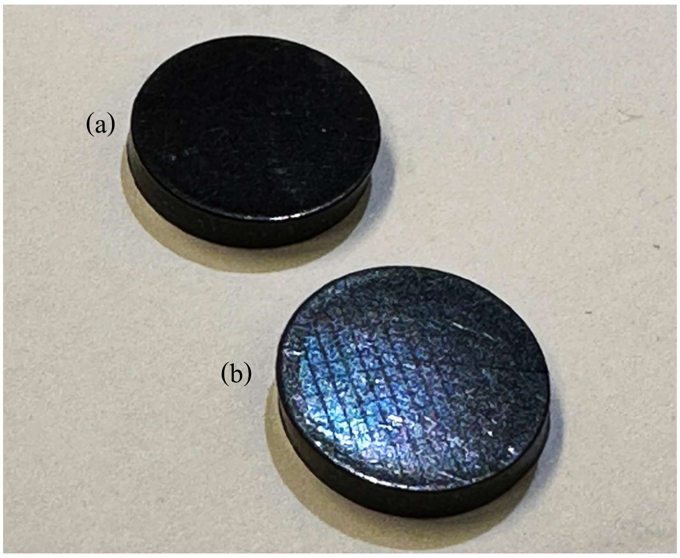

Figure 2.19: Effect of proton irradiation on the polyethylene sample: (a) The sample prior to irradiation, and (b) The sample after irradiation, exhibiting noticeable discoloration on the left side, likely corresponding to the area impacted by the proton beam.

The second phase subjected a separate set of samples to four temperature cycles ranging from 200 K to 350 K, with a rate of 5 K/min, to simulate lunar surface temperature variations. In the final phase, the samples were exposed to both temperature cycling (200 K to 350 K) and proton irradiation, replicating 42 years of combined solar wind and thermal cycling effects.

Post-experiment observations of the polyethylene sample under an optical microscope revealed notable changes. In the first phase, the simulated 42-year proton irradiation resulted in visible surface degradation due to ionisation and excitation from radiation interactions, which induced structural modifications. The most immediate visual change was discolouration, as shown in Figure 2.19, likely caused by chemical transformations, such as free radical formation and oxidation state changes affecting the sample's surface composition [118]. Additionally, a crack with a depth of 9.41 μm was detected (Figure 2.20), possibly due to increased material hardness from cross-linking between polymer chains [119]. Surface deposits up to 11.52 μm in height were also observed, likely originating from interactions between the ion beam and the mesh in the sample holder, which melted and transferred onto the sample during irradiation.

In the second phase, involving thermal cycling between 200 K and 350 K, the surface changes were less pronounced than in the first phase. Figure 2.21 shows minor surface scratches, with a depth of 4.07 μm, and deposits up to 9.74 μm in height, though no significant cracking occurred. Large circular impression marks were also observed, likely caused by pressure during the cutting process. These marks remained unchanged throughout the temperature cycling. The HDPE sample, with a melting point of 403 K,

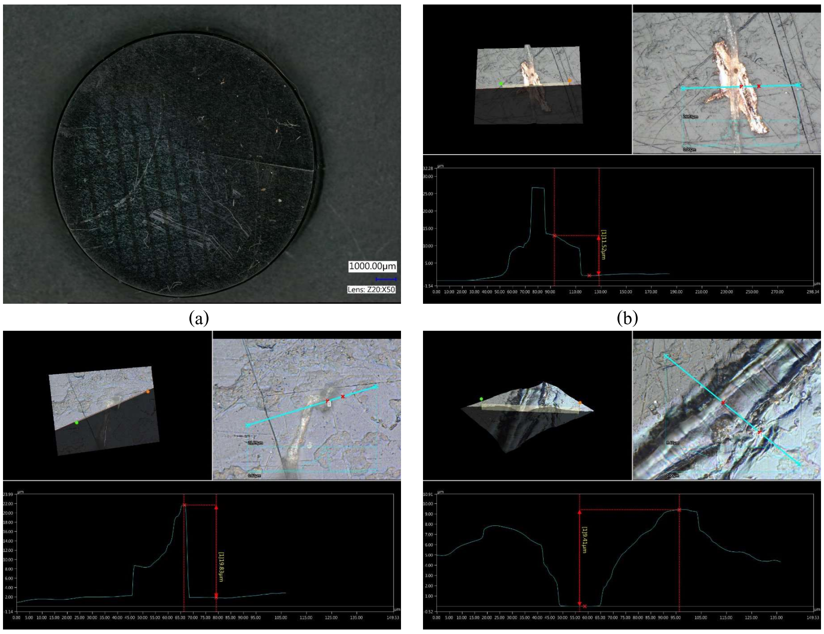

(a) (b)

(c) (d)

FIGURE 2.20: Optical microscope images (500x magnification) showing surface changes on the polyethylene sample after proton irradiation: (a) The irradiated sample displaying surface scratches and cracks, (b) Surface deposition with a measured height of 11.52 μm, (c) Another deposition on the surface with a height of 19.83 μm, and (d) A crack on the surface with a depth of 9.41 μm.

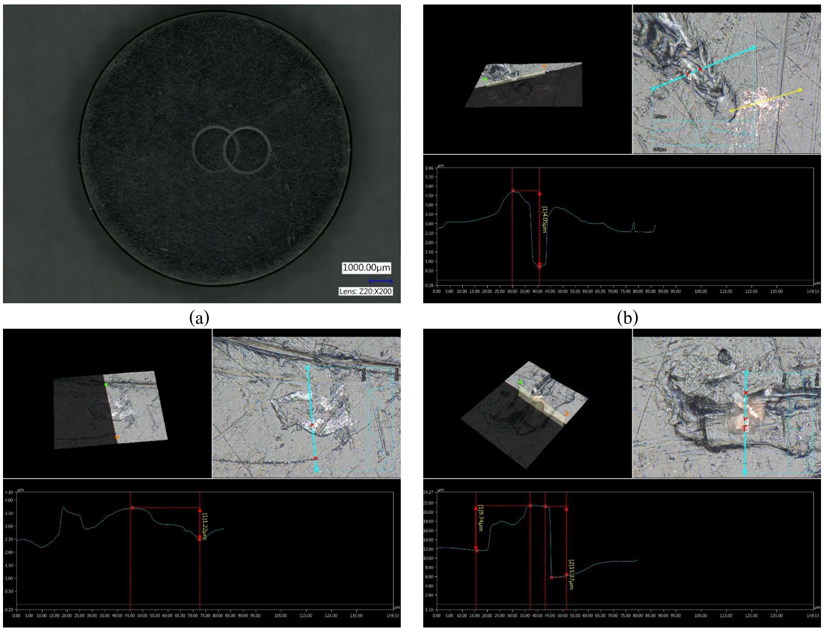

(a) (b)

(c) (d)

FIGURE 2.21: Optical microscope images (500x magnification) showing surface changes on the polyethylene sample after temperature cycle between 200 K and 350 K: (a) The sample after the temperature cycle displaying surface scratches, (b) A crack on the surface with a depth of 4.05 μm (c) Surface deposition with a measured height of 1.22 μm, and (d) Another deposition on the surface with a height of 9.74 μm.

demonstrated strong resistance to amorphisation, which is consistent with its crystallisation behaviour [120]. Although extended exposure could lead to plastic deformation, the material maintained good stability under the temperature cycles applied in this phase.

In the final phase, combining temperature cycling and proton irradiation, similar surface changes were observed. As shown in Figure 2.22, surface deposits of 6.49 μm and 68.36 μm were measured, along with a crack depth of 13.23 μm. This crack was deeper than those observed in the separate proton irradiation or temperature cycling phases, likely due to the compounded effects of temperature and radiation. During the high-temperature portion, approaching HDPE's melting point, the concurrent proton irradiation likely exacerbated surface damage. Upon cooling, thermal cycling partially closed some of the surface cracks, though deeper cracks persisted, indicating incomplete healing. This self-healing potential of polyethylene during thermal cycling highlights its suitability for withstanding combined temperature and radiation exposure over extended periods, such as the simulated 42-year duration.

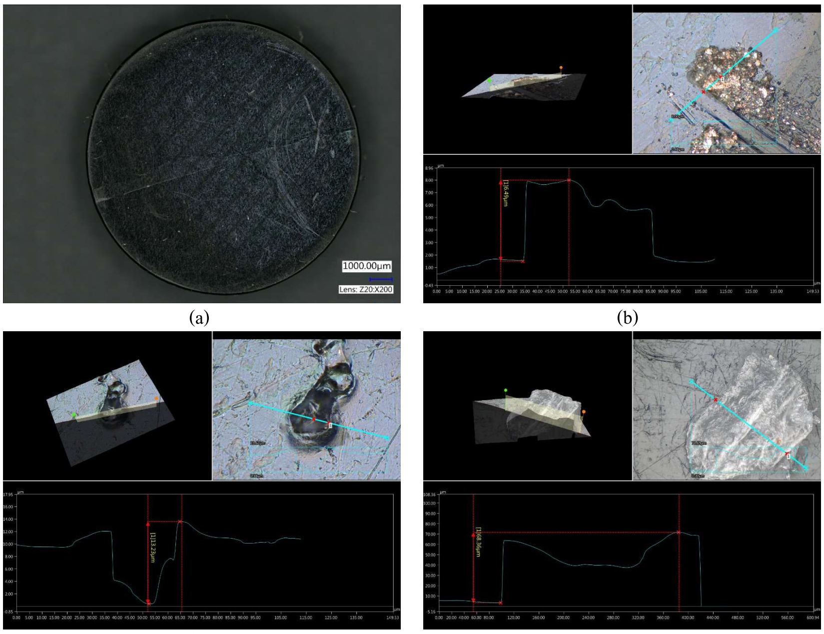

(a) (b)

(c) (d)

Figure 2.22: Optical microscope images (500x magnification) showing surface changes on the polyethylene sample after a simultaneous combination of both temperature cycling (200 K to 350 K) and proton irradiation: (a) The sample after irradiation and temperature cycle displaying surface scratches and cracks, (b) Surface deposition with a measured height of 6.49 μm, (c) A crack on the surface with a depth of 13.23 μm, and (d) A large deposition on the surface with a height of 68.36 μm.

2.3.2 Kevlar Experiments

Experiments similar to those conducted on polyethylene were also performed on the Kevlar fabric sample. To maintain the fabric's integrity, the sample was secured with cellophane tape on both sides to preserve its shape during testing. The sample underwent proton irradiation with a fluence of 2×10^{16} ions/cm^2 at 10 keV protons at 300 K, simulating approximately 42 years of solar wind exposure within a vacuum chamber, as shown in Figure 2.23, at a pressure of 4.2×10^{-8} mbar. Unlike many polymers that experience significant mechanical and chemical alterations under high-energy proton exposure, Kevlar exhibited exceptional resistance to irradiation. Although the cellophane tape melted under the proton beam, the Kevlar fabric remained completely unaffected, as illustrated in Figure 2.24. This resistance aligns with findings by Narici, Casolino, and Di Fino [117], who, using the ALTEA silicon detector units (SDUs) particle telescope, highlighted Kevlar's superior impact resistance and flexibility, particularly in deep-space-like radiation environments, which underscores its potential for integrated shielding applications.

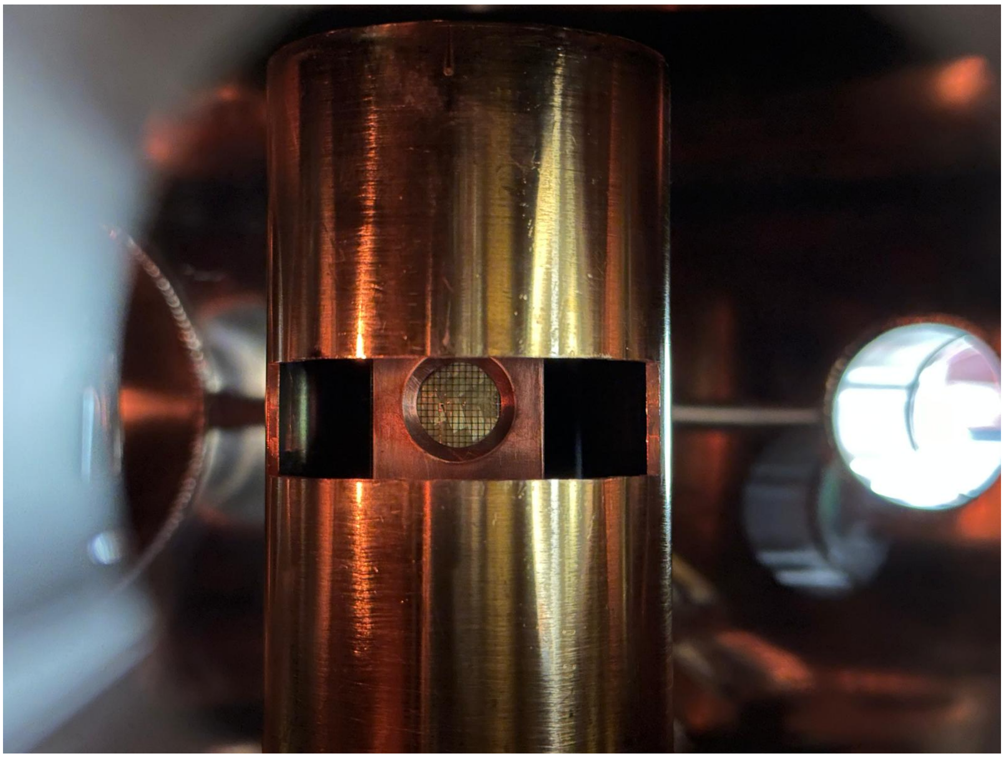

FIGURE 2.23: Vacuum chamber with a pressure of 4.2x10^{-8} mbar, holding a Kevlar fabric sample for proton irradiation.

These findings underscore Kevlar's potential in radiation shielding applications, while polyethylene, despite being a versatile polymer, exhibits notable surface degradation under similar conditions. These experiments establish a foundational benchmark for further analysis and modelling. By comparing the molecular changes induced in polyethylene

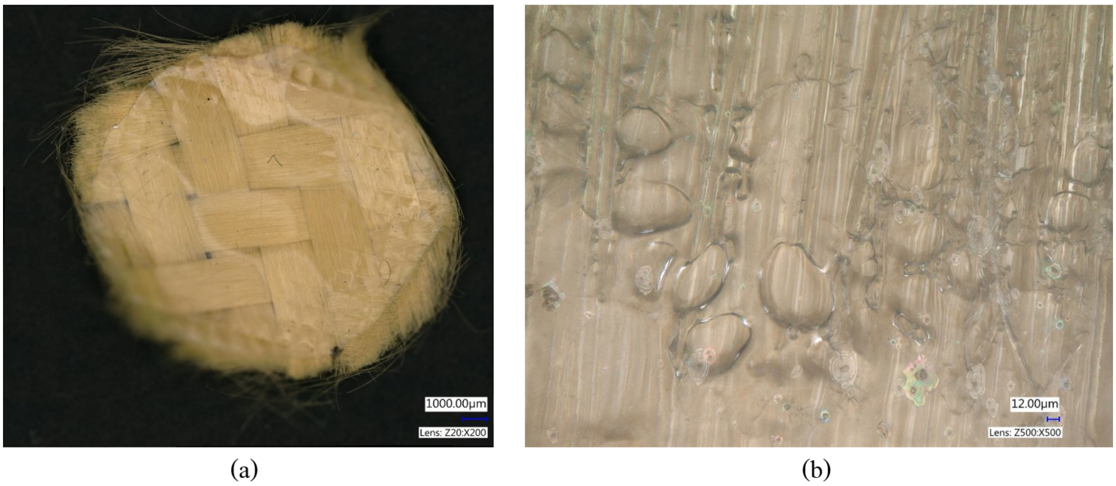

(a) (b)

Figure 2.24: Optical microscope images (500x magnification) illustrating the effects of proton irradiation on the Kevlar sample: (a) The irradiated Kevlar fabric showing no visible damage or structural changes, and (b) The Kevlar sample with melted cello tape coating, which liquefied during irradiation while the fabric remained unaffected.

and Kevlar under proton irradiation and temperature cycling, predictive models could be developed to better understand the mechanisms of degradation at the molecular level, providing a deeper understanding of how polymers respond to space-like conditions and guiding the development of more resilient materials for aerospace applications.

Chapter 3

Theoretical Framework

To achieve the objectives of this research, a multiscale modelling approach has been employed, bridging the gap between detailed atomistic simulations and practical, real-world applications. Through the integration between experimental data and advanced computational tools, this study aims to provide a comprehensive understanding of material performance under lunar conditions. The use of multiscale techniques allows for the investigation of complex physical phenomena across different length and time scales, uncovering key points that are potentially both fundamental and application-driven.

The chapter begins with an overview of the computational tools used, followed by a detailed exploration of multiscale molecular dynamics (MD) simulations. The Meso-Bio-Nano (MBN) Explorer software is introduced as a key platform for conducting these simulations, and its capabilities are discussed in terms of their application to lunar material studies. The chapter also describes the simulation parameters used, with a focus on the specialised technique of Irradiation-Driven Molecular Dynamics (IDMD), a method crucial for understanding how radiation affects material properties. Finally, previous works utilising IDMD will be reviewed to contextualize the contributions of this research to the field.

3.1 Multiscale Molecular Dynamics

Multiscale modelling has emerged as a powerful and promising computational paradigm, gaining recognition across various scientific disciplines, including the broad field of process engineering [121–123]. Unlike traditional single-scale models, which operate within a single level of detail, multiscale modelling combines simulations at different resolution scales, from the atomic to the macroscopic, to capture the full complexity of a system

[124]. Through the integration of multiple scales, this approach has the potential to offer a high-quality characterisation of complex systems at an enhanced computational efficiency. It enables to address phenomena occurring at different levels of granularity, making it especially valuable in disciplines where interactions between scales are crucial, such as in chemical processes, materials design, and biological systems.

In process engineering, for instance, multiscale modelling sheds light on intricate processes that occur at both the molecular and system levels. It allows for the detailed analysis of microscopic phenomena, such as chemical reactions, and their larger-scale impacts, such as production efficiency or process optimisation [124]. They can capture fine-grained details while maintaining computational feasibility for large-scale simulations.

Computational modelling is becoming increasingly essential as the power and capabilities of modern computers continue to advance. Today, engineering and scientific problems can be thoroughly investigated through numerical simulations, whether at the atomic scale or within a continuum framework, thereby minimising many of the inherent limitations of experimental approaches. The range of scales at which systems, such as nano-lubricated films, can be analysed is broad, and as a result, a variety of simulation techniques have been developed. However, each scale brings its own set of challenges that must be addressed during the modelling process. Figure 3.1, taken from Ewen et al. (2018) [125], illustrates some common simulation methods applicable across different time and length scales.

At one end of the spectrum, long time and length scales are handled using macroscopic continuum methods, such as finite element analysis (FEA), finite difference analysis (FDA), or computational fluid dynamics (CFD). These methods rely on solving governing equations, like conservation laws, which are coupled with constitutive relationships to describe the material properties. While these techniques are well-suited for most engineering applications, they come with specific limitations. For instance, the validity of continuum models hinges on the assumption that material properties remain constant across the entire volume represented by the elements, which may not always hold, particularly in complex or heterogeneous materials.

Moreover, macroscopic models often oversimplify real-world phenomena, relying heavily on empirical data. As a result, they are typically only accurate under narrowly defined conditions. These limitations are further compounded by the need to incorporate transport coefficients—such as thermal conductivity or viscosity—into the model, which can vary significantly under different operational conditions. Despite these challenges, macroscopic continuum methods remain indispensable for studying large-scale systems, provided that their assumptions and constraints are carefully considered [126].

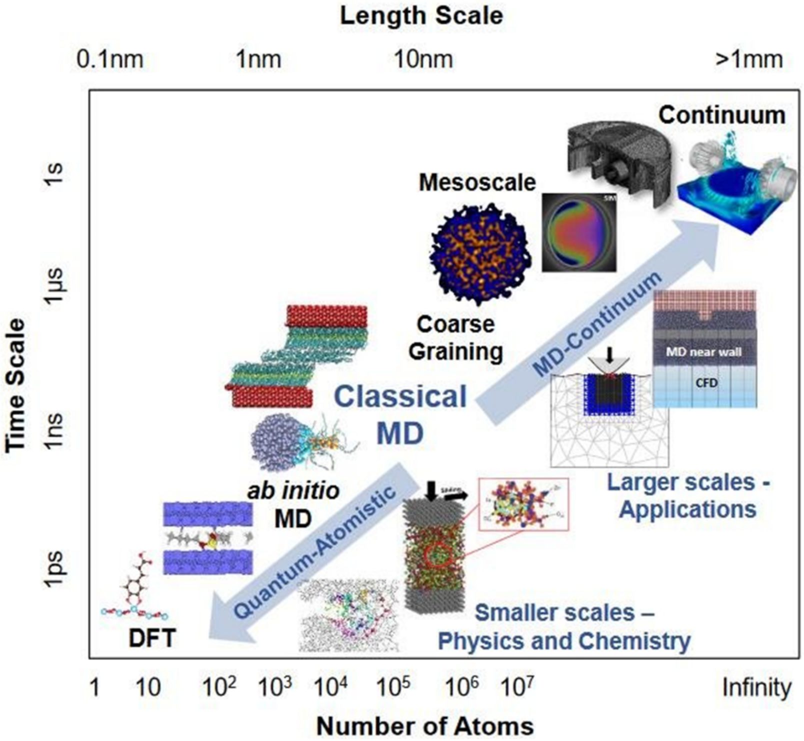

FIGURE 3.1: Simulation through the different scales, from first principle simulations (quantum) to continuum simulations (Ewen et al. 2018, Ref. [125]).

Many of the limitations associated with macroscopic simulations can be mitigated by employing smaller-scale approaches, such as Molecular Dynamics (MD) simulations. Originally introduced in the late 1950s by Alder and Wainwright, the MD method was devised as a way to solve Newton's equations of motion for systems consisting primarily of particles modelled as hard spheres. Initially developed to study phase transitions and the interfacial behaviour of simple molecular systems, MD simulations have since expanded their scope, becoming indispensable for investigating complex phenomena across various fields, including physics [127–130], chemistry [131–133] and biology [134–137], and any system where molecular-scale effects play a critical role [138–140].

What makes MD simulations particularly powerful is their ability to calculate structural, chemical, and dynamic parameters that are inaccessible through larger-scale methods, such as mesoscale coarse-graining techniques or continuum models. To illustrate, one field where these methods prove particularly relevant is tribology, where MD simulations provide unparalleled insights into the configuration traits of highly confined liquid films. These films, which are notoriously difficult to study experimentally, are critical in applications involving lubrication at the nanoscale [141].

However, despite their versatility, MD simulations come with their own set of challenges. One significant hurdle is the validation of MD results against experimental data. MD and experiments operate in very different time and length scales, which complicates direct comparison. For example, MD simulations typically analyse lubricant film thicknesses of just a few nanometers (comprising only a few molecular layers) and cover timescales of only a few nanoseconds. This results in deformation rates that are several orders of magnitude higher than those found in experiments [142]. Furthermore, MD simulations are confined to small nano-sized patches, typically just a few square nanometers, and assume constant pressure and temperature conditions. This contrasts sharply with real-world elastohydrodynamic lubrication, where pressure and temperature vary across gradients.

Despite these challenges, MD simulations remain invaluable for studying nano-confined fluids. They not only offer precise control over variables such as temperature and pressure [143], but also allow the capture of phenomena like phase transitions, which are critical to understanding molecular-scale interactions in confined environments [129, 144]. This makes MD a crucial tool in bridging the gap between atomic-scale understanding and practical, real-world applications.

MD is a powerful, explicit computational technique that simulates the time evolution of a system of interacting particles by solving Newton's equations of motion directly [127]. At any given time t, the position r_i of every particle i within the system is known. The system's potential energy, denoted by U, is defined as a function of interatomic distances and various particle interactions, governed by force fields. These force fields describe the relationships between a particle and its neighbouring particles, incorporating forces such as van der Waals, electrostatic, and covalent bonding.

The total force f_i acting on each particle in the system is derived from the gradient of the potential energy U, following the principles of classical mechanics [127]. The relationship is expressed as:

$$f_i = -\nabla_{r_i} U \tag{3.1}$$

This formulation enables the calculation of how each particle moves over time by integrating the equations of motion, thereby providing a detailed, dynamic picture of the system's characteristics at the molecular level. MD simulations thus offer the ability to investigate the complex interactions and emergent properties of materials and systems across a wide range of scientific disciplines.

Once the force f_i acting on particle i is determined, the particle's acceleration $\vec{a}_i$ can be directly calculated using Newton's second law of motion. This law relates the force acting on a particle to its acceleration, with m_i representing the particle's atomic mass:

$$\vec{a}_i = \ddot{r}_i = \frac{f_i}{m_i} \tag{3.2}$$

Generally, the Verlet algorithm [145] is used to compute the new position of a particle at an updated time $t + \delta t$ by performing a double integration, where δt represents the time step length. For the algorithm to function effectively, the particle's position at the previous time step $t - \delta t$ must also be known:

$$r_i(t + \delta t) = 2r_i(t) - r_i(t - \delta t) + \delta t^2 \ddot{r}_i(t) \tag{3.3}$$

This method is straightforward to implement, time-reversible, and does not require initial velocity input, simplifying the computation. If velocities are needed, they can be estimated through finite differences:

$$\dot{r}_i(t) = \frac{r_i(t + \delta t) - r_i(t - \delta t)}{2\delta t} \tag{3.4}$$

The accuracy of these calculations relies on the choice of the time step δt. Equation 3.3 has an associated error of order δt^4, while the error in Equation 3.4 is of order δt^2 [127, 142]. Therefore, selecting an appropriate δt is crucial to maintaining the stability of the algorithm and conserving the system's total energy over time.

While the classic Verlet algorithm is effective, two enhanced variants are commonly employed in MD to improve the accuracy of position and velocity calculations: the Velocity Verlet and Leapfrog algorithms. The Velocity Verlet algorithm modifies the classic Verlet method by calculating both positions and velocities at each time step, which allows direct computation of velocity-dependent properties and improves energy conservation in MD simulations. The Velocity Verlet update equations are:

$$r_i(t + \delta t) = r_i(t) + \dot{r}_i(t)\delta t + \frac{1}{2}\ddot{r}_i(t)\delta t^2 \tag{3.5}$$

$$\dot{r}_i(t + \delta t) = \dot{r}_i(t) + \frac{1}{2}\left(\ddot{r}_i(t) + \ddot{r}_i(t + \delta t)\right)\delta t \tag{3.6}$$

The Leapfrog algorithm, on the other hand, calculates velocities at half time steps, $t+\delta t/2$, rather than at full time steps. In this method, velocities and positions "leapfrog" over each other, with positions updated at t and velocities at $t + \delta t/2$, improving numerical stability and energy conservation.

In MD simulations, these algorithms are used iteratively to model atomic motion over very short time steps, typically on the order of femtoseconds (10^{-15} s), to accurately

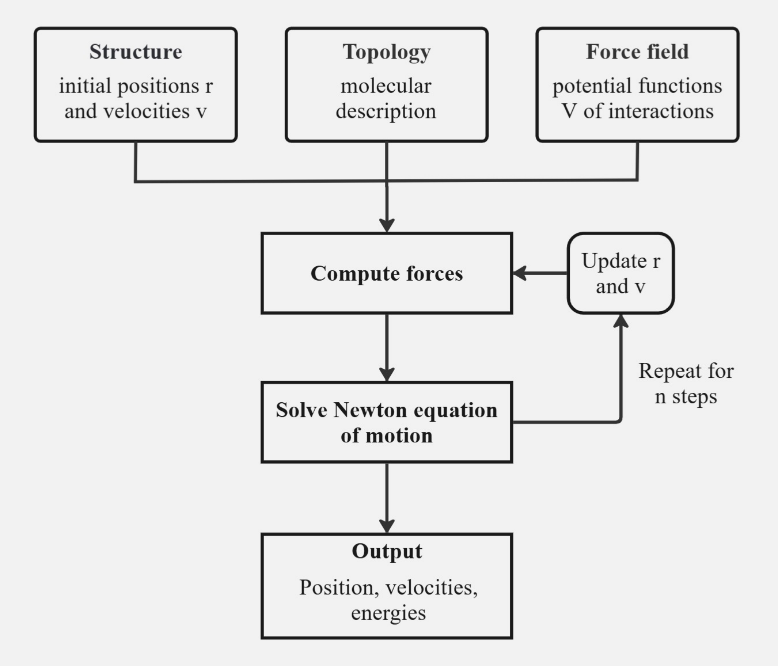

FIGURE 3.2: Flow chart of the Molecular Dynamics method during a time step of the simulation (Sonavane et al. 2014, Ref. [146]).

capture atomic interactions. The small time scale ensures that the positions and forces on atoms remain stable between consecutive steps, which is essential for conserving the system's total energy. Figure 3.2 [146] illustrates the steps involved in a single MD simulation time step.

Force fields characterise the behaviour of molecules by modelling all interactions between the constituent atoms of a molecule, as well as between atoms of neighboring molecules, based on their positions within the system [147, 148]. They encompass both the mathematical representation of potential energy associated with these interactions and a corresponding set of parameters for their coefficients. Selecting an appropriate force field is essential for accurately predicting material properties, leading to a wide variety of force fields available in the literature, derived from either experimental data or quantum-mechanical calculations.

The potential energy function defined by the force field can be divided into two components [127], as shown in equation 3.7. The first component addresses intramolecular interactions, representing the bonded interactions among atoms within a single molecule linked by covalent bonds. The second component accounts for intermolecular interactions, or non-bonded interactions, where atoms are not covalently connected.

$$U_{total} = U_{bonded} + U_{non-bonded} \tag{3.7}$$

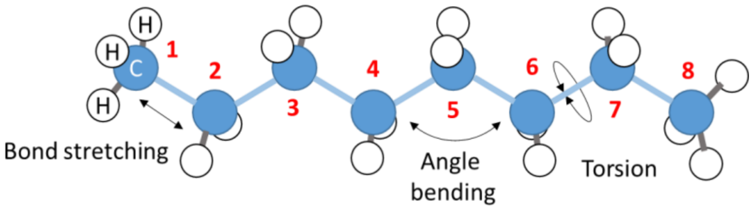

Figure 3.3: Schematic representation of bonded interactions in a simple linear n-alkane molecule using the all-atom (AA) force field formulation. The diagram illustrates the three primary types of bonded interactions: (1) bond stretching, which depicts the elongation of covalent bonds between adjacent atoms; (2) angle bending, representing the variation in angles between bonded atoms; and (3) dihedral interactions (torsion), showcasing the rotational dynamics around the bonds. These interactions collectively define the molecular flexibility and structural properties of the n-alkane (Gunsteren et al. 1990, Ref. [131]).

Bonded interactions

In classical force field formulations, the bonded interactions between atoms within the same molecule are modelled as harmonic springs. This approach effectively captures the flexibility and degrees of freedom of the molecule. These bonded interactions can be categorised into three types: bond stretching, which accounts for the elongation of covalent bonds; angle bending; and dihedral interactions, or torsion [127]. Figure 3.3 [131] illustrates these bonded interactions using the all-atom (AA) formulation for a simple linear n-alkane molecule.

$$U_{bonded} = U_{bond} + U_{angle} + U_{dihedral} \tag{3.8}$$

Bond stretching

Bond stretching interactions are modelled as harmonic springs to account for both elongations and compressions of covalent bonds. In Figure 3.3, these interactions are represented by atoms 1 and 2, and are described by the following equation:

$$U_{\text{bond}} = \frac{1}{2}k(r - r_0)^2 \tag{3.9}$$

where k represents the stiffness of the bond, r is the current bond length, and r_0 is the equilibrium bond length.

Angle bending interactions are similarly modelled using harmonic springs. In Figure 3.3, these interactions are illustrated by atoms 4 to 6, and are defined by the equation:

$$U_{\text{angle}} = \frac{1}{2}k_\theta(\theta - \theta_0)^2 \tag{3.10}$$

where k_θ denotes the angle stiffness, θ is the current angle, and θ_0 is the equilibrium angle. In this study, the stiffness values for both bond stretching and angle bending follow the classic factor of $\frac{1}{2}$ derived from Hooke's law, ensuring an accurate representation of the molecular dynamics.

Dihedral torsion

Finally, the last type of bonded interaction considers proper dihedrals formed by groups of four atoms that define two planes of the same molecule. In Figure 3.3, this interaction is represented by atoms 5 to 8 and described by the following formula:

$$U_{\text{dihedral}} = \sum_{n=1}^{N} [1 + \cos(n\phi - \gamma)] \tag{3.11}$$

where N is the multiplicity, ϕ is the angle created during torsion, γ is the phase angle, and n is the term number in the series, representing the periodicity of each term in the dihedral interaction. For increased precision in describing dihedral interactions, torsion can be represented as a sum of N terms. For example, the OPLS (optimised potentials for liquid simulations) dihedral potential [147] is defined by the first three to four terms of the series in equation 3.11:

$$U_{\text{dihedral}}(OPLS) = \frac{1}{2}D_1\left[1 + \cos(\phi)\right] + \frac{1}{2}D_2\left[1 - \cos(2\phi)\right] + \frac{1}{2}D_3\left[1 + \cos(3\phi)\right] \tag{3.12}$$

In some cases, to account for the effects of improper dihedrals, additional terms may be incorporated into equation 3.12. These terms help enforce the planarity of molecular groups or prevent the molecules from flipping across boundary conditions.

Non-bonded Interactions

Non-bonded interactions consist of two main components: a Lennard−Jones (LJ) potential term that combines Pauli repulsive forces and van der Waals attraction, and an electrostatic term described by Coulomb's law. These interactions are expressed as:

$$U_{\text{non-bonded}} = U_{\text{LJ}} + U_{\text{Coulomb}} \tag{3.13}$$

where U_{LJ} accounts for both repulsive and attractive forces, and U_{Coulomb} represents electrostatic interactions.

Lennard–Jones Interaction

The LJ potential models the attraction (van der Waals) and repulsion (Pauli) forces between two atoms [127]. For distances shorter than a predefined cutoff, the interaction between an atom i and its neighbour j is given by:

$$U_{\text{LJ}}(r_{ij}) = 4\epsilon_{ij}\left[\left(\frac{\sigma_{ij}}{r_{ij}}\right)^{12} - \left(\frac{\sigma_{ij}}{r_{ij}}\right)^{6}\right] \tag{3.14}$$

where ϵ is the depth of the potential well, dependent on the nature of the two interacting atoms, and σ_{ij} is the distance at which the potential equals zero. Atoms i and j are in equilibrium when the distance between them is $r_{ij} = 2^{1/6}\sigma_{ij}$. The first term in equation 3.14 represents the repulsive contribution of the LJ potential, while the second term represents the attractive contribution. This formula is referred to as the 12-6 Lennard–Jones potential, named after the exponents used (Figure 3.4 taken from [149]).

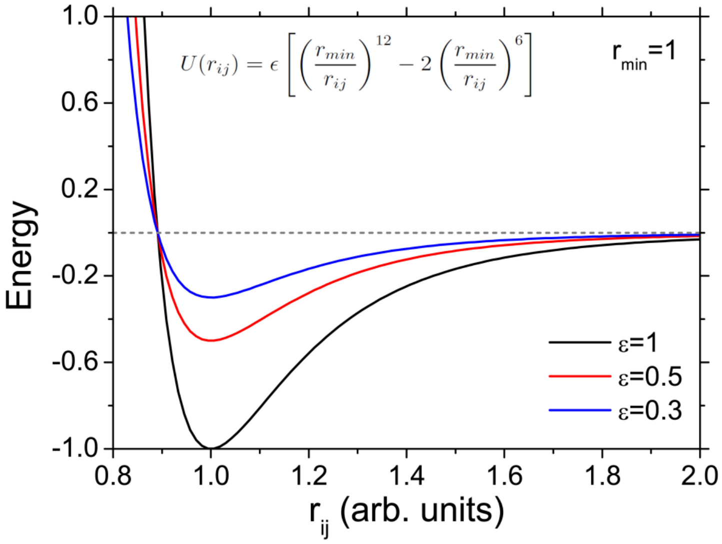

Figure 3.4: Lennard–Jones Potential Energy Curve Showing Interaction Energy Variation with Interatomic Distance. The plot illustrates the potential energy $U(r_{ij})$ as a function of interatomic distance r_{ij} for different values of the depth of the potential well ϵ (black: $\epsilon = 1$, red: $\epsilon = 0.5$, blue: $\epsilon = 0.3$). The graph highlights the effect of ϵ on the strength of the attractive interaction, with larger ϵ values indicating deeper and more stable minima, thereby reflecting stronger attractive forces between particles (Solov'yov et al. 2017, Ref. [149]).

Values for ϵ and σ are assigned to each atom i. The Lorentz–Berthelot mixing rules define the coefficients $epsilon_{ij}$ and σ_{ij} as follows:

$$\epsilon_{ij} = \sqrt{\epsilon_i \epsilon_j} \tag{3.15}$$

$$\sigma_{ij} = \frac{\sigma_i + \sigma_j}{2} \tag{3.16}$$

To reduce computational costs, the LJ potential can be truncated at a specific cutoff distance ($r_{ij} > r_{\text{cutoff}}$), beyond which interatomic interactions become negligible.

Coulomb Interaction

The Coulomb interaction potential accounts for electrostatic interactions between two bonded or non-bonded partially charged atoms. The long-range Coulomb potential is expressed as:

$$U_{\text{Coulomb}}(r_{ij}) = \frac{q_i q_j}{4\pi\varepsilon_0 r_{ij}} \tag{3.17}$$

where q_i and q_j are the partial charges of atoms i and j, respectively, r_{ij} is the distance between the two atoms, and ε_0 is the vacuum permittivity constant, equal to 8.85×10^{-12} F/m.

As indicated by equation 3.17, long-range Coulomb interactions decrease with increasing distance between atoms as r^{-1} (Figure 3.5, taken from Solov'yov et al. (2017) [149]). In contrast, the Van der Waals attractive interactions from equation 3.14 decrease as r^{-6}. Therefore, it is evident that electrostatic interactions can become significant even at larger distances, necessitating their consideration beyond the cutoff distance. When this occurs, electrostatic interactions can be approximated using the particle-particle particle-mesh (PPPM) algorithm [150, 151]. This algorithm is particularly useful for systems with periodic boundary conditions (PBCs), as it allows for the efficient calculation of electrostatic interactions among the infinite particles of the periodic images of the simulation box.

The PPPM method addresses long-range electrostatic interactions by creating a three-dimensional mesh that overlays the simulation cell. This mesh allows the system to account for periodic boundary conditions (PBCs) by treating the simulation cell as part of an infinite lattice of repeating images. The core of the PPPM method involves calculating the electrostatic potential across this mesh, which is achieved by solving Poisson's equation:

$$\nabla^2 \phi = -\frac{\rho}{\epsilon_0} \tag{3.18}$$

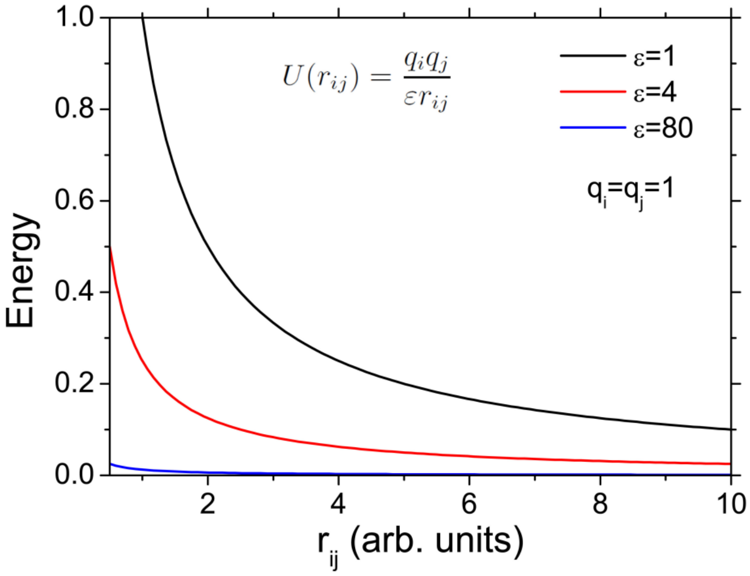

FIGURE 3.5: Coulomb Interaction Energy Between Two Charged Particles as a Function of Distance. The plot illustrates the Coulomb potential energy $U(r_{ij})$ between two particles with charges $q_i = q_j = 1$ as a function of interparticle distance r_{ij}. The energy curves are plotted for different values of the permittivity ϵ (black: $\epsilon = 1$, red: $\epsilon = 4$, blue: $\epsilon = 80$). As the value of ϵ increases, the potential energy decreases, indicating a weaker electrostatic interaction at larger ϵ values, which corresponds to a lower energy barrier at larger distances (Solov'yov et al. 2017, Ref. [149]).

where ϕ is the electrostatic potential and ρ is the charge density. Poisson's equation relates the spatial distribution of charge within the simulation cell to the resulting electrostatic potential. To solve this equation efficiently, the PPPM method employs the Fast Fourier Transform (FFT), a mathematical technique that quickly transforms spatial data into frequency space. The FFT method significantly accelerates the computation of convolution operations required for the potential by working in frequency space, reducing the computational cost associated with long-range interactions.

Once the potential is calculated, it is transformed back to real space, where the force on each particle due to Coulomb interactions is obtained by interpolating the potential from the mesh points to the actual positions of the particles. This approach ensures that each particle experiences a smooth and accurate approximation of the long-range electrostatic forces, allowing for efficient calculations even in systems with PBCs.

Intramolecular Non-Bonded Interaction Scaling

In molecular simulations, it is often advantageous to only partially include or completely exclude certain non-bonded interactions within the same molecule. Indeed, many force fields simplify calculations by neglecting non-bonded interactions between atoms separated by one or two bonds within a molecule (e.g. interactions between atoms 1 and 2, or 1 and 3, in Figure 3.3). For atoms separated by more than two bonds (e.g. atoms

1 and 4 and beyond in Figure 3.3), non-bonded interactions are typically included but scaled by a factor to better align with experimental properties.

For instance, the OPLS potential and its variants [147, 152] apply a scaling factor of 0.5 to both Lennard−Jones and Coulomb interactions for atoms separated by three or more bonds, reducing the overestimation of these forces within the molecule. This scaling method enhances the accuracy of intramolecular interactions, yielding a closer alignment with experimentally observed molecular properties.

Having established the theoretical framework for multiscale molecular dynamics, it is essential to implement these principles within a computational environment that can efficiently handle complex molecular systems. In this work, we utilised the MBN Explorer software, a versatile and robust platform specifically designed for simulating molecular structures, dynamics, and interactions. The next section provides an overview of the capabilities of MBN Explorer and details how it will be employed to simulate the molecular systems of interest in this study.

3.2 Meso-Bio-Nano (MBN) Explorer

MBN Explorer is a software designed to model molecular systems with varying degrees of complexity. It excels at calculating the system's energy, optimising molecular structures, and simulating molecular and random walk dynamics. MBN Explorer supports a wide variety of interatomic potentials, enabling the modelling of diverse molecular systems, such as atomic clusters [153–156], fullerenes, nanotubes [157], proteins, composite systems [158–160], nanofractals [161], and more. Figure 3.6 [162] illustrates the range of molecular systems that can be simulated using MBN Explorer.

What sets MBN Explorer apart from other molecular simulation codes is its universality and applicability to a broad range of problems, whether they involve biological or non-biological systems. Unlike many existing codes that are limited to specific molecular systems, MBN Explorer overcomes these constraints, providing a comprehensive tool for studying an array of molecular systems. The software offers several key features that enhance both its flexibility and performance, as outlined below.

Universality of Systems: MBN Explorer can be applied to a broad spectrum of physical systems, ranging from individual atoms and molecules to complex biomolecular assemblies. A unique feature of the software is its ability to simulate arbitrary combinations of different systems, such as interactions between metallic nanoparticles and biomolecules, which is often outside the scope of other molecular dynamics packages.

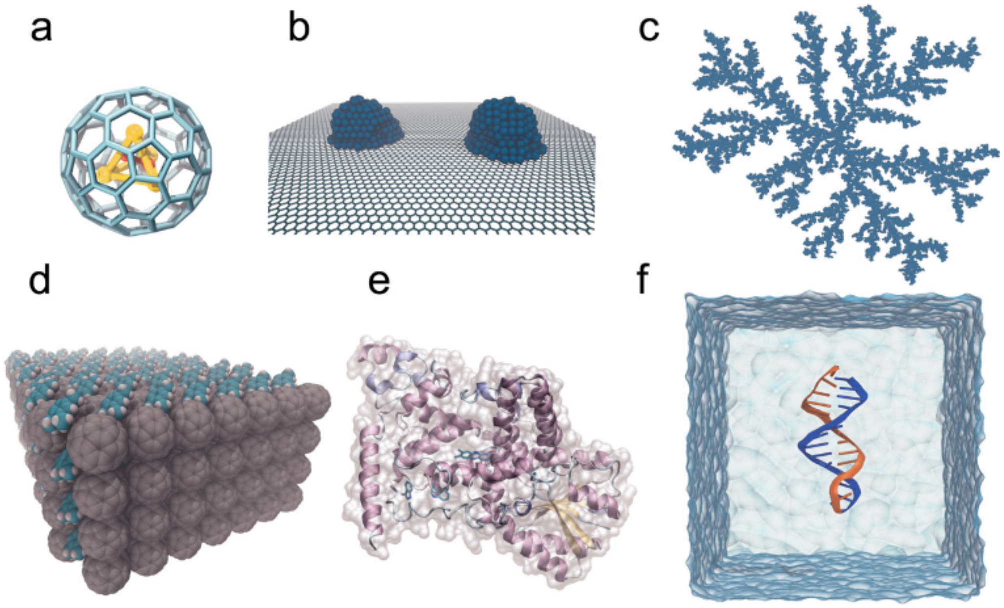

Figure 3.6: Variety of molecular systems that can be simulated using MBN Explorer: a) encapsulated clusters, b) deposited nanoparticles, c) nanofractals, d) composite nanowires, e) proteins, f) biomolecules (e.g., DNA in solution). MBN Explorer allows the study of the structure and properties of these systems and their combinations (Solov'yov et al. 2012, Ref. [162]).

Broad Range of Interaction Potentials: Designed to study various molecular systems, MBN Explorer incorporates a wide selection of interatomic potentials. A distinctive feature is the ability to combine different potentials and assign specific interactions to individual atoms or groups of atoms, providing enhanced modelling accuracy.

Rigid Body Dynamics: MBN Explorer allows particles in the system to be grouped into rigid bodies, significantly reducing the degrees of freedom and simplifying the equations of motion. This feature is particularly useful in the study of complex systems consisting of large interacting building blocks, such as proteins or fullerene-based nanowires [158–160]. Unlike many other molecular dynamics codes (such as MALDY [163] and LAMMPS [164]), MBN Explorer enables flexible interaction interfaces between individual particles and rigid bodies, making it a valuable tool for studying composite systems, such as bio-nano objects.

Computational Efficiency: Despite its versatility, MBN Explorer remains computationally efficient, often comparable to, and in some cases faster than, existing programs. While it may be slower than certain specialised codes like NAMD [165] in some scenarios, it can perform orders of magnitude faster than alternatives like GULP [166], depending on the system and simulation requirements.

Force Field Compatibility: MBN Explorer utilises the same molecular mechanics force field as CHARMM [167], X-PLOR [168], and NAMD [165], which includes local interaction terms for bonded interactions (2, 3, and 4 atoms) and pairwise interactions (electrostatic and van der Waals forces). This compatibility simplifies the comparison of simulations across these programs, providing a valuable tool for practical applications.

Input and Output Compatibility: In addition to its native input/output formats, MBN Explorer supports a range of standard formats. It can read Protein Data Bank (PDB) files, X-PLOR PSF structure files, and energy parameter files from CHARMM or X-PLOR. Output formats include XYZ coordinate files, which can be visualised using popular programs like VMD [169].

Example Database: MBN Explorer comes with an extensive database of examples covering molecular systems of various complexities. These examples illustrate the implemented algorithms and serve as a helpful starting point for users to familiarise themselves with the software.

The following part of this section provides an overview of the implementation of MD techniques in MBN Explorer.

As discussed previously, MBN Explorer is designed to simulate a wide range of atomic and molecular systems. The main assumptions are as follows:

(i) The system consists of assemblies of rigid molecules, atoms, or biological polymers.

(ii) Interatomic interactions and forces within the system are described by continuous functions and applied to each atom.

(iii) The dynamics of the system are governed by classical Newtonian and Euler equations, or relativistic equations of motion, where applicable.

Let us consider a molecular system consisting of N atoms, where N_{at} atoms have three degrees of freedom, and $N - N_{\mathrm{at}}$ atoms are constrained within N_{rb} rigid bodies.

Newton's Equations of Motion:

Newton's second law of motion is applied to each atom in the system, which possesses three degrees of freedom. Consider an arbitrary atom labeled with the index i, where $i = 1, 2, \ldots, N_{\mathrm{at}}$. The equation of motion for this atom is expressed as:

$$m_i \vec{a}_i = m_i \frac{d^2 \vec{r}_i}{dt^2} = \vec{F}_i \tag{3.19}$$

Here, m_i is the mass of atom i, $\vec{a}_i$ is its acceleration, and $\vec{F}_i$ represents the total force acting on the i-th atom, generated by the interactions with all other atoms in the system.

The force $\vec{F}_i$ is determined by interatomic potentials, which can be either pairwise or many-body in nature. Equation 3.19 is a second-order differential equation. To solve it numerically, initial conditions must be provided, including the positions and velocities of all atoms at time $t = 0$.

Relativistic Equations of Motion:

MBN Explorer also allows for simulations of relativistic dynamics. This is achieved by solving the relativistic equations of motion for particles experiencing relativistic effects. The equations of motion in this case are:

$$\begin{cases} \dot{\vec{v}}_i = \frac{1}{m_i\gamma_i}\left(\vec{F}_i - \frac{\vec{v}_i(\vec{F}_i\cdot\vec{v}_i)}{c^2}\right) \\ \dot{\vec{r}}_i = \vec{v}_i \end{cases} \tag{3.20}$$

where

$$\gamma_i = \frac{1}{\sqrt{1 - \frac{\vec{v}_i\cdot\vec{v}_i}{c^2}}} \tag{3.21}$$

In these equations, γ_i is the Lorentz factor for the i-th atom, and c is the speed of light. The relativistic equations 3.20 are highly nonlinear, making their numerical integration more challenging. For accurate results, MBN Explorer employs a fourth-order Runge-Kutta method [170] with adaptive step size to integrate these equations.

Similar to the Velocity Verlet algorithm discussed in the previous section, the Runge-Kutta method requires specifying initial conditions at the start of each simulation step. For each particle undergoing relativistic motion, at a given time t, the initial condition is represented as:

$$y_i(t) = y_{i_0} \tag{3.22}$$

where $y_i(t)$ denotes the state vector of the i-th particle, which includes its position and velocity (or momentum) at time t. These initial conditions allow the system to be propagated forward in time.

For each relativistic particle, a set of intermediate variables is is computed to update the state vector. These terms are given by:

$$\begin{aligned}
k_{i_1} &= \Delta t \cdot f_i(t, y_i) \\
k_{i_2} &= \Delta t \cdot f_i\left(t + \frac{1}{2}\Delta t, y_i + \frac{1}{2}k_{i_1}\right) \\
k_{i_3} &= \Delta t \cdot f_i\left(t + \frac{1}{2}\Delta t, y_i + \frac{1}{2}k_{i_2}\right) \\
k_{i_4} &= \Delta t \cdot f_i\left(t + \Delta t, y_i + k_{i_3}\right)
\end{aligned} \tag{3.23}$$

These intermediate steps are used to compute the velocities $\vec{v}_i$ and positions $\vec{r}_i$ of the relativistic particles at time $t + \Delta t$. This is done by evaluating $y_i(t + \Delta t)$ as:

$$y_i(t + \Delta t) = y_i(t) + \frac{1}{6}(k_{i_1} + 2k_{i_2} + 2k_{i_3} + k_{i_4}) \tag{3.24}$$

The updated values $y_i(t + \Delta t)$ are then used to compute the velocities $\vec{v}_i(t + \Delta t)$ and positions $\vec{r}_i(t + \Delta t)$. These results serve as the initial conditions for the subsequent simulation step.

To maintain computational accuracy, energy conservation is monitored at each step. If the relative difference in the total system's energy exceeds a pre-defined threshold, the simulation step is repeated with the timestep reduced by half. This procedure continues until the desired precision is achieved or the timestep reaches its minimal allowable value.

Euler Equations:

Rigid body molecular dynamics focuses on the motion of rigid molecules or rigid fragments, where the internal distances between any two atoms within the rigid fragment remain fixed. In this framework, the dynamics of a molecule can be separated into two components: the translational motion of the centre of mass and the rotational motion of the molecule. These motions are described in a fixed reference frame, known as the lab-frame, and in a rotating reference frame attached to the molecule itself, called the molecular-frame (Figure 3.7).

The translational motion of a rigid molecule is governed by Newton's equations, which describe the motion of the centre of mass. The rotational motion is more complex and is governed by Euler's equations. To fully describe the dynamics of a rigid molecule, both the position of the centre of mass and the orientation of the molecule must be specified. These are represented by three spatial coordinates (for the centre of mass) and three angular coordinates (for orientation). Thus, the equations of motion for a rigid molecule consist of:

- Newton's equations for the translational motion of the centre of mass.

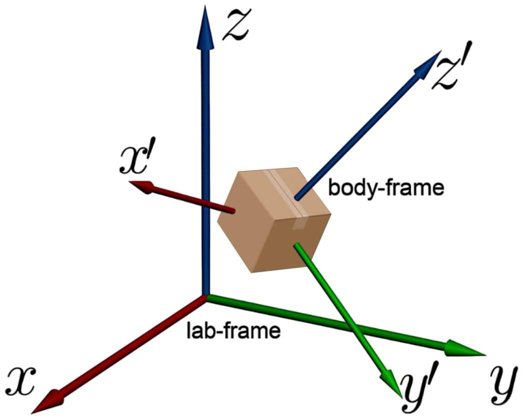

FIGURE 3.7: Two coordinate frames used to describe the motion of a rigid molecular object: (x, y, z) represents the fixed laboratory frame, while the non-inertial coordinate frame (x', y', and z') is the object frame, in which its tensor of inertia is diagonal.

- Euler's equations for the rotational motion around the centre of mass.

The rotational motion of a rigid molecule is described by the following equation [171]:

$$\frac{d\vec{L}_\alpha}{dt} = \vec{T}_\alpha, \quad \alpha = 1, \ldots, N_{rm} \tag{3.25}$$

Here, $\vec{L}_\alpha$ represents the total angular momentum of the α-th rigid molecule about the origin of the lab-frame, and $\vec{T}_\alpha$ is the total torque acting on the molecule. N_{rm} refers to the total number of rigid molecules in the system. This equation expresses the fact that the rate of change of angular momentum is equal to the applied torque.

The description of rigid body dynamics in molecular simulations is fundamental for understanding the rotational and translational features of complex molecules. By using the lab-frame and molecular-frame (Figure 3.7), the rotational dynamics of a molecule can be expressed more simply in terms of its principal moments of inertia.

Equation (3.25) is valid in an inertial reference frame (the lab-frame), but for simplicity, it is often convenient to describe rotational motion in the molecular-frame, where the coordinate axes are aligned with the principal axes of rotation of the molecule. To fully describe the motion in both frames, we introduce two coordinate systems:

- The **lab-frame** with coordinates (x, y, z), which is fixed in space.
- The **molecular-frame** with coordinates (x', y', z'), which rotates with the molecule such that the x', y', and z' axes always align with the molecule's principal axes of rotation.

Since the molecular-frame corotates with the molecule, the angular velocity of the molecular-frame is the same as that of the molecule. In the molecular-frame, the angular momentum is expressed as:

$$\frac{d\vec{L}_\alpha}{dt} = \frac{d\vec{L'}_\alpha}{dt} + \vec{\omega'}_\alpha \times \vec{L'}_\alpha \tag{3.26}$$

In this equation, $\vec{\omega'}_\alpha$ is the angular velocity vector of the molecule, and $\vec{L'}_\alpha$ is the angular momentum vector, both expressed in the molecular-frame. The second term on the right-hand side, $\vec{\omega'}_\alpha \times \vec{L'}_\alpha$, represents the change in angular momentum due to the rotation of the molecular-frame itself.

In the molecular-frame, the angular velocity and angular momentum are expressed in terms of the principal moments of inertia of the molecule. We define the following quantities:

$$\vec{T'}_\alpha = (T'_{\alpha_{x'}}, T'_{\alpha_{y'}}, T'_{\alpha_{z'}}), \tag{3.27}$$

$$\vec{\omega'}_\alpha = (\omega'_{\alpha_{x'}}, \omega'_{\alpha_{y'}}, \omega'_{\alpha_{z'}}), \tag{3.28}$$

$$\vec{L'}_\alpha = (I_{\alpha_{x'x'}}\omega'_{\alpha_{x'}}, I_{\alpha_{y'y'}}\omega'_{\alpha_{y'}}, I_{\alpha_{z'z'}}\omega'_{\alpha_{z'}}) \tag{3.29}$$

where $I_{\alpha_{x'x'}}$, $I_{\alpha_{y'y'}}$, and $I_{\alpha_{z'z'}}$ are the principal moments of inertia of the rigid molecule. Using these quantities, we can express the components of the angular momentum equation (3.25) in the molecular-frame as follows:

$$T'_{\alpha_{x'}} = I_{\alpha_{x'x'}}\dot{\omega'}_{\alpha_{x'}} - (I_{\alpha_{y'y'}} - I_{\alpha_{z'z'}})\omega'_{\alpha_{y'}}\omega'_{\alpha_{z'}} \tag{3.30}$$

This equation describes how the angular velocity of the molecule changes due to torques acting on it. The same form holds for the y' and z' components of the motion, with cyclic permutations of the variables.

3.3 Software Capabilities and Applications

In this section, we explore how the principles discussed above are implemented in MBN Explorer. Figure 3.8, taken from Solov'yov et al. (2012) [162], presents a general workflow diagram outlining the four core task types in MBN Explorer: calculation of system energies, optimisation of molecular structures, and simulation of molecular and random

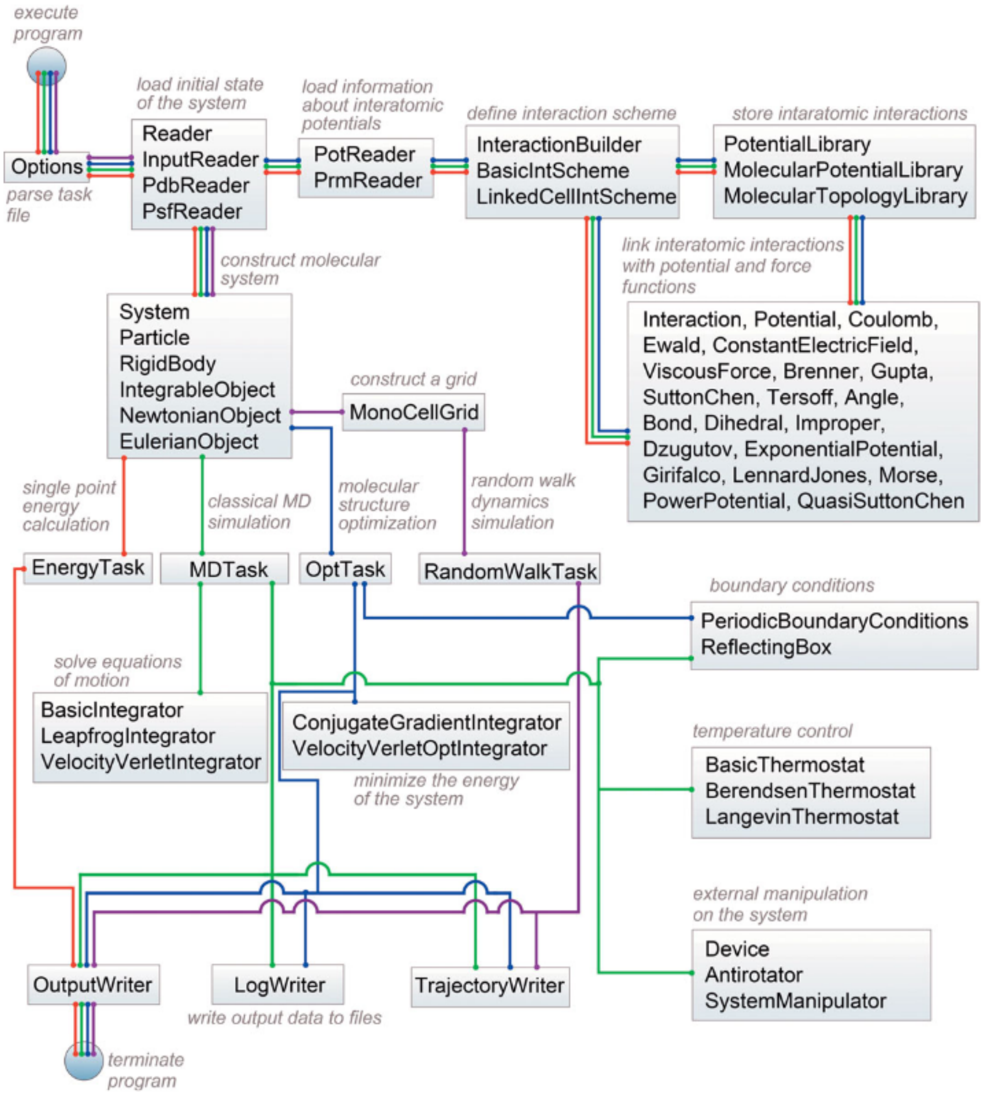

Figure 3.8: Generalised schematic illustration of MBN Explorer workflow for single-point energy calculation (red line), molecular system optimisation (blueline), molecular dynamics (green line), and random walk dynamics simulation (purple line). The most essential modules of MBN Explorer are shown asboxes while lines define links between classes (Solov'yov et al. 2012, Ref. [162]).

walk dynamics. The figure highlights the essential modules that form the computational backbone of MBN Explorer, showing which modules are required for each type of computational task.

All four task types in MBN Explorer share a common input interface. After loading the necessary information from configuration files, the system is prepared for simulations. The results of the simulations are then written by three output modules: *OutputWriter*, *LogWriter*, and *TrajectoryWriter*, all of which are employed in similar ways across different tasks.

The modular structure of MBN Explorer's code makes it highly adaptable. For example, it is possible to add new thermostats and barostats by implementing a single additional module, as reflected in Figure 3.8. Operations that impose constraints on equations of motion and affect particle trajectories are structured within the so-called *devices*. One notable example is the *Periodic Boundary Conditions* module, which modifies particle coordinates when particles cross the simulation box boundary, translating them to the opposite side of the box. The *device* concept is central to introducing new features into the code.

A critical set of modules within MBN Explorer are the *integrators*, which are responsible for advancing the system according to the equations of motion. In MD simulations, an integrator advances the system in time, whereas in structure optimisation, it drives particles toward configurations with lower potential energy. These integrators calculate new particle velocities based on the forces acting on them and update positions based on the computed velocities. Key integrator modules are *LeapfrogIntegrator* and *VelocityVerletIntegrator*, depicted in Figure 3.8.

MBN Explorer accepts input information from up to six different file formats, as illustrated in Figure 3.9: (i) the MBN Explorer structure file, (ii) Protein Data Bank (PDB) file, (iii) topology file, (iv) MBN Explorer potential file, (v) CHARMM force field file, and (vi) optional system manipulation files. The input structure of atoms can be specified in Cartesian coordinates, and MBN Explorer supports the standard elements of the periodic table. Additionally, ”non-standard” particles can be defined with specific properties, such as custom masses or charges.

The PDB format, commonly used in biomolecular simulations for storing coordinate data, is also supported by MBN Explorer for molecules like proteins and DNA. The PDB file can be used in conjunction with other input files to provide a comprehensive description of the molecular system. While the PDB format focuses on atomic coordinates, it can be combined with the MBN Explorer structure format to fully specify the system.

For simulations involving molecular mechanics (MM) potentials, a topology file is required, containing molecular-specific information such as atomic types, charges, and details on molecular bonds, angles, and dihedral angles. MBN Explorer is fully compatible with the CHARMM/NAMD topology file format.

The potential file used by MBN Explorer allows the definition of a wide variety of interatomic potentials, including pairwise, many-body, and external potentials. Unique cutoff distances can be specified for each potential, allowing for the efficient handling of long-range interactions without significant loss of accuracy.

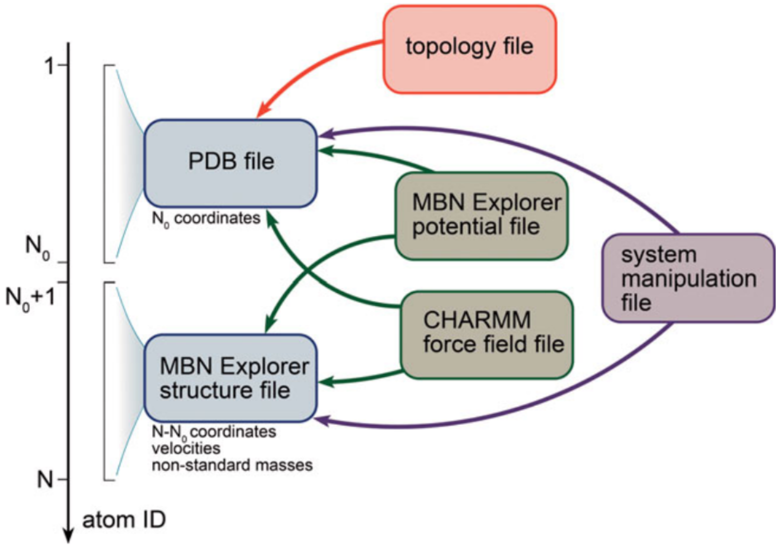

FIGURE 3.9: Schematic diagram illustrating the interlink of input files in MBN Explorer (Solov'yov et al. 2012, Ref. [162]).

The topology file is necessary for MBN Explorer calculations involving MMpotentials, as given by equation 3.31. The form of the MM potential differs significantly from the pairwise and many-body potentials mentioned earlier because it requires the explicit definition of the system's topology, which outlines the chemical bonding structure. The total energy of a molecular system interacting via the MM potential is expressed as:

$$U_{\text{tot}} = U_{\text{cov}} + U_{\text{vdW}} + U_{\text{Coul}}, \tag{3.31}$$

Here, U_{vdW} represents the van der Waals interactions in the system, which are modelled in MBN Explorer through the Lennard–Jones potential, and U_{Coul} accounts for Coulombic interactions between charged particles. The topology file contains detailed molecular information, such as atom types, partial charges, molecular bonds, angles, and dihedrals. MBN Explorer is fully compatible with the CHARMM/NAMD topology file format, which specifies these properties for biomolecules and other molecular systems.

Finally, MBN Explorer produces three primary output files: the output file, the log file, and the trajectory file. The output file stores task-related information, including input data, final system configuration, and computational parameters such as CPU time. The log file records system properties like energies, momenta, and temperatures at user-defined intervals during MD and optimisation simulations. The trajectory file, which logs the evolution of atomic coordinates over time, can also include additional data such as velocities and forces upon request. The trajectory data is saved in the XYZ format, compatible with visualisation tools such as VMD [169].

With this modular and flexible structure, MBN Explorer enables the simulation of diverse molecular systems and processes, offering advanced customisation options for a wide range of computational tasks. In the next section, we will explore specific capabilities of MBN Explorer, along with its various applications in molecular dynamics, nanoscience, and beyond.

3.3.1 Simulation Parameters

In order to run the simulation on MBN Explorer, the main required files are: `Task File`; `Initial coordinate` of the system, and `Potential File`, describing interatomic interactions. Additional files such as topology and chemistry rules may be required for some calculations. A discussion of some of the key simulation parameters commonly employed in MBN Explorer, with a particular focus on the specific parameters relevant to the simulations conducted in this study, can be found in Appendix A.

In this study, thermostat parameters were primarily employed to control the temperature cycle, along with other relevant simulation parameters. Depending on the specific requirements, various task types and associated parameters are available, which can be referenced in detail in the MBN Explorer User Guide [149].

To simulate radiation-induced transformations in the system, the Irradiation Driven Molecular Dynamics (IDMD) method [172] was utilised. The details of this approach are discussed in the subsequent section.

3.3.2 Irradiation Driven Molecular Dynamics (IDMD)

Despite its numerous advantages, standard classical MD simulations cannot adequately model irradiation-driven processes. Classical MD typically does not account for the coupling between the system and incident radiation, nor does it capture the quantum transformations within a molecular system induced by irradiation. Examples of such processes include: (i) the inactivation of living cells by ionising radiation, which causes complex DNA strand breaks [173–175]; (ii) the formation and composition of cosmic ices in the interstellar medium and planetary atmospheres due to the interplay of molecular surface adsorption and irradiation [176]; and (iii) the formation of biologically relevant molecules under extreme irradiation conditions [177].

To overcome these limitations, the IDMD methodology has been developed. This new approach enables atomistic simulations of irradiation-driven chemistry (IDC) in complex molecular systems. The IDMD method has been implemented in the MBN Explorer software package [149, 178, 179].

IDC is now widely used in modern nanotechnologies, such as focused electron beam-induced deposition (FEBID) [180–182] and extreme ultraviolet (EUV) lithography [183, 184], both of which are discussed in the next section. These techniques represent the next generation of nanofabrication, allowing for the controlled creation of complex three-dimensional nanostructures with nanometer resolution. Additionally, IDC plays a crucial role in nuclear waste decomposition technologies [185] and medical radiotherapies [173, 174, 186].

IDC explores transformations in molecular systems caused by irradiation with photons, neutrons, or charged-particle beams. It is also relevant for molecular systems subjected to external fields, mechanical stress, or plasma environments. While quantum mechanical methods such as time-dependent density functional theory (TD-DFT) can rigorously describe irradiation-driven processes, they are feasible only for relatively small molecular systems, typically containing a few hundred atoms at most [187–190]. This limitation restricts the applicability of TD-DFT in studying the complex supramolecular systems and materials involved in IDC.

Classical MD offers an alternative theoretical framework for modelling large and complex molecular systems. For example, the classical MM approach allows for the simulation of molecular systems containing millions of atoms [191, 192] and evolving on timescales of hundreds of nanoseconds [193–195]. In this framework, the system is treated classically, with atoms interacting through parametric, phenomenological potentials that depend on the network of chemical bonds in the system. This bond network defines the molecular topology, which imposes constraints on the system, maintaining its natural shape and preserving its mechanical and thermodynamic properties.

Within the IDMD framework, quantum collision processes such as ionisation, electronic excitation, and bond dissociation (via electron attachment or charge transfer) are incorporated into classical MD simulations in a stochastic manner. These processes are modelled as fast, local transformations, with probabilities derived from quantum mechanics. The probability of each quantum process is proportional to the product of its cross section and the flux density of incident particles [196]. Cross sections for collision processes can be obtained from (i) *ab initio* calculations, (ii) analytical estimates and models, (iii) experimental data, or (iv) atomic and molecular databases. The flux densities depend on the specific system and problem under investigation. The properties of atoms and molecules, such as energy, momentum, charge, and interaction potentials, are adjusted according to their final quantum states after the collision.

During quantum processes, the energy transferred to the system through irradiation is absorbed by the electronic and ionic degrees of freedom, creating chemically reactive sites in the system. The subsequent dynamics of these reactive sites are handled by classical MD until further irradiation-driven transformations occur. These reactive sites may also undergo chemical reactions, forming stable and neutral species.

IDMD also captures the dynamics of secondary electrons and the energy and momentum transfer from the excited electronic subsystem to the system's vibrational modes, leading to heating. For small gas-phase systems, ejected electrons can be decoupled and excluded from post-irradiation dynamics. In extended or condensed systems, secondary electron interactions can be modelled using electron transport theories, such as diffusion [174, 197] or Monte Carlo (MC) methods [198], providing spatial distributions of energy deposition. Immobilised electrons and excitations transfer energy to the system's heat via electron-phonon coupling, which occurs on picosecond timescale [199]. IDMD accounts for these relaxation processes, determining their temporal and spatial characteristics, and how much energy is converted to heat.

IDMD enables the computational analysis of physicochemical processes in radiation-exposed systems across time and spatial scales far beyond the reach of quantum mechanical methods like DFT, TD-DFT, nonadiabatic MD, and Ehrenfest dynamics. The analysis is rooted in the atomistic approach, similar to traditional MD, and relies on input parameters such as bond dissociation energies, molecular fragmentation cross sections, energy transfer rates, and spatial regions for energy relaxation. These parameters can be obtained through quantum mechanical calculations or, when computationally prohibitive, from experimental data or analytical models. A similar approach is employed in Monte Carlo particle transport models, where cross sections serve as inputs for simulating particle interactions in various materials [172].

Due to its relatively few input parameters and the vast range of output characteristics accessible for analysis, IDMD offers unique capabilities for modelling irradiation-driven modifications and chemistry in complex molecular systems. By linking outputs from Monte Carlo codes that simulate radiation and particle transport (e.g., Geant4 [200, 201], SEED [202], and others) to the inputs of IDMD, a multiscale description of irradiation-driven chemistry and structure formation can be achieved in various Meso-Bio-Nano systems. This capability has been demonstrated in the recent FEBID case study [203] and can be applied to many other systems exposed to different radiation fields, geometries, and temporal profiles.

The IDMD methodology is suitable for any molecular system exposed to radiation, accounting for major dissociative transformations, such as topological changes, redistribution of atomic partial charges, changes in atomic valences, bond multiplicities, and interatomic interactions, as well as further reactive transformations [203]. These transformations can be simulated using MD with reactive force fields, particularly the reactive CHARMM (rCHARMM) force field [204], which is implemented in MBN Explorer.

rCHARMM enables the modelling of bond rupture events and the formation of new bonds by chemically active atoms, while continuously tracking changes in the system's topology during its transformations. As an extension of the widely used CHARMM force field [167, 205], rCHARMM is directly applicable to organic and biomolecular systems. Its combination with other force fields [206, 207] facilitates simulations of a broader range of molecular systems undergoing chemical transformations, while monitoring changes in molecular composition and topology [203, 206, 208–211].

Compared to the standard CHARMM force field, rCHARMM requires the specification of two additional parameters for bonded interactions: the bond dissociation energy and the cutoff radius for bond breaking or formation. By defining these parameters, MBN Explorer treats all molecular mechanics interactions (bonded, angular, and dihedral) using an alternative parametrisation. If the distance between two atoms exceeds the cutoff radius, the bonded interaction is removed from the system's topology and is not considered in subsequent calculations.

The standard CHARMM force field [167] employs a harmonic approximation to describe interatomic interactions, which limits its applicability to small deformations of molecular systems. For larger perturbations, the potential should approach zero as valence bonds rupture. To account for covalent bond rupture, MBN Explorer uses a modified interaction potential for atoms connected by chemical bonds. The standard CHARMM force field for covalent bonds is defined as:

$$U^{(bond)}(r_{ij}) = k^{b}_{ij}(r_{ij} - r_0)^2 \tag{3.32}$$

where k^{b}_{ij} is the bond stretching force constant, r_{ij} is the distance between atoms i and j, and r_0 is the equilibrium bond length. This parametrisation accurately describes the bond stretching regime for small deviations from r_0, but becomes inaccurate for larger distortions.

To better model covalent bond rupture, it is more appropriate to use the Morse potential, which requires an additional parameter—the bond dissociation energy—compared to the harmonic potential in equation 3.32. The Morse potential for a pair of atoms is expressed as:

$$U^{(bond)}(r_{ij}) = D_{ij}\left[e^{-2\beta_{ij}(r_{ij}-r_0)} - 2e^{-\beta_{ij}(r_{ij}-r_0)}\right] \tag{3.33}$$

where D_{ij} is the bond dissociation energy, and $\beta_{ij} = \left(\frac{k^{b}_{ij}}{D_{ij}}\right)^{1/2}$ determines the steepness of the potential. Figure 3.10 [204] illustrates the Morse potential for the CN7–CN8B

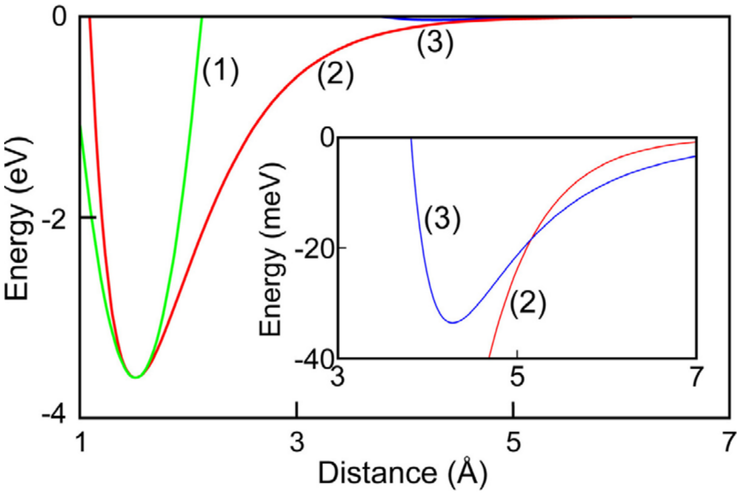

FIGURE 3.10: Pairwise carbon-carbon interaction potential (CHARMM types CN7-CN8B) shown using harmonic (1) and Morse (2) approximations. The van der Waals interaction between the two atoms is depicted by the blue line labeled as (3) (Sushko et al. 2016, Ref. [204]).

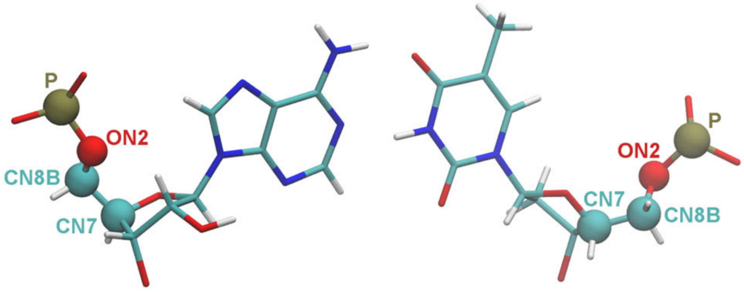

FIGURE 3.11: Structure of a complementary adenine–thymine nucleobase pair, representing a segment of a DNA molecule. Solid spheres highlight specific atoms in the DNA backbone, classified by CHARMM atom types CN7, CN8B, ON2, and P. The bonded, angular, and dihedral interaction potentials involving these atoms are illustrated in Figure 3.10 and 3.12 (Sushko et al. 2016, Ref. [204]).

bond, one of the covalent bonds in the DNA backbone (see notations in Figure 3.11 [204]). For small deviations from r_0, the Morse and harmonic potentials are nearly identical.

The rupture of covalent bonds during simulations automatically utilises an improved potential for valence angles. This potential increases rapidly with larger angular distortions, potentially leading to non-physical results when modelling bond rupture. In the CHARMM force field, the potential associated with the change of a valence angle between bonds with indices ij and jk is given by:

$$U^{(angle)}(\theta_{ijk}) = k^{\theta}_{ijk}(\theta_{ijk} - \theta_0)^2 \tag{3.34}$$

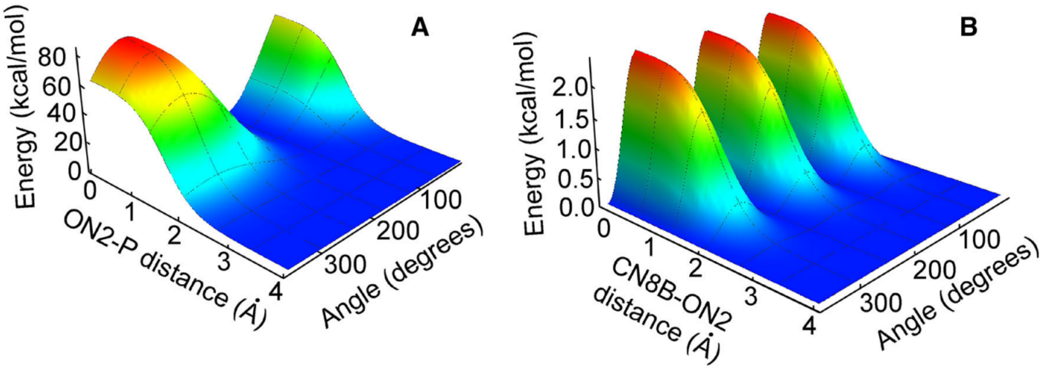

FIGURE 3.12: (**A**) The CN8B–ON2–P angular potential calculated using equation 3.37 with account for the ON2–P bond rupture. (**B**) The CN7–CN8B–ON2–P dihedral potential calculated using equation 3.39 with account for the CN8B–ON2 bond rupture. See the atom-type notations in in Figure 3.11 (Sushko et al. 2016, Ref. [204]).

where k^{θ}_{ijk} and θ_0 are parameters of the potential, and θ_{ijk} is the actual angle formed by the atoms. This potential grows rapidly with increasing angle, which may lead to non-physical results when simulating covalent bond rupture. To avoid such issues, the harmonic potential in equation 3.34 is replaced in rCHARMM with the following alternative parametrisation:

$$U^{(angle)}(\theta_{ijk}) = 2k^{\theta}_{ijk}[1 - \cos(\theta_{ijk} - \theta_0)] \tag{3.35}$$

For small variations in the valence angle, this parametrisation is equivalent to the harmonic approximation (equation 3.34) used in the standard CHARMM force field. However, for larger angles, the parametrisation in equation 3.35 introduces an energy threshold, which is critical for accurate modelling of bond rupture.

When a covalent bond breaks, the associated angular interactions are also disrupted. The effect of bond rupture on the angular potential is modelled by a smooth step function:

$$\sigma(r_{ij}) = \frac{1}{2}\left[1 - \tanh\left(\beta_{ij}(r_{ij} - r^*_{ij})\right)\right] \tag{3.36}$$

where $r^*_{ij} = \frac{R^{\mathrm{vdW}}_{ij} + r_0}{2}$. This function introduces a correction to the angular interaction potential by taking into account the distance r_{ij} between atoms involved in the angular interaction, which transitions from the equilibrium bond length r_0 to the van der Waals contact distance R^{vdW}.

Since angular interactions involve two bonds between atoms with indices ij and jk, the potential energy for the valence angle interaction subject to bond rupture is parameterised as:

$$\widetilde{U}^{(angle)}(\theta_{ijk}) = \sigma(r_{ij})\sigma(r_{jk})U^{(angle)}(\theta_{ijk}) \tag{3.37}$$

As seen in equation 3.37, the angular potential decreases as the bond length between any pair of atoms ij or jk increases. Figure 3.12**A** [204] illustrates the CN8B–ON2–P angular potential in the context of DNA modelling (see notations in Figure 3.11 [204]). The angular potential is calculated using equation 3.37 while considering the rupture of the bond between the oxygen and phosphorus atoms, with the CN8B–ON2 bond length taken as its equilibrium value r_0.

Dihedral interactions arise in molecular mechanics due to changes in the dihedral angle between every set of four connected atoms. Consider a quadruple of atoms with indices i, j, k, and l, where the dihedral interaction depends on the angle between the planes formed by atoms i, j, k, and atoms j, k, l. In the harmonic approximation, the dihedral energy contribution is expressed as:

$$U^{(dihedral)}(\chi_{ijkl}) = 2k^{d}_{ijkl}[1 + \cos(n_{ijkl}\chi_{ijkl} - \delta_{ijkl})] \tag{3.38}$$

where k^{d}_{ijkl}, n_{ijkl}, and δ_{ijkl} are potential parameters, and χ_{ijkl} is the angle between the planes formed by atoms i, j, k and j, k, l.

Dihedral interactions are also affected by bond rupture. Therefore, equation 3.38 must be adjusted to account for bond breakage. The dihedral interaction involving atoms i, j, k, and l depends on three bonds, and the dihedral potential energy considering bond rupture is given by:

$$\widetilde{U}^{(dihedral)}(\chi_{ijkl}) = \sigma(r_{ij})\sigma(r_{jk})\sigma(r_{kl})U^{(dihedral)}(\chi_{ijkl}) \tag{3.39}$$

Here, $U^{(dihedral)}(\chi_{ijkl})$ from equation 3.38 describes the dihedral interaction within the standard CHARMM force field. The step functions $\sigma(r_{ij})$, $\sigma(r_{jk})$, and $\sigma(r_{kl})$ (as defined in equation 3.36) are used to limit the dihedral interaction as the corresponding bond lengths increase. Figure 3.12 **B** illustrates the profile of the CN7–CN8B–ON2–P dihedral potential, accounting for the rupture of the CN8B–ON2 bond. This dihedral interaction is crucial for e.g. modelling strand breaks in the DNA sugar-phosphate backbone [172].

While the primary focus of this study is on thermal cycling and its effects on material stability, it is important to emphasise that the simulation framework developed here is inherently designed to incorporate radiation effects through the use of Irradiation-Driven Molecular Dynamics (IDMD). This consideration is essential, as materials used on the lunar surface will inevitably be subjected to simultaneous exposure to temperature extremes and radiation from solar wind and galactic cosmic rays.

The MBN Explorer software and associated simulation setup detailed in this chapter have been selected not only for their robustness in handling thermal stress simulations, but also for their capability to model radiation-induced phenomena at the atomistic level. Although radiation simulations are not included in the present work, they represent a critical component of the research programme and are planned for future implementation. By establishing this dual-purpose framework, the present thesis serves as both a standalone investigation of thermal effects and a foundational reference for continued studies on the synergistic impact of lunar environmental stressors.

We now proceed to review several key studies that have employed IDMD to investigate complex molecular systems. These examples showcase the methodology's effectiveness in simulating chemical transformations, biomolecular processes, and radiation-induced effects under various conditions. A comprehensive overview of simulations for condensed matter systems exposed to radiation, including case studies using the IDMD code, is provided in Solov'yov et al. (2024) [212].

3.3.3 Previous works on IDMD

The IDMD methodology is applicable to any molecular system exposed to radiation, effectively capturing the key dissociative transformations of irradiated systems. It accounts for topological changes, redistribution of atomic partial charges, variations in atomic valences, bond multiplicities, and interatomic interactions, along with potential pathways for further reactive transformations [203].

This advanced IDMD framework enables multiscale modelling of IDC processes, which are crucial for emerging technologies. These range from the precise fabrication of nanostructures with nanometer resolution [182–184, 213] to cancer treatment via radiotherapy [173, 174], both of which are discussed further in this thesis.

The IDMD algorithm has been validated in numerous case studies involving collision and radiation processes, such as atomistic simulations of the FEBID process and related IDC [203, 207], collision-induced multifragmentation of fullerenes [206], electron impact-induced fragmentation of the organometallic molecule $W(CO)_6$ [209], thermal splitting of water [204], radiation chemistry of water near ion tracks [208], and ion-induced DNA damage of varying complexity [178, 210]. Some of these case studies are discussed in detail in this section.

Multi-fragmentation of carbon fullerenes upon collision

Irradiation- and collision-induced processes involving carbon fullerenes have been extensively investigated over the past few decades, both experimentally and theoretically [214–217]. In particular, collisions involving neutral and charged C_{60} and C_{70} fullerenes have been the subject of numerous studies [214, 218–222].

Verkhovtsev et al. (2017) [206] explored the collision-induced fusion and fragmentation of C_{60} fullerenes through classical MD simulations using the rCHARMM force field, implemented in MBN Explorer. The many-body Brenner potential (REBO) [223] was used to model interactions between carbon atoms, and combined with rCHARMM to monitor changes in molecular topology and the yields of atomic and molecular fragments produced during the process.

Two thousand simulations of C_{60}+C_{60} collisions were conducted to account for the statistical nature of fusion and fragmentation. Each simulation lasted 10 ps, with the fullerenes randomly oriented with respect to one another. Initial geometries were prepared using MBN Studio [224], and quantitative data on fragment production (i.e. the number of fragments of each type) were extracted from the simulation outputs. The ensemble-averaged fragment size distribution was calculated for each collision energy by summing the data from all trajectories and normalising the results by the total number of fragments.

Figure 3.13 from Verkhovtsev et al. (2021) [172] presents the average size of the molecular system at the end of the simulations as a function of the centre-of-mass collision energy. The average system size is defined as the total number of atoms divided by the total number of molecular species at a given collision energy. The data from various trajectories were combined and normalised, accounting for molecular fragments, non-fragmented C_{60} molecules, and fused C_{120} products. The results, represented by open circles, were obtained at zero initial fullerene temperature. The maximal average molecular size, indicating the highest fusion probability, was observed at collision energies around 200 eV—significantly higher than experimental results for C_{60}^{+} + C_{60} collisions [219, 225].

In experiments, the average temperature of colliding fullerenes was estimated to be around 2000 K [219]. To better replicate experimental conditions, additional simulations were performed with initial fullerene temperatures set to 2000 K. Each thermally excited molecule had an internal kinetic energy of approximately 30 eV. Initial structures and velocities for these simulations were derived from a 10 ns constant temperature simulation of a single C_{60} molecule at 2000 K. These simulations showed that C_{60} maintains its cage-like structure up to $T \approx 2300$ K, after which a transition, often referred

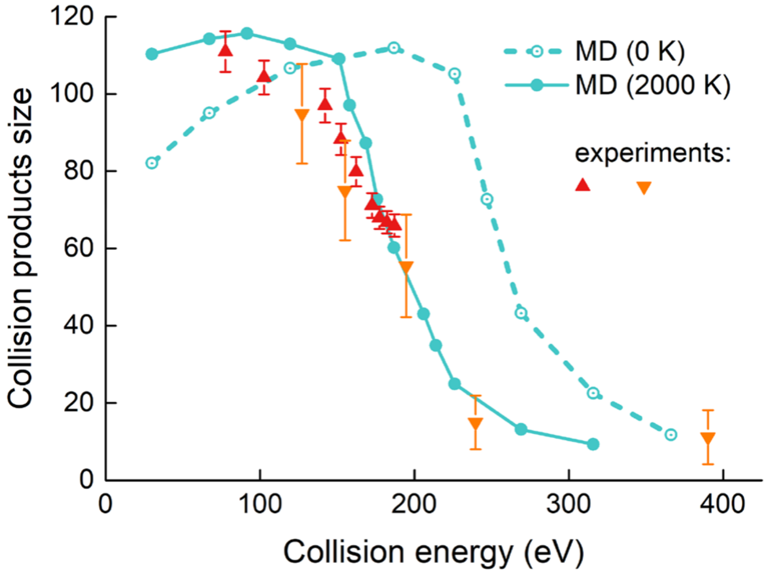

Figure 3.13: The average size of molecular products produced in C60–C60 collisions as a function of the centre-of-mass collision energy. The collision products, including different molecular fragments as well as non-fragmented C60 molecules and fused C120 compounds, were recorded after 10 ps of the simulations. Open and filled circles describe the simulations performed at the fullerene initial temperature of 0 K and 2000 K, respectively. In the experiments, an average temperature of the colliding fullerenes was estimated around 2000 (Verkhovtsev et al. 2021, Ref. [172]).

to as fullerene melting, occurs. This melting involves the opening of the fullerene cage and the formation of a highly distorted, non-fragmented structure [226, 227].

The thermally excited simulations aligned more closely with experimental findings. Accounting for a statistical uncertainty of around 10%, the calculated average product sizes agree well with experimental data. The largest average product size, and thus the highest probability of fusion, was found for collisions with energies between 90 and 120 eV significantly lower than the 200 eV observed in simulations at zero initial temperature. This reduction in the fusion barrier is attributed to the thermal energy stored in the fullerenes.

To further investigate the effect of initial fullerene temperature on fragmentation dynamics, fragment size distributions for clusters containing up to 10 carbon atoms were analysed after 10 ps of simulation. As shown in Figure 3.14 from Verkhovtsev et al. (2021) [172], simulations with zero temperature fullerenes (Figure 3.14**A**) revealed minimal fragmentation at 225 eV, while at 270 eV, a phase transition led to multifragmentation and the formation of numerous small fragments. This phase transition is consistent with the energy difference between a C_{60} fullerene and a gas of 30 C_2 dimers, $\Delta E(C_{60} - 30C_2)$ = 233 eV, calculated using the Brenner potential. At 225 eV, the energy is below the threshold for multifragmentation, resulting in limited fragment production. However,

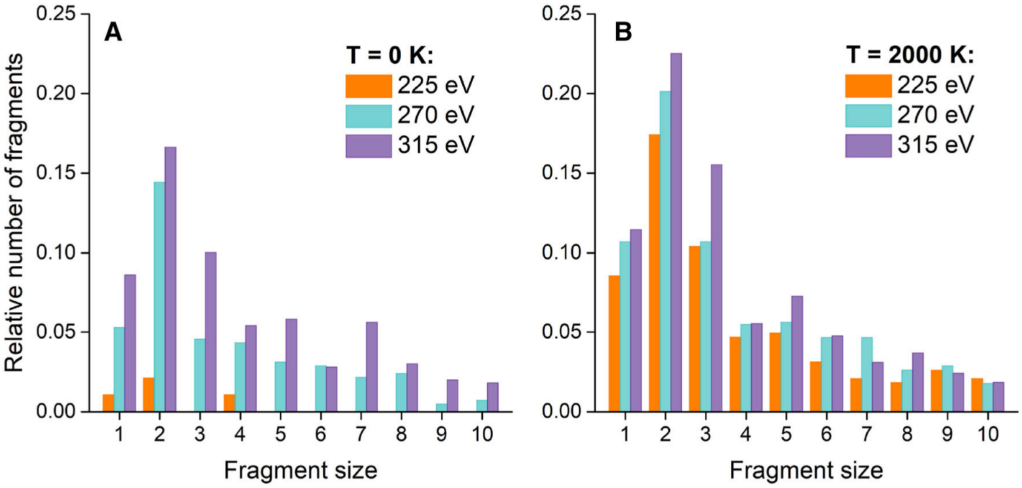

FIGURE 3.14: Number of $C_n (n \leq 10)$ fragments, normalised to the total number of fragments produced after 10 ps, for the centre-of-mass collision energies of 225, 270 and 315 eV. Panels A and B show the results obtained at the 0 K and 2000 K temperature of colliding fullerenes, respectively (Verkhovtsev et al. 2021, Ref. [172]).

at 270 eV, the collision energy surpasses the multifragmentation threshold, enabling the formation of numerous small carbon fragments. In contrast, simulations with an initial fullerene temperature of 2000 K (Figure 3.14**B**) show the phase transition occurring at a lower collision energy of approximately 185 eV. Notably, thermally excited fullerenes produce a larger number of C_2 and C_3 fragments. At 315 eV, the relative number of larger fragments is around 3–6% of the total number, regardless of the initial internal energy.

It is well established that the size distribution of small fragments, C_n, produced in fullerene collisions follows a power law $n^{-\lambda}$ [228, 229]. Fitting the simulated fragment distributions for $n \geq 2$ yielded a power law exponent $\lambda = 1.47 \pm 0.04$, which closely matches the value of 1.54 obtained in earlier MD simulations at 500 eV centre-of-mass collision energy [230].

Atomistic simulation of the FEBID process:

One of the innovative applications of IDC is in focused electron beam-induced deposition (FEBID), an advanced nanofabrication technique that enables precise construction of metal nanostructures with nanometer resolution [180–182]. The process of FEBID involves irradiating precursor molecules (mostly organometallics) [231] with keV electron beams as they are deposited onto a substrate. This electron-induced dissociation releases the metallic component of the precursor, forming a deposit on the substrate with a size comparable to the incident electron beam, typically a few nanometers [213]. A common class of precursor molecules used in FEBID includes metal carbonyl compounds of the form $M_m(CO)_n$ [182, 232], where one or more metal atoms (M) are bonded to several carbon monoxide (CO) ligands. These compounds have been extensively studied over the years, with a wealth of data available on their thermal decomposition and electron-induced fragmentation [233–239]. The unique structure of metal carbonyls, which feature strong C–O bonds and weaker M–C bonds, has drawn significant interest; the weaker M–C bonds tend to break readily under sufficient internal energy, typically resulting in the sequential loss of CO ligands.

The FEBID process operates through repetitive cycles of precursor deposition, diffusion, aggregation, and desorption on the substrate, followed by irradiation from a finely focused electron beam. This irradiation drives the dissociation of metal-free ligands and initiates the growth of metal-enriched nanostructures. modelling FEBID involves addressing a variety of complex phenomena occurring on different spatial and temporal scales, requiring both theoretical and computational approaches [162]. These phenomena include: (i) the deposition and diffusion of precursor molecules on the substrate, (ii) the transport of primary, secondary, and backscattered electrons, (iii) electron-induced dissociation of the adsorbed molecules, (iv) subsequent chemical reactions, and (v) energy relaxation into electronic and vibrational modes, which can lead to thermo-mechanical effects.

Traditionally, simulations of FEBID and nanostructure growth have been based on Monte Carlo (MC) methods and diffusion theory, which allow for the prediction of average process characteristics but lack molecular-level detail. The IDMD method extends beyond these limitations, enabling atomistic-level simulations of the nanostructures formed during FEBID, while accounting for quantum and chemical transformations in the adsorbed material [203].

In a prior study [203], atomistic IDMD simulations of the FEBID process were performed for tungsten hexacarbonyl, $W(CO)_6$, on a hydroxylated SiO_2 surface, using the MBN Explorer software. The results were validated through comparison with experimental data [240]. The simulations employed the rCHARMM force field to describe the structural and dynamic properties of irradiated $W(CO)_6$ molecules on the SiO_2 substrate. The rCHARMM approach requires several parameters to be specified, including equilibrium bond lengths, bond stiffness, and dissociation energies. Moreover, the dissociative chemistry of the precursors, involving molecular fragments and atomic valences, must be defined. In the model considered, only the dissociation and formation of W–C and W–W bonds were allowed, while the C–O bonds were treated harmonically according to equation 3.32, preventing their breakage.

Figure 3.15 from Sushko et al. (2016) [203] illustrates the results of MD simulations during the initial phase of irradiation, where a cylindrical electron beam irradiates the

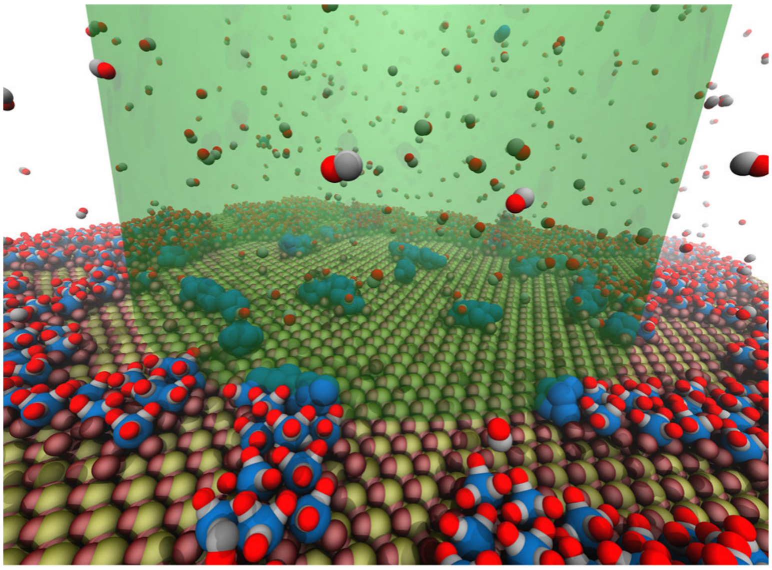

FIGURE 3.15: Snapshot from MD simulation of $W(CO)_6$ precursor adsorption onto SiO_2 surface during the initial stages of electron beam irradiation (green cylinder). Fragmentation of precursors and formation of tungsten clusters (blue) are visible (Sushko et al. 2016, Ref. [203]).

system. Only precursor molecules within the beam were exposed to irradiation, resulting in their dissociation. The dissociation rate of the precursors was estimated from experimental data [240].

The FEBID process was simulated [203] using rescaled irradiation parameters such as beam current and exposure time. These parameters may differ from experimental conditions but were chosen to correspond to the number of electrons (N_e) impacting the system, thus ensuring that irradiation-induced effects occur on a similar scale as observed in experiments. In IDMD simulations, irradiation times are typically shortened compared to experimental values.

The probability of W–C bond dissociation in $W(CO)_6$ due to electron collisions per unit time is given by:

$$P = \sigma \times J_0 \tag{3.40}$$

where σ represents the bond dissociation cross section, and

$$J_0 = \frac{I_0}{e \times S_0} \tag{3.41}$$

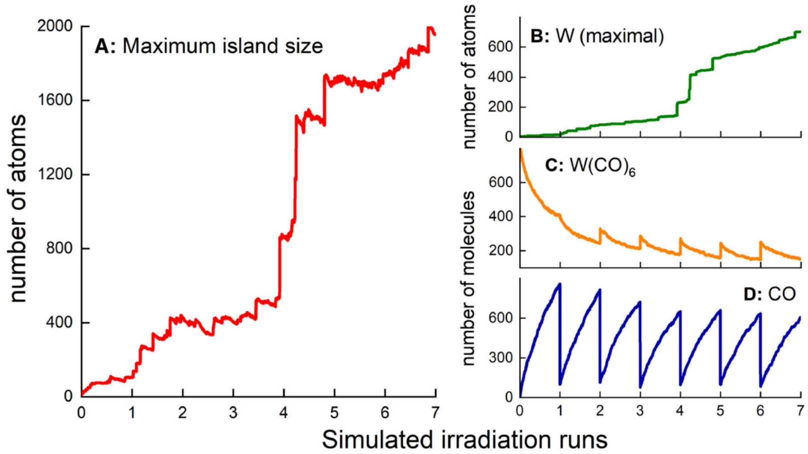

FIGURE 3.16: Time evolution of **(A)** size of the largest W-enriched island, **(B)** number of W atoms, **(C)** number of $W(CO)_6$ molecules, and **(D)** number of CO molecules during irradiation. Irradiation periods are indicated by numbers, with each period lasting 10 ns (Sushko et al. 2016, Ref. [203]).

is the electron flux density, with I_0 being the electron beam current, e the electron charge, and $S_0 = \pi R^2$ the cross-sectional area of the beam, where R is the beam radius. Substituting equation 3.41 into 3.40, we obtain:

$$P_0 = \frac{I_0}{e}\frac{\sigma}{S_0} \tag{3.42}$$

With $I_0 = 4\mu A$ and $\sigma = 1.2 \times 10^{-2}$ nm^2 [240], the dissociation probability is calculated as $P_0 = 3.8 \times 10^{-6}$ fs^{-1}. This analysis can be further refined by more accurately calculating the fragmentation cross section, as well as the yield and spatial distribution of secondary electrons, which depend on the energy of the primary beam [208]. These findings illustrate the potential for linking IDMD inputs with outputs from MC codes simulating radiation transport, thereby enabling multiscale modelling of the FEBID process.

Figure 3.16**A** depicts the time evolution of the size of the largest W-enriched island, while panels **B**, **C**, and **D** show changes in the numbers of W atoms, $W(CO)_6$, and CO molecules during irradiation, respectively. The irradiation periods are marked sequentially, with each period lasting 10 ns.

During the irradiation phases, dissociation of W–C bonds in the precursors leads to the formation of CO molecules, which evaporate into the vacuum chamber over time. Figure 3.16**D** illustrates the nonlinear increase in CO molecules during each irradiation period. After each phase, CO molecules are removed from the simulation box, and new $W(CO)_6$ molecules are deposited on the surface in preparation for the next cycle.

The results demonstrate that the IDMD approach has proven to be a powerful tool for simulating the growth of W-granular metal structures during FEBID at an atomistic level [203]. The simulations reveal details into the morphology, composition, and growth mechanisms of these structures, which are in good agreement with experimental data. This methodology holds great potential for wider application in various irradiation-driven processes, where detailed understanding of molecular transformations is essential [172].

Chapter 4

Computational Methods

This chapter outlines the computational strategies used to model material characteristics under lunar conditions, focusing on multiscale simulation techniques. By using advanced computational tools, this study aims to accurately replicate the harsh lunar environment and provide a detailed understanding of material performance.

Key aspects of this methodology include the use of MD simulations using MBN Explorer, which allows for the analysis of atomic-scale interactions. These simulations are essential in capturing complex phenomena that occur under lunar conditions, such as extreme temperatures, and vacuum.

In the following sections, the specific computational tools, software, and methodologies are detailed, starting with the materials selected to model and progressing to multiscale molecular dynamics simulations and the parameters used.

4.1 Selection of Materials

The selection of appropriate materials for lunar applications is critical, as discussed in detail in section 2.2. Materials choice extends beyond merely withstanding the physical stresses of launch and landing; it also involves ensuring long-term resilience to the extreme environmental conditions of the Moon. As previously discussed, the lunar environment presents unique challenges, including high radiation levels, extreme temperature fluctuations, low gravity, and the abrasive nature of lunar dust. Consequently, the materials selected for lunar structures and systems must not only survive these conditions but also perform efficiently in terms of thermal regulation, durability, and resource management.

In the following sections, we discuss the two key materials selected for this study, providing detailed reasoning for their choice based on both their properties and the practical challenges posed by the lunar environment. The materials chosen—silicon dioxide (SiO_2, Figure 4.1) and polyethylene (PE, $(C_2H_4)_n$, Figure 4.2)—bring distinct advantages in their structural, thermal, and mechanical properties. Their significance in space exploration, electronics, and industrial applications further underscores their suitability for this study. The following subsections elaborate on the rationale for their selection and their relevance to this study.

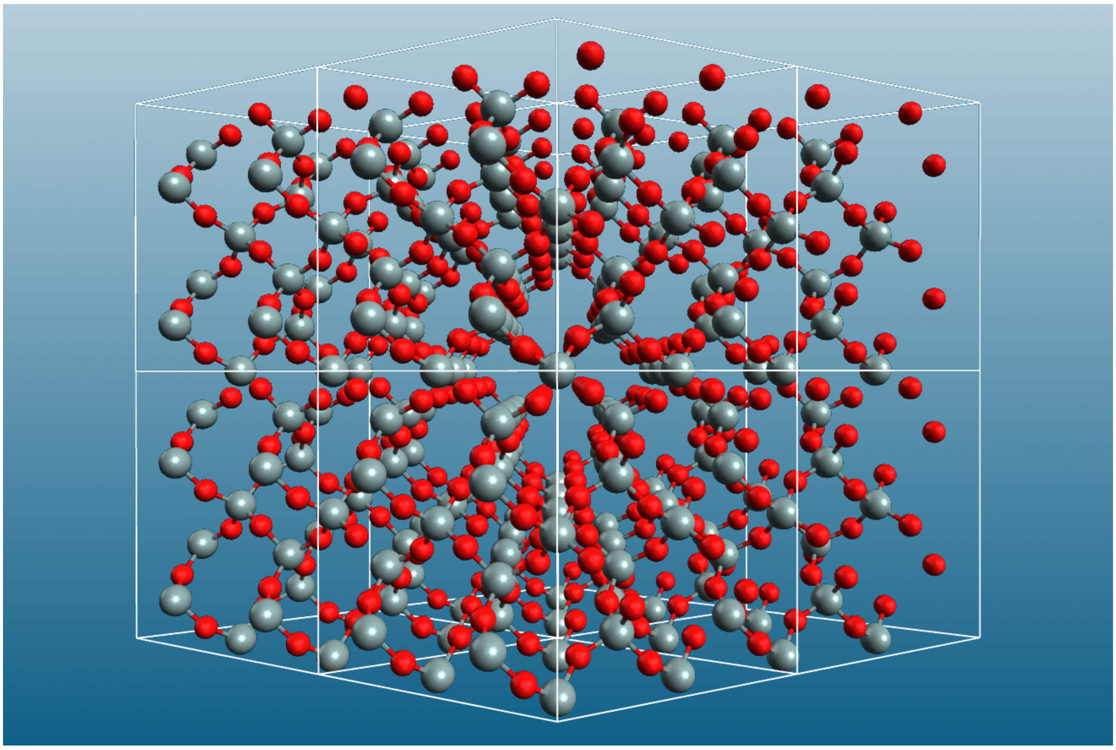

FIGURE 4.1: Schematic representation of the SiO_2 alpha crystal structure, visualised using Avogadro software. This structure serves as the basis for generating systems used in calculations.

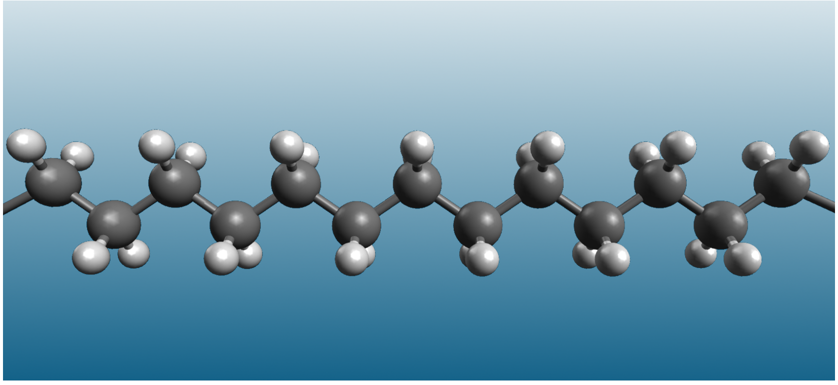

FIGURE 4.2: Schematic representation of the polyethylene structure, visualised using Avogadro software.

4.1.1 Silicon Dioxide (SiO_2)

Silicon dioxide, found abundantly in lunar regolith, is pivotal for its chemical stability, mechanical robustness, and versatility. This study investigates its **crystalline** and **amorphous** forms to understand how atomic structure influences thermal and mechanical performance under extreme conditions.

4.1.1.1 Crystalline SiO_2

- **Structure**: The ordered lattice of crystalline silica, such as quartz, makes it an ideal benchmark for studying thermal stability and mechanical resilience.
- **Applications**: Crystalline SiO_2 is extensively used in optical devices, sensors, and piezoelectric components, where structural precision is critical. Its use in lunar construction aligns with ISRU strategies, enabling the creation of robust, thermally stable structures from local resources.
- **Research Objective**: The study focuses on crystalline SiO_2's behaviour under extreme thermal fluctuations, mimicking lunar day-night cycles, to evaluate its reliability in high-performance and extraterrestrial applications.

4.1.1.2 Amorphous SiO_2

- **Structure**: Unlike its crystalline counterpart, amorphous silica lacks long-range atomic order, which affects its thermal and mechanical properties.
- **Applications**: Amorphous SiO_2 is a key material in glass, coatings, and insulation. Its thermal insulation capabilities and ease of fabrication make it a candidate for extraterrestrial habitats and protective structures.
- **Research Objective**: By examining the molten-to-amorphous transition during rapid heating and quenching while making glass, this study illuminates aspects into how the material may behave under rapid heating and cooling. It will assess its resilience under cyclic thermal stress and evaluate its potential for advanced manufacturing techniques, such as 3D printing in space environments.

Relevance to Study Goals:

The dual-phase approach—analysing both crystalline and amorphous SiO_2—provides a comparative framework for understanding how atomic arrangements influence material properties. These findings are critical for applications in extreme environments, such as lunar surfaces, where temperature swings and mechanical loads are significant.

4.1.2 Polyethylene (PE), $(C_2H_4)_n$

Polyethylene, a lightweight and chemically versatile polymer, was selected for its unique properties, including radiation shielding, thermal insulation, and mechanical flexibility. Its amorphous nature makes it ideal for evaluating structural dynamics under non-ideal conditions.

4.1.2.1 Amorphous PE, $(C_2H_4)_n$

- **Structure**: Amorphous polyethylene consists of disordered polymer chains, offering intrinsic flexibility and resilience.
- **Applications**: PE's low density and insulating properties make it indispensable for space equipment, ranging from lightweight protective layers to inflatable structures.
- **Research Objectives**: The research will focus on investigating the molecular dynamics of polyethylene chains under cyclic thermal stress to simulate the temperature fluctuations experienced on the lunar surface.

Relevance to Study Goals:

The disordered structure of amorphous PE allows for a detailed examination of its conformational flexibility and thermal response. This understanding is crucial for designing polymers tailored to withstand dynamic stresses in practical applications.

4.2 Computational Simulations

The simulations were carried out using MD techniques, with atomistic models constructed from experimental crystallographic data (for SiO_2) and polymer chain configurations (for polyethylene). Using these computational tools, we investigate how these materials behave at the atomic and molecular levels when subjected to various temperature cycles, according to lunar surface conditions. All MM/MD simulations were carried out with MBN Explorer [162].

This chapter is divided into two main sections, each covering the simulations of the respective materials. SiO_2 was modelled in its α-quartz crystalline form as a slab, representing a key structural component that could be used in lunar construction. In turn, polyethylene, a widely used polymer with excellent mechanical properties and flexibility, was modelled as an amorphous system to explore its potential as a flexible material for lunar applications, such as habitat construction or radiation shielding.

4.2.1 SiO_2 - Slab/Crystal Simulations

Preparation of the Input File

The input file for the SiO_2 crystal simulations was prepared using Avogadro [241], an open-source molecular editor and visualiser. Avogadro allows users to import crystal structures and generate geometries suitable for computational studies. In this case, the initial α-quartz crystal structure of SiO_2 was obtained from a Crystallographic Information File (CIF) [242], which contains precise atomic coordinates and symmetry information based on experimental data.

After loading the CIF file into Avogadro, the structure could be manipulated and visualised, as shown in Figure 4.3. MBN Explorer was then used to replicate the unit cell, maintaining the periodic boundary conditions required for crystal simulations. This created a larger simulation cell, essential for computational studies of the crystalline structure.

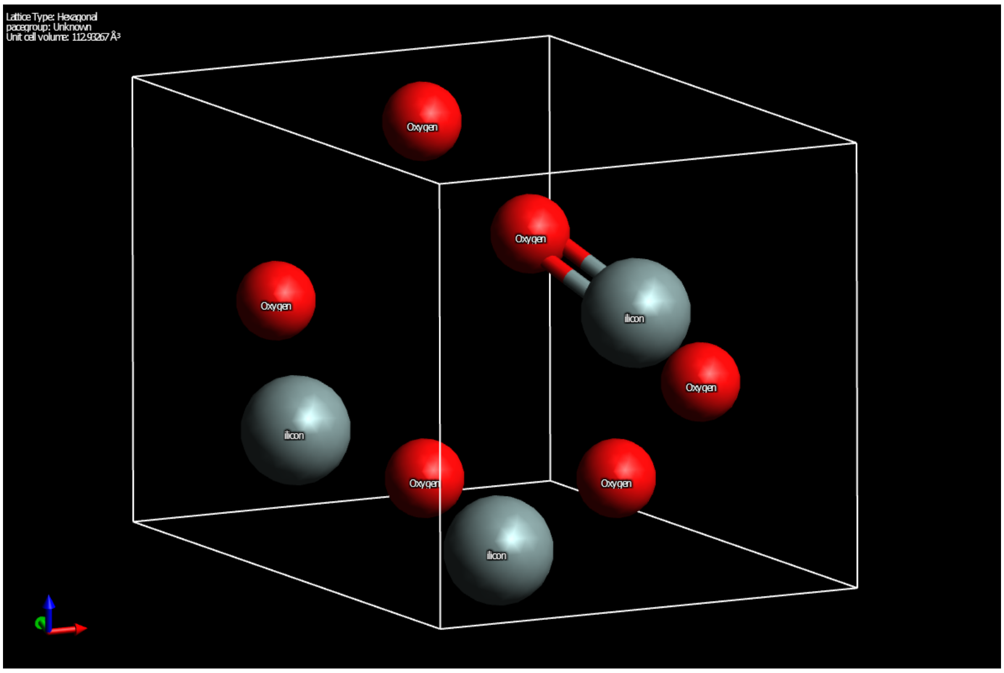

FIGURE 4.3: The initial CIF structure of SiO_2 visualised in Avogadro, used to extract the cell dimensions and lattice vectors for further computational modelling.

To prepare the input file for MBN Explorer, the lattice vectors and atomic coordinates of **α-quartz** (the most thermodynamically stable crystalline polymorph of SiO_2 at ambient conditions) were extracted from the CIF file. The lattice parameters used were a = 4.91239 Å, b = 4.91239 Å, and c = 5.40358 Å, with 9 atoms per unit cell (Si_3O_6). These parameters were used to construct a periodic supercell that accurately reflects the crystal symmetry.

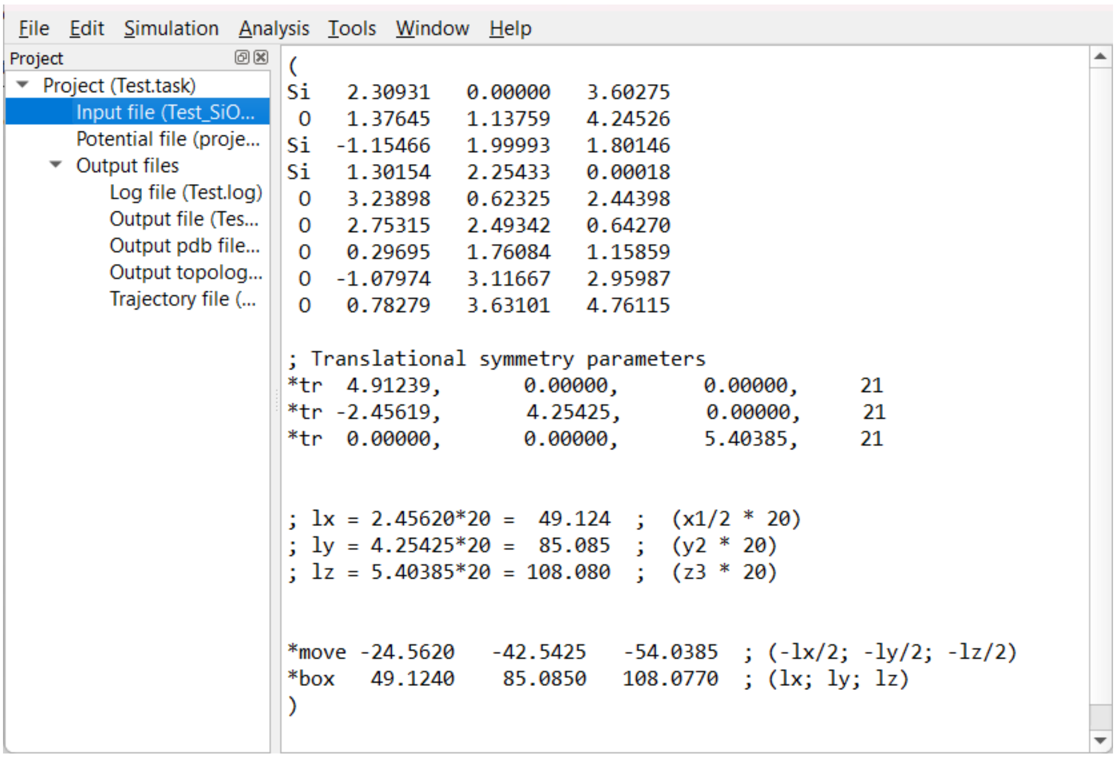

```
(
Si   2.30931   0.00000   3.60275
 O   1.37645   1.13759   4.24526
Si  -1.15466   1.99993   1.80146
Si   1.30154   2.25433   0.00018
 O   3.23898   0.62325   2.44398
 O   2.75315   2.49342   0.64270
 O   0.29695   1.76084   1.15859
 O  -1.07974   3.11667   2.95987
 O   0.78279   3.63101   4.76115

; Translational symmetry parameters
*tr  4.91239,       0.00000,       0.00000,     21
*tr -2.45619,       4.25425,       0.00000,     21
*tr  0.00000,       0.00000,       5.40385,     21


; lx = 2.45620*20 =  49.124  ;  (x1/2 * 20)
; ly = 4.25425*20 =  85.085  ;  (y2 * 20)
; lz = 5.40385*20 = 108.080  ;  (z3 * 20)


*move -24.5620   -42.5425   -54.0385  ; (-lx/2; -ly/2; -lz/2)
*box   49.1240    85.0850   108.0770  ; (lx; ly; lz)
)
```

FIGURE 4.4: A SiO_2 supercell containing 36,200 atoms is generated using the crystal generator tool of MBN Explorer.

In MBN Explorer, the crystal was replicated using translation vectors specified in the input file, with $10 \times 20 \times 20$ repetitions along the x, y, and z directions, respectively. This corresponds to a supercell of 4,000 unit cells, or 36,000 atoms in an ideal case. However, the final structure contained 36,200 atoms, likely due to additional atoms introduced at the boundaries by the crystal generation algorithm or adjustments made to resolve overlapping atoms during the build process.

The SiO_2 supercell was translated in space according to the translation vectors specified in the input file. The translational symmetry parameters were defined using the `*tr` commands, as depicted in Figure 4.4.

Defining Simulation Box Geometry

The geometry of the system was critical for ensuring accurate simulation results. The simulation box dimensions were based on the unit cell structure, with sufficient space added around the slab to avoid interactions between periodic images. The final SiO_2 structure was centered at the origin and set within a rectangular simulation box with dimensions of 49.1240 Å × 85.0850 Å × 108.0770 Å, calculated as shown in Figure 4.4 and equation 4.1:

$$l_x = \frac{x_1}{2} \times 20, \quad l_y = y_2 \times 20, \quad l_z = z_3 \times 20 \tag{4.1}$$

Force Field and Potentials Setup

To model the interactions between atoms in the SiO_2 crystal, potentials were selected based on prior research. In this study, the Tersoff potential, originally used for atomic simulations of Si and O systems [243, 244], was applied to balance computational efficiency and accuracy. While less accurate than bond-order or *ab initio* calculations, the Tersoff potential is well-suited for large-scale simulations of SiO_2. The potential excludes Coulomb interactions and uses parameters derived from Munetoh et al. [245], which are well-validated for Si–O systems. The parameter setup for the Tersoff potential is illustrated in Figure 4.5.

The results from Munetoh et al. (2007) [245] showed good agreement with both experimental data and numerical predictions from *ab initio* calculations, indicating that this potential accurately captures the structural and dynamical properties of SiO_2, including phase stability in α-quartz and α-cristobalite.

Optimisation of the System

After preparing the input geometry and setting the potentials, the first stage of the simulation was optimisation. The goal of optimisation was to find the lowest energy configuration of the system before conducting dynamic simulations, by minimising the potential energy. The method used for this process was the *velocity quenching* algorithm, a standard energy minimisation technique. This method relaxes the atomic positions by gradually reducing the system's kinetic energy, effectively "quenching" the system into a low-energy configuration, thus eliminating any artificial stresses or strains that may have been introduced during the creation of the simulation cell.

The velocity quenching was performed with a time step of 1 fs. Key parameters such as force tolerance, torque tolerance, displacement tolerance, and maximum particle displacement were all set to 1×10^{-4} eV/Å, ensuring precise control over the relaxation process. These tolerances were critical to ensure that the system reached a physically meaningful minimum energy state. The optimisation parameters specified in the MBN Explorer task file are shown in Figure 4.6.

Equilibration of the System

Once the system was optimised, the output file was used as the input for the next stage of the simulation: thermal equilibration. The equilibration process aimed to stabilise the system at the target simulation temperature, ensuring a representative atomic configuration for subsequent analyses. A molecular dynamics simulation was carried out, applying a thermostat to gradually bring the system to the desired temperature of 300 K. The Velocity Verlet algorithm was used for integrating the equations of motion.

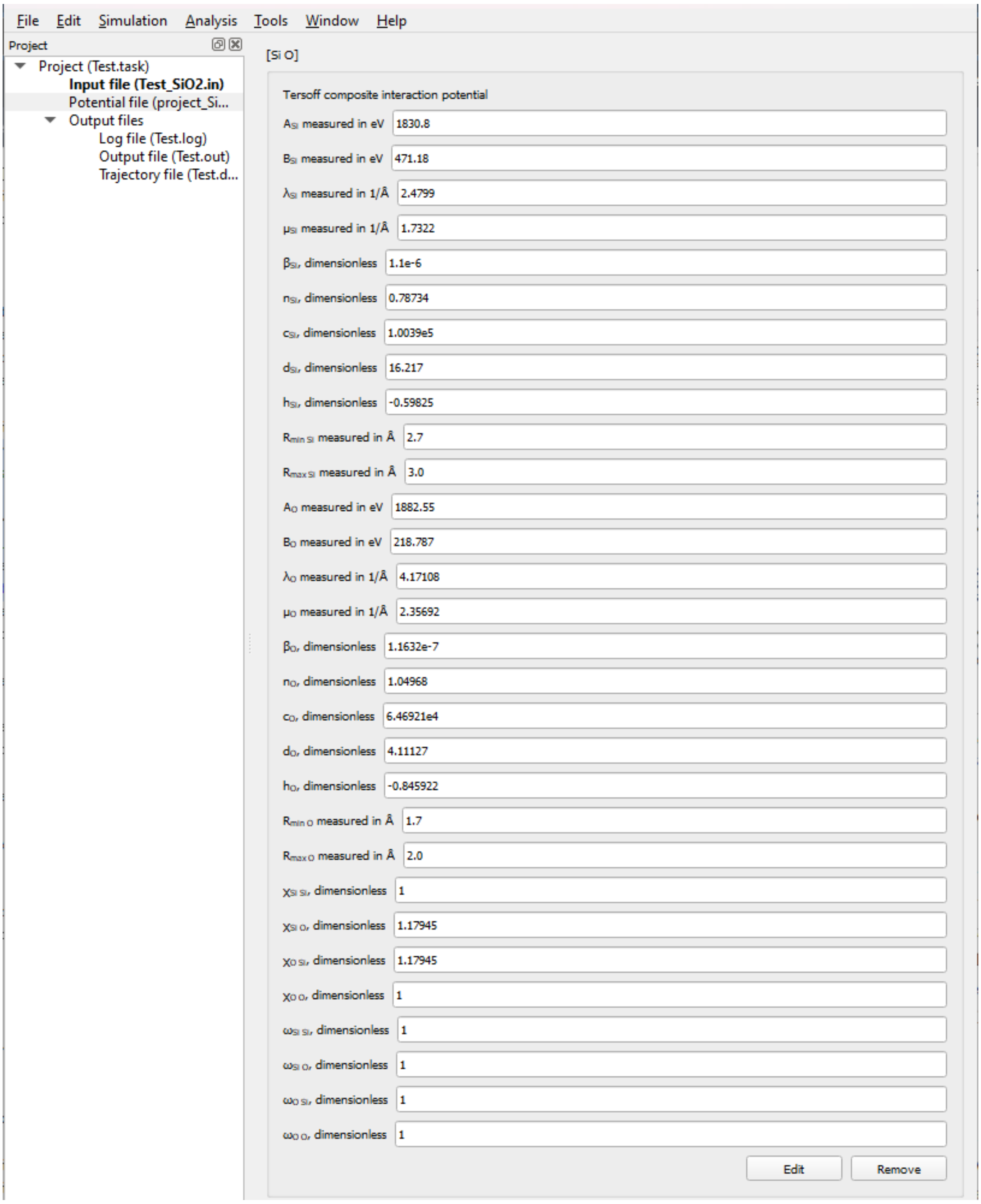

[Si O]

Tersoff composite interaction potential

A_{Si} measured in eV 1830.8
B_{Si} measured in eV 471.18
λ_{Si} measured in 1/Å 2.4799
μ_{Si} measured in 1/Å 1.7322
β_{Si}, dimensionless 1.1e-6
n_{Si}, dimensionless 0.78734
c_{Si}, dimensionless 1.0039e5
d_{Si}, dimensionless 16.217
h_{Si}, dimensionless -0.59825
$R_{min\,Si}$ measured in Å 2.7
$R_{max\,Si}$ measured in Å 3.0
A_{O} measured in eV 1882.55
B_{O} measured in eV 218.787
λ_{O} measured in 1/Å 4.17108
μ_{O} measured in 1/Å 2.35692
β_{O}, dimensionless 1.1632e-7
n_{O}, dimensionless 1.04968
c_{O}, dimensionless 6.46921e4
d_{O}, dimensionless 4.11127
h_{O}, dimensionless -0.845922
$R_{min\,O}$ measured in Å 1.7
$R_{max\,O}$ measured in Å 2.0
$\chi_{Si\,Si}$, dimensionless 1
$\chi_{Si\,O}$, dimensionless 1.17945
$\chi_{O\,Si}$, dimensionless 1.17945
$\chi_{O\,O}$, dimensionless 1
$\omega_{Si\,Si}$, dimensionless 1
$\omega_{Si\,O}$, dimensionless 1
$\omega_{O\,Si}$, dimensionless 1
$\omega_{O\,O}$, dimensionless 1

FIGURE 4.5: Tersoff potential parameters used for modelling the SiO_2 system in MBN Explorer.

The system was equilibrated over a period of 20 ps, with a time step of 1 fs. Trajectory and log steps were set at 0.1 ns, allowing for periodic recording of the atomic positions and other physical properties throughout the simulation. The temperature parameters, as specified in the MBN Explorer task file, are presented in Figure 4.7.

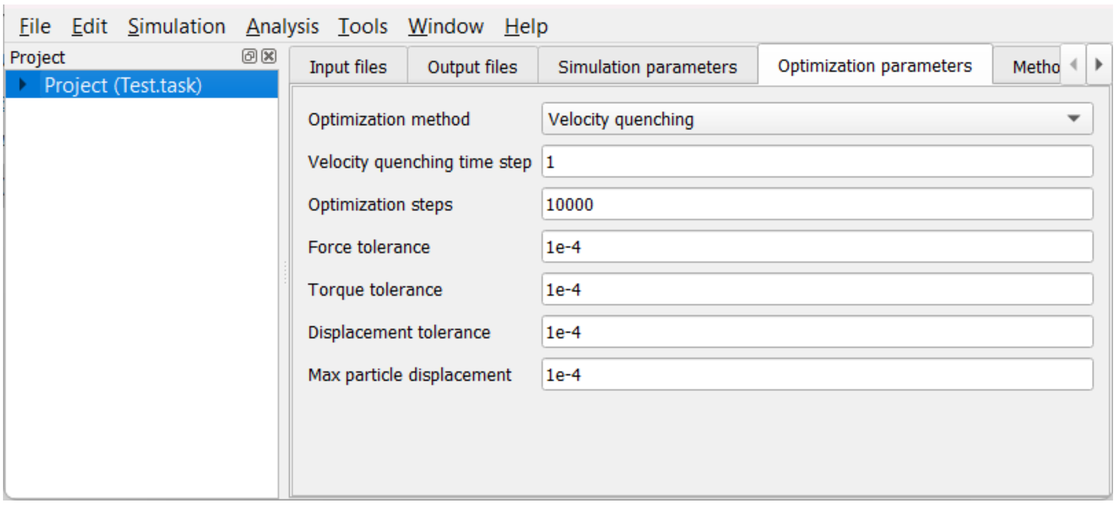

Optimization method: Velocity quenching
Velocity quenching time step: 1
Optimization steps: 10000
Force tolerance: 1e-4
Torque tolerance: 1e-4
Displacement tolerance: 1e-4
Max particle displacement: 1e-4

FIGURE 4.6: Optimisation parameters used for modelling the SiO_2 system in MBN Explorer.

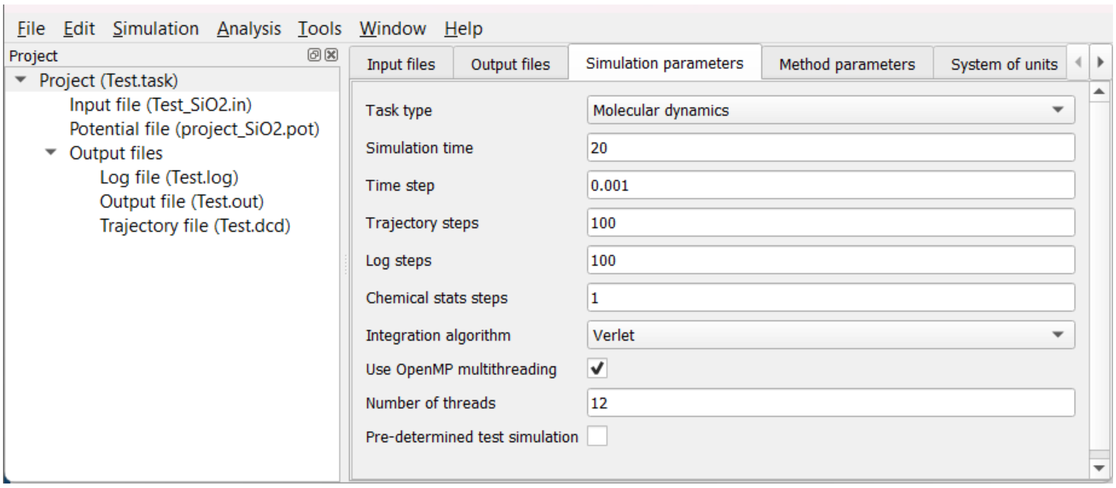

Task type: Molecular dynamics
Simulation time: 20
Time step: 0.001
Trajectory steps: 100
Log steps: 100
Chemical stats steps: 1
Integration algorithm: Verlet
Use OpenMP multithreading: ☑
Number of threads: 12
Pre-determined test simulation: ☐

FIGURE 4.7: Thermal Equilibration parameters used for modelling the SiO_2 system in MBN Explorer.

Temperature Cycling

After the system was equilibrated, it was subjected to temperature cycling to simulate the extreme thermal variations of the lunar day-night cycle. The temperature was gradually increased to represent daytime conditions on the lunar surface, followed by a cooling phase to simulate nighttime. To automate this process, a Python script (see Appendix B) was developed to perform MD simulations using the MBN Explorer software. The script executed a sequence of MD simulations involving system optimisation, equilibration, and repeated heating and cooling cycles between defined temperature limits. The objective of this temperature cycling process was to investigate the material's behaviour under cyclic thermal stresses. The workflow of the simulation can be summarised as follows:

(i) System Optimisation: The initial configuration of the system underwent an energy minimisation process to eliminate any artificial stresses or strains that may have been introduced during the setup phase. This ensured that the system achieved a stable low-energy state before commencing the dynamic simulations.

(ii) Thermal Equilibration: Following optimisation, the system was equilibrated at a standard temperature of 300 K. This step utilised a thermostat to regulate the system's temperature, allowing it to reach a state of thermal equilibrium. Simulations were conducted over 20 ps with a 1 fs time step, ensuring sufficient time for the system to stabilise before proceeding to the next phase.

(iii) Initial Heating: After equilibration, the system was gradually heated from the equilibration temperature of 300 K to a peak temperature of 400 K, mimicking the onset of high-temperature conditions. The heating rate was set at 10 K/ps (faster than reality), and the total simulation time for this phase was 10 ps. This initial heating phase served to transition the system into conditions that mimic the extreme thermal environments experienced during the daytime.

(iv) Temperature Cycling: Once the system was heated to 400 K, it was subjected to controlled heating and cooling cycles designed to mimic extreme thermal stresses. Eight complete temperature cycles were performed, with each cycle consisting of cooling and heating phases. Each phase lasted for a defined period, providing a total simulation time of 20 ps per cycle. This cyclic approach enabled an investigation into the material's structural and thermodynamic responses under repeated thermal stress. The cycling protocol consisted of the following phases:

- **Cooling Phase:** The system was gradually cooled from 400 K to 110 K at a controlled rate of 10 K/ps, simulating low-temperature conditions.
- **Heating Phase:** After cooling, the system was reheated to 400 K at the same rate of 10 K/ps. This phase simulated the recovery from low-temperature conditions.

(v) Final Equilibration: Upon completing the temperature cycling, the system underwent a final equilibration phase at 300 K. This step was critical for allowing the relaxation of any residual thermal stresses, ensuring that the system reached a stable state for subsequent analyses.

It is important to acknowledge that the thermal cycling simulations in this study were conducted over timescales on the order of picoseconds, whereas a full lunar day or night spans approximately 14 Earth days. This discrepancy reflects a known limitation of MD simulations, which require femtosecond integration time steps to maintain numerical stability and are therefore restricted to short total simulation durations. Despite this, the use of accelerated thermal cycling is a well-established approach in computational materials science and has been successfully applied to investigate structural responses under extreme temperature variations. For example, Bruns and Varnik employed deep cryogenic cycles in a model glass and observed intermittent enhancements in atomic mobility and shear-band formation [246], while Shang et al. studied ultrafast heating and cooling in a Cu–Zr metallic glass and reported local non-affine rearrangements associated with rejuvenation and relaxation phenomena [247]. In the present context, although the applied temperature gradients and rates are higher than those encountered under lunar conditions, they are sufficient to trigger representative structural and energetic changes. Nevertheless, limitations remain: the current approach may not adequately capture slower kinetic processes such as long-range diffusion, defect migration, or rare-event nucleation. Addressing these effects would require the integration of MD with coarse-grained or mesoscale methods capable of spanning longer timescales and broader spatial domains.

Analysis and Data Output

Upon concluding the simulation, an in-depth analysis of both structural and thermodynamic properties was undertaken to assess the stability and response of the material. For structural properties, the radial distribution functions (RDFs), changes in lattice parameters, and atomic displacement values were evaluated. The RDF, $g(r)$, describes the probability of finding an atom at a distance r from a reference atom, relative to the probability expected for a completely random distribution. Mathematically, it is expressed as [248]:

$$g(r) = \frac{\rho(r)}{\rho_0} = \frac{1}{4\pi r^2 \rho_0} \left\langle \sum_{i \neq j} \delta(r - |\mathbf{r}_i - \mathbf{r}_j|) \right\rangle \tag{4.2}$$

where $\rho(r)$ is the local atomic density at a distance r, ρ_0 is the average atomic density, $\mathbf{r}_i$ and $\mathbf{r}_j$ are the positions of atoms i and j, and the sum is taken over all pairs of atoms. Here, $\delta(x)$ is the Dirac delta function, which is defined to be zero for all values except $x = 0$, where it is infinite, and integrates to 1 over its entire range. The delta function effectively "selects" the distance between atoms i and j that equals r. The RDF provides information about the structural organisation of atoms within the material.

In order to determine thermodynamic properties, the total energy, temperature fluctuations, and any phase transitions observed during the simulation were also analysed.

4.2.2 SiO_2 - Glass/Amorphous

To model the SiO_2 glass/amorphous structure, we began by optimising the SiO_2 crystal file while maintaining all initial parameters and force field potential values unchanged. This optimisation step is crucial as it ensures a reliable starting point for the subsequent simulations of the amorphous phase.

Simulations

The SiO_2 glass structure was generated through MD simulations utilising the Tersoff potential, with the same parameters employed in the SiO_2 slab/crystal simulation. The dimensions of the MD cell were set to 49.1240 Å × 85.0850 Å × 108.0770 Å, as calculated in earlier analyses. To produce the SiO_2 glass, the material was first heated to a temperature of 5,000 K, effectively melting the structure, and subsequently quenched to 300 K at a cooling rate of 1×10^{11} K/s. This rapid cooling process is essential for achieving the amorphous state, preventing the formation of crystalline structures.

Analysis and Data Output

At the end of the simulation, a thorough analysis of various structural and thermodynamic properties was performed to assess the stability and performance of the material in its glassy state. For structural properties, the RDFs both before and after the quenching process were computed, along with variations in lattice constants and atomic displacement values. These calculations bring clarity the local structural arrangement and overall stability of the SiO_2 glass, revealing critical information about the material's properties and response under different conditions.

While temperature cycling was not included on the SiO_2 glass during this initial set of simulations due to computational limitations and the focus on achieving the glassy phase, the current system is well-suited for such analyses in the future. Given the material's now well-characterised structure and stability, it is expected that conducting temperature cycle simulations would provide valuable information into its thermal resilience and structural integrity under repeated thermal stress, which could be crucial for performance evaluation in space exploration and extraterrestrial environments. Future simulations could explore this aspect to further assess the material's operational profile under lunar-like conditions.

4.2.3 Polyethylene, $(C_2H_4)_n$ - Amorphous

The simulation of polyethylene (PE), $(C_2H_4)_n$ was initiated by creating a simulation box using CHARMM-GUI [249]. CHARMM-GUI was developed to facilitate and standardise

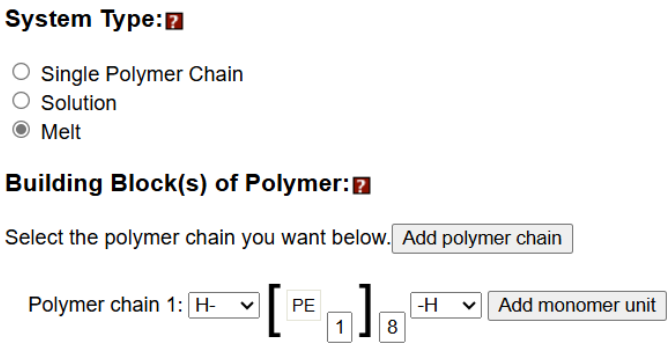

System Type:

○ Single Polymer Chain
○ Solution
● Melt

Building Block(s) of Polymer:

Select the polymer chain you want below.

Polymer chain 1: H- [PE 1] 8 -H

FIGURE 4.8: Polymer chain setup for polyethylene (PE) using CHARMM-GUI Polymer Builder.

the use of common and advanced simulation techniques primarily within the biomolecular simulation program CHARMM [250] (Chemistry at HARvard Macromolecular Mechanics). CHARMM is a widely used academic research tool for molecular mechanics and dynamics, with potential energy functions designed for proteins, nucleic acids, lipids, and carbohydrates. Additionally, CHARMM can be employed for various chemical and conformational free energy calculations with different types of restraints. It also provides a versatile set of tools for analysing atomic coordinates and dynamics trajectories. By leveraging web-based environments, CHARMM-GUI offers a graphical user interface (GUI) to generate diverse input files and molecular systems for CHARMM interactively, streamlining the process for users.

In the initial phase of the simulation, the positions of the polymer chains were equilibrated, treating each chain as a single entity or sphere. This simplification allows for more efficient calculations during the early stages of the simulation, facilitating the setup of the polymer system. For PE, which has the chemical formula $(C_2H_4)_n$, CHARMM-GUI utilises predefined molecular building blocks (monomers), with each building block representing a repeating unit of the polymer. The Chain Assembly algorithm constructs the polymer chain by sequentially linking these monomeric units, ensuring proper atomic connectivity by following the rules of chemical valency.

In this study, PE was generated using the CHARMM-GUI Polymer Builder, selecting the system type as "melt," and specifying 8 repeating units per chain as shown in Figure 4.8. Since each monomer unit is C_2H_4, a chain of 8 units corresponds to $C_{16}H_{34}$ (16 carbon and 34 hydrogen atoms), resulting in 50 atoms per chain. With 160 such chains in the system, the total number of atoms is $160 \times 50 = 8000$ atoms, consistent with the system description.

The box type was set to cubic, and the box generation algorithm created a periodic simulation box around the constructed polymer structure. This involved calculating the

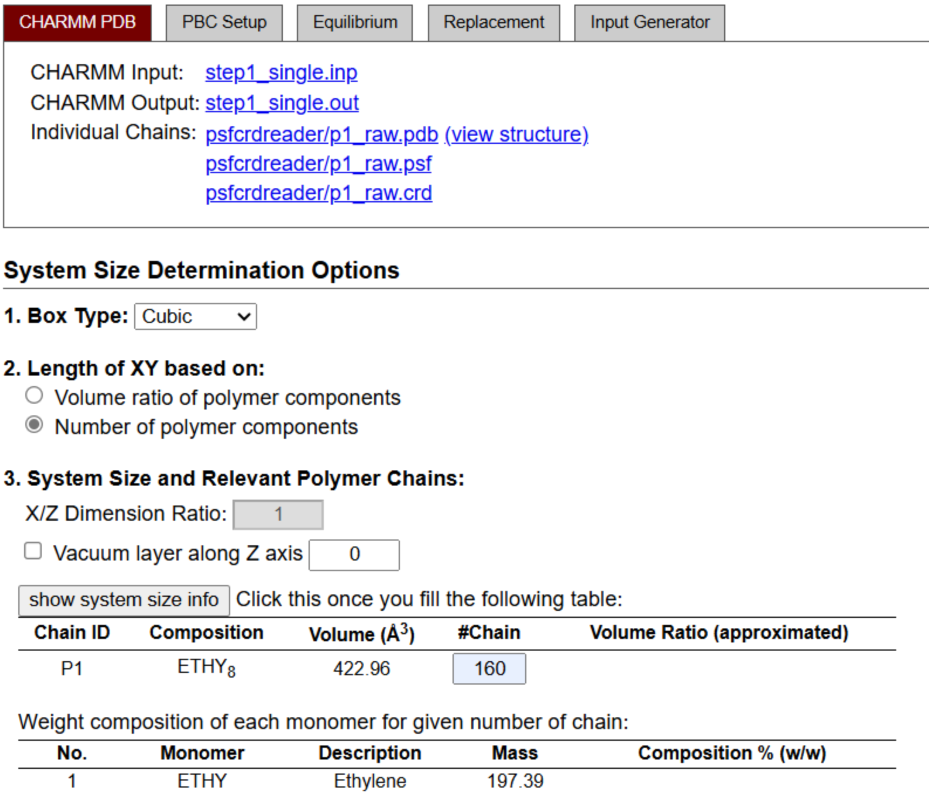

CHARMM Input: step1_single.inp
CHARMM Output: step1_single.out
Individual Chains: psfcrdreader/p1_raw.pdb (view structure)
psfcrdreader/p1_raw.psf
psfcrdreader/p1_raw.crd

System Size Determination Options

1. Box Type: Cubic

2. Length of XY based on:
○ Volume ratio of polymer components
● Number of polymer components

3. System Size and Relevant Polymer Chains:
X/Z Dimension Ratio: 1
☐ Vacuum layer along Z axis 0

Click this once you fill the following table:

Chain ID	Composition	Volume (Å^3)	#Chain	Volume Ratio (approximated)
P1	ETHY$_8$	422.96	160	

Weight composition of each monomer for given number of chain:

No.	Monomer	Description	Mass	Composition % (w/w)
1	ETHY	Ethylene	197.39	

FIGURE 4.9: Simulation box setup and system environment for PE.

box dimensions based on user-defined criteria such as desired density or volume. The box dimensions (XY) were determined based on the number of polymer components, with a ratio of X/Z equal to 1. The volume and mass were computed to be 422.96 Å^3 and 197.39 g, respectively. The setup panel is shown in Figure 4.9.

Following the initial setup, a detailed atomistic equilibration was performed on a system of dimensions $X = 46.3$ Å, $Y = 46.3$ Å, $Z = 46.3$ Å. During this phase, each individual atom in the polymer chains was considered as a bead. This stage is essential for accurately capturing the interactions and conformational dynamics of the polymer chains at the atomic level. To prepare the structure for simulation, CHARMM-GUI performs an energy minimisation step using optimisation algorithms such as steepest descent or conjugate gradient, which help relieve steric clashes and bring the system to a local energy minimum. The initial equilibration conditions involved a Lennard−Jones potential, with temperature, pressure, and simulation time set to 300 K, 0.91 Pa, and 10 ns, respectively, as illustrated in Figure 4.10.

After constructing the polymer and setting up the environment, CHARMM-GUI generated the necessary output files, including PDB and PSF files. These files contain all the structural and topological information required for running molecular dynamics simulations. Once the PDB and PSF files were generated, a thermal cycle was performed on

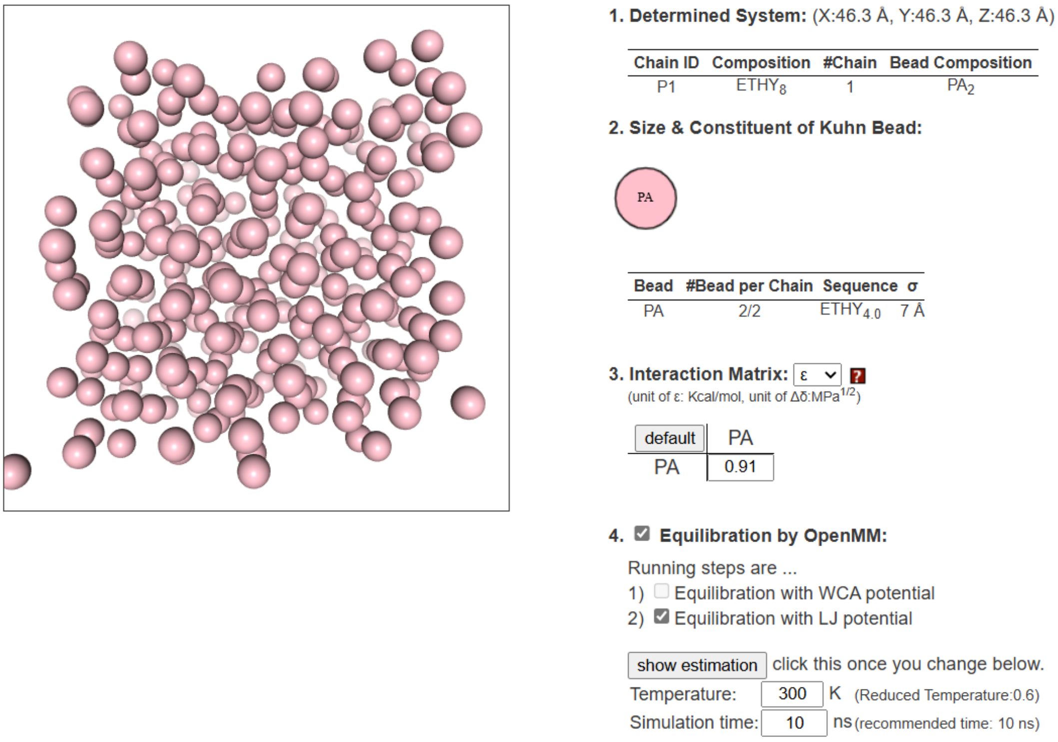

1. Determined System: (X:46.3 Å, Y:46.3 Å, Z:46.3 Å)

Chain ID	Composition	#Chain	Bead Composition
P1	$ETHY_8$	1	PA_2

2. Size & Constituent of Kuhn Bead:

Bead	#Bead per Chain	Sequence	σ
PA	2/2	$ETHY_{4.0}$	7 Å

3. Interaction Matrix: ε

(unit of ε: Kcal/mol, unit of Δδ:$MPa^{1/2}$)

default	PA
PA	0.91

4. ☑ **Equilibration by OpenMM:**

Running steps are ...
1) ☐ Equilibration with WCA potential
2) ☑ Equilibration with LJ potential

click this once you change below.
Temperature: 300 K (Reduced Temperature:0.6)
Simulation time: 10 ns (recommended time: 10 ns)

FIGURE 4.10: Equilibration setup for PE using Lennard-Jones potential.

this system using the same code applied to the thermal cycling of SiO_2 crystal. During this cycle, the temperature of the system was systematically varied to achieve thermal equilibrium, allowing us to observe how the polymer chains responded to temperature fluctuations. This step is crucial for mimicking realistic conditions that polyethylene might experience in practical applications.

Finally, to analyse the structural and thermodynamic properties, RDFs were calculated both before and after the thermal cycle. These calculations provide an understanding of the local structural arrangement and overall stability of the PE, revealing critical information about the material's properties and performance under varying conditions.

In addition to these methods, validation and force field checks were performed. The isolated molecule's geometry obtained from MM optimisation was compared to that derived from a quantum mechanics (QM) optimisation using density functional theory (DFT) calculations *via* the Gaussian software package [251], and further optimised using MBN Explorer. This comparison was essential for validating the force field employed in our simulations. Specifically, we assessed whether the force field could reproduce the geometry determined by DFT calculations. Such validation is critical to ensure that the force field effectively captures the key structural and dynamic features of polyethylene, confirming its reliability for future studies.

Although the present simulations focus exclusively on thermal cycling to assess material response to temperature fluctuations, the simulation framework (using MBN Explorer) has been designed to later include radiation effects as well. This is essential for capturing the full range of environmental stressors experienced on the lunar surface. Details of irradiation-driven molecular dynamics (IDMD) approaches, relevant to this future work, are outlined in Section 3.3.2.

Chapter 5

Results and Discussion

In this chapter, the results of MD simulations for SiO_2 and polyethylene under lunar environmental conditions are presented and analysed. The simulations focus on understanding the structural, thermodynamic, and mechanical features of these materials when subjected to temperature fluctuations characteristic of the lunar surface, ranging from 110 K to 400 K.

The study explores both crystalline and amorphous phases of SiO_2, evaluating the structural integrity and energy dynamics of these materials. The crystalline SiO_2 slab is assessed for its stability and atomic arrangement over multiple temperature cycles, while the amorphous SiO_2 phase, created through rapid quenching, is analysed for its disordered atomic structure and overall stability. Polyethylene, modelled in its amorphous form, is examined for its mechanical flexibility and temperature response.

This section provides a detailed discussion of key findings, including radial distribution function (RDF) analyses, energy profiles, and lattice parameter variations. The implications of these results are discussed in terms of material suitability for lunar applications, such as construction and radiation shielding, highlighting the potential for both silica and polyethylene materials to withstand extreme thermal conditions.

5.1 Crystalline SiO_2

5.1.1 Simulations of the molecular structures

The SiO_2 crystal structure was equilibrated over a period of 20 ps, using a time step of 1 fs. The purpose of equilibration was to bring the system to a stable thermodynamic state before conducting further simulations, ensuring that any residual stresses or non-equilibrium forces introduced during the system setup were eliminated. This step is essential to achieve a realistic configuration for the crystalline structure that accurately represents its characteristics under real-world conditions. During equilibration, the velocity of atoms was adjusted to stabilise the temperature at 300 K, representative of a typical intermediate temperature in lunar cycles.

The trajectory and log steps were set at intervals of 0.1 ns, enabling periodic recording of atomic positions, velocities, and other physical properties throughout the simulation. These recordings provided detailed snapshots of the atomic configuration, allowing for a precise assessment of how the system evolves over time and how the atoms interact under different temperature conditions. The structure of the SiO_2 crystal after equilibration is shown in Figure 5.1.

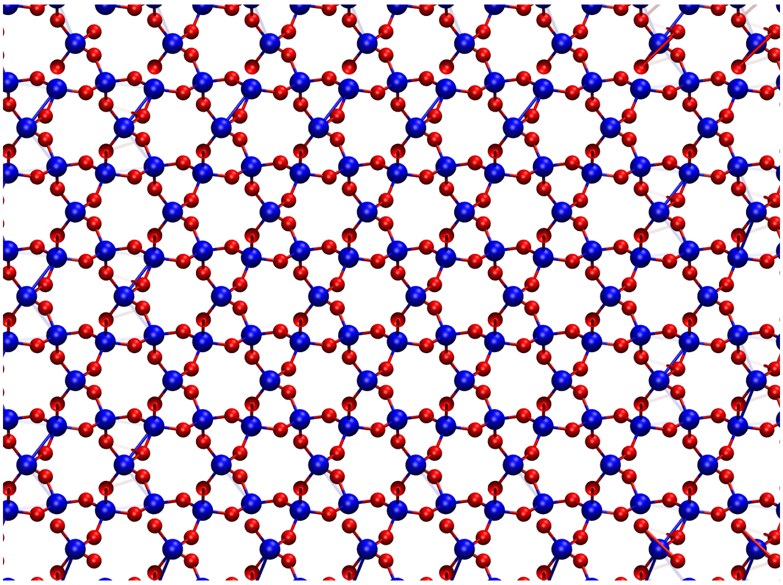

FIGURE 5.1: A figure showing the SiO_2 lattice structure, emphasising the tetrahedral arrangement of Si (blue) and O (orange) atoms in a stable configuration after the thermal equilibration.

After equilibration, the SiO_2 crystal exhibits a highly regular, ordered structure, characteristic of crystalline solids. The arrangement of Si atoms surrounded by O atoms in a tetrahedral coordination is typical of the SiO_2 crystal lattice, specifically the α-quartz phase, which was chosen for its relevance to lunar surface applications due to its high structural stability. The arrangement seen post-equilibration (Figure 5.1) is a result of both the inherent properties of SiO_2 and the force field parameters, particularly the Tersoff potential used in the simulation. This potential, known for accurately modelling Si$-$O interactions, ensures that the bond lengths and angles reflect those observed in experimental crystal structures.

Equilibration was performed to allow the system to relax to a state of minimum energy, where the forces on atoms are balanced, and the system has achieved thermodynamic

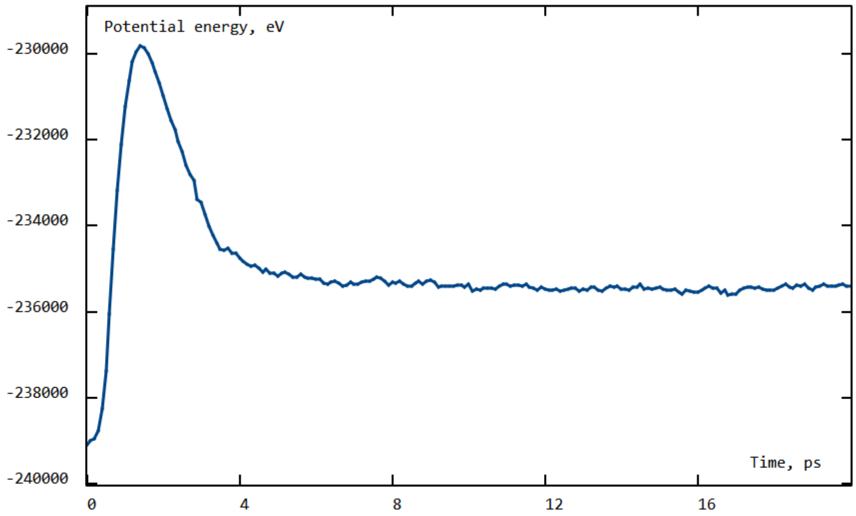

Figure 5.2: A graph showing Potential Energy (eV) on the y-axis and Time (ps) on the x-axis. After an initial decrease, the energy should fluctuate slightly but stay within a consistent range.

equilibrium. Without equilibration, the material could exhibit unphysical dynamics, such as excessive atomic vibrations or unnatural configurations, which could distort the results of subsequent analyses.

To confirm that the system had reached equilibrium, several physical properties were monitored throughout the simulation. Potential energy vs. time was recorded, and the plot (Figure 5.2) shows an initial rapid decrease, followed by stabilisation where the energy fluctuated around a constant average. This indicates that the system reached an energetically favourable configuration, eliminating any excessive forces or stresses. Additionally, temperature vs. time was plotted (Figure 5.3), showing that the system temperature stabilised at the target 350 K after initial fluctuations. This stability confirms that the system reached a consistent thermal state, ensuring realistic kinetic energy distributions.

For further validation, the pressure vs. time plot was generated (Figure 5.4), which remained stable around 4000 bar, indicating that no excessive external stresses were acting on the system, a crucial requirement for simulating an idealised SiO_2 crystal.

The reported pressure value of approximately 4,000 bar in the simulations corresponds to the instantaneous internal pressure calculated via the virial theorem. This approach relates the system's average kinetic energy to the interatomic forces and positions, capturing the internal mechanical state of the atoms. It is important to clarify that this pressure is not a result of any externally applied constraint, but rather reflects the intrinsic structural stress present within the confined simulation volume. Given the high atomic density and rigidity of the crystal lattice under periodic boundary conditions,

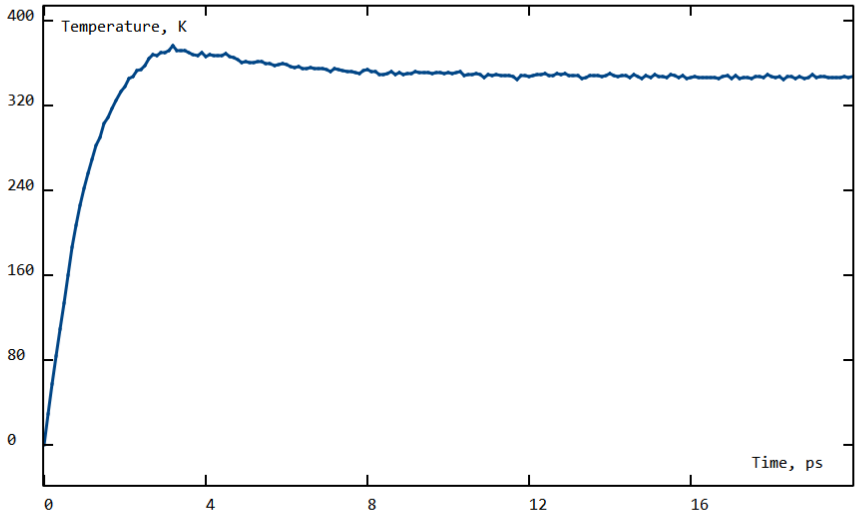

Figure 5.3: A graph showing Temperature (K) on the y-axis and Time (ps) on the x-axis. The temperature should stabilise around 350 K after some initial fluctuations.

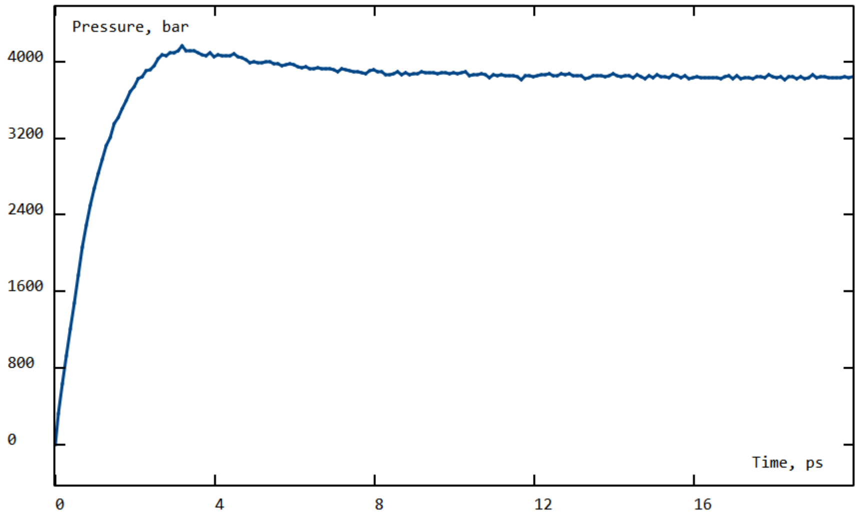

Figure 5.4: A plot of Pressure (bar) on the y-axis vs. Time (ps) on the x-axis.

elevated internal pressures are a typical outcome. Therefore, the pressure should not be interpreted as a direct analogue to experimentally applied pressure, but as a reflection of the local atomic interactions within the simulated system. Instead, their relative stability over time confirms that the system has equilibrated and is free from large internal stresses or instabilities.

The radial distribution function (RDF) of Si−O bonds was also analysed, showing sharp, well-defined peaks corresponding to the known bond lengths in SiO_2 (Figure 5.5). This consistency in bond lengths and angles confirms that the local atomic arrangement is in line with the experimental crystalline structure.

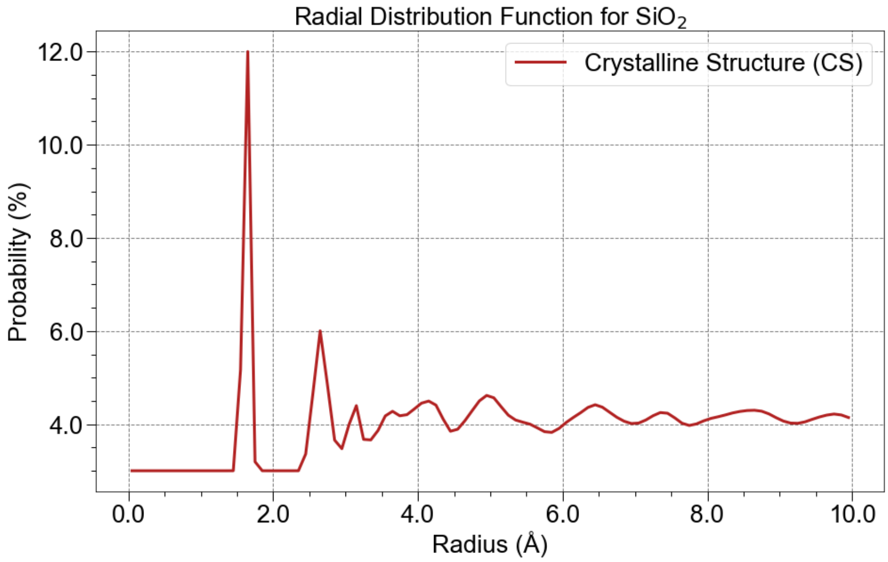

FIGURE 5.5: A plot showing the RDF probability (%)on the y-axis and the radius (Å) on the x-axis. The clear, sharp peaks that indicate a well-ordered atomic structure. For Si−O bond, the first is observed at 1.62 Å, which is typical for the quartz phase of SiO_2. Vertical offsets were applied to the RDF curves for visual clarity, which is why the functions do not reach zero at small interatomic distances, despite the theoretical expectation.

The equilibrated SiO_2 crystal appears as a well-ordered atomic arrangement, maintaining its crystalline symmetry and repeating unit cell. This stability is a result of the successful application of the velocity quenching algorithm during the optimisation phase, which reduced kinetic energy and eliminated artificial stresses. The lattice vectors were preserved, and atomic positions relaxed into an energetically favourable configuration.

The mean squared displacement (MSD) of atoms was also computed during equilibration. The plot (Figure 5.6) showed minimal changes, indicative of atoms vibrating around fixed positions rather than diffusing, as expected in a solid crystal. This lack of diffusion is another key marker of a stable, equilibrated system, where atoms remain bound to their equilibrium positions in the crystal lattice.

For the SiO_2 crystal, equilibration not only stabilised the temperature but also allowed the lattice structure to adjust naturally in response to the simulation conditions. This process eliminated any initial artifacts from the simulation setup, such as non-physical overlaps between atoms or misaligned bonds, providing a reliable starting point for further investigation into its structural and thermodynamic properties under varying thermal conditions.

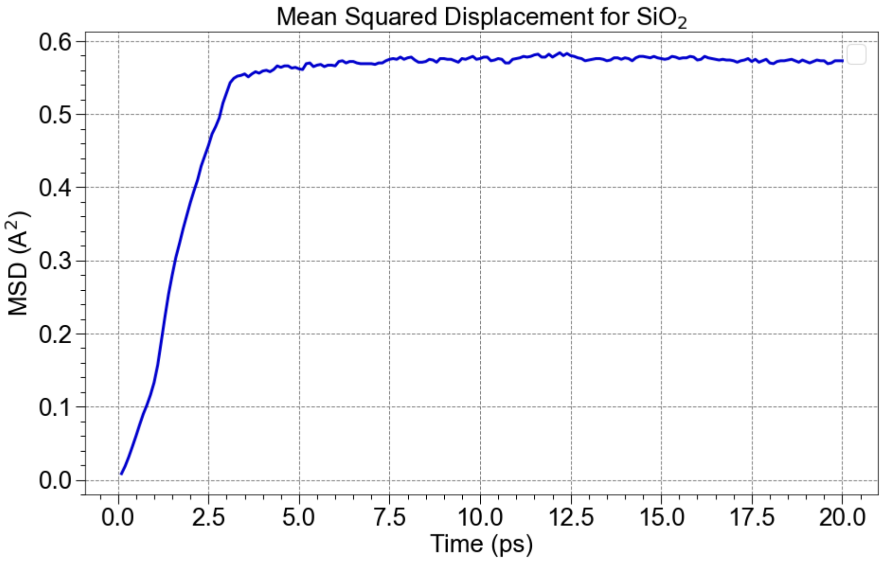

FIGURE 5.6: A plot of Mean Squared Displacement MSD (A^2) on the y-axis vs. Time (ps) on the x-axis, showing a relatively flat curve after equilibration.

5.1.2 Temperature Cycle

After completing the equilibration phase, the SiO_2 slab was subjected to repeated cycles of temperature fluctuations, ranging from high temperatures (400 K) to low temperatures (110 K), mimicking the extreme thermal environment experienced on the lunar surface. The goal of these simulations was to assess the structural integrity and stability of the SiO_2 slab under conditions of thermal cycling, which can introduce significant mechanical and thermal stress to the system.

To evaluate how well the SiO_2 structure withstands these temperature cycles, the radial distribution function (RDF) was calculated before and after the thermal cycling. The RDF provides a measure of the short-range ordering of atoms in the structure, allowing us to assess any changes in the atomic arrangement due to thermal stresses.

As shown in Figure 5.5, the initial RDF for the Si−O exhibits a sharp peak, characteristic of a well-ordered crystalline structure. The most prominent peak for the Si−O pairs occurs around 1.62 Å, which is consistent with the known Si−O bond length for silicas and silicates [252]. This peak, along with other distinct features in the RDF, confirms the highly ordered arrangement of atoms in the slab before thermal cycling.

After eight cycles of temperature fluctuations, the RDFs were recalculated to detect any potential structural changes. Figure 5.7 illustrates that the positions of the RDF peaks for Si−O remained largely unchanged after the temperature cycles, indicating that the SiO_2 slab retained its crystalline order throughout the simulation.

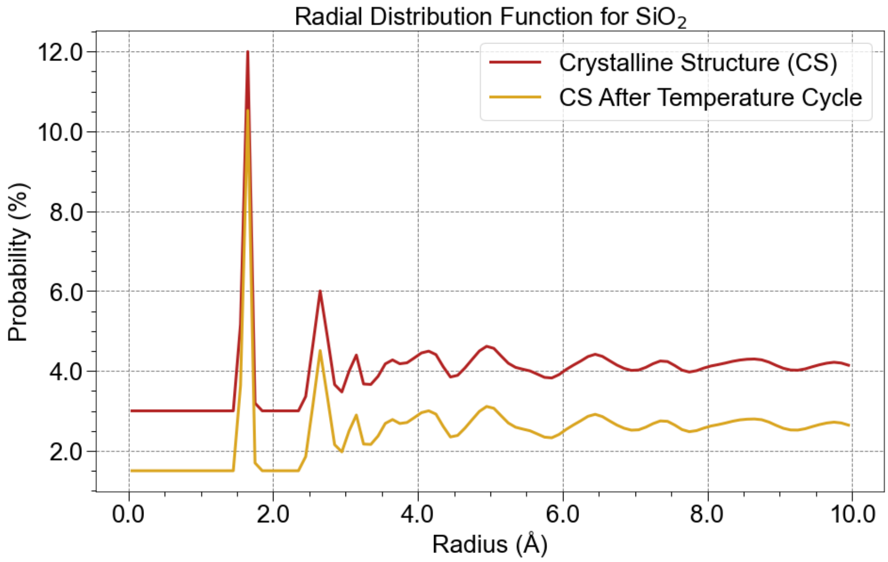

Figure 5.7: Plot of Radial distribution functions (RDF) of SiO$_2$ before and after the temperature cycle. The sharp peaks in the crystalline phase reflect the well-ordered atomic structure. The persistence of the first Si−O peak at 1.62 Å confirms the RDF after completing eight cycles of temperature fluctuations highlight that the positions of the RDF peaks remain largely unchanged, suggesting that the crystal structure remained intact.
Note: Vertical offsets were applied to the RDF curves for visual clarity, which is why the functions do not reach zero at small interatomic distances, despite the theoretical expectation.

In addition to the RDF analysis, the mean squared displacement (MSD) of the atoms was computed to measure atomic mobility throughout the temperature cycling process as shown in Figure 5.8. The MSD results show that atomic displacements remained low, indicating that the atoms are confined to their lattice positions even after repeated heating and cooling cycles. This further supports the conclusion that the SiO$_2$ slab does not undergo significant atomic rearrangements or damage during thermal cycling.

The system's temperature vs. time profile (Figure 5.9) shows the distinct temperature cycles applied during the simulation, with sharp transitions between high (400 K) and low (110 K) temperatures. Despite these large temperature swings, the SiO$_2$ structure remained stable, as evidenced by both the RDF and MSD analyses.

Furthermore, the potential energy vs. time plot (Figure 5.10) demonstrates that while the potential energy fluctuated with temperature during each cycle, the system returned to a stable energy state after each cycle, showing no signs of accumulating stress or energy imbalances over time. This strongly suggests that the SiO$_2$ slab can withstand cyclic thermal stress without suffering from structural degradation.

Visual comparisons of the atomic arrangement before and after thermal cycling (Figure 5.11) further illustrate that the crystal structure remains visually intact, with no

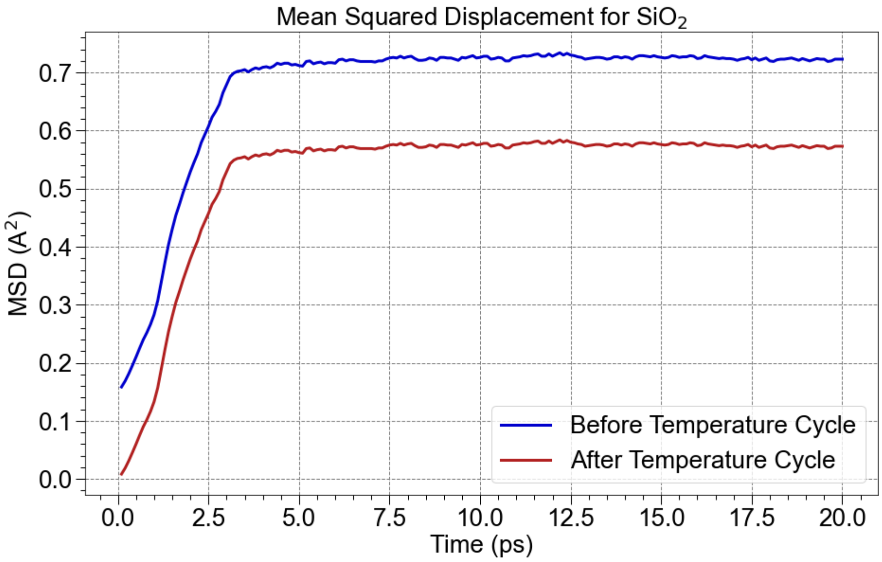

FIGURE 5.8: Plot of Mean Squared Displacement MSD (A^2) vs. Time (ps) of atoms before and after thermal cycling. The lower MSD values post-thermal cycling indicate that atoms remain largely confined to their lattice sites, suggesting minimal structural damage or amorphisation as a result of thermal stress.

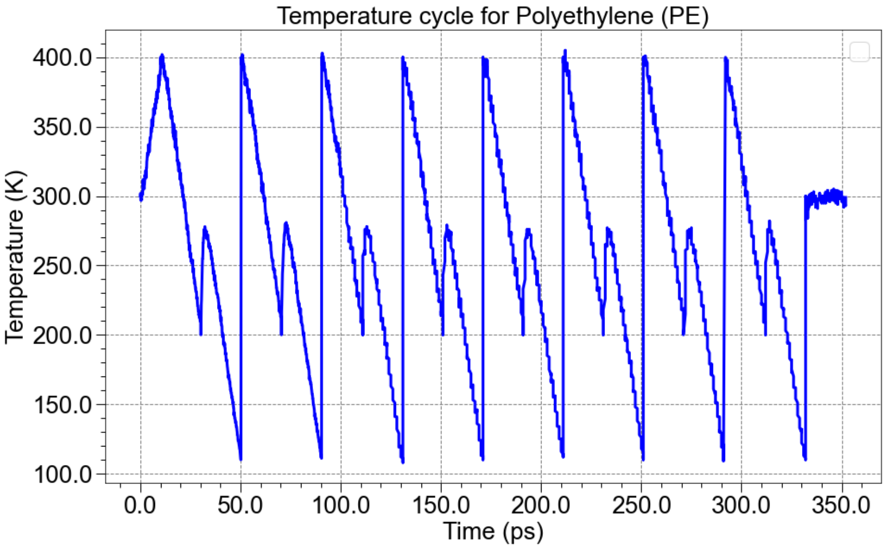

FIGURE 5.9: Plot of Temperature (K) vs. Time (ps) illustrating repeated heating and cooling cycles applied to the SiO_2 system. The system was initially equilibrated at 300 K, followed by a heating phase. Subsequently, 8 cooling and heating cycles were performed between 110 K and 400 K, reflecting the extremes of lunar temperature. After each cycle, the system was re-equilibrated at 300 K, with a final equilibration at 350 K after the last cycle. The graph depicts the transitions between high and low temperatures, confirming the system's exposure to rigorous thermal cycling.

apparent defects or amorphisation. These visualisations provide an additional layer of confirmation that the SiO_2 slab preserves its structural integrity even under extreme and repetitive temperature fluctuations.

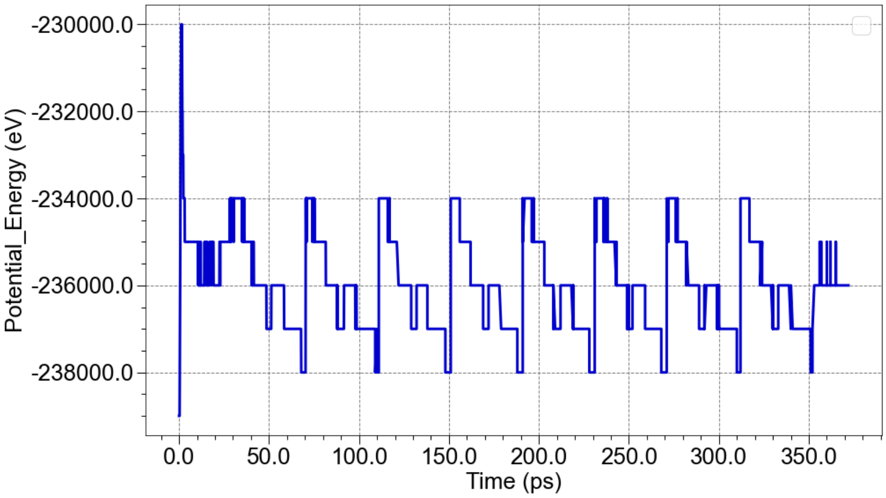

FIGURE 5.10: Plot of Potential Energy (eV) vs. Time (ps) showing the effect of repeated thermal cycling on the system. The stepwise pattern reflects the fluctuations in potential energy as the system undergoes alternating heating and cooling phases. Each plateau represents periods of energy stabilisation, corresponding to the equilibration stages between cycles. The overall trend demonstrates the controlled energy changes induced by the thermal cycling process.

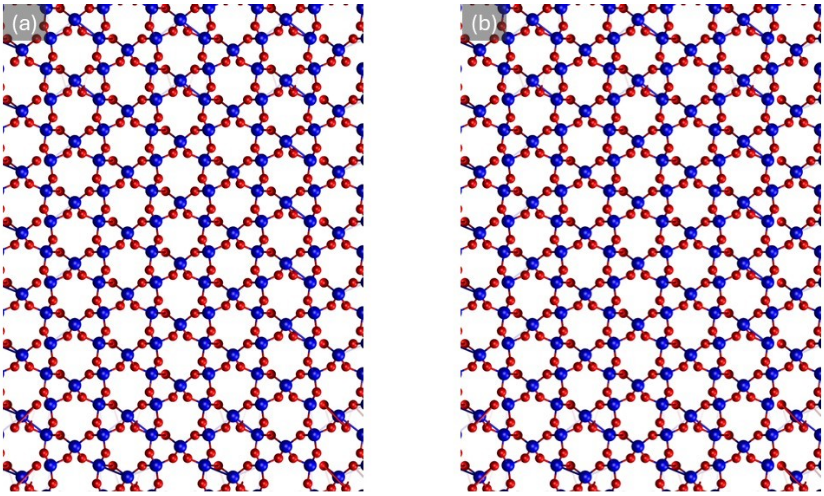

FIGURE 5.11: Figure showing the atomic structure of the SiO_2 system before and after temperature cycling. (a) The initial crystalline structure at 300 K before cycling, and (b) the final atomic arrangement at 300 K after cycling. The preservation of long-range order in both images confirms that the crystal structure remains intact, with no significant amorphisation occurring due to thermal cycling.

5.2 Amorphous SiO_2 (Glass)

In this section, we present and discuss the results of the molecular dynamics simulations conducted to model the transformation of SiO_2 from its crystalline phase to an amorphous glassy state. The SiO_2 crystal was heated to 5000 K and rapidly quenched to 300 K at a cooling rate of 1×10^{11} K/s, simulating the formation of amorphous SiO_2. Through

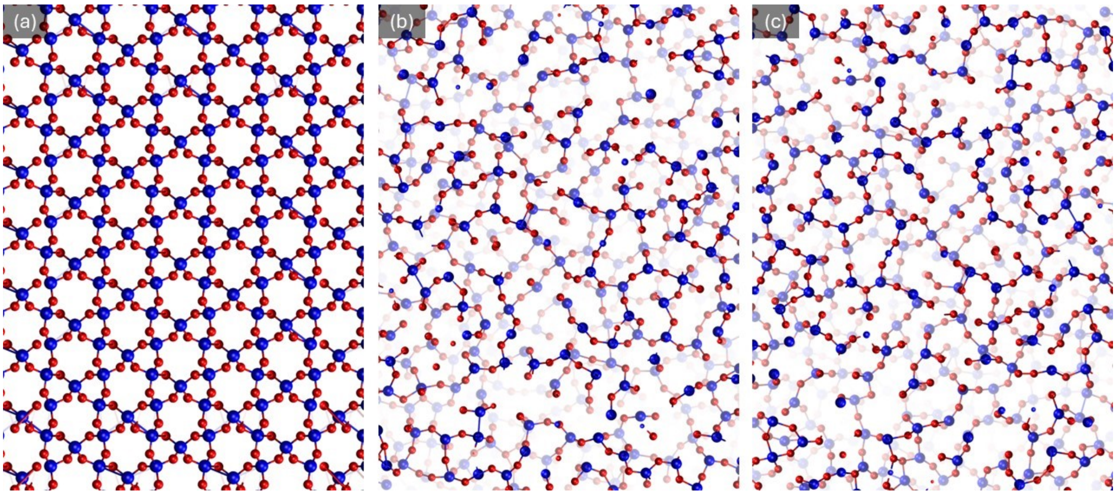

Figure 5.12: Figure of the SiO_2 system showing the transition from crystalline to amorphous structure. (a) The initial crystalline structure at 300 K before heating, (b) the disordered atomic arrangement at 5000 K during melting, and (c) the final glassy structure after quenching to 300 K. The loss of long-range order in the final figure confirms the formation of an amorphous SiO_2 network.

detailed structural analyses, including radial distribution functions (RDFs), atomic displacement, and potential energy evaluations, we examine the changes in atomic ordering and stability of the material. These results provide crucial information about the local atomic environment, bonding characteristics, and overall structural integrity of the glass, highlighting its suitability for applications in extreme thermal conditions.

5.2.1 Simulations of the molecular structures

The transition from crystalline SiO_2 to its amorphous form was successfully modelled through rapid quenching. During the heating phase, the ordered atomic structure of the crystal was disrupted as the high temperature allowed atoms to overcome their bonding forces, resulting in a molten state where atomic positions became highly disordered.

As the system was quenched, the rapid reduction in temperature prevented the atoms from reordering into a crystalline structure, instead forming a glassy state. This process is shown in Figure 5.12, where snapshots of the atomic configuration reveal the transformation from a well-ordered crystal lattice to a disordered atomic arrangement characteristic of amorphous SiO_2. The structure after quenching exhibits no long-range order, as evidenced by the lack of a repeating unit cell, confirming the successful formation of an amorphous network.

The quenching process also preserved the short-range ordering within the structure, particularly the Si$-$O bonds. This short-range order is vital for maintaining the fundamental tetrahedral SiO_2 units, even in the absence of long-range periodicity. Overall, the rapid cooling effectively transitioned the system into a stable glassy state, as shown by the stable atomic positions at 300 K.

The structural transformation from crystalline to amorphous SiO_2 is further quantified using the RDF analysis. Figure 5.13 shows the RDFs for Si−O before and after the amorphisation process. As previously discussed, in the crystalline phase, the Si−O RDF exhibits a sharp peak around 1.62 Å, corresponding to the typical Si−O bond length, with well-defined secondary peaks representing long-range ordering. The O−O RDF similarly displays distinct peaks that correspond to the regular arrangement of oxygen atoms in the crystal lattice.

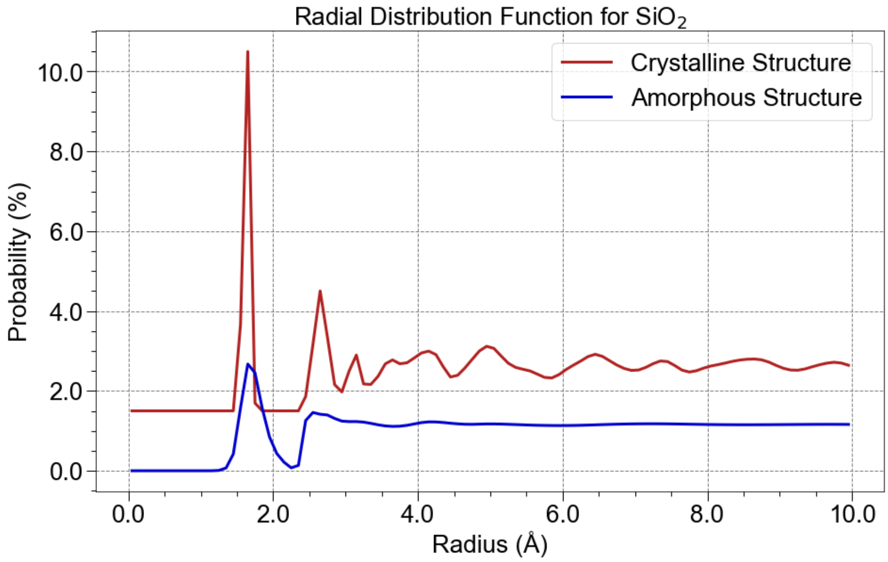

FIGURE 5.13: Plot of Radial distribution functions (RDF) of SiO_2 before and after the amorphisation process. The sharp peaks in the crystalline phase reflect the well-ordered atomic structure, while the broadened peaks in the amorphous phase indicate the loss of long-range order. The persistence of the first Si−O peak at 1.62 Å confirms that the short-range Si−O bonds remain intact in the glassy state.
Note: Vertical offsets were applied to the RDF curves for visual clarity, which is why the functions do not reach zero at small interatomic distances, despite the theoretical expectation.

After quenching, the RDF shows significant broadening of the peaks, particularly beyond the first-neighbour interactions, reflecting the loss of long-range order in the glass structure. However, the first peak in the Si−O RDF remains at approximately 1.62 Å, indicating that the short-range Si−O bonds are retained in the glassy state, even as the longer-range periodicity is disrupted. This RDF analysis confirms that the fundamental local tetrahedral coordination of silicon atoms remains intact in the glass structure, while the overall atomic arrangement loses its crystalline symmetry, as expected in an amorphous material. The retention of short-range ordering while long-range periodicity is lost is a hallmark of glass formation [253].

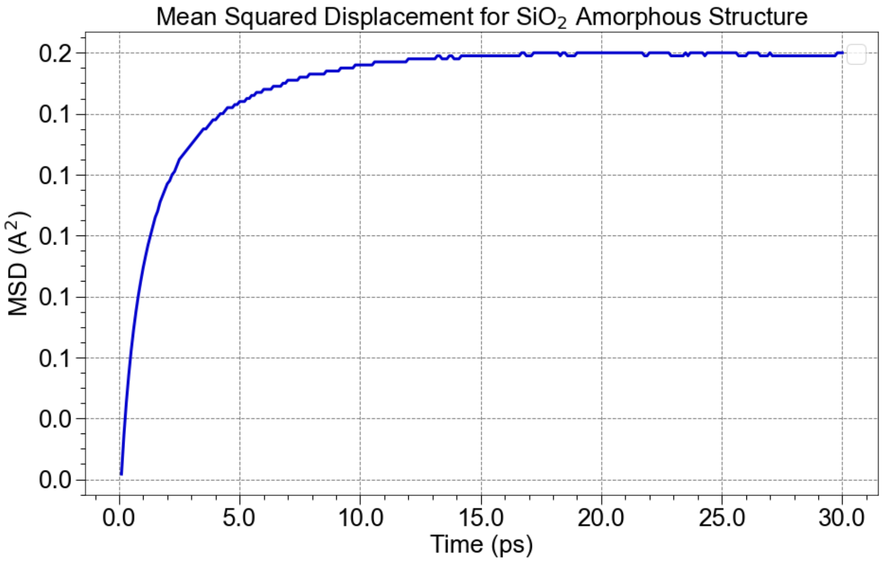

FIGURE 5.14: A plot of Mean Squared Displacement (MSD) of Si and O atoms as a function of time during the quenching process, transition to an amorphous SiO_2 structure. Initially, the steep rise in MSD reflects high atomic mobility, consistent with a disordered, high-energy phase. As time progresses, the MSD levels off, forming a plateau that signifies the stabilisation of atomic positions in a glassy, amorphous structure.

The MSD values of atoms were calculated throughout the quenching process to assess the extent of atomic mobility during the transition from a disordered, high-mobility phase to a stable, glassy state (Figure 5.14). At the start of the plot, the steep initial rise in MSD reflects a period of high atomic mobility, indicative of a phase where atoms possess significant energy and are moving freely. This phase corresponds to the early stages of the quenching process described in the text, where the high-temperature molten state allows for substantial atomic displacement as bonds are disrupted.

As the simulation progresses, the curve gradually flattens, indicating a decrease in atomic movement. This transition aligns with the quenching process, during which the system rapidly cools and atomic motion is progressively restricted. The gradual leveling of the MSD suggests that atoms are settling into more stable, fixed positions as the temperature decreases, eventually forming a disordered but rigid network characteristic of an amorphous structure.

The plateau observed in the MSD at later times is particularly significant, as it implies that atomic mobility has nearly ceased. This stabilisation in MSD values indicates that the system has reached a glassy state, where the atoms are effectively ”locked” in place, exhibiting only minimal thermal vibrations. In this glassy phase, atomic positions remain stable over time, reflecting the thermodynamic stability of an amorphous solid at low temperatures.

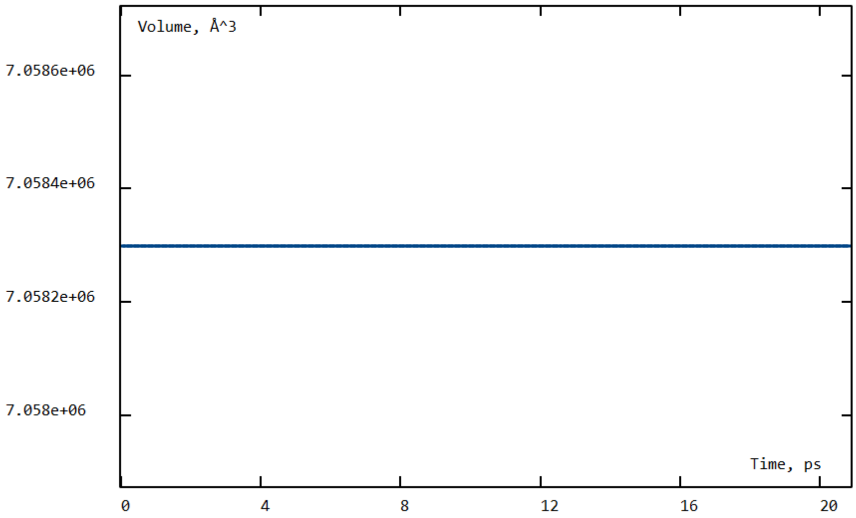

FIGURE 5.15: Volume of the SiO_2 system as a function of time during the quenching process. The stable volume indicates that the density of the system remained steady and the amorphous structure has reached a thermodynamically stable, glassy configuration.

In terms of lattice dimensions, the MD cell experienced slight fluctuations in size during the heating and quenching processes due to thermal expansion and contraction. However, the overall volume change was minimal and almost constant as shown in Figure 5.15, suggesting that while the atomic arrangement transformed from an ordered crystal to a disordered glass, the density of the material remained relatively steady. This stability in volume is consistent with experimental observations of SiO_2 glass, where the amorphous structure typically retains a similar density to the crystalline phase.

The stability of the amorphous SiO_2 structure was evaluated by tracking the system's potential energy throughout the simulation. As shown in Figure 5.16, at the start of the simulation, the potential energy is relatively high, reflecting the ordered crystalline phase. During the early stages of the quenching process, the potential energy drops sharply, signifying the rapid cooling and loss of long-range order as the crystal transitions to a disordered molten state. This phase corresponds to the disruption of the Si−O network as atomic positions become more random.

As the simulation progresses, the rate of potential energy decrease slows, and the curve begins to stabilise, indicating that the system is settling into a glassy, amorphous state. By the end of the simulation, the potential energy reaches a plateau, suggesting that the structure has achieved thermodynamic stability. This stabilisation reflects the successful formation of an amorphous network, where atomic positions are locked into place, with only minimal thermal vibrations remaining.

The stable potential energy at later times provides evidence that the amorphous SiO_2 structure is robust and resistant to further structural rearrangements. The absence of

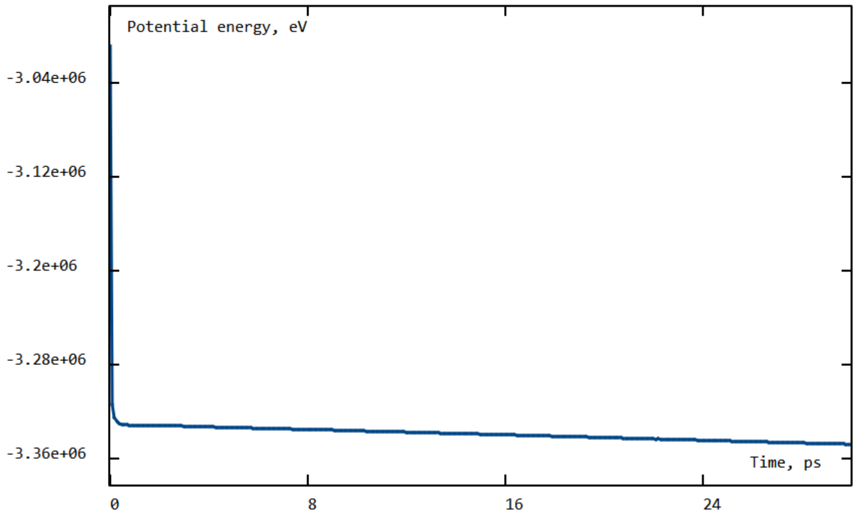

FIGURE 5.16: Potential energy profile of the SiO_2 system as a function of time during quenching. The sharp drop in energy corresponds to the rapid cooling from the molten state, and the subsequent stabilisation indicates the formation of a thermodynamically stable amorphous structure.

significant energy fluctuations confirms that recrystallisation was effectively suppressed during the rapid quenching process.

The amorphous SiO_2 structure sometimes exhibits a disordered network of SiO_4 tetrahedra (shown in Figure 5.17 at the bottom right), with silicon atoms remaining fourfold coordinated with oxygen atoms, despite the overall loss of long-range order. The persistence of this local atomic environment is crucial for the material's structural integrity in the glassy state.

The Tersoff potential used in the simulation, which accurately models Si−O interactions, plays a significant role in preserving the short-range bonding patterns. The force field ensures that bond lengths and angles remain consistent with those observed in experimental glass structures, providing a realistic representation of the amorphous SiO_2 network. Figure 5.17 illustrates the local tetrahedral coordination in the glassy phase, highlighting the preservation of Si−O bonds even as the overall structure becomes disordered.

Although temperature cycling was not performed in this set of simulations due to computational constraints, the current results suggest that the system is well-suited for such analysis in future work. The stability of the amorphous SiO_2 under static conditions indicates its potential to withstand thermal fluctuations typical of extraterrestrial environments, such as the lunar surface. Future simulations could explore its properties under cyclic thermal stress, providing comprehensive knowledge of its durability and performance in space applications.

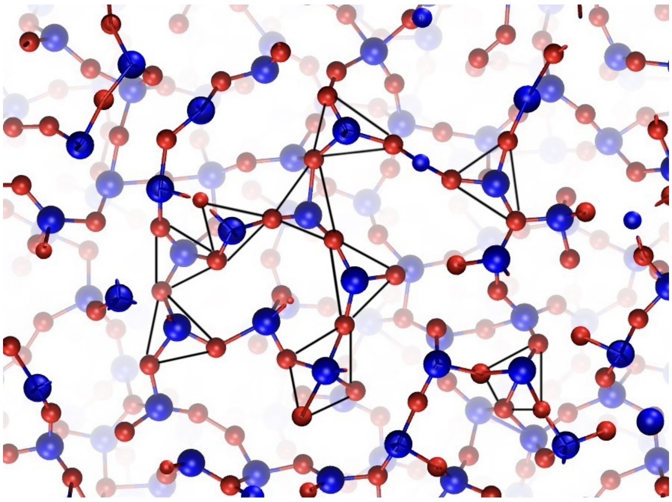

Figure 5.17: Local atomic coordination in the amorphous SiO_2 structure. Silicon atoms remain mostly in tetrahedral coordination with oxygen atoms (triangular arrangement of O around Si) even in the disordered glassy state.

5.3 Polyethylene (PE), $(C_2H_4)_n$

After completing the analysis of the SiO_2 crystalline and amorphous structures, the focus shifted to an organic compound—polyethylene (PE). Polyethylene, a widely used polymer in various applications, was selected for molecular dynamics simulations to assess its structural and thermal characteristics under different conditions. The simulations aimed to evaluate how the polymer chains respond to equilibration and temperature cycling, particularly in terms of local atomic arrangements and overall stability. By utilising a polymer melt model, constructed through CHARMM-GUI, we analysed the structural and thermodynamic properties of PE and investigated its resilience to thermal stress.

5.3.1 Simulations of the Molecular Structures

The molecular dynamics simulations of PE were initiated using CHARMM-GUI, where 160 polymer chains were constructed and equilibrated within a periodic cubic simulation box. The initial equilibration process, performed with a Lennard−Jones potential at a temperature of 300 K, brought the polymer system to a stable thermodynamic state. The equilibration was essential to eliminate any non-physical configurations or steric clashes introduced during the polymer chain assembly process. For instance, if two hydrogen atoms from adjacent polymer chains were positioned too close, they could overlap or interfere with each other, leading to an unreasonably high repulsive force and a non-physically stable configuration. This would be corrected during equilibration, allowing the system to reach a more realistic and stable state.

During equilibration, the system's potential energy decreased and stabilised after approximately 20 ns, indicating that the polymer chains had reached an energetically favourable conformation. The final dimensions of the simulation box were $X, Y, Z = 46.3$ Å. The stable energy profile, shown in Figure 5.18, confirms that the system has reached equilibrium, with minimal fluctuations observed in both energy and pressure. This suggests that the simulation accurately captured the interactions between polymer chains, laying the foundation for reliable analysis in subsequent stages.

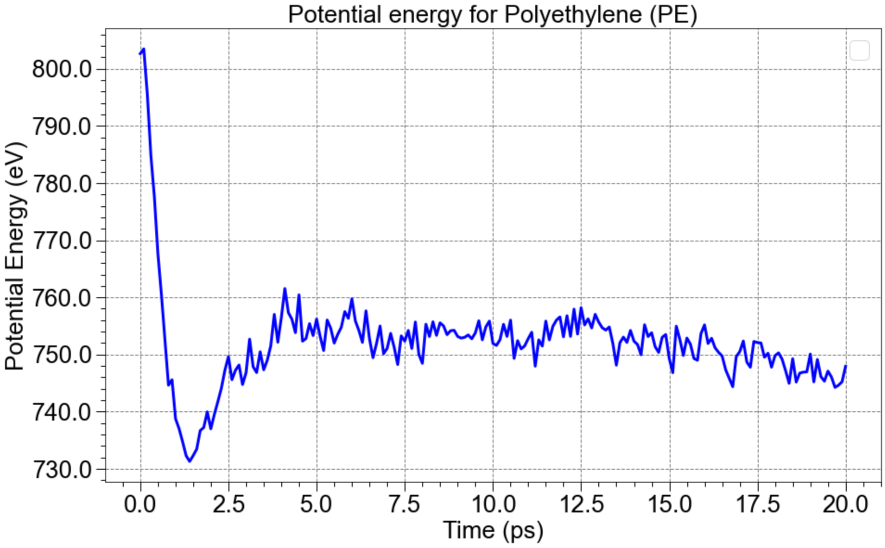

Figure 5.18: A plot of Potential Energy (eV) vs. Time (ps) showing the potential energy stabilisation of the PE system during the equilibration phase. The graph indicates a rapid decrease in potential energy followed by stabilisation, confirming successful energy minimisation and thermodynamic stability.

After equilibration, RDFs were computed for the carbon-carbon (C−C) bond to assess the local structural arrangement (Figure 5.19). The radial distribution function (RDF) for C−C pairs exhibited a prominent peak at approximately 1.54 Å, aligning with the C−C bond length of 1.54 Å determined experimentally through X-ray scattering in polyethylene [254]. The RDF peak suggest that the polymer system retains its expected local structural characteristics, confirming the accuracy of the force field used in the simulation.

5.3.2 Temperature Cycle

Following the equilibration phase, the polyethylene system underwent a series of thermal cycling steps to simulate how the polymer responds to temperature fluctuations. The temperature was systematically varied between 100 and 400 K, over a simulation time of 20 ps per cycle, as illustrated in Figure 5.20. To allow the system to relax and adapt to these temperature changes, the simulation box size was increased to $X, Y, Z = 100$

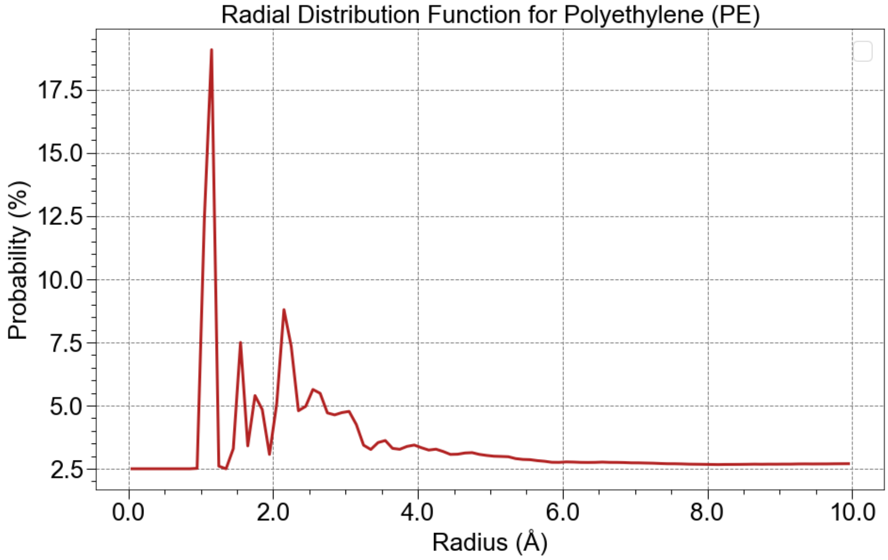

FIGURE 5.19: A plot showing the RDF probability (%) on the y-axis and the radius (Å) on the x-axis. The sharp RDF peak was observed at 1.54 Å that indicate a well-ordered atomic structure.

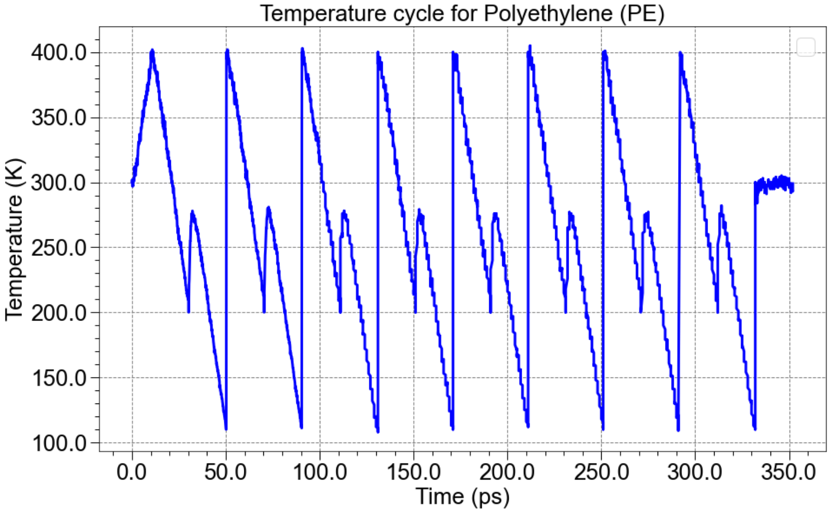

FIGURE 5.20: Plot of Temperature (K) vs. Time (ps) plot illustrating the gradual heating and cooling phases experienced by the PE system during thermal cycling. The system was initially equilibrated at 300 K, followed by a heating phase. Subsequently, 8 cooling and heating cycles were performed between 110 K and 400 K, reflecting the extremes of lunar temperature. After each cycle, the system was re-equilibrated at 300 K, with a final equilibration at 350 K after the last cycle. The smooth transitions indicate the system's ability to maintain thermal equilibrium throughout the cycling process.

Å, enabling the observation of any structural rearrangements or bond breakages under thermal stress.

The temperature (K) vs. time (ps) plot in Figure 5.20 shows smooth transitions during the heating and cooling phases, with the system maintaining equilibrium throughout. Importantly, no significant temperature spikes or deviations were observed, suggesting

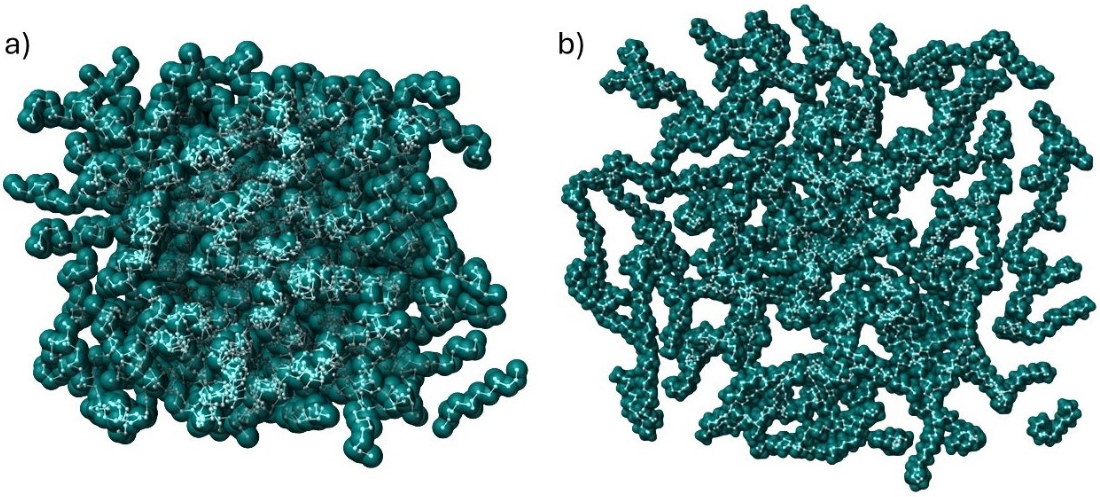

Figure 5.21: Figure showing the atomic structure of the amorphous polyethylene system before and after temperature cycling. (a) The initial amorphous structure at 300 K before cycling, and (b) the final atomic arrangement at 300 K after cycling. The polymer chains exhibit noticeable expansion and increased mobility due to thermal energy gained during the cycles. Despite the morphological change, no chain scission or loss of structural coherence was observed, indicating preserved molecular integrity.

that the polyethylene system was able to respond predictably to the imposed thermal stress.

Visual comparisons of the atomic arrangements before and after the thermal cycling process (Figure 5.21) reveal distinct changes in the morphology of the PE structure. In the pre-cycled state, the polymer chains appear compact and densely packed, indicative of a relatively rigid and constrained configuration. After undergoing thermal cycling, the polymer chains exhibit a more expanded and relaxed arrangement, reflecting a possible increase in thermal energy and enhanced chain mobility. This expansion suggests that the material becomes softer and more flexible due to the thermal cycling process.

To assess the structural integrity of the polyethylene chains, RDFs were calculated before and after the thermal cycling process (Figure 5.22). The RDF for the pre-cycled system (red line) shows a sharp, well-defined peak at 1.54 Å, corresponding to the C−C bond length in polyethylene, along with additional peaks indicative of the ordered local structure. After the thermal cycling (blue line), the primary peak remains prominent at 1.54 Å, but its intensity decreases, and additional peaks show a reduction in sharpness. Minor broadening of the peaks was observed, which could indicate slight thermal distortions caused by increased atomic vibrations during the higher temperature phases of the cycle. However, the lack of significant peak shifts confirms that the polyethylene structure remained stable and did not undergo any phase transition or significant degradation under the thermal cycling conditions.

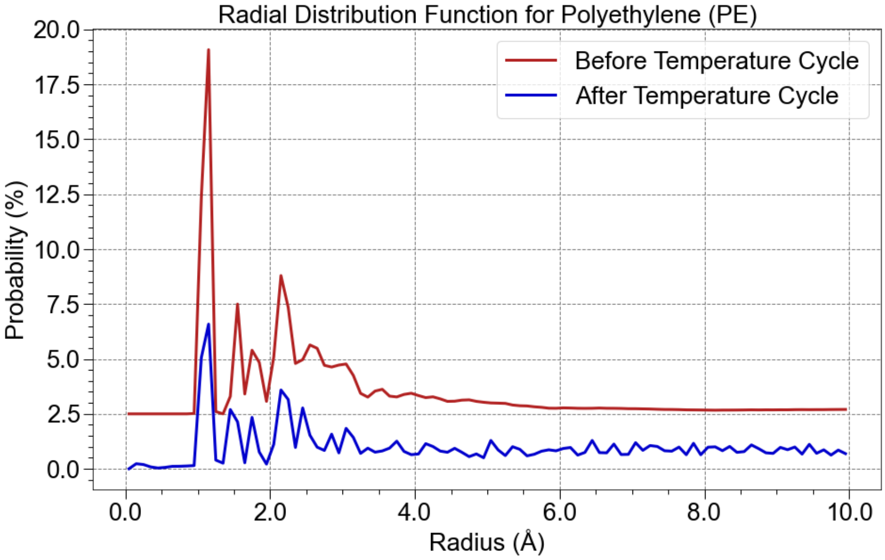

FIGURE 5.22: Plot of Radial distribution functions (RDF) of amorphous PE $(C_2H_4)_n$ before and after the temperature cycle. The persistence of the first peak at 1.54 Å confirms the RDF after completing eight cycles of temperature fluctuations highlight that the positions of the RDF peaks remain unchanged, suggesting that polyethylene structure remained stable.
Note: Vertical offsets were applied to the RDF curves for visual clarity. As a result, the functions do not reach zero at small interatomic distances, despite the theoretical expectation.

Additionally, the pressure was monitored throughout the temperature cycles, revealing a steady profile with only minor fluctuations around a stable average, as shown in Figure 5.23. This consistent pressure trend indicates that, although the polymer chains expanded and became more mobile during thermal cycling, the system did not experience degradation or significant structural failure.

The elevated pressure observed in the PE simulations—approximately 1,000 bar—can be understood using the same reasoning outlined previously for the SiO_2 system. Specifically, the reported pressure reflects the instantaneous internal pressure calculated from atomic interactions and kinetic energies via the virial theorem. This value arises from the system's molecular configuration and density under periodic boundary conditions, and should be interpreted as an intrinsic measure of internal structural stress rather than an externally applied condition. Such high internal pressures are typical in molecular dynamics simulations and do not indicate any physical instability or inaccuracy in the simulation setup.

The observed morphological changes reflect increased flexibility and thermal motion rather than instability. Combined with the unshifted RDF peaks, these results confirm that polyethylene retained its molecular integrity and remained structurally resilient under thermal stress conditions.

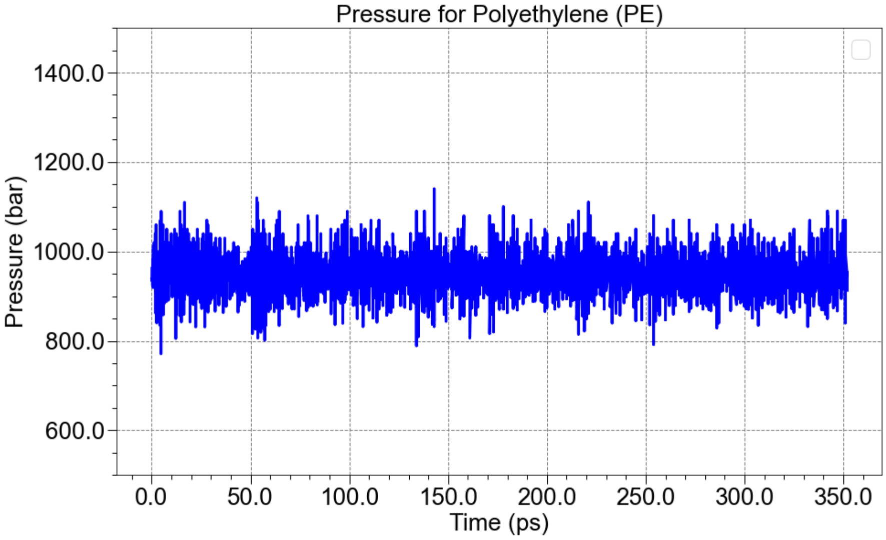

FIGURE 5.23: Pressure profile of PE over time during thermal cycling, showing a stable and consistent pattern with minimal fluctuations. This stability indicates polyethylene's strong resilience to thermal stresses, confirming its structural integrity and reliability in thermally dynamic environments.

The results presented here demonstrate the structural and thermal stability of both SiO_2 crystal and amorphous polyethylene structures under varying conditions, providing valuable information regarding their properties. The next step in this research will involve applying IDMD simulations to evaluate the response of these systems to radiation-induced effects, providing a deeper understanding of their structural and thermodynamic behaviour under extreme conditions.

The findings provide insights into the structural and thermal stability of selected materials under rapid thermal cycling. However, it is recognised that radiation from solar wind and galactic cosmic rays constitutes another significant challenge for long-term material performance on the Moon. Although not included in the current simulations, the programme is prepared for future inclusion of IDMD (see Section 3.3.2) modelling to assess combined effects. As such, this thesis establishes a foundation for subsequent studies that will incorporate simultaneous thermal and radiation stressors.

Chapter 6

Conclusions

This chapter summarises the key findings and insights gained from the MD simulations performed in this study, focusing on the structural dynamics and resilience of materials under lunar-like conditions. The goal was to assess the stability of both inorganic and organic materials, specifically SiO_2 and polyethylene, under extreme temperature fluctuations characteristic of the lunar environment, with proton irradiation reserved for future investigation. Additionally, we examine the study's limitations, highlighting areas where future research can expand upon the groundwork established by these simulations. These findings contribute to a deeper understanding of material behaviour in space, which is essential for developing sustainable lunar habitats and other space infrastructure.

6.1 Summary of Findings

The quest for durable materials capable of withstanding the Moon's extreme environment is essential for the future of lunar exploration and habitation, as envisioned by NASA's Artemis program. Through molecular dynamics simulations, this study focused on evaluating the thermal and radiation stability of two critical materials—SiO_2 and PE. These materials were chosen based on their relevance to lunar construction: silica as a primary component of lunar soil and potential construction material, and polyethylene as a polymer binder in lunar concrete.

The MD simulations revealed several key findings:

1. **Crystalline SiO_2 Stability:** The molecular dynamics simulations of crystalline SiO_2 revealed its impressive stability under the extreme temperature cycling conditions typically found on the lunar surface, where temperatures can fluctuate

between 110 K and 400 K. Crystalline SiO_2, with its highly ordered atomic structure and inherent high melting point, showed remarkable resilience throughout the thermal cycling process. Despite being subjected to repeated heating and cooling phases, the simulations indicated that the lattice structure remained intact without significant deformations or disruptions. This robustness underscores the potential of crystalline SiO_2 for structural applications in environments like the Moon, where materials must withstand extreme thermal stresses.

Detailed analyses, including the RDF and MSD analyses, temperature vs. time plots, and potential energy profiles, all converged to confirm the stability of the SiO_2 slab. The RDFs showed only minimal broadening of peaks, indicative of slight thermal distortions due to atomic vibrations at higher temperatures. However, the key peaks, particularly those corresponding to Si−O bonds, remained sharp and well-defined, confirming that the local atomic arrangement was largely preserved. This consistency highlights the system's ability to maintain its crystalline order even under fluctuating thermal conditions.

The MSD results further reinforced the stability of the material, showing low atomic mobility throughout the simulations. Atoms remained confined to their lattice positions, demonstrating that there was no significant atomic diffusion or displacement, which would have indicated structural degradation. Additionally, the temperature vs. time plots revealed smooth transitions during both heating and cooling phases, with the system effectively equilibrating between temperature cycles. This smooth response indicates that the material can handle rapid thermal changes without experiencing stress-induced damage.

Finally, the potential energy profile exhibited controlled, stable fluctuations in response to the temperature cycles, with the system consistently returning to a low-energy, stable state after each cycle. This tendency suggests that the SiO_2 slab absorbed and released thermal energy efficiently without accumulating mechanical stress or internal defects.

In conclusion, the combined results of the RDF, MSD, temperature, and potential energy analyses illustrate that crystalline SiO_2 is highly resilient to the extreme thermal cycling encountered in lunar environments. Despite minor thermal distortions, the material maintained its structural integrity and crystalline order, affirming its suitability for use in thermally demanding applications, such as lunar surface structures. Its ability to resist significant deformation or phase changes under repeated thermal stress positions SiO_2 as a highly promising material for future lunar exploration and construction efforts.

2. **Amorphous SiO_2 Glass Resilience:** The resilience of amorphous SiO_2 was investigated by subjecting a crystalline SiO_2 structure to a melting process at high temperatures (5000 K) followed by a rapid quenching to 300 K, producing a glassy state. While this amorphous structure exhibited a higher susceptibility to thermal distortions compared to its crystalline form, it demonstrated remarkable stability throughout the temperature cycling. Notably, the RDF analysis showed only minor broadening of peaks, suggesting that the local atomic arrangement remained largely intact. This resilience suggests that amorphous SiO_2 could be a promising candidate for lunar structures, where thermal stability is crucial.

   The molecular dynamics simulations effectively captured the transition from a crystalline to an amorphous phase, with the rapid cooling process eliminating the long-range periodicity characteristic of the crystal. The RDF analysis confirmed the loss of long-range order, a hallmark of the glassy state, while preserving the short-range Si−O bonds, essential for maintaining structural integrity. Despite the structural transition, the MSD values remained low, indicating that atoms were not freely diffusing but remained confined to their local positions. Additionally, the potential energy analysis revealed a stable profile at room temperature, with no signs of recrystallisation or instability.

   These results highlight the efficacy of rapid quenching in producing a stable amorphous SiO_2 structure, which retains its essential bonding network despite the absence of crystalline order. The inherent stability of this amorphous form, even under thermal cycling, positions it as a material of great interest for construction in extreme environments such as the lunar surface. Its ability to withstand thermal fluctuations without significant structural degradation underscores its potential for long-term performance in extraterrestrial applications.

3. **PE Stability:** In the simulations, a system consisting of 160 polyethylene polymer chains was constructed and equilibrated within a periodic cubic simulation box. The equilibration phase was critical in ensuring that the polymer chains reached a stable thermodynamic state before undergoing further analysis. The use of a Lennard−Jones potential at 300 K helped to eliminate any non-physical configurations, ensuring an accurate representation of the polymer's natural configuration.

   During equilibration, the system's potential energy stabilised, indicating that the polymer chains adopted an energetically favorable conformation. The final dimensions of the simulation box were approximately 46.3 Å in each direction, and a stable energy profile was observed, confirming that the system had reached equilibrium. RDF values for the C−C bond, computed after equilibration, revealed peaks at 1.54 Å, which correspond to the expected bond lengths in polyethylene.

This data indicates that the polymer retained its local structural characteristics, validating the accuracy of the force field parameters.

Following equilibration, the PE system was subjected to a series of thermal cycling steps, where the temperature was varied between 110 K and 400 K over a simulation time of 20 ps per cycle. This process was designed to simulate the temperature fluctuations that polyethylene might encounter in various practical applications, particularly in harsh environments such as lunar habitats, where temperature extremes can pose significant challenges to material stability.

The results of the thermal cycling simulation showed minimal structural deviations in the polymer chains. The RDFs for both C−C and C−H bonds, recalculated after the thermal cycling process, exhibited only slight broadening of the peaks, with no significant shifts observed. This suggests that the polymer structure remained largely intact, despite the thermal stress imposed during the cycles. The broadening of the peaks can be attributed to increased atomic vibrations at higher temperatures, but this did not lead to any noticeable degradation or phase transitions.

Moreover, the potential energy and pressure profiles during thermal cycling remained stable, with no drastic fluctuations, further indicating the polymer's resilience to repeated heating and cooling. The temperature vs. time plot showed smooth transitions between the different temperature phases, and the system maintained equilibrium throughout the process. This predictable thermal response, with no major spikes or deviations, highlights polyethylene's ability to withstand thermal cycling without undergoing significant structural or thermodynamic changes.

The implications of these findings are significant for the potential use of polyethylene as a binder in composite materials, such as lunar concrete. In such applications, where materials are exposed to extreme environmental conditions, flexibility and durability are paramount. Polyethylene's ability to maintain its structural integrity under fluctuating temperatures suggests that it could play a crucial role in enhancing the performance of polymer-based materials. Its resilience to thermal stress makes it a strong candidate for use in construction materials designed for harsh, thermally dynamic environments like the lunar surface, where temperature extremes could otherwise cause materials to crack or degrade over time.

Overall, the MD simulations confirm that polyethylene exhibits strong resistance to thermal stress, retaining its local atomic arrangement and thermodynamic stability even under challenging conditions. This reinforces its potential as a durable material for various industrial applications, including as a key component in construction materials designed to endure thermal cycling, ensuring long-term performance and reliability.

The findings of this study underline the potential of both crystalline and amorphous forms of SiO_2, as well as polyethylene, to serve as core materials in lunar construction. Their ability to withstand extreme temperatures and radiation without significant degradation makes them strong candidates for sustaining the integrity of lunar habitats.

The findings from this study underscore the robustness and stability of both amorphous SiO_2 and polyethylene systems, bringing a deeper understanding of their structural and thermal behaviour under various conditions. The amorphisation process of SiO_2 demonstrated that while long-range order is disrupted, the fundamental short-range $Si-O$ tetrahedral bonds are preserved, a hallmark of glassy materials. The stabilisation of mean squared displacement and potential energy during the quenching process further confirmed the thermodynamic equilibrium of the amorphous structure. For polyethylene, the thermal cycling simulations showed that the polymer chains exhibit exceptional resilience to temperature fluctuations, with minimal distortion in bond arrangements and consistent thermodynamic stability. Collectively, these results validate the use of molecular dynamics simulations for accurately modelling the transition to and responses of amorphous and polymeric systems, reflecting their suitability for real-world applications in dynamic environments.

6.2 Limitations of Study

Despite the promising insights derived from the molecular dynamics (MD) simulations, this study presents several limitations that should be acknowledged. These limitations highlight areas where future research can build upon the groundwork established here to further refine our understanding of material performance under lunar-like conditions.

1. **System Size and Scale:**
   The simulations in this study were conducted on relatively small-scale systems containing a limited number of atoms. While such system sizes are appropriate for capturing atomistic-level mechanisms and thermodynamic trends, they may not fully represent the macroscopic properties of materials in real-world applications. In particular, phenomena such as grain boundary behaviour, porosity effects, and large-scale mechanical responses cannot be adequately captured within

these constrained system sizes. Future studies should consider scaling up simulations or employing multiscale modelling frameworks to incorporate mesoscale and continuum-level features that influence material performance in structural applications.

2. **Number of Temperature Cycles:**
   The thermal cycling conducted in this study consisted of a relatively small number of heating and cooling cycles due to computational cost constraints. However, materials intended for lunar habitats must endure thousands of such cycles over their operational lifetime, given the Moon's month-long diurnal cycle and long-term mission timelines. While the current simulations reveal short-term structural resilience, they may not fully capture the cumulative effects of prolonged cyclic stress, such as fatigue, microcracking, or progressive densification. Future simulations with extended cycling protocols will be necessary to more accurately model long-term behaviour and predict lifecycle degradation of candidate materials.

3. **Timescale Limitations of Thermal Cycling Simulations:**
   It is important to acknowledge that the thermal cycling simulations were conducted over timescales on the order of picoseconds, which are significantly shorter than the actual lunar day-night cycle that spans approximately 14 Earth days per phase. This discrepancy is a recognised limitation of MD simulations, which are inherently constrained by computational demands and the stability requirements of femtosecond-level time steps.

   Although the accelerated thermal cycling applied in this study is widely used in computational materials science to investigate fundamental thermomechanical responses, the imposed temperature gradients and rapid rates—while exaggerated—are sufficient to induce representative structural behaviours. However, certain kinetic processes, such as defect migration, phase separation, or long-range atomic rearrangements, may not fully manifest within these limited timescales. Future work could benefit from coupling MD simulations with higher-level modelling approaches such as kinetic Monte Carlo, phase-field methods, or finite element modelling to bridge the gap between atomistic insights and macroscopic time-dependent phenomena.

4. **Simplification of Environmental Factors:**
   This study was intentionally focused on evaluating the effects of thermal cycling and, to a limited extent, radiation damage through proton irradiation simulations. However, the lunar environment presents a multifaceted set of challenges that extend beyond these two stressors. Realistic lunar surface conditions involve complex radiation spectra including alpha particles, gamma rays, cosmic rays, and

solar wind plasma, as well as micrometeorite impacts and prolonged exposure to vacuum and abrasive lunar regolith. These environmental factors can induce synergistic damage mechanisms, such as sputtering, radiation-assisted creep, or erosion, which are not accounted for in the current simulations. Future research should aim to develop more comprehensive simulation environments that incorporate multiple concurrent stressors to better reflect actual lunar surface conditions.

5. **Material Scope and Generalisability:**
   The present study focused exclusively on two material systems: SiO_2 and PE. While these materials are highly relevant for potential lunar construction—due to silica's abundance in lunar regolith and polyethylene's radiation-shielding properties—the range of viable materials for lunar infrastructure is considerably broader. Advanced composites, metal alloys, geopolymers, and other polymeric systems may offer superior performance or synergistic properties when used in tandem. Expanding the material portfolio in future simulations will not only help identify more optimal materials but also enable the design of hybrid systems that combine the benefits of multiple constituents for enhanced durability and resilience.

6. **Lack of Experimental Validation:**
   As with many computational studies, the findings presented here rely solely on simulation data. While molecular dynamics simulations offer powerful insights into atomistic behaviour, they are ultimately models that depend on the accuracy of interatomic potentials and simulation parameters. Experimental validation under controlled conditions—such as thermal cycling in vacuum chambers, proton irradiation tests, or mechanical performance measurements—is necessary to confirm the predictions made in this study. Integrating computational and experimental approaches will be essential to develop robust, space-qualified materials and validate their behaviour under extreme environmental stresses.

This study's findings highlight the potential of these materials for long-term use on the Moon, but they also emphasise the need for further investigation. While the simulations provided valuable data on thermal resilience, additional studies, including long-term irradiation simulations and experimental validation under real-world conditions, are crucial to confirm these results. Thermal cycle experiments on PE (as discussed in 2.3.1) have already shown promising outcomes demonstrating temperature resistance. However, the effects of prolonged radiation exposure and other environmental factors like micrometeorite impacts and lunar dust should be examined in future research.

In conclusion, this study lays a solid foundation for understanding how key materials like SiO_2 and polyethylene behave under lunar-like conditions. The results provide a starting point for the continued development of robust materials tailored for space exploration and lunar habitation. Moving forward, more complex simulations involving larger system sizes, additional environmental factors, and expanded material testing will be essential to fully realize the potential of these materials in building long-lasting, resilient structures on the Moon and beyond.

Chapter 7

Future work and Contributions to the Field

The findings of this study lay a solid foundation for understanding the stability and properties of materials, particularly SiO_2 and polyethylene, under lunar environmental temperature. However, several avenues for future research are essential to fully optimise these materials for long-term space applications. Future work would focus on:

> **Irradiation Studies to Validate Material Stability:** While this study has provided significant insights into the thermal response and structural transformations of SiO_2 and PE, their behaviour under radiation exposure remains to be explored. A critical next step involves applying irradiation-driven molecular dynamics (IDMD) simulations to investigate how these materials respond to high-energy radiation. Such simulations will enable the examination of radiation-induced phenomena, including bond scission, defect formation, and structural rearrangements in both amorphous SiO_2 networks and PE polymer chains.
>
> These studies are essential for assessing the materials' long-term durability and adaptability in harsh space environments, where exposure to cosmic and solar radiation is inevitable. Conducting IDMD simulations with high-energy protons representative of lunar conditions will help validate the materials' resilience.
>
> Moreover, comparing simulation outcomes with real-world irradiation experiments, such as those conducted by Mr. Jonathan Cousins and described in Section 2.3, will provide a valuable benchmark for accuracy. This integration of computational and experimental approaches will strengthen model validation and support the refinement of material design strategies for lunar infrastructure and other high-radiation environments.

Refining Molecular Models through Experimental Comparison: The molecular models employed in this study, while robust, would benefit from further refinement through comparison with additional experimental data. Future research would focus on integrating more empirical data—such as neutron scattering or X-ray diffraction results—into the simulation frameworks to enhance the accuracy of the MD models. This process will allow for better characterisation of material behaviours and further alignment between computational and experimental findings.

System Size Optimisation for Practical Applications: The scale of the computational models used in this study was limited to meet the constraints of available computational resources. To bridge the gap between simulation and practical application, future research should explore optimising system sizes to match real-world engineering applications. Scaling up these models will be crucial in predicting the performance of larger structures, such as habitats or radiation shields, that are integral to lunar infrastructure.

Expanding the Database of Suitable Materials: While this study focused on SiO_2 and PE, lunar construction requires a wider range of materials to meet various functional demands, such as strength, thermal insulation, and radiation protection. Future research should expand the database of potential materials, examining their response under lunar conditions through both computational and experimental methods. This will contribute to the growing knowledge base and identify materials that can be used in composite structures or as alternatives to the materials currently considered.

7.1 Potential for New Materials and Methods

Beyond SiO_2 and PE, the future of lunar material science stands to benefit significantly from the exploration of other high-performance polymers and composite materials, as discussed in Section 2.2. Two materials of particular interest for future investigation are polychlorotrifluoroethylene (PCTFE) and Kevlar and an initial geometry has been started for further simulations. Both materials have demonstrated exceptional properties in terrestrial applications, including high thermal stability, radiation resistance, and mechanical strength—qualities that make them promising candidates for the extreme conditions of lunar construction.

7.1.1 Polychlorotrifluoroethylene (PCTFE)

Polychlorotrifluoroethylene (PCTFE) is a high-performance polymer widely recognised for its outstanding chemical resistance and thermal stability, making it ideal for applications in harsh environments. Its ability to withstand extremely low temperatures further enhances its suitability for space and cryogenic applications. Additionally, PCTFE's thermal properties can be enhanced by reinforcing it with glass fibers, which improve its performance at higher temperatures and increase its structural integrity under challenging conditions.

To facilitate future simulations and analyses, preliminary structure of PCTFE with a chain length of 9.611 Å was generated. Initial input files were prepared using the molecular modelling software Avogadro, followed by structural optimisation performed in MBN Explorer, which yielded a stable molecular configuration. Figure 7.1 presents the optimised visual structure of PCTFE that was generated using VMD [169]. This initial setup establishes a foundational model for advanced simulations.

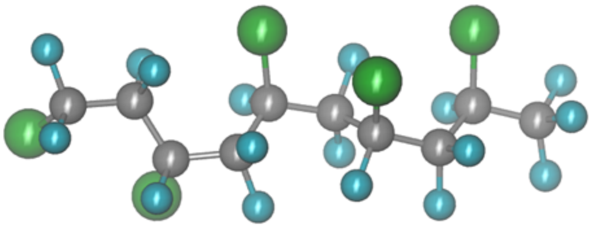

Figure 7.1: Optimised molecular structure of polychlorotrifluoroethylene (PCTFE) visualised using VMD. The visualisation highlights the arrangement and stability of the molecular structure after optimisation with MBN Explorer.

Future research would focus on refining PCTFE's molecular structure evaluating its resilience under thermal cycling and radiation conditions similar to those on the lunar surface. Additionally, assessing the mechanical and thermal properties of PCTFE through both computational and experimental approaches will be crucial to understanding its full potential as a material for lunar infrastructure.

7.1.2 Kevlar

Kevlar is a well-known high-performance polymer celebrated for its remarkable tensile strength and lightweight properties, making it an ideal candidate for a wide range of protective and structural applications. Its exceptional durability and resistance to wear and tear allow it to perform effectively in demanding environments, which is particularly relevant for the challenges posed by lunar habitation.

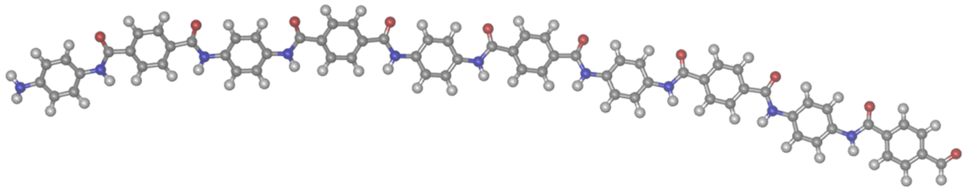

Figure 7.2: Optimised molecular structure of Kevlar visualised using VMD. This visualization illustrates the arrangement and stability of the molecular structure following optimization with MBN Explorer, showcasing the polymer's unique tensile strength properties and potential for structural applications in lunar environments.

Preliminary experiments on Kevlar, conducted by Mr. Jonathan Cousins (see Section 2.3.2), offer a critical foundation for correlating computational simulations with empirical data. This integration of computational models with experimental findings will enhance our ability to accurately predict material characteristics under lunar conditions, paving the way for informed material selection and design.

In preparation for future simulations, input files for Kevlar were generated using Avogadro, followed by molecular optimisation performed in the MBN Explorer software suite. Figure 7.2 presents the optimised visual structure of PCTFE with a chain length of 64.288 Å that was generated using VMD [169]. The unique properties of Kevlar, including its capacity to withstand high-impact forces and its inherent resistance to radiation-induced degradation, make it particularly promising for lunar applications.

Further research would focus on exploring Kevlar's performance in lunar environments, specifically its potential uses in radiation shields or as a reinforcement material in lunar concrete. Investigating the interactions between Kevlar and other materials, as well as its response under extreme temperature fluctuations and radiation exposure, will provide key information into its suitability for lunar construction. Ultimately, by combining both computational and experimental approaches, we can better understand how Kevlar can contribute to the creation of a safe and sustainable habitat on the Moon.

Bibliography

[1] C. M. Warner. Lunar living: Nasa's artemis base camp concept, 2020.

[2] D. Clery. Impact theory gets whacked. *Science*, 342(6155):183–185, 2013. doi: 10.1126/science.342.6155.183. URL `https://www.science.org/doi/abs/10.1126/science.342.6155.183`.

[3] M. J. Harrell, G. S. Schroeder, and S. A. Daire. *Lunar Environment, Overview*, pages 1–23. Springer International Publishing, 2021. doi: 10.1007/978-3-319-09575-2_15-1.

[4] E. D. Young, I. E. Kohl, P. H. Warren, D. C. Rubie, S. A. Jacobson, and A. Morbidelli. Oxygen isotopic evidence for vigorous mixing during the moon-forming giant impact. *Science (New York, N.Y.)*, 351(6272):493—496, January 2016. ISSN 0036-8075. doi: 10.1126/science.aad0525. URL `https://science.sciencemag.org/content/sci/351/6272/493.full.pdf`.

[5] S. Drake. Galileo's first telescopic observations. *Journal for the History of Astronomy*, 7(3):153–168, 1976. doi: 10.1177/002182867600700301. URL `https://doi.org/10.1177/002182867600700301`.

[6] G. Righini. New light on galileo's lunar observations. *Reason, Experiment, and Mysticism in the Scientific Revolution, Science History Publications, New York*, pages 59–76, 1975.

[7] G. Galilei. *Sidereus Nuncius, or the sidereal messenger.* University of Chicago Press, 2016.

[8] B. L. Jolliff and M. S. Robinson. The scientific legacy of the Apollo program. *Physics Today*, 72(7):44–50, 07 2019. ISSN 0031-9228. doi: 10.1063/PT.3.4249. URL `https://doi.org/10.1063/PT.3.4249`.

[9] NASA. Apollo 11, 2024. URL `https://www.nasa.gov/mission/apollo-11/`.

[10] S. Glasstone. Sourcebook on the space sciences. *Van Nostrand*, 1965.

[11] M. B Langseth and S. J. Keihm. In-situ measurements of lunar heat flow, 1977. URL `https://ntrs.nasa.gov/citations/19780005001`.

[12] R. R. Hodges Jr. Formation of the lunar atmosphere. *The Moon*, 14(1):139–157, 1975.

[13] W. F. Carroll and P. M. Blair. Discoloration and lunar dust contamination of surveyor iii surfaces. In *Proceedings of the Lunar Science Conference, vol. 2, p. 2735*, volume 2, page 2735, 1971.

[14] A. L. Bean, C. Conrad Jr, and R. F. Gordon. Crew observations. *NASA Special Publication*, 235:29, 1970.

[15] E. E. Aldrin, N. A. Armstrong, and M. Collins. Crew observations. In *Apollo*, volume 11, pages 35–40, 1969.

[16] D. R. Scott. What is it like to walk on the moon? *National geographic*, 144(3): 326–331, 1973.

[17] L. Brennan, R. Siecinski, M. Tremayne, A. Patel, P. Patel, S. Singh, B. Basily, and H. Benaroya. Mechanical design of a lunar habitat structure and deployment mechanism. *Acta Astronautica*, 213:102–120, 2023. ISSN 0094-5765. doi: https://doi.org/10.1016/j.actaastro.2023.09.001. URL `https://www.sciencedirect.com/science/article/pii/S0094576523004551`.

[18] M. Smith, D. Craig, N. Herrmann, E. Mahoney, J. Krezel, N. McIntyre, and K. Goodliff. The artemis program: An overview of nasa's activities to return humans to the moon. In *2020 IEEE Aerospace Conference*, pages 1–10, 2020. doi: 10.1109/AERO47225.2020.9172323.

[19] G. Sanders, J. Kleinhenz, and D. Linne. Nasa plans for in situ resource utilization (isru) development, demonstration, and implementation. In *Committee on Space Research (COSPAR) 2022*, 2022.

[20] Z. Hu, T. Shi, M. Cen, J. Wang, X. Zhao, C. Zeng, Y. Zhou, Y. Fan, Y. Liu, and Z. Zhao. Research progress on lunar and martian concrete. *Construction and Building Materials*, 343:128117, 2022. ISSN 0950-0618. doi: https://doi.org/10.1016/j.conbuildmat.2022.128117. URL `https://www.sciencedirect.com/science/article/pii/S0950061822017822`.

[21] J. Lee, K. Yong Ann, T. S. Lee, and B. B. Mitikie. Bottom-up heating method for producing polyethylene lunar concrete in lunar environment. *Advances in Space Research*, 62(1):164–173, 2018. ISSN 0273-1177. doi: https://doi.org/10.1016/

j.asr.2018.03.039. URL `https://www.sciencedirect.com/science/article/pii/S0273117718302795`.

[22] D. Vaniman, R. Reedy, G. Heiken, G. Olhoeft, and W Mendell. The lunar environment. In Grant H. Heiken, David T. Vaniman, and Bevan M. French, editors, *Lunar Sourcebook: A User's Guide to the Moon*, pages 27–76. Cambridge University Press, 1991.

[23] O. E. Berg, F. F. Richardson, and H. Burton. Lunar ejecta and meteorites experiment. *Apollo 17 Preliminary Science Report, NASA SP-330*, pages 16–1 to 16–9, 1973.

[24] L. R. Utreja. Lunar environment. *Applied Mechanics Reviews*, 46(6):278–284, 1993.

[25] NASA. Moon fact sheet — nssdc.gsfc.nasa.gov, 2007. URL `https://nssdc.gsfc.nasa.gov/planetary/factsheet/moonfact.html`.

[26] W. K. Hartmann and D. R. Davis. Satellite-sized planetesimals and lunar origin. *Icarus*, 24(4):504–515, 1975.

[27] S. A. Jacobson, A. Morbidelli, S. N. Raymond, D. P. O'Brien, K. J. Walsh, and D. C. Rubie. Highly siderophile elements in earth's mantle as a clock for the moon-forming impact. *Nature*, 508(7494):84–87, 2014.

[28] R. H. Lewis. Nss human safety in the lunar environment, 1992. URL `https://space.nss.org/settlement/nasa/spaceresvol4/human.htm`. NASA Technical Reports Server.

[29] W. C. Feldman, J. R. Asbridge, S. J. Bame, and J. T. Gosling. Plasma and magnetic fields from the sun. *The solar output and its variation*, page 351, 1977.

[30] S. J. Bame, W. C. Feldman, J. T. Gosling, D. T. Young, and R. D. Zwickl. What magnetospheric workers should know about solar wind composition. *Energetic Ion Composition in the Earth's Magnetosphere*, page 73, 1983.

[31] R. E. McGuire, T. T. Von Rosenvinge, and F. B. McDonald. The composition of solar energetic particles. *Astrophysical Journal*, 301:938–961, 1986. ISSN 0004-637X.

[32] J. A. Simpson. Elemental and isotopic composition of the galactic cosmic rays. *Annu. Rev. Nucl. Sci.*, 33(1), 1983.

[33] A. Ambastha. Solar activity. In *AIP Conference Proceedings*, pages 173–213. AIP, 2007. doi: 10.1063/1.2756787.

[34] M. J. Owens. *Solar-Wind Structure*, pages 14–15. Oxford University Press, 2 2020. doi: 10.1093/acrefore/9780190871994.013.19.

[35] J. V. Hollweg. Collisionless solar wind: 1. constant electron temperature. *Journal of Geophysical Research*, 75:2403–2418, 5 1970. ISSN 01480227. doi: 10.1029/JA075i013p02403.

[36] N. F. Ness. Interaction of the solar wind with the moon. *Physics of the Earth and Planetary Interiors*, 4:197–198, 4 1971. ISSN 00319201. doi: 10.1016/0031-9201(71)90041-0.

[37] E. G. Berezhko. Origin of galactic cosmic rays from supernova remnants. *Nuclear Physics B - Proceedings Supplements*, 256-257:23–35, 11 2014. ISSN 09205632. doi: 10.1016/j.nuclphysbps.2014.10.003.

[38] C. Huang, H. E. Spence, and B. T. Kress. Assessing access of galactic cosmic rays at moon's orbit. *Geophysical Research Letters*, 36, 5 2009. ISSN 0094-8276. doi: 10.1029/2009GL037916.

[39] R. A. Mewaldt, A. J. Davis, K. A. Lave, R. A. Leske, E. C. Stone, M. E. Wiedenbeck, W. R. Binns, E. R. Christian, A. C. Cummings, G. A. de Nolfo, M. H. Israel, A. W. Labrador, and T. T. von Rosenvinge. Record-setting cosmic-ray intensities in 2009 and 2010. *The Astrophysical Journal*, 723:L1–L6, 11 2010. ISSN 2041-8205. doi: 10.1088/2041-8205/723/1/L1.

[40] D. J. McComas, R. W. Ebert, H. A. Elliott, B. E. Goldstein, J. T. Gosling, N. A. Schwadron, and R. M. Skoug. Weaker solar wind from the polar coronal holes and the whole sun. *Geophysical Research Letters*, 35, 9 2008. ISSN 0094-8276. doi: 10.1029/2008GL034896.

[41] N. A. Schwadron and D. J. McComas. The solar wind power from magnetic flux. *The Astrophysical Journal*, 686:L33–L36, 10 2008. ISSN 0004-637X. doi: 10.1086/592877.

[42] David E. Connick, Charles W. Smith, and Nathan A. Schwadron. Interplanetary magnetic flux depletion during protracted solar minima. *The Astrophysical Journal*, 727:8, 1 2011. ISSN 0004-637X. doi: 10.1088/0004-637X/727/1/8.

[43] A. Posner, B. Heber, O. Rother, and S. Guetersloh. A new trend in forecasting solar radiation hazards. *Space Weather*, 7, 5 2009. ISSN 1542-7390. doi: 10.1029/2009SW000476.

[44] N. A. Schwadron, L. Townsend, K. Kozarev, M. A. Dayeh, F. Cucinotta, M. Desai, M. Golightly, D. Hassler, R. Hatcher, M.-Y. Kim, A. Posner, M. PourArsalan,

H. E. Spence, and R. K. Squier. Earth-moon-mars radiation environment module framework. *Space Weather*, 8:n/a–n/a, 1 2010. ISSN 15427390. doi: 10.1029/2009SW000523.

[45] H. E. Spence, A. W. Case, M. J. Golightly, T. Heine, B. A. Larsen, J. B. Blake, P. Caranza, W. R. Crain, J. George, M. Lalic, A. Lin, M. D. Looper, J. E. Mazur, D. Salvaggio, J. C. Kasper, T. J. Stubbs, M. Doucette, P. Ford, R. Foster, R. Goeke, D. Gordon, B. Klatt, J. O'Connor, M. Smith, T. Onsager, C. Zeitlin, L. W. Townsend, and Y. Charara. Crater: The cosmic ray telescope for the effects of radiation experiment on the lunar reconnaissance orbiter mission. *Space Science Reviews*, 150:243–284, 1 2010. ISSN 0038-6308. doi: 10.1007/s11214-009-9584-8.

[46] N. A. Schwadron, T. Baker, B. Blake, A. W. Case, J. F. Cooper, M. Golightly, A. Jordan, C. Joyce, J. Kasper, K. Kozarev, J. Mislinski, J. Mazur, A. Posner, O. Rother, S. Smith, H. E. Spence, L. W. Townsend, J. Wilson, and C. Zeitlin. Lunar radiation environment and space weathering from the cosmic ray telescope for the effects of radiation (crater). *Journal of Geophysical Research: Planets*, 117, 12 2012. ISSN 0148-0227. doi: 10.1029/2011JE003978.

[47] D.Stuart Nachtwey and Tracy Chui hsu Yang. Radiological health risks for exploratory class missions in space. *Acta Astronautica*, 23:227–231, 1991. ISSN 00945765. doi: 10.1016/0094-5765(91)90122-L.

[48] J. Rask, W. Vercoutere, B. J. Navarro, and A. Krause. Space faring: The radiation challenge, 2017. URL `https://www.nasa.gov/wp-content/uploads/2017/04/radiationchallenge.pdf?emrc=ba69fb`.

[49] R. S. Johnston, L. F. Dietlein, C. A. Berry, J. F. Parker Jr., V. West, and W. L. Jones. Apollo_medical_report. *NASA*, NASA-SP-368, 1 1975. URL `https://ntrs.nasa.gov/api/citations/19760005580/downloads/19760005580.pdf`.

[50] R. F. Wimmer-Schweingruber, J. Yu, S. I. Böttcher, S. Zhang, S. Burmeister, H. Lohf, J. Guo, Z. Xu, B. Schuster, L. Seimetz, J. L. Freiherr von Forstner, A. Ravanbakhsh, V. Knierim, S. Kolbe, H. Woyciechowski, S. R. Kulkarni, B. Yuan, G. Shen, C. Wang, Z. Chang, T. Berger, C. E. Hellweg, D. Matthiä, D. Hou, A. Knappmann, C. Büschel, X. Hou, B. Ren, and Q. Fu. The lunar lander neutron and dosimetry (lnd) experiment on chang'e 4. *Space Science Reviews*, 216:104, 9 2020. ISSN 0038-6308. doi: 10.1007/s11214-020-00725-3.

[51] M. Dixit. How space radiation threatens lunar exploration. *Supercluster*, 2023.

[52] S. Zhang, R. F. Wimmer-Schweingruber, J. Yu, C. Wang, Q. Fu, Y. Zou, Y. Sun, C. Wang, D. Hou, S. I. Böttcher, S. Burmeister, L. Seimetz, B. Schuster,

V. Knierim, G. Shen, B. Yuan, H. Lohf, J. Guo, Z. Xu, J. L. Freiherr von Forstner, S. R. Kulkarni, H. Xu, C. Xue, J. Li, Z. Zhang, H. Zhang, T. Berger, D. Matthiä, C. E. Hellweg, X. Hou, J. Cao, Z. Chang, B. Zhang, Y. Chen, H. Geng, and Z. Quan. First measurements of the radiation dose on the lunar surface. *Science Advances*, 6, 9 2020. ISSN 2375-2548. doi: 10.1126/sciadv.aaz1334.

[53] R. Matthewman, I. A. Crawford, A. P. Jones, K. H. Joy, and M. A. Sephton. Organic matter responses to radiation under lunar conditions. *Astrobiology*, 16: 900–912, 11 2016. ISSN 1531-1074. doi: 10.1089/ast.2015.1442.

[54] R. K. Tripathi, J. W. Wilson, F. F. Badavi, and G. De Angelis. A characterization of the moon radiation environment for radiation analysis. *Advances in Space Research*, 37:1749–1758, 1 2006. ISSN 02731177. doi: 10.1016/j.asr.2006.03.016.

[55] G. De Angelis, F. F. Badavi, J. M. Clem, S. R. Blattnig, M. S. Clowdsley, J. E. Nealy, R. K. Tripathi, and J. W. Wilson. Modeling of the lunar radiation environment. *Nuclear Physics B - Proceedings Supplements*, 166:169–183, 4 2007. ISSN 09205632. doi: 10.1016/j.nuclphysbps.2006.12.034.

[56] P. Lucey. Understanding the lunar surface and space-moon interactions. *Reviews in Mineralogy and Geochemistry*, 60:83–219, 1 2006. ISSN 1529-6466. doi: 10.2138/rmg.2006.60.2.

[57] R. B. Malla and K. M. Brown. Determination of temperature variation on lunar surface and subsurface for habitat analysis and design. *Acta Astronautica*, 107: 196–207, 2 2015. ISSN 00945765. doi: 10.1016/j.actaastro.2014.10.038. URL `https://linkinghub.elsevier.com/retrieve/pii/S0094576514004160`.

[58] J. P. Williams, B. T. Greenhagen, D. A. Paige, N. Schorghofer, E. Sefton-Nash, P. O. Hayne, P. G. Lucey, M. A. Siegler, and K. Michael Aye. Seasonal polar temperatures on the moon. *Journal of Geophysical Research: Planets*, 124:2505–2521, 10 2019. ISSN 2169-9097. doi: 10.1029/2019JE006028.

[59] M. G. Langseth, S. P. Clark, J. L. Chute, S. J. Keihm, and A. E. Wechsler. The apollo 15 lunar heat-flow measurement. *The Moon*, 4:390–410, 1972. ISSN 0027-0903. doi: 10.1007/BF00562006.

[60] S. Nagihara, W. S. Kiefer, P. T. Taylor, D. R. Williams, and Y. Nakamura. Examination of the long-term subsurface warming observed at the apollo 15 and 17 sites utilizing the newly restored heat flow experiment data from 1975 to 1977. *Journal of Geophysical Research: Planets*, 123:1125–1139, 5 2018. ISSN 2169-9097. doi: 10.1029/2018JE005579.

[61] D. Garrett. Apollo 17 press kit. *Apollo 17 Lunar Surface Journal*, 1972. URL `https://www.nasa.gov/wp-content/uploads/static/history/alsj/a17/A17_PressKit.pdf`.

[62] V. D. Krotikov and V. S. Troitski. Detecting heat flow from the interior of the moon. *Soviet Astronomy*, 7:822–826, 6 1964. URL `https://ui.adsabs.harvard.edu/abs/1964SvA.....7..822K`.

[63] T. V. Tikhonova and V. S. Troitski. Effect of heat from within the moon on its radio emission for the case of lunar properties which vary with depth. *Soviet Astronomy*, 13:120–128, 8 1969. URL `https://ui.adsabs.harvard.edu/abs/1969SvA....13..120T`.

[64] W. W. Lauderdale and W. F. Eichelman. Apollo scientific experiments data handbook, 8 1974. URL `https://ntrs.nasa.gov/citations/19760007062`.

[65] A. R. Vasavada, D. A. Paige, and S. E. Wood. Near-surface temperatures on mercury and the moon and the stability of polar ice deposits. *Icarus*, 141:179–193, 10 1999. ISSN 00191035. doi: 10.1006/icar.1999.6175.

[66] M. J. Marov, A. V. Kolesnichenko, V. N. Lebedev, and K. K. Manuilov. On the problem of determining the thermal properties of the soil of phobos. *Inst. Appl. Math., The Russian Academy of Science, 2007.*, 2007.

[67] E. Pettit and S. B. Nicholson. Lunar radiation and temperatures. *The Astrophysical Journal*, 71:102–135, 3 1930. ISSN 0004-637X. doi: 10.1086/143236.

[68] L. C. Thomas. *Heat_Transfer*. PTR Prentice Hall, 1993. ISBN 0133827488,9780133827484. URL `https://books.google.co.uk/books?id=UKceAQAAIAAJ`.

[69] M. F. Modest. *Fundamentals of Thermal Radiation*, pages 1–29. Academic Press, 3 edition, 2003. doi: 10.1016/B978-012503163-9/50002-3.

[70] J. S. Lewis. *Mining the sky : untold riches from the asteroids, comets, and planets*. Helix Books, 1996. ISBN 97802014795910201479591. URL `https://archive.org/details/miningskyuntoldr00lewi`.

[71] J. S. Lewis, M. S. Matthews, and M. L. Guerrieri. *In Resources of Near-Earth Space*. The University of Arizona Press, 1933.

[72] P. D. Spudis. *The once and future moon*. Smithsonian Institution Press, 1996. ISBN 1560986344. URL `https://archive.org/details/oncefuturemoon0000spud`.

[73] P. Spudis and A. Lavoie. Using the resources of the moon to create a permanent, cislunar space fairing system. In *AIAA SPACE 2011 Conference & Exposition*. American Institute of Aeronautics and Astronautics, 9 2011. ISBN 978-1-60086-953-2. doi: 10.2514/6.2011-7185.

[74] G. Sanders. Isru - an overview of nasa's current development activities and long-term goals. In *38th Aerospace Sciences Meeting and Exhibit*. American Institute of Aeronautics and Astronautics, 1 2000. doi: 10.2514/6.2000-1062.

[75] G. B. Sanders and W. E. Larson. Progress made in lunar in situ resource utilization under nasa's exploration technology and development program. *Journal of Aerospace Engineering*, 26:5–17, 1 2013. ISSN 0893-1321. doi: 10.1061/(ASCE) AS.1943-5525.0000208.

[76] D.S. McKay, G.H. Heiken, A. Basu, G. Blanford, S. Simon, R. Reedy, B.M. French, and J. Papike. *The lunar regolith*, pages 285–356. Cambridge University Press, 1991. URL `https://www.lpi.usra.edu/publications/books/lunar_sourcebook/pdf/Chapter07.pdf`.

[77] P. S. Greenberg, D. Chen, and S. A. Smith. Aerosol measurements of the fine and ultrafine particle content of lunar regolith, 2007. URL `https://ntrs.nasa.gov/citations/20070031906`.

[78] Y. Liu, D. W. Schnare, B. C. Eimer, and L. A. Taylor. Dry separation of respirable lunar dust: Providing samples for the lunar airborne dust toxicity advisory group. *Planetary and Space Science*, 56:1517–1523, 10 2008. ISSN 00320633. doi: 10.1016/j.pss.2008.08.003.

[79] Y. Liu and L. A. Taylor. Characterization of lunar dust and a synopsis of available lunar simulants. *Planetary and Space Science*, 59:1769–1783, 11 2011. ISSN 00320633. doi: 10.1016/j.pss.2010.11.007.

[80] J. J. Papike, S. B. Simon, and J. C. Laul. The lunar regolith: Chemistry, mineralogy, and petrology. *Reviews of Geophysics*, 20:761–826, 11 1982. ISSN 8755-1209. doi: 10.1029/RG020i004p00761.

[81] L. T. Elkins-Tanton. Water on the moon. *Physics Today*, 64:74–75, 3 2011. ISSN 0031-9228. doi: 10.1063/1.3563829.

[82] W. J. Kaufmann. *Universe*. W.H. Freeman & Company, 2 edition, 1988. ISBN 0716719274. URL `https://archive.org/details/universe0002kauf/page/n5/mode/2up`.

[83] J.W. Delano. Apollo 15 green glass: chemistry and possible origin. *Lunar and Planetary Science Conference Proceedings*, 1:275–300, jan 1979.

[84] D. E. Wilhelms. To a rocky moon: a geologist's history of lunar exploration. *Tucson: University of Arizona Press*, 1933. URL `https://ui.adsabs.harvard.edu/abs/1993trmg.book.....W`.

[85] R. Christoffersen, J. F. Lindsay, S. K. Noble, and J. A. Lawrence. Lunar dust effects on spacesuit systems: Insights from the apollo spacesuits. In LPI Editorial Board, editor, *Joint Annual Meeting of LEAG-ICEUM-SRR*, volume 1446, page 34. Johnson Space Center, 10 2008. URL `https://ui.adsabs.harvard.edu/abs/2008LPICo1446...34C`.

[86] M. Anand, I.A. Crawford, M. Balat-Pichelin, S. Abanades, W. van Westrenen, G. Péraudeau, R. Jaumann, and W. Seboldt. A brief review of chemical and mineralogical resources on the moon and likely initial in situ resource utilization (isru) applications. *Planetary and Space Science*, 74:42–48, 12 2012. ISSN 00320633. doi: 10.1016/j.pss.2012.08.012.

[87] L. A. Haskin, R. O. Colson, and D. Vaniman. A geochemical assessment of possible lunar ore formation. In *Resources of Near-Earth Space*, page 9. Arizona University, 1 1991. URL `https://ui.adsabs.harvard.edu/abs/1991rnes.nasaQ...9H`.

[88] T. D. Lin. Concrete for lunar base construction. *Lunar Bases and Space Activities of the 21st Century*, pages 381–390, 1 1985. URL `https://ui.adsabs.harvard.edu/abs/1985lbsa.conf..381L`.

[89] R. V. Morris, R. Score, C. Dardano, and G. Heiken. *Handbook of lunar soils.* Lyndon B. Johnson Space Center, 67 edition, 1983.

[90] G. Ryder and Norman M. D. *Catalog of Apollo 16 Rocks: 67015-69965*, volume 52. Lyndon B. Johnson Space Center, 1980.

[91] R. M. Fruland. *Introduction to the Core Samples from the Apollo 16 Landing Site, 17659.* NASA Johnson Space Center, 58 edition, 1981.

[92] Z. Kopal. *Chemical Composition of the Moon*, volume 4, pages 147–153. Springer, 1966. doi: 10.1007/978-94-011-7545-6_11.

[93] M. Ohtake, T. Matsunaga, J. Haruyama, Y. Yokota, T. Morota, C. Honda, Y. Ogawa, M. Torii, H. Miyamoto, T. Arai, and N. Hirata. The global distribution of pure anorthosite on the moon. *Nature*, 461:236–240, 9 2009. ISSN 0028-0836. doi: 10.1038/nature08317.

[94] S. Yamamoto, R. Nakamura, T. Matsunaga, Y. Ogawa, Y. Ishihara, T. Morota, N. Hirata, M. Ohtake, T. Hiroi, Y. Yokota, and J. Haruyama. Possible mantle origin of olivine around lunar impact basins detected by selene. *Nature Geoscience*, 3:533–536, 8 2010. ISSN 1752-0894. doi: 10.1038/ngeo897.

[95] C. R. Neal and L. A. Taylor. Petrogenesis of mare basalts: A record of lunar volcanism. *Geochimica et Cosmochimica Acta*, 56:2177–2211, 6 1992. ISSN 00167037. doi: 10.1016/0016-7037(92)90184-K.

[96] G. J. Taylor, P. Warren, G. Ryder, J. Delano, C. Pieters, and G. Lofgren. *Lunar Rocks*, pages 183–284. Cambridge University Press, 1991. ISBN 0521334446. URL `https://ui.adsabs.harvard.edu/abs/1991lsug.book..183T`.

[97] J. J. Papike, G. Ryder, and C. K. Shearer. *Chapter 5. LUNAR SAMPLES*, pages 719–952. De Gruyter, Berlin, Boston, 1998. ISBN 9781501508806. doi: doi:10.1515/9781501508806-020. URL `https://doi.org/10.1515/9781501508806-020`.

[98] L. A. Taylor and W. D. Carrier. Oxygen production on the moon: An overview and evaluation. *Resources of near-earth space*, page 69, 1993.

[99] E. Ohtani, S. Ozawa, M. Miyahara, Y. Ito, T. Mikouchi, M. Kimura, T. Arai, K. Sato, and K. Hiraga. Coesite and stishovite in a shocked lunar meteorite, asuka-881757, and impact events in lunar surface. *Proceedings of the National Academy of Sciences*, 108:463–466, 1 2011. ISSN 0027-8424. doi: 10.1073/pnas.1009338108.

[100] M. Kayama, H. Nagaoka, and T. Niihara. Lunar and martian silica. *Minerals*, 8: 267, 6 2018. ISSN 2075-163X. doi: 10.3390/min8070267.

[101] M. Miyahara, S. Kaneko, E. Ohtani, T. Sakai, T. Nagase, M. Kayama, H. Nishido, and N. Hirao. Discovery of seifertite in a shocked lunar meteorite. *Nature Communications*, 4:1737, 4 2013. ISSN 2041-1723. doi: 10.1038/ncomms2733.

[102] D. A. Noever, D. D. Smith, L. Sibille, S. C. Brown, R. J. Cronise, and S. L. Lehoczky. High performance materials applications to moon/mars missions and bases. In *Space 98*, pages 275–285. American Society of Civil Engineers, 4 1998. ISBN 9780784403396. doi: 10.1061/40339(206)33.

[103] A. Brecher, W. H. Menke, J. B. Adams, and M. J. Gaffey. The effects of heating and subsolidus reduction on lunar materials: an analysis by magnetic methods, optical, mössbauer, and x-ray diffraction spectroscopy. *Lunar and Planetary Science Conference Proceedings*, 3:3091–3109, 1 1975. URL `https://ui.adsabs.harvard.edu/abs/1975LPSC....6.3091B`.

[104] K. Nishioka, R. D. Arno, A. D. Alexander, and R. E. Slye. Feasibility of mining lunar resources for earth use: Circa 2000 a.d, 1973. URL `https://ntrs.nasa.gov/citations/19730022066`.

[105] C. C. Allen, D. S. McKay, and R. V. Morris. Lunar oxygen - the reduction of glass by hydrogen. In Willy Z Sadeh, Stein Sture, and Russell J Miller, editors, *Engineering, Construction, and Operations in space - III: Space 1992*, volume 1, pages 629–640, 1 1992. URL `https://ui.adsabs.harvard.edu/abs/1992ecos.proc..629A`.

[106] C. C. Massieon. Reduction of iron-bearing lunar minerals for the production of oxygen, 1992. URL `https://www.proquest.com/openview/2da8a602437c4d8319abb9f72f8c7d5f/1?pq-origsite=gscholar&cbl=18750&diss=y`.

[107] C. C. Allen, R.V. Morris, H.V. Lauer, and D.S. McKay. Microscopic iron metal on glass and minerals—a tool for studying regolith maturity. *Icarus*, 104:291–300, 8 1993. ISSN 00191035. doi: 10.1006/icar.1993.1102.

[108] C. C. Allen, D. S. McKay, and R. V. Morris. Hydrogen reduction of lunar simulant glass. In *Lunar and Planetary Science Conference*, volume 23, pages 21–22. Lunar and Planetary Science Institute, 3 1992. URL `https://ui.adsabs.harvard.edu/abs/1992LPI....23...21A`.

[109] A. P. Jordan, T. J. Stubbs, C. J. Joyce, N. A. Schwadron, H. E. Spence, and J. K. Wilson. The formation of molecular hydrogen from water ice in the lunar regolith by energetic charged particles. *Journal of Geophysical Research: Planets*, 118: 1257–1264, 6 2013. ISSN 2169-9097. doi: 10.1002/jgre.20095.

[110] K. L. Robinson and G. J. Taylor. Heterogeneous distribution of water in the moon. *Nature Geoscience*, 7:401–408, 6 2014. ISSN 1752-0894. doi: 10.1038/ngeo2173.

[111] L. A. Haskin and R. O. Colson. Lunar resources: Toward living off the lunar land. In *NASA Space Engineering Research Center for Utilization of Local Planetary Resources*. Arizona University, 1 1990.

[112] R. Matthewman, R. W. Court, I. A. Crawford, A. P. Jones, K. H. Joy, and M. A. Sephton. The moon as a recorder of organic evolution in the early solar system: A lunar regolith analog study. *Astrobiology*, 15:154–168, 2 2015. ISSN 1531-1074. doi: 10.1089/ast.2014.1217.

[113] T. Chen, B. J. Chow, M. Wang, Y. Shi, C. Zhao, and Y. Qiao. Inorganic–organic hybrid of lunar soil simulant and polyethylene. *Journal of Materials in Civil*

Engineering, 28, 4 2016. ISSN 0899-1561. doi: 10.1061/(ASCE)MT.1943-5533.0001450.

[114] Z. Hu, T. Shi, M. Cen, J. Wang, X. Zhao, C. Zeng, Y. Zhou, Y. Fan, Y. Liu, and Z. Zhao. Research progress on lunar and martian concrete. *Construction and Building Materials*, 343:128117, 2022. ISSN 0950-0618. doi: https://doi.org/10.1016/j.conbuildmat.2022.128117. URL `https://www.sciencedirect.com/science/article/pii/S0950061822017822`.

[115] C. Razeto, D. Foncheva, G. Trotti, and V. Sumini. Optimizing translucent multilayer membrane for lunar habitats: A design study. *Acta Astronautica*, 223: 316–327, 10 2024. ISSN 00945765. doi: 10.1016/j.actaastro.2024.07.007.

[116] J. Ma, Q. Wei, H. Fan, Z. Qi, and N. Hu. Mechanical properties evolution and damage mechanism of kevlar fiber under ozone exposure in near-space simulation. *Coatings*, 12:584, 4 2022. ISSN 2079-6412. doi: 10.3390/coatings12050584.

[117] L. Narici, M. Casolino, L. D. Fino, M. Larosa, P. Picozza, A. Rizzo, and V. Zaconte. Performances of kevlar and polyethylene as radiation shielding on-board the international space station in high latitude radiation environment. *Scientific Reports*, 7:1644, 5 2017. ISSN 2045-2322. doi: 10.1038/s41598-017-01707-2.

[118] L. Calcagno, G. Compagnini, and G. Foti. Structural modification of polymer films by ion irradiation. *Nuclear Instruments and Methods in Physics Research Section B: Beam Interactions with Materials and Atoms*, 65(1):IN7–422, 1992. ISSN 0168-583X. doi: https://doi.org/10.1016/0168-583X(92)95077-5. URL `https://www.sciencedirect.com/science/article/pii/0168583X92950775`.

[119] S. Luo. *Radiation Processing*, pages 183–262. Springer Nature Singapore, Singapore, 2023. ISBN 978-981-99-3087-6. doi: 10.1007/978-981-99-3087-6_5. URL `https://doi.org/10.1007/978-981-99-3087-6_5`.

[120] Z. Cai, H. Dai, and X. Fu. Investigation on the hot melting temperature field simulation of hdpe water supply pipeline in gymnasium pool. *Results in Physics*, 9:1050–1056, 2018. ISSN 2211-3797. doi: https://doi.org/10.1016/j.rinp.2018.04.019. URL `https://www.sciencedirect.com/science/article/pii/S2211379718306946`.

[121] J. Charpentier. The triplet “molecular processes–product–process” engineering: the future of chemical engineering ? *Chemical Engineering Science*, 57:4667–4690, 11 2002. ISSN 00092509. doi: 10.1016/S0009-2509(02)00287-7.

[122] R. D. Braatz, R. C. Alkire, E. Rusli, and T. O. Drews. Multiscale systems engineering with applications to chemical reaction processes. *Chemical Engineering Science*, 59:5623–5628, 11 2004. ISSN 00092509. doi: 10.1016/j.ces.2004.09.022.

[123] D. G. Vlachos. *A Review of Multiscale Analysis: Examples from Systems Biology, Materials Engineering, and Other Fluid–Surface Interacting Systems*, volume 30, pages 1–61. Academic Press, 2005. doi: 10.1016/S0065-2377(05)30001-9. URL `https://linkinghub.elsevier.com/retrieve/pii/S0065237705300019`.

[124] Y. Zhao and A. Yang. *Towards a Generic Tool to Support Multiscale Modelling of Discrete Event Systems*, volume 30, pages 1177–1181. Elsevier, 2012. doi: https://doi.org/10.1016/B978-0-444-59520-1.50094-4. URL `https://www.sciencedirect.com/science/article/pii/B9780444595201500944`.

[125] J. P. Ewen, D. M. Heyes, and D. Dini. Advances in nonequilibrium molecular dynamics simulations of lubricants and additives. *Friction*, 6:349–386, 12 2018. ISSN 2223-7690. doi: 10.1007/s40544-018-0207-9.

[126] A. P. Vázquez. *A molecular approach to the ultimate friction response of confined fluids.* PhD thesis, Universite de Lyon, 2019. URL `https://tel.archives-ouvertes.fr/tel-02882466`.

[127] M. P. Allen and D. J. Tildesley. *Computer Simulation of Liquids.* Oxford University PressOxford, 2 edition, 1989. ISBN 0198803192. doi: 10.1093/oso/9780198803195.001.0001.

[128] E. T. Thostenson, Z. Ren, and T. Chou. Advances in the science and technology of carbon nanotubes and their composites: a review. *Composites Science and Technology*, 61:1899–1912, 10 2001. ISSN 02663538. doi: 10.1016/S0266-3538(01)00094-X.

[129] P. A. Thompson, G. S. Grest, and M. O. Robbins. Phase transitions and universal dynamics in confined films. *Physical Review Letters*, 68:3448–3451, 6 1992. ISSN 0031-9007. doi: 10.1103/PhysRevLett.68.3448.

[130] M. S. Green. Markoff random processes and the statistical mechanics of time-dependent phenomena. ii. irreversible processes in fluids. *The Journal of Chemical Physics*, 22:398–413, 3 1954. ISSN 0021-9606. doi: 10.1063/1.1740082.

[131] W. F. van Gunsteren and H. J. C. Berendsen. Computer simulation of molecular dynamics: Methodology, applications, and perspectives in chemistry. *Angewandte Chemie International Edition in English*, 29:992–1023, 9 1990. ISSN 0570-0833. doi: 10.1002/anie.199009921.

[132] R. Car and M. Parrinello. Unified approach for molecular dynamics and density-functional theory. *Physical Review Letters*, 55:2471–2474, 11 1985. ISSN 0031-9007. doi: 10.1103/PhysRevLett.55.2471.

[133] K. Binder. *Monte Carlo and Molecular Dynamics Simulations in Polymer Science*. Oxford University PressNew York, NY, 8 1995. ISBN 9780195094381. doi: 10.1093/oso/9780195094381.001.0001.

[134] R. O. Dror, R. M. Dirks, J.P. Grossman, H. Xu, and D. E. Shaw. Biomolecular simulation: A computational microscope for molecular biology. *Annual Review of Biophysics*, 41:429–452, 6 2012. ISSN 1936-122X. doi: 10.1146/annurev-biophys-042910-155245.

[135] J. D. Durrant and J. A. McCammon. Molecular dynamics simulations and drug discovery. *BMC Biology*, 9:71, 12 2011. ISSN 1741-7007. doi: 10.1186/1741-7007-9-71.

[136] M. Karplus and J. A. McCammon. Molecular dynamics simulations of biomolecules. *Nature Structural Biology*, 9:646–652, 9 2002. ISSN 10728368. doi: 10.1038/nsb0902-646.

[137] M. Karplus and G. A. Petsko. Molecular dynamics simulations in biology. *Nature*, 347:631–639, 10 1990. ISSN 0028-0836. doi: 10.1038/347631a0.

[138] P. A. Thompson and M. O. Robbins. Shear flow near solids: Epitaxial order and flow boundary conditions. *Physical Review A*, 41:6830–6837, 6 1990. ISSN 1050-2947. doi: 10.1103/PhysRevA.41.6830.

[139] H. Berro, N. Fillot, and P. Vergne. Molecular dynamics simulation of surface energy and zddp effects on friction in nano-scale lubricated contacts. *Tribology International*, 43:1811–1822, 10 2010. ISSN 0301679X. doi: 10.1016/j.triboint.2010.02.011.

[140] J. Cao and A. E. Likhtman. Shear banding in molecular dynamics of polymer melts. *Physical Review Letters*, 108:028302, 1 2012. ISSN 0031-9007. doi: 10.1103/PhysRevLett.108.028302.

[141] L. Martinie and P. Vergne. Lubrication at extreme conditions: A discussion about the limiting shear stress concept. *Tribology Letters*, 63:21, 8 2016. ISSN 1023-8883. doi: 10.1007/s11249-016-0709-4.

[142] H. Berro. *A Molecular Dynamics Approach to Nano-scale Lubrication*. PhD thesis, Universite de Lyon, 2010. URL `http://www.theses.fr/2010ISAL0084`.

[143] H. Berro, N. Fillot, P. Vergne, T. Tokumasu, T. Ohara, and G. Kikugawa. Energy dissipation in non-isothermal molecular dynamics simulations of confined liquids under shear. *The Journal of Chemical Physics*, 135, 10 2011. ISSN 0021-9606. doi: 10.1063/1.3644938.

[144] S. Yamada. General shear-thinning dynamics of confined fluids. *Tribology Letters*, 13:167–171, 2002. ISSN 10238883. doi: 10.1023/A:1020151824274.

[145] L. Verlet. Computer ”experiments” on classical fluids. i. thermodynamical properties of lennard-jones molecules. *Physical Review*, 159:98–103, 7 1967. ISSN 0031-899X. doi: 10.1103/PhysRev.159.98.

[146] Y. Sonavane, A. Paajanen, J. Ketoja, S. Paavilainen, and T. Maloney. Molecular dynamics simulation of functionalized nanofibrillar cellulose. In *nternational Conference on Theoretical Biology and Computational Chemistry*, pages 1–8, 10 2014. URL `https://www.researchgate.net/publication/301636360_Molecular_Dynamics_Simulation_of_Functionalized_Nanofibrillar_Cellulose#fullTextFileContent`.

[147] W. L. Jorgensen and J. Tirado-Rives. The opls [optimized potentials for liquid simulations] potential functions for proteins, energy minimizations for crystals of cyclic peptides and crambin. *Journal of the American Chemical Society*, 110: 1657–1666, 3 1988. ISSN 0002-7863. doi: 10.1021/ja00214a001.

[148] W. D. Cornell, P. Cieplak, C. I. Bayly, I. R. Gould, K. M. Merz, D. M. Ferguson, D. C. Spellmeyer, T. Fox, J. W. Caldwell, and P. A. Kollman. A second generation force field for the simulation of proteins, nucleic acids, and organic molecules. *Journal of the American Chemical Society*, 117:5179–5197, 5 1995. ISSN 0002-7863. doi: 10.1021/ja00124a002.

[149] I.A. Solov'yov, G.B. Sushko, and A.V. Solov'yov. *MBN Explorer Users' Guide*. MesoBioNano Science Publishing, 3 edition, 2017. URL `https://mbnresearch.com/sites/mbn-migrate/files/MBNExplorer_Users_Guide_ToC.pdf`.

[150] R.W Hockney and J.W Eastwood. *Computer Simulation Using Particles*. CRC Press, 1 edition, 3 2021. ISBN 9780367806934. doi: 10.1201/9780367806934.

[151] S. Nosé. A unified formulation of the constant temperature molecular dynamics methods. *The Journal of Chemical Physics*, 81:511–519, 7 1984. ISSN 0021-9606. doi: 10.1063/1.447334.

[152] W. L. Jorgensen, D. S. Maxwell, and J. Tirado-Rives. Development and testing of the opls all-atom force field on conformational energetics and properties of organic

liquids. *Journal of the American Chemical Society*, 118:11225–11236, 11 1996. ISSN 0002-7863. doi: 10.1021/ja9621760. URL `https://pubs.acs.org/doi/10.1021/ja9621760`. doi: 10.1021/ja9621760.

[153] I. Solov'yov, A. Solov'yov, and W. Greiner. Formation of global energy minimum structures in the fusion process of lennard-jones clusters. *Phys. Rev. Lett. Northby Phys. Rev. Lett*, 90:184–194, 10 2003.

[154] I. A. Solov'yov, A. V. Solov'yov, W. Greiner, A. Koshelev, and A. Shutovich. Cluster growing process and a sequence of magic numbers. *Physical Review Letters*, 90:053401, 2 2003. ISSN 0031-9007. doi: 10.1103/PhysRevLett.90.053401.

[155] I. A. Solov'yov, A. V. Solov'yov, and W. Greiner. Fusion process of lennard–jones clusters: Global minima and magic numbers formation. *International Journal of Modern Physics E*, 13:697–736, 8 2004. ISSN 0218-3013. doi: 10.1142/S0218301304002454.

[156] O. I. Obolensky, I. A. Solov'yov, A. V. Solov'yov, and W. Greiner. Fusion and fission of atomic clusters: recent advances. *Computing Letters*, 1:313–318, 3 2005. ISSN 1574-0404. doi: 10.1163/157404005776611501.

[157] I. A. Solov'yov, M. Mathew, A. V. Solov'yov, and W. Greiner. Liquid surface model for carbon nanotube energetics. *Physical Review E*, 78:051601, 11 2008. ISSN 1539-3755. doi: 10.1103/PhysRevE.78.051601.

[158] J. Geng, I. A. Solov'yov, W. Zhou, A. V. Solov'yov, and B. F. G. Johnson. Uncovering a solvent-controlled preferential growth of buckminsterfullerene (c60) nanowires. *The Journal of Physical Chemistry C*, 113:6390–6397, 4 2009. ISSN 1932-7447. doi: 10.1021/jp809664g. URL `https://pubs.acs.org/doi/10.1021/jp809664g`. doi: 10.1021/jp809664g.

[159] I. A. Solov'yov, J. Geng, A. V. Solov'yov, and B. F. G. Johnson. Understanding the formation process of exceptionally long fullerene-based nanowires. *AIP Conference Proceedings*, 1197:89–102, 12 2009. ISSN 0094-243X. doi: 10.1063/1.3275692. URL `https://doi.org/10.1063/1.3275692`.

[160] I. A. Solov'yov, J. Geng, A. V. Solov'yov, and B. F. G. Johnson. On the possibility of the electron polarization to be the driving force for the c60-tmb nanowire growth. *Chemical Physics Letters*, 472:166–170, 4 2009. ISSN 00092614. doi: 10.1016/j.cplett.2009.03.006.

[161] V. V. Dick, I. A. Solov'yov, A. V. Solov'yov, A. Solov'yov, and E. Surdutovich. Theoretical study of fractal growth and stability on surface. In *AIP Conference*

Proceedings, volume 1197, pages 76–88, 12 2009. doi: 10.1063/1.3275691. URL `https://pubs.aip.org/aip/acp/article/1197/1/76-88/865890`.

[162] I. A. Solov'yov, A. V. Yakubovich, P. V. Nikolaev, I. Volkovets, and A. V. Solov'yov. Mesobionano explorer—a universal program for multiscale computer simulations of complex molecular structure and dynamics. *Journal of Computational Chemistry*, 33:2412–2439, 11 2012. ISSN 0192-8651. doi: 10.1002/jcc.23086.

[163] K. Refson. Moldy: a portable molecular dynamics simulation program for serial and parallel computers. *Computer Physics Communications*, 126:310–329, 4 2000. ISSN 00104655. doi: 10.1016/S0010-4655(99)00496-8.

[164] S. Plimpton. Fast parallel algorithms for short-range molecular dynamics. *Journal of Computational Physics*, 117:1–19, 3 1995. ISSN 00219991. doi: 10.1006/jcph.1995.1039.

[165] J. C. Phillips, R. Braun, W. Wang, J. Gumbart, E. Tajkhorshid, E. Villa, C. Chipot, R. D. Skeel, L. Kalé, and K. Schulten. Scalable molecular dynamics with namd. *Journal of Computational Chemistry*, 26:1781–1802, 12 2005. ISSN 0192-8651. doi: 10.1002/jcc.20289.

[166] J. D. Gale. Gulp: A computer program for the symmetry-adapted simulation of solids. *Journal of the Chemical Society, Faraday Transactions*, 93:629–637, 1997. ISSN 09565000. doi: 10.1039/a606455h.

[167] A. D. MacKerell, D. Bashford, M. Bellott, R. L. Dunbrack, J. D. Evanseck, M. J. Field, S. Fischer, J. Gao, H. Guo, S. Ha, D. Joseph-McCarthy, L. Kuchnir, K. Kuczera, F. T. K. Lau, C. Mattos, S. Michnick, T. Ngo, D. T. Nguyen, B. Prodhom, W. E. Reiher, B. Roux, M. Schlenkrich, J. C. Smith, R. Stote, J. Straub, M. Watanabe, J. Wiórkiewicz-Kuczera, D. Yin, and M. Karplus. All-atom empirical potential for molecular modeling and dynamics studies of proteins. *The Journal of Physical Chemistry B*, 102:3586–3616, 4 1998. ISSN 1520-6106. doi: 10.1021/jp973084f. URL `https://pubs.acs.org/doi/10.1021/jp973084f`. doi: 10.1021/jp973084f.

[168] A. T. Brunger. *X-PLOR: version 3.1: a system for x-ray crystallography and NMR*. Yale University Press, 3.1 edition, 1992.

[169] W. Humphrey, A. Dalke, and K. Schulten. Vmd: Visual molecular dynamics. *Journal of Molecular Graphics*, 14:33–38, 2 1996. ISSN 02637855. doi: 10.1016/0263-7855(96)00018-5.

[170] W. H. Press, S. A. Teukolsky, W. T. Vetterling, and B. P. Flannery. *Numerical recipes: example book C*. Cambridge University Press, 2 edition, 1992.

[171] L.D. Landau and E.M. Lifshitz. *MOTION OF A RIGID BODY*, volume 1, pages 96–130. Elsevier, 3 edition, 1 1976. ISBN 978-0-7506-2896-9. doi: 10.1016/B978-0-08-050347-9.50011-3. URL `https://linkinghub.elsevier.com/retrieve/pii/B9780080503479500113`.

[172] A. V. Verkhovtsev, I. A. Solov'yov, and A. V. Solov'yov. Irradiation-driven molecular dynamics: a review. *The European Physical Journal D*, 75:213, 7 2021. ISSN 1434-6060. doi: 10.1140/epjd/s10053-021-00223-3. URL `https://link.springer.com/10.1140/epjd/s10053-021-00223-3`.

[173] D. Schardt, T. Elsässer, and D. Schulz-Ertner. Heavy-ion tumor therapy: Physical and radiobiological benefits. *Reviews of Modern Physics*, 82:383–425, 2 2010. ISSN 0034-6861. doi: 10.1103/RevModPhys.82.383.

[174] E. Surdutovich and A. V. Solov'yov. Multiscale approach to the physics of radiation damage with ions. *The European Physical Journal D*, 68:353, 11 2014. ISSN 1434-6060. doi: 10.1140/epjd/e2014-50004-0.

[175] A. V. Solov'yov. *Nanoscale Insights into Ion-Beam Cancer Therapy.* Springer International Publishing, 2017. ISBN 978-3-319-43028-7. doi: 10.1007/978-3-319-43030-0.

[176] A. G. G. M. Tielens. The molecular universe. *Reviews of Modern Physics*, 85:1021–1081, 7 2013. ISSN 0034-6861. doi: 10.1103/RevModPhys.85.1021.

[177] G. Horneck and C. Baumstark-Khan. *Astrobiology: The Quest for the Conditions of Life.* Springer Verlag, 2002. ISBN 3-540-42101-7. URL `https://elib.dlr.de/5218/`.

[178] I. A. Solov'yov, A. V. Korol, and A. V. Solov'yov. *Multiscale Modeling of Complex Molecular Structure and Dynamics with MBN Explorer.* Springer International Publishing, 2017. ISBN 978-3-319-56085-4. doi: 10.1007/978-3-319-56087-8.

[179] I. A. Solov'yov, G. Sushko, A. Verkhovtsev, A Korol, and A. V. Solov'yov. *MBN Explorer and MBN Studio Tutorials: Version 3.0.* MesoBioNano Science Publishing, 3 edition, 2017. URL `https://mbnresearch.com/sites/mbn-migrate/files/MBN-Tutorials_3.0_ToC.pdf`.

[180] W. F. van Dorp and C. W. Hagen. A critical literature review of focused electron beam induced deposition. *Journal of Applied Physics*, 104, 10 2008. ISSN 0021-8979. doi: 10.1063/1.2977587.

[181] I. Utke, S. Moshkalev, and P. Russell. Nanofabrication using focused ion and electron beams: Principles and applications, edited by ivo utke, stanisislav moshkalev

and phillip russell. *Contemporary Physics*, 54:140–141, 4 2013. ISSN 0010-7514. doi: 10.1080/00107514.2013.810671.

[182] M. Huth, F. Porrati, C. Schwalb, M. Winhold, R. Sachser, M. Dukic, J. Adams, and G. Fantner. Focused electron beam induced deposition: A perspective. *Beilstein Journal of Nanotechnology*, 3:597–619, 8 2012. ISSN 2190-4286. doi: 10.3762/bjnano.3.70.

[183] B. Wu and A. Kumar. Extreme ultraviolet lithography: A review. *Journal of Vacuum Science & Technology B: Microelectronics and Nanometer Structures Processing, Measurement, and Phenomena*, 25:1743–1761, 11 2007. ISSN 1071-1023. doi: 10.1116/1.2794048.

[184] A. M. Hawryluk and L. G. Seppala. Soft x-ray projection lithography using an x-ray reduction camera. *Journal of Vacuum Science & Technology B: Microelectronics Processing and Phenomena*, 6:2162–2166, 11 1988. ISSN 0734-211X. doi: 10.1116/1.584107.

[185] F. Heidet, N. R. Brown, and M. H. Tahar. Accelerator–reactor coupling for energy production in advanced nuclear fuel cycles. *Reviews of Accelerator Science and Technology*, 08:99–114, 1 2015. ISSN 1793-6268. doi: 10.1142/S1793626815300066.

[186] U. Linz. *Ion Beam Therapy*, volume 320. Springer Berlin Heidelberg, 2012. ISBN 978-3-642-21413-4. doi: 10.1007/978-3-642-21414-1.

[187] P.M. Dinh, P.-G. Reinhard, and E. Suraud. Dynamics of clusters and molecules in contact with an environment. *Physics Reports*, 485:43–107, 1 2010. ISSN 03701573. doi: 10.1016/j.physrep.2009.07.006.

[188] J. Alexander Maruhn, P. G. Reinhard, and E. Suraud. *Simple Models of Many-Fermion Systems*. Springer Berlin Heidelberg, 2010. ISBN 978-3-642-03838-9. doi: 10.1007/978-3-642-03839-6.

[189] D. Jacquemin, V. Wathelet, E. A. Perpète, and C. Adamo. Extensive td-dft benchmark: Singlet-excited states of organic molecules. *Journal of Chemical Theory and Computation*, 5:2420–2435, 9 2009. ISSN 1549-9618. doi: 10.1021/ct900298e. URL `https://pubs.acs.org/doi/10.1021/ct900298e`. doi: 10.1021/ct900298e.

[190] A. D. Bochevarov, E. Harder, T. F. Hughes, J. R. Greenwood, D. A. Braden, D. M. Philipp, D. Rinaldo, M. D. Halls, J. Zhang, and R. A. Friesner. Jaguar: A high-performance quantum chemistry software program with strengths in life and materials sciences. *International Journal of Quantum Chemistry*, 113:2110–2142, 9 2013. ISSN 0020-7608. doi: 10.1002/qua.24481.

[191] K.Y. Sanbonmatsu and C. S. Tung. High performance computing in biology: Multimillion atom simulations of nanoscale systems. *Journal of Structural Biology*, 157:470–480, 3 2007. ISSN 10478477. doi: 10.1016/j.jsb.2006.10.023.

[192] G. Zhao, J. R. Perilla, E. L. Yufenyuy, X. Meng, B. Chen, J. Ning, J. Ahn, A. M. Gronenborn, K. Schulten, C. Aiken, and P. Zhang. Mature hiv-1 capsid structure by cryo-electron microscopy and all-atom molecular dynamics. *Nature*, 497:643–646, 5 2013. ISSN 0028-0836. doi: 10.1038/nature12162.

[193] P. Husen and I. A. Solov'yov. Spontaneous binding of molecular oxygen at the qo-site of the bc1 complex could stimulate superoxide formation. *Journal of the American Chemical Society*, 138:12150–12158, 9 2016. ISSN 0002-7863. doi: 10.1021/jacs.6b04849. URL `https://pubs.acs.org/doi/10.1021/jacs.6b04849`. doi: 10.1021/jacs.6b04849.

[194] R. Salomon-Ferrer, A. W. Götz, D. Poole, S. Le Grand, and R. C. Walker. Routine microsecond molecular dynamics simulations with amber on gpus. 2. explicit solvent particle mesh ewald. *Journal of Chemical Theory and Computation*, 9:3878–3888, 9 2013. ISSN 1549-9618. doi: 10.1021/ct400314y. URL `https://doi.org/10.1021/ct400314y`. doi: 10.1021/ct400314y.

[195] A. C. Pan, T. M. Weinreich, S. Piana, and D. E. Shaw. Demonstrating an order-of-magnitude sampling enhancement in molecular dynamics simulations of complex protein systems. *Journal of Chemical Theory and Computation*, 12:1360–1367, 3 2016. ISSN 1549-9618. doi: 10.1021/acs.jctc.5b00913. URL `https://doi.org/10.1021/acs.jctc.5b00913`. doi: 10.1021/acs.jctc.5b00913.

[196] L. D. Landau, E. M. Lifshitz, J. B. Sykes, J. S. Bell, and M. E. Rose. *Quantum Mechanics (Non-Relativistic Theory)*, volume 3. Pergamon Press, 3 edition, 12 1958. doi: 10.1063/1.3062347.

[197] E. Surdutovich and A. V. Solov'yov. Transport of secondary electrons and reactive species in ion tracks. *The European Physical Journal D*, 69:193, 8 2015. ISSN 1434-6060. doi: 10.1140/epjd/e2015-60242-1.

[198] M. Dapor. *Transport of Energetic Electrons in Solids*, volume 290. Springer International Publishing, 2023. ISBN 978-3-031-37241-4. doi: 10.1007/978-3-031-37242-1.

[199] L. G. Gerchikov, A. N. Ipatov, A. V. Solov'yov, and W. Greiner. Non-adiabatic electron-ion coupling in dynamical jellium model for metal clusters. *Journal of Physics B: Atomic, Molecular and Optical Physics*, 33:4905–4926, 11 2000. ISSN 0953-4075. doi: 10.1088/0953-4075/33/21/330.

[200] S. Agostinelli, J. Allison, K. Amako, J. Apostolakis, H. Araujo, P. Arce, M. Asai, D. Axen, S. Banerjee, G. Barrand, F. Behner, L. Bellagamba, J. Boudreau, L. Broglia, A. Brunengo, H. Burkhardt, S. Chauvie, J. Chuma, R. Chytracek, G. Cooperman, G. Cosmo, P. Degtyarenko, A. Dell'Acqua, G. Depaola, D. Dietrich, R. Enami, A. Feliciello, C. Ferguson, H. Fesefeldt, G. Folger, F. Foppiano, A. Forti, S. Garelli, S. Giani, R. Giannitrapani, D. Gibin, J.J. Gómez Cadenas, I. González, G. Gracia Abril, G. Greeniaus, W. Greiner, V. Grichine, A. Grossheim, S. Guatelli, P. Gumplinger, R. Hamatsu, K. Hashimoto, H. Hasui, A. Heikkinen, A. Howard, V. Ivanchenko, A. Johnson, F.W. Jones, J. Kallenbach, N. Kanaya, M. Kawabata, Y. Kawabata, M. Kawaguti, S. Kelner, P. Kent, A. Kimura, T. Kodama, R. Kokoulin, M. Kossov, H. Kurashige, E. Lamanna, T. Lampén, V. Lara, V. Lefebure, F. Lei, M. Liendl, W. Lockman, F. Longo, S. Magni, M. Maire, E. Medernach, K. Minamimoto, P. Mora de Freitas, Y. Morita, K. Murakami, M. Nagamatu, R. Nartallo, P. Nieminen, T. Nishimura, K. Ohtsubo, M. Okamura, S. O'Neale, Y. Oohata, K. Paech, J. Perl, A. Pfeiffer, M.G. Pia, F. Ranjard, A. Rybin, S. Sadilov, E. Di Salvo, G. Santin, T. Sasaki, N. Savvas, Y. Sawada, S. Scherer, S. Sei, V. Sirotenko, D. Smith, N. Starkov, H. Stoecker, J. Sulkimo, M. Takahata, S. Tanaka, E. Tcherniaev, E. Safai Tehrani, M. Tropeano, P. Truscott, H. Uno, L. Urban, P. Urban, M. Verderi, A. Walkden, W. Wander, H. Weber, J.P. Wellisch, T. Wenaus, D.C. Williams, D. Wright, T. Yamada, H. Yoshida, and D. Zschiesche. Geant4—a simulation toolkit. *Nuclear Instruments and Methods in Physics Research Section A: Accelerators, Spectrometers, Detectors and Associated Equipment*, 506:250–303, 7 2003. ISSN 01689002. doi: 10.1016/S0168-9002(03)01368-8.

[201] J. Allison, K. Amako, J. Apostolakis, P. Arce, M. Asai, T. Aso, E. Bagli, A. Bagulya, S. Banerjee, G. Barrand, B.R. Beck, A.G. Bogdanov, D. Brandt, J.M.C. Brown, H. Burkhardt, Ph. Canal, D. Cano-Ott, S. Chauvie, K. Cho, G.A.P. Cirrone, G. Cooperman, M.A. Cortés-Giraldo, G. Cosmo, G. Cuttone, G. Depaola, L. Desorgher, X. Dong, A. Dotti, V.D. Elvira, G. Folger, Z. Francis, A. Galoyan, L. Garnier, M. Gayer, K.L. Genser, V.M. Grichine, S. Guatelli, P. Guèye, P. Gumplinger, A.S. Howard, I. Hřivnáčová, S. Hwang, S. Incerti, A. Ivanchenko, V.N. Ivanchenko, F.W. Jones, S.Y. Jun, P. Kaitaniemi, N. Karakatsanis, M. Karamitros, M. Kelsey, A. Kimura, T. Koi, H. Kurashige, A. Lechner, S.B. Lee, F. Longo, M. Maire, D. Mancusi, A. Mantero, E. Mendoza, B. Morgan, K. Murakami, T. Nikitina, L. Pandola, P. Paprocki, J. Perl, I. Petrović, M.G. Pia, W. Pokorski, J.M. Quesada, M. Raine, M.A. Reis, A. Ribon, A. Ristić Fira, F. Romano, G. Russo, G. Santin, T. Sasaki, D. Sawkey, J.I. Shin, I.I. Strakovsky, A. Taborda, S. Tanaka, B. Tomé, T. Toshito, H.N. Tran, P.R. Truscott, L. Urban,

V. Uzhinsky, J.M. Verbeke, M. Verderi, B.L. Wendt, H. Wenzel, D.H. Wright, D.M. Wright, T. Yamashita, J. Yarba, and H. Yoshida. Recent developments in geant4. *Nuclear Instruments and Methods in Physics Research Section A: Accelerators, Spectrometers, Detectors and Associated Equipment*, 835:186–225, 11 2016. ISSN 01689002. doi: 10.1016/j.nima.2016.06.125.

[202] M. Azzolini, M. Angelucci, R. Cimino, R. Larciprete, N. M. Pugno, S. Taioli, and M. Dapor. Secondary electron emission and yield spectra of metals from monte carlo simulations and experiments. *Journal of Physics: Condensed Matter*, 31: 055901, 2 2019. ISSN 0953-8984. doi: 10.1088/1361-648X/aaf363.

[203] G. B. Sushko, I. A. Solov'yov, and A. V. Solov'yov. Molecular dynamics for irradiation driven chemistry: application to the febid process*. *The European Physical Journal D*, 70:217, 10 2016. ISSN 1434-6060. doi: 10.1140/epjd/e2016-70283-5.

[204] G. B. Sushko, I. A. Solov'yov, A. V. Verkhovtsev, S. N. Volkov, and A. V. Solov'yov. Studying chemical reactions in biological systems with mbn explorer: implementation of molecular mechanics with dynamical topology. *The European Physical Journal D*, 70:12, 1 2016. ISSN 1434-6060. doi: 10.1140/epjd/e2015-60424-9.

[205] R. B. Best, X. Zhu, J. Shim, P. E. M. Lopes, J. Mittal, M. Feig, and A. D. MacKerell. Optimization of the additive charmm all-atom protein force field targeting improved sampling of the backbone ϕ, ψ and side-chain χ_1 and χ_2 dihedral angles. *Journal of Chemical Theory and Computation*, 8:3257–3273, 9 2012. ISSN 1549-9618. doi: 10.1021/ct300400x. URL `https://pubs.acs.org/doi/10.1021/ct300400x`. doi: 10.1021/ct300400x.

[206] A. Verkhovtsev, A. V. Korol, and A. V. Solovyov. Classical molecular dynamics simulations of fusion and fragmentation in fullerene-fullerene collisions. *The European Physical Journal D*, 71:212, 8 2017. ISSN 1434-6060. doi: 10.1140/epjd/e2017-80117-7.

[207] A. Prosvetov, A. V. Verkhovtsev, G. Sushko, and A. V. Solov'yov. Irradiation-driven molecular dynamics simulation of the febid process for pt(pf 3) 4. *Beilstein Journal of Nanotechnology*, 12:1151–1172, 10 2021. ISSN 2190-4286. doi: 10.3762/bjnano.12.86.

[208] P. de Vera, E. Surdutovich, N. J. Mason, F. J. Currell, and A. V. Solov'yov. Simulation of the ion-induced shock waves effects on the transport of chemically reactive species in ion tracks. *The European Physical Journal D*, 72:147, 9 2018. ISSN 1434-6060. doi: 10.1140/epjd/e2018-90167-x.

[209] P. de Vera, A. Verkhovtsev, G. Sushko, and A. V. Solov'yov. Reactive molecular dynamics simulations of organometallic compound w(co)6 fragmentation,. *The European Physical Journal D*, 73:215, 10 2019. ISSN 1434-6060. doi: 10.1140/epjd/e2019-100232-9.

[210] I. Friis, A. Verkhovtsev, I. A. Solov'yov, and A. V. Solov'yov. Modeling the effect of ion-induced shock waves and dna breakage with the reactive charmm force field. *Journal of Computational Chemistry*, 41:2429–2439, 10 2020. ISSN 0192-8651. doi: 10.1002/jcc.26399.

[211] E. Surdutovich and A. V. Solov'yov. Exploration of multifragmentation of ar clusters with incident protons. *The European Physical Journal D*, 73:241, 11 2019. ISSN 1434-6060. doi: 10.1140/epjd/e2019-100295-0.

[212] A. V. Solov'yov, A. V. Verkhovtsev, N. J. Mason, R. A. Amos, I. Bald, G. Baldacchino, B. Dromey, M. Falk, J. Fedor, L. Gerhards, M. Hausmann, G. Hildenbrand, M. Hrabovský, S. Kadlec, J. Kočišek, F. Lépine, S. Ming, A. Nisbet, K. Ricketts, L. Sala, T. Schlathölter, A. E. H. Wheatley, and I. A. Solov'yov. Condensed Matter Systems Exposed to Radiation: Multiscale Theory, Simulations, and Experiment. *Chem. Rev.*, 124(13):8014–8129, jul 2024. ISSN 0009-2665. doi: 10.1021/acs.chemrev.3c00902. URL `https://pubs.acs.org/doi/10.1021/acs.chemrev.3c00902`.

[213] I. Utke, P. Hoffmann, and J. Melngailis. Gas-assisted focused electron beam and ion beam processing and fabrication. *Journal of Vacuum Science & Technology B: Microelectronics and Nanometer Structures Processing, Measurement, and Phenomena*, 26:1197–1276, 7 2008. ISSN 1071-1023. doi: 10.1116/1.2955728.

[214] E. E. B. Campbell. *Fullerene Collision Reactions*, volume 5. Springer Dordrecht, 1 edition, 2004. ISBN 1-4020-1750-2. doi: 10.1007/1-4020-2524-6.

[215] Jean-Patrick Connerade and Andrey Solov'yov. *Latest Advances in Atomic Cluster Collisions: Structure and Dynamics from the Nuclear to the Biological Scale*. Imperial College Press, 2008.

[216] E. E. B. Campbell and F. Rohmund. Fullerene reactions. *Reports on Progress in Physics*, 63:1061–1109, 7 2000. ISSN 0034-4885. doi: 10.1088/0034-4885/63/7/202.

[217] M. Gatchell and H. Zettergren. Knockout driven reactions in complex molecules and their clusters. *Journal of Physics B: Atomic, Molecular and Optical Physics*, 49:162001, 8 2016. ISSN 0953-4075. doi: 10.1088/0953-4075/49/16/162001.

[218] E. E. B. Campbell, V. Schyja, R. Ehlich, and I. V. Hertel. Observation of molecular fusion and deep inelastic scattering in c 60 + + c 60 collisions. *Physical Review Letters*, 70:263–266, 1 1993. ISSN 0031-9007. doi: 10.1103/PhysRevLett.70.263.

[219] F. Rohmund, A. V. Glotov, K. Hansen, and E. E. B. Campbell. Experimental studies of fusion and fragmentation of fullerenes. *Journal of Physics B: Atomic, Molecular and Optical Physics*, 29:5143–5161, 11 1996. ISSN 0953-4075. doi: 10.1088/0953-4075/29/21/025.

[220] H. Bräuning, R. Trassl, A. Diehl, A. Theiß, E. Salzborn, A. A. Narits, and L. P. Presnyakov. Resonant electron transfer in collisions between two fullerene ions. *Physical Review Letters*, 91:168301, 10 2003. ISSN 0031-9007. doi: 10.1103/PhysRevLett.91.168301.

[221] J. Jakowski, S. Irle, B. G. Sumpter, and K. Morokuma. Modeling charge transfer in fullerene collisions via real-time electron dynamics. *The Journal of Physical Chemistry Letters*, 3:1536–1542, 6 2012. doi: 10.1021/jz3004377. URL `https://doi.org/10.1021/jz3004377`. doi: 10.1021/jz3004377.

[222] J. Handt and R. Schmidt. Fusion mechanism in fullerene-fullerene collisions: The deciding role of giant oblate-prolate motion. *EPL (Europhysics Letters)*, 109: 63001, 3 2015. ISSN 0295-5075. doi: 10.1209/0295-5075/109/63001.

[223] D. W. Brenner. Empirical potential for hydrocarbons for use in simulating the chemical vapor deposition of diamond films. *Physical Review B*, 42:9458–9471, 11 1990. ISSN 0163-1829. doi: 10.1103/PhysRevB.42.9458.

[224] G. B. Sushko, I. A. Solov'yov, and A. V. Solov'yov. Modeling mesobionano systems with mbn studio made easy. *Journal of Molecular Graphics and Modelling*, 88:247–260, 5 2019. ISSN 10933263. doi: 10.1016/j.jmgm.2019.02.003.

[225] A. V. Glotov and E. E. B. Campbell. Angular-resolved studies of fragmentation in fullerene-fullerene collisions. *Physical Review A*, 62:033202, 8 2000. ISSN 1050-2947. doi: 10.1103/PhysRevA.62.033202.

[226] S. G. Kim and D. Tománek. Melting the fullerenes: A molecular dynamics study. *Physical Review Letters*, 72:2418–2421, 4 1994. ISSN 0031-9007. doi: 10.1103/PhysRevLett.72.2418.

[227] A. Hussien, A. V. Yakubovich, A. V. Solov'yov, and W. Greiner. Phase transition, formation and fragmentation of fullerenes. *The European Physical Journal D*, 57: 207–217, 4 2010. ISSN 1434-6060. doi: 10.1140/epjd/e2010-00026-7.

[228] A. Rentenier, P. Moretto-Capelle, D. Bordenave-Montesquieu, and A. Bordenave-Montesquieu. Analysis of fragment size distributions in collisions of monocharged ions with the c 60 molecule. *Journal of Physics B: Atomic, Molecular and Optical Physics*, 38:789–806, 4 2005. ISSN 0953-4075. doi: 10.1088/0953-4075/38/7/002.

[229] L. Horváth and T. A. Beu. Tight-binding molecular dynamics simulations of radiation-induced fragmentation of c60. *Physical Review B*, 77:075102, 2 2008. ISSN 1098-0121. doi: 10.1103/PhysRevB.77.075102.

[230] J. Schulte. Multifragmentation of fullerenes: a molecular dynamics statistical trajectory ensemble study of a cross-beam experiment. *International Journal of Mass Spectrometry and Ion Processes*, 145:203–210, 7 1995. ISSN 01681176. doi: 10.1016/0168-1176(95)04232-A.

[231] S. Barth, M. Huth, and F. Jungwirth. Precursors for direct-write nanofabrication with electrons. *Journal of Materials Chemistry C*, 8:15884–15919, 2020. ISSN 2050-7526. doi: 10.1039/D0TC03689G.

[232] Ragesh Kumar T P, Paul Weirich, Lukas Hrachowina, Marc Hanefeld, Ragnar Bjornsson, Helgi Rafn Hrodmarsson, Sven Barth, D Howard Fairbrother, Michael Huth, and Oddur Ingólfsson. Electron interactions with the heteronuclear carbonyl precursor h 2 feru 3 (co) 13 and comparison with hfeco 3 (co) 12 : from fundamental gas phase and surface science studies to focused electron beam induced deposition. *Beilstein Journal of Nanotechnology*, 9:555–579, 2 2018. ISSN 2190-4286. doi: 10.3762/bjnano.9.53.

[233] V. H. Wysocki, H. I. Kenttämaa, and R. G. Cooks. Internal energy distributions of isolated ions after activation by various methods. *International Journal of Mass Spectrometry and Ion Processes*, 75:181–208, 3 1987. ISSN 01681176. doi: 10.1016/0168-1176(87)83054-9.

[234] Š. Beranová and C. Wesdemiotis. Internal energy distributions of tungsten hexacarbonyl ions after neutralization—reionization. *Journal of the American Society for Mass Spectrometry*, 5:1093–1101, 12 1994. doi: 10.1016/1044-0305(94)85070-4. URL `https://doi.org/10.1016/1044-0305(94)85070-4`. doi: 10.1016/1044-0305(94)85070-4.

[235] R. G. Cooks, T. Ast, B. Kralj, V. Kramer, and D. Ž. igon. Internal energy distributions deposited in doubly and singly charged tungsten hexacarbonyl ions generated by charge stripping, electron impact, and charge exchange. *Journal of the American Society for Mass Spectrometry*, 1:16–27, 2 1990. doi: 10.1016/1044-0305(90)80003-6. URL `https://doi.org/10.1016/1044-0305(90)80003-6`. doi: 10.1016/1044-0305(90)80003-6.

[236] K. Wnorowski, M. Stano, W. Barszczewska, A. Jówko, and Š. Matejčík. Electron ionization of w(co)6: Appearance energies. *International Journal of Mass Spectrometry*, 314:42–48, 3 2012. ISSN 13873806. doi: 10.1016/j.ijms.2012.02.002.

[237] K. Wnorowski, M. Stano, C. Matias, S. Denifl, W. Barszczewska, and Š. Matejčík. Low-energy electron interactions with tungsten hexacarbonyl – w(co)6. *Rapid Communications in Mass Spectrometry*, 26:2093–2098, 9 2012. ISSN 0951-4198. doi: 10.1002/rcm.6324.

[238] M. Neustetter, E. Jabbour Al Maalouf, P. Limão-Vieira, and S. Denifl. Fragmentation pathways of tungsten hexacarbonyl clusters upon electron ionization. *The Journal of Chemical Physics*, 145, 8 2016. ISSN 0021-9606. doi: 10.1063/1.4959278.

[239] M. Lacko, P. Papp, K. Wnorowski, and Š. Matejčík. Electron-induced ionization and dissociative ionization of iron pentacarbonyl molecules. *The European Physical Journal D*, 69:84, 3 2015. ISSN 1434-6060. doi: 10.1140/epjd/e2015-50721-8.

[240] J. D. Fowlkes and P. D. Rack. Fundamental electron-precursor-solid interactions derived from time-dependent electron-beam-induced deposition simulations and experiments. *ACS Nano*, 4:1619–1629, 3 2010. ISSN 1936-0851. doi: 10.1021/nn901363a. URL `https://doi.org/10.1021/nn901363a`. doi: 10.1021/nn901363a.

[241] M. D. Hanwell, D. E. Curtis, D. C. Lonie, T. Vandermeersch, E. Zurek, and G. R. Hutchison. Avogadro: an advanced semantic chemical editor, visualization, and analysis platform. *Journal of Cheminformatics*, 4:17, 12 2012. ISSN 1758-2946. doi: 10.1186/1758-2946-4-17.

[242] S. R. Hall, F. H. Allen, and I. D. Brown. The crystallographic information file (cif): a new standard archive file for crystallography. *Acta Crystallographica Section A Foundations of Crystallography*, 47:655–685, 11 1991. ISSN 01087673. doi: 10.1107/S010876739101067X.

[243] M. Ishimaru, S. Munetoh, and T. Motooka. Generation of amorphous silicon structures by rapid quenching: A molecular-dynamics study. *Physical Review B*, 56:15133–15138, 12 1997. ISSN 0163-1829. doi: 10.1103/PhysRevB.56.15133.

[244] S. Munetoh, K. Moriguchi, A. Shintani, K. Nishihira, and T. Motooka. Molecular dynamics simulations of solid-phase epitaxy of si: Defect formation processes. *Physical Review B*, 64:193314, 10 2001. ISSN 0163-1829. doi: 10.1103/PhysRevB.64.193314.

[245] S. Munetoh, T. Motooka, K. Moriguchi, and A. Shintani. Interatomic potential for si–o systems using tersoff parameterization. *Computational Materials Science*, 39:334–339, 4 2007. ISSN 09270256. doi: 10.1016/j.commatsci.2006.06.010.

[246] Marian Bruns and Fathollah Varnik. Enhanced dynamics in deep thermal cycling of a model glass. *J. Chem. Phys.*, 156(23), jun 2022. ISSN 0021-9606. doi: 10.1063/5.0094024. URL `https://pubs.aip.org/jcp/article/156/23/234501/2841384/Enhanced-dynamics-in-deep-thermal-cycling-of-a`.

[247] Baoshuang Shang, Weihua Wang, Alan Lindsay Greer, and Pengfei Guan. Atomistic modelling of thermal-cycling rejuvenation in metallic glasses. *Acta Mater.*, 213:116952, jul 2021. ISSN 13596454. doi: 10.1016/j.actamat.2021.116952. URL `https://linkinghub.elsevier.com/retrieve/pii/S1359645421003323`.

[248] T. Egami and S. J. L. Billinge. *Underneath the Bragg Peaks: Structural Analysis of Complex Materials*. Pergamon, Kidlington, Oxford, first edition, 2003. ISBN 0080426980.

[249] S. Jo, T. Kim, V. G. Iyer, and W. Im. Charmm-gui: A web-based graphical user interface for charmm. *Journal of Computational Chemistry*, 29:1859–1865, 8 2008. ISSN 0192-8651. doi: 10.1002/jcc.20945.

[250] B. R. Brooks, R. E. Bruccoleri, B. D. Olafson, D. J. States, S. Swaminathan, and M. Karplus. Charmm : A program for macromolecular energy, minimization, and dynamics calculations. *Journal of Computational Chemistry*, 4:187–217, 6 1983. ISSN 0192-8651. doi: 10.1002/jcc.540040211.

[251] M. J. Frisch, G. W. Trucks, H. B. Schlegel, G. E. Scuseria, M. A. Robb, J. R. Cheeseman, G. Scalmani, V. Barone, G. A. Petersson, H. Nakatsuji, X. Li, M. Caricato, A. V. Marenich, J. Bloino, B. G. Janesko, R. Gomperts, B. Mennucci, H. P. Hratchian, J. V. Ortiz, A. F. Izmaylov, J. L. Sonnenberg, D. Williams-Young, F. Ding, F. Lipparini, F. Egidi, J. Goings, B. Peng, A. Petrone, T. Henderson, D. Ranasinghe, V. G. Zakrzewski, J. Gao, N. Rega, G. Zheng, W. Liang, M. Hada, M. Ehara, K. Toyota, R. Fukuda, J. Hasegawa, M. Ishida, T. Nakajima, Y. Honda, O. Kitao, H. Nakai, T. Vreven, K. Throssell, J. A. Montgomery, Jr., J. E. Peralta, F. Ogliaro, M. J. Bearpark, J. J. Heyd, E. N. Brothers, K. N. Kudin, V. N. Staroverov, T. A. Keith, R. Kobayashi, J. Normand, K. Raghavachari, A. P. Rendell, J. C. Burant, S. S. Iyengar, J. Tomasi, M. Cossi, J. M. Millam, M. Klene, C. Adamo, R. Cammi, J. W. Ochterski, R. L. Martin, K. Morokuma, O. Farkas, J. B. Foresman, and D. J. Fox. Gaussian˜16 Revision C.01, 2016.

[252] I. G. Polyakova. *4. The Main Silica Phases and Some of Their Properties*, pages 197–268. DE GRUYTER, 12 2014. doi: 10.1515/9783110298581.197.

[253] K. A. Kirchner, D. R. Cassar, E. D. Zanotto, M. Ono, S. H. Kim, K. Doss, M. L. Bødker, M. M. Smedskjaer, S. Kohara, L. Tang, M. Bauchy, C. J. Wilkinson, Y. Yang, R. S. Welch, M. Mancini, and J. C. Mauro. Beyond the average: Spatial and temporal fluctuations in oxide glass-forming systems. *Chemical Reviews*, 123: 1774–1840, 2 2023. ISSN 0009-2665. doi: 10.1021/acs.chemrev.1c00974.

[254] G. R. Mitchell, R. Lovell, and A. H. Windle. The local structure of molten polyethylene. *Polymer*, 23:1273–1285, 8 1982. ISSN 00323861. doi: 10.1016/0032-3861(82)90267-1.

Appendix A

MBN Simulation Parameters

The `Task File` in MBN Explorer contains a set of options and their corresponding values, determining the behaviour of the program. These options control which features are active, how long the simulation runs, and more. The key required parameters include `Task_Type`, `Input_File` (or `PDB_File`), `Potential_File` (or `Molmech_Potential_File`), and `Output_File`. These are described in detail below:

Task_Type = (Type of calculation)
Acceptable values: SP, Energy, MD, Molecular_Dynamics, Opt, optimisation, RW, Random_Walk, Spectrum.
Description: Specifies the type of calculation to be performed:

1. Single point energy calculation (`SP` or `Energy`),
2. Molecular dynamics simulations (`MD` or `Molecular_Dynamics`),
3. Structure optimisation (`Opt` or `optimisation`),
4. Random walk dynamics simulation (`RW` or `Random_Walk`),
5. Radiation spectrum calculation (`Spectrum`).

Input File parameters:

Input_File = (File with coordinates in MBN Explorer format)
Acceptable values: UNIX filename.
Description: This file contains the initial position coordinates of the system, formatted according to MBN Explorer's specifications (see Section 3.1). Only one value may be specified, and file paths can be absolute or relative.

PDB_File = (File with coordinates in PDB format)
Acceptable values: UNIX filename.
Description: For certain simulations, especially when using molecular mechanics potentials, it is convenient to specify initial coordinates in the standard PDB format. This file may also include other molecular information. The structure of the PDB file is described in Section 3.1.2. Users may combine PDB and MBN Explorer formats for different parts of the system.

Topology_File = (PSF file)
Acceptable values: UNIX filename.
Description: A topology file (PSF format) that describes the molecular system being simulated. Only one value may be specified.

Potential_File = (Potential file in MBN Explorer format)
Acceptable values: UNIX filename.
Description: A file defining all or part of the interaction parameters in MBN Explorer format. It describes the molecular interactions necessary for the simulation.

Molmech_Potential_File = (Potential file in CHARMM format)
Acceptable values: UNIX filename.
Description: A CHARMM parameter file required for molecular mechanics simulations. It defines the interaction parameters for the molecular system, including bonded interactions and optionally non-bonded van der Waals interactions.

Manipulation_File = (File describing user-defined manipulations)
Acceptable values: UNIX filename.
Description: A file specifying user-defined manipulations of particles and rigid objects in the system. It allows displacement of particles with constant velocity or acceleration, and rotation of rigid bodies with a specified angular velocity around a defined axis.

Chem_Rules_File = (File with chemistry rules for simulations)
Acceptable values: UNIX filename.
Description: A file used for simulating chemical reactions in MBN Explorer. It contains information about possible reactants and products, bond multiplicities, and partial charges of atoms involved in the reactions.

Output File Parameters:

Output_File = (Output file name)
Acceptable values: UNIX filename.

Description: The output file is written after each completed simulation and contains task-related information. It stores all information read from the input files, which can be used to resubmit the task. Additionally, it includes the final configuration of the system, i.e., the positions and velocities of all atoms. The output file also stores the names of the potential files used in the calculation and the CPU time consumed. See Section 3.2 for more details on the output file structure.

Output_File_Coords = (Print coordinates of particles in the output file)
Acceptable values: `on`, `off`.
Default value: `on`.
Description: If set to `off`, MBN Explorer will exclude the coordinates and velocities of particles from the output file, reducing its size. In this case, the trajectory file must be used to read the coordinates of atoms.

Output_PDB_File = (File for the final configuration in PDB format)
Acceptable values: UNIX filename.
Description: This keyword instructs MBN Explorer to save the final configuration of the system in PDB format, which is especially useful for macromolecular systems.

Output_Topology_File = (File for the final topology)
Acceptable values: UNIX filename.
Description: Saves the final molecular topology of the system in the PSF format, including all bonds, angles, and dihedrals. This is particularly useful for macromolecular systems undergoing chemical reactions and is recommended to be used with `Output_PDB_File`.

Log File Parameters:

Log_File = (Filename for logging information)
Acceptable values: UNIX filename.
Description: Required for molecular dynamics and optimisation tasks (see Section 3.2). In molecular dynamics, the log file stores system characteristics such as potential energy, kinetic energy, total energy, momenta, and temperature at intervals determined by the `Log_Steps` keyword. In optimisation tasks, the log file records the total energy of the system at given intervals.

Log_Steps = (Periodicity of log file update)
Acceptable values: Positive integer.
Default value: 1.
Description: Controls how often the log file is updated during molecular dynamics

or optimisation simulations. Smaller values result in more frequent logging but increase computation time.

Log_Parameter = (Characteristics to be printed in the log file)
Acceptable values: Step, Time, T_Energy (Total_Energy), DT_Energy (Delta_Total_Energy), K_Energy, P_Energy, CP_Energy, MP_Energy, AMP_Energy, BMP_Energy, DMP_Energy, IMP_Energy, PP_Energy, MBP_Energy, EP_Energy, M (Momentum), AM (Angular_Momentum), T (Temperature), Max_Torque, Max_Force, Max_Disp.
Default value: Step, Time, T_Energy, K_Energy, P_Energy.
Description: Defines the system characteristics that will be logged. By default, MBN Explorer logs the time step, current simulation time, total energy, kinetic energy, and potential energy. Additional characteristics can be specified to obtain more detailed outputs.

Trajectory File Parameters:

Trajectory_File = (System's trajectory file)
Acceptable values: UNIX filename.
Description: Required for molecular dynamics, random walk dynamics, and optimisation tasks (see Section 3.2). The file records the system's time evolution or optimisation process, including atom coordinates and optionally velocities, written at intervals determined by the `Trajectory_Steps` keyword. The format is determined by `Trajectory_Format`.

Trajectory_Format = (Trajectory file format)
Acceptable values: `Auto`, `XYZ`, `DCD`, `DCD+XYZ`.
Default value: `Auto`.
Description: Specifies the format of the trajectory file. If set to `Auto`, MBN Explorer deduces the format from the file extension (.xyz for XYZ, .dcd for DCD). `DCD+XYZ` is a hybrid mode where the initial step is saved in XYZ format, and subsequent steps in DCD format.

Trajectory_Steps = (Periodicity of trajectory file update)
Acceptable values: Positive integer.
Default value: 1.
Description: Controls how often the trajectory file is updated during simulations. A smaller value results in more detailed output but increases the simulation time.

Trajectory_Parameter = (Characteristics to be printed in the trajectory file)
Acceptable values: `coordinates`, `velocities`, `accelerations`, `forces`.

Default value: `coordinates`.

Description: Specifies what characteristics to store in the trajectory file. For XYZ format, this keyword controls the output, while for DCD format, only coordinates and velocities are stored. Other parameters like accelerations and forces are only relevant for XYZ format.

Trajectory_Selection = (Selection criteria)

Acceptable values: `Nofixed`, `fixed`.

Default value: All particles.

Description: Controls which particles are included in the trajectory file. By default, all particles are recorded, but this keyword can reduce the file size by excluding fixed particles.

Trajectory_Precision = (Precision of atomic coordinates)

Acceptable values: Positive integer.

Default value: 8.

Description: Defines the number of decimal places used for printing coordinates and velocities in the trajectory file. Relevant only for XYZ format.

Trajectory_Size_Limit = (Maximum size of the trajectory file)

Acceptable values: Positive real number (in megabytes).

Default value: Maximal storage capacity.

Description: Limits the size of the trajectory file. When the file exceeds the specified size, MBN Explorer creates a new file and continues the output. Successive files are named using a numerical index (e.g., `Trajectory_File001.xyz`). See Section 3.2 for more details on the trajectory file structure.

Parameters for some general molecular dynamics are:

Integration and Simulation Settings

Integrator = (integration method)

Acceptable values: Verlet, Leapfrog, Relativistic

Default value: Verlet

Description: Defines the numerical algorithm for solving the equations of motion that describe the time evolution of the system. `Verlet` refers to the velocity Verlet integrator, `Leapfrog` refers to the leapfrog integrator, and `Relativistic` is designed for simulating the motion of relativistic particles.

Time_Step = (integration time step)

Acceptable values: positive real number

Description: Specifies the timestep size used when integrating each step of the simulation with a constant time step. This value is specified in the units set by the `Time_Unit` keyword.

Simulation_Time = (molecular dynamics simulation time)
Acceptable values: positive real number
Description: Defines the total time for which the simulation is run, specified in units defined by `Time_Unit`. The total number of simulation steps is determined as $\frac{\texttt{Simulation\_Time}}{\texttt{Time\_Step}}$.

Initial_Temperature = (initial temperature value)
Acceptable values: positive real number
Description: Sets the initial temperature of the system. This keyword generates a random velocity distribution for particles in the system such that the system is at the desired temperature. If used, the temperature is interpreted using the units defined by `Temperature_Unit`.

Antirotator = (neutralize system's momentum and angular momentum?)
Acceptable values: on, off, none
Default value: off
Description: When turned on, it ensures that the total momentum and angular momentum of the system are zero. This is particularly important if the initial velocities are generated randomly using the `Initial_Temperature` keyword.

Manipulate_System = (allow user-defined manipulation)
Acceptable values: on, off, none
Default value: off
Description: If enabled, it allows user-defined manipulation of particles or rigid objects using a file specified by `Manipulation_File`. Particles can be displaced with a constant velocity or acceleration, or rotated around a fixed axis.

Temperature Control

Thermostat = (thermostat type)
Acceptable values: Berendsen, Langevin, None
Default value: None
Description: Specifies the type of thermostat used for constant temperature simulations. If `None`, MBN Explorer runs a constant energy simulation.

Thermostat_Temperature = (thermostat temperature)

Acceptable values: positive real number

Description: Specifies the temperature to which the atoms in contact with an external heat bath are adjusted, in units defined by `Temperature_Unit`.

Thermostat_Rise_Time = (Berendsen thermostat parameter)

Acceptable values: positive real number

Default value: Time_Step

Description: A parameter defining the rate of velocity rescaling in the Berendsen thermostat, measured in units defined by `Time_Unit`.

Thermostat_Damping_Time = (Langevin thermostat parameter)

Acceptable values: positive real number

Default value: None

Description: Defines the viscous velocity damping in the Langevin thermostat, measured in units defined by `Time_Unit`.

Thermostat_Temperature_Increase_Rate = (Langevin thermostat temperature increase rate)

Acceptable values: positive real number

Default value: None

Description: Specifies the linear rate at which the temperature is increased in the Langevin thermostat. Measured in units of `Temperature_Unit`/`Time_Unit`.

Molecular Mechanics and Chemical Reactions

Molmech_Exclusion_Model = (exclusion policy)

Acceptable values: None, 1-2, 1-3, 1-4, Scaled-1-4

Default value: 1-4

Description: Specifies which pairs of bonded atoms should be excluded from non-bonded interactions.

Molmech_Exclusion_Scale = (scaling factor for 1-4 interactions)

Acceptable values: positive real number

Default value: 1

Description: Defines the scaling factor for electrostatic interactions between 1-4 atom pairs. Only used when `Molmech_Exclusion_Model = Scaled-1-4`.

Update_Molecular_Structures = (change bonded topology during simulation?)

Acceptable values: on, off

Default value: off

Description: Enables simulations where the bonded topology of the system can change.

Structure optimisation

optimisation_Method = (optimisation method)

Acceptable values: Velocity_Quenching, Conjugate_Gradient

Description: Defines the computational method for structure optimisation.

optimisation_Steps = (max number of optimisation steps)

Acceptable values: positive integer

Description: Specifies the maximum number of steps for the optimisation procedure.

Velocity_Quenching_Time_Step = (integration time step for velocity quenching)

Acceptable values: positive real number

Description: Defines the time step for the velocity Verlet algorithm used in the velocity quenching method.

Force_Tolerance = (max force tolerance)

Acceptable values: positive real number

Default value: 0.01 a.u.

Description: Defines the maximum allowed force acting on any particle in the system.

Disp_Tolerance = (max displacement tolerance)

Acceptable values: positive real number

Default value: 0.01 a.u.

Description: Defines the maximum allowed displacement of any particle in the system per optimisation step.

Torque_Tolerance = (max torque tolerance)

Acceptable values: positive real number

Default value: 0.01 a.u.

Description: Specifies the maximum allowed torque acting on particles in the system.

Appendix B

Temperature Cycle Script

```
# -*- coding: utf-8 -*-
"""
Created on Wed Jul 31 13:21:44 2024
@author: adrijabhowmick
"""
import os
import shutil
import subprocess
import glob
import time
import numpy as np

# Parameters
nprocs = 1
lowest_temp = 200        # Lowest temperature in K
highest_temp = 400       # Highest temperature in K
cycles = 8               # Number of temperature cycles
temp_rate = 10           # Rate of temperature change in K/ps
optimise = True          # Option to optimise the system before the
↪   temperature cycle (Set 'True' to proceed or 'False' to skip)
equilibrate = True       # Option to equilibrate the system before the
↪   temperature cycle (Set 'True' to proceed or 'False' to skip)
equi_temp = 300          # Equilibration temperature in K (Set your
↪   equilibration temperature if you want to proceed)
basepath = os.getcwd()   # Path of the current working directory
```

```
def read_task(task_file, flatten=False):
    '''This function splits a given Task file into a a dictionary of
    ↪  task file options and their respective
parameters. Useful if you want to get a specific set of task file
↪  options for use in calculations for example.
by default it is split into the task file subsections as a dictionary of
↪  dictionaries. Use flatten=True to flatten
into a single dictionary.'''
    file_options = {}
    with open(task_file) as f:
        data = f.read().split('\n')

    section_options = {}
    for line in data:
        try:
            if line[0] ==';' and len(line)>1:
                if len(section_options)>0:
                    file_options[section] = section_options
                    section_options = {}
                section = line.replace(';','').strip()
            if '=' in line:
                line=line.split('=')
                section_options[line[0].strip()] = str(line[1].strip())
        except IndexError:
            pass
    file_options[section] = section_options

    if flatten:
        file_options_flat = {}
        for key in file_options.keys():
            file_options_flat.update(file_options[key])
        return file_options_flat
    else:
        return file_options


def write_task(task_file, file_options):
    '''This function writes the contents nested dictionary containing
    ↪  task file options to a task file.
```

```
The input format is the same as a non-flattened read_task output
↪   dictionary.'''
    with open(task_file, 'w') as f:
        f.write(';\n')
        for key in file_options:
            f.write('\n; '+key+'\n')
            for sub_key in file_options[key]:
                if sub_key == 'Random':
                    f.write('\n'+'{:<31}'.format(sub_key)+' =
                    ↪   '+file_options[key][sub_key]+'\n')
                else:
                    f.write('{:<31}'.format(sub_key)+' =
                    ↪   '+file_options[key][sub_key]+'\n')


def lastframe_to_input(output_file, input_file):
    '''This function will extract the last frame from the provided
    ↪   output file and write as an input file.'''
    with open(output_file) as out:
        file = out.readlines()
        to_write = []
        write = False
        for line in file:
            if 'System Final Configuration' in line:
                write = True
                continue
            if 'Output characteristics' in line:
                break
            if write:
                to_write.append(line)
        with open(input_file, 'w') as inp:
            for line in to_write[2:-2]:
                inp.write(line)


def set_run():
    template_path = os.path.join(basepath, 'Templates/')
    simulation_path = os.path.join(basepath, 'Temperature_cycle')
    os.makedirs(simulation_path, exist_ok=True)
```

```
os.chdir(simulation_path)
prev_completed = True

# Optimisation
if optimise:
    prev_completed = False
    optimisation_path = os.path.join(simulation_path,
    ↪  'Optimisation')
    os.makedirs(optimisation_path, exist_ok=True)
    os.chdir(optimisation_path)
    if len(glob.glob('*.out'))>0:
        with open(glob.glob('*.out')[0]) as file:
            prev_completed = 'Have a nice day!' in file.read()
    if not prev_completed:
        shutil.copy2(template_path+'Optimisation.task',
        ↪  './Test.task')
        shutil.copy2(template_path+'Test.pdb', './')
        shutil.copy2(template_path+'Test.psf', './')
        shutil.copy2(template_path+'Test.pot', './')
        shutil.copy2(template_path+'Test.prm', './')
        print('Running optimisation')
        result = subprocess.run(['mbnexplorer',
        ↪  '-use-server-license', '129.12.24.24'],
        ↪  capture_output=True, text=True)
        print(result.stdout)
        print(result.stderr)
        result = subprocess.run(['mpirun', '-np', str(nprocs),
        ↪  '--bind-to', 'socket', 'mbnexplorer', '-t',
        ↪  'Test.task'], capture_output=True, text=True)
        print(result.stdout)
        print(result.stderr)
        if len(glob.glob('*.out'))>0:
            with open(glob.glob('*.out')[0]) as file:
                prev_completed = 'Have a nice day!' in file.read()

# Equilibration
if equilibrate:
    if prev_completed:
        prev_completed = False
```

```
equilibration_path = os.path.join(simulation_path,
↪   'Equilibration')
os.makedirs(equilibration_path, exist_ok=True)
os.chdir(equilibration_path)
if len(glob.glob('*.out'))>0:
    with open(glob.glob('*.out')[0]) as file:
        prev_completed = 'Have a nice day!' in file.read()
if not prev_completed:
    shutil.copy2(template_path+'Dynamics.task',
    ↪   './Test.task')
    shutil.copy2(template_path+'Test.pot', './')
    shutil.copy2(template_path+'Test.prm', './')

    if optimise:
        lastframe_to_input(optimisation_path+'/Test.out',
        ↪   'Test.in')
    else:
        shutil.copy2(template_path+'Initial.in',
        ↪   './Test.in')

    task = read_task('Test.task')
    task['DYNAMICS PARAMETERS']['Thermostat_Temperature'] =
    ↪   str(equi_temp)
    write_task('Test.task', task)

    print('Running equilibration')
    result = subprocess.run(['mbnexplorer',
    ↪   '-use-server-license', '129.12.24.24'],
    ↪   capture_output=True, text=True)
    print(result.stdout)
    print(result.stderr)
    result = subprocess.run(['mpirun', '-np', str(nprocs),
    ↪   '--bind-to', 'socket', 'mbnexplorer', '-t',
    ↪   'Test.task'], capture_output=True, text=True)
    print(result.stdout)
    print(result.stderr)
    if len(glob.glob('*.out'))>0:
        with open(glob.glob('*.out')[0]) as file:
```

```
                    prev_completed = 'Have a nice day!' in
                    ↪   file.read()


# Initial Heating
if prev_completed:
    prev_completed = False
    Initial_heating_path = os.path.join(simulation_path,
    ↪   'Initial_heating')
    os.makedirs(Initial_heating_path, exist_ok=True)
    os.chdir(Initial_heating_path)
    if len(glob.glob('*.out'))>0:
        with open(glob.glob('*.out')[0]) as file:
            prev_completed = 'Have a nice day!' in file.read()
    if not prev_completed:
        shutil.copy2(template_path+'Dynamics.task', './Test.task')
        shutil.copy2(template_path+'Test.pot', './')
        shutil.copy2(template_path+'Test.prm', './')

        if equilibrate:
            lastframe_to_input(equilibration_path+'/Test.out',
            ↪   'Test.in')
        else:
            shutil.copy2(template_path+'Initial.in', './Test.in')

        task = read_task('Test.task')
        task['DYNAMICS PARAMETERS']['Initial_Temperature'] =
        ↪   str(equi_temp)
        task['DYNAMICS PARAMETERS']['Thermostat_Temperature'] =
        ↪   str(equi_temp)
        task['DYNAMICS
        ↪   PARAMETERS']['thermostat_temperature_increase_rate'] =
        ↪   str(temp_rate)
        task['SIMULATION PARAMETERS']['Simulation_Time'] =
        ↪   str(abs(highest_temp-equi_temp)/temp_rate)

        write_task('Test.task', task)

        print('Running initial heating')
```

```
        result = subprocess.run(['mbnexplorer',
        ↪   '-use-server-license', '129.12.24.24'],
        ↪   capture_output=True, text=True)
        print(result.stdout)
        print(result.stderr)
        result = subprocess.run(['mpirun', '-np', str(nprocs),
        ↪   '--bind-to', 'socket', 'mbnexplorer', '-t',
        ↪   'Test.task'], capture_output=True, text=True)
        print(result.stdout)
        print(result.stderr)
        if len(glob.glob('*.out'))>0:
            with open(glob.glob('*.out')[0]) as file:
                 prev_completed = 'Have a nice day!' in file.read()

        print('Initial heating completed')

# Temperature Cycle
for cycle in range(cycles):

    # Cooling stage
    if prev_completed:
        prev_completed = False
        cooling_path = os.path.join(simulation_path,
        ↪   f'{cycle+1}_Cooling/')
        os.makedirs(cooling_path, exist_ok=True)
        os.chdir(cooling_path)
        if len(glob.glob('*.out'))>0:
            with open(glob.glob('*.out')[0]) as file:
                prev_completed = 'Have a nice day!' in file.read()
        if not prev_completed:
            shutil.copy2(template_path+'Dynamics.task',
            ↪   './Test.task')
            shutil.copy2(template_path+'Test.pot', './')
            shutil.copy2(template_path+'Test.prm', './')

            lastframe_to_input(Initial_heating_path+'/Test.out',
            ↪   'Test.in')

            task = read_task('Test.task')
```

```
        task['DYNAMICS PARAMETERS']['Initial_Temperature'] =
        ↪   str(highest_temp)
        task['DYNAMICS PARAMETERS']['Thermostat_Temperature'] =
        ↪   str(highest_temp)
        task['DYNAMICS
        ↪   PARAMETERS']['thermostat_temperature_increase_rate']
        ↪   = str(-temp_rate)
        task['SIMULATION PARAMETERS']['Simulation_Time'] =
        ↪   str(abs(highest_temp-lowest_temp)/temp_rate)

        write_task('Test.task', task)

        print('Running cooling cycle '+str(cycle+1))
        result = subprocess.run(['mbnexplorer',
        ↪   '-use-server-license', '129.12.24.24'],
        ↪   capture_output=True, text=True)
        print(result.stdout)
        print(result.stderr)
        result = subprocess.run(['mpirun', '-np', str(nprocs),
        ↪   '--bind-to', 'socket', 'mbnexplorer', '-t',
        ↪   'Test.task'], capture_output=True, text=True)
        print(result.stdout)
        print(result.stderr)
        if len(glob.glob('*.out'))>0:
            with open(glob.glob('*.out')[0]) as file:
                 prev_completed = 'Have a nice day!' in
                 ↪   file.read()

        print(f"Cooling {cycle+1} completed.")

# Heating stage
if prev_completed:
    prev_completed = False
    heating_path = os.path.join(simulation_path,
    ↪   f'{cycle+1}_Heating/')
    os.makedirs(heating_path, exist_ok=True)
    os.chdir(heating_path)
    if len(glob.glob('*.out'))>0:
        with open(glob.glob('*.out')[0]) as file:
```

```
        prev_completed = 'Have a nice day!' in file.read()
if not prev_completed:
    shutil.copy2(template_path+'Dynamics.task',
    ↪   './Test.task')
    shutil.copy2(template_path+'Test.pot', './')
    shutil.copy2(template_path+'Test.prm', './')

    lastframe_to_input(cooling_path+'/Test.out', 'Test.in')

    task = read_task('Test.task')
    task['DYNAMICS PARAMETERS']['Initial_Temperature'] =
    ↪   str(lowest_temp)
    task['DYNAMICS PARAMETERS']['Thermostat_Temperature'] =
    ↪   str(equi_temp)
    task['DYNAMICS
    ↪   PARAMETERS']['thermostat_temperature_increase_rate']
    ↪   = str(-temp_rate)
    task['SIMULATION PARAMETERS']['Simulation_Time'] =
    ↪   str(abs(highest_temp-lowest_temp)/temp_rate)

    write_task('Test.task', task)

    print('Running heating cycle '+str(cycle))
    result = subprocess.run(['mbnexplorer',
    ↪   '-use-server-license', '129.12.24.24'],
    ↪   capture_output=True, text=True)
    print(result.stdout)
    print(result.stderr)
    result = subprocess.run(['mpirun', '-np', str(nprocs),
    ↪   '--bind-to', 'socket', 'mbnexplorer', '-t',
    ↪   'Test.task'], capture_output=True, text=True)
    print(result.stdout)
    print(result.stderr)
    if len(glob.glob('*.out'))>0:
        with open(glob.glob('*.out')[0]) as file:
            prev_completed = 'Have a nice day!' in
            ↪   file.read()

    print(f"Heating {cycle+1} completed.")
```

```
    # Equilibration
    if prev_completed:
        prev_completed = False
        equilibration_path = os.path.join(simulation_path,
        ↪  'Final_Equilibration')
        os.makedirs(equilibration_path, exist_ok=True)
        os.chdir(equilibration_path)
        shutil.copy2(template_path+'Dynamics.task', './Test.task')
        shutil.copy2(template_path+'Test.pot', './')
        shutil.copy2(template_path+'Test.prm', './')

        lastframe_to_input(heating_path+'/Test.out', 'Test.in')

        task = read_task('Test.task')
        task['DYNAMICS PARAMETERS']['Initial_Temperature'] =
        ↪  str(highest_temp)
        task['DYNAMICS PARAMETERS']['Thermostat_Temperature'] =
        ↪  str(equi_temp)

        write_task('Test.task', task)

        print('Running final equilibration')
        result = subprocess.run(['mbnexplorer', '-use-server-license',
        ↪  '129.12.24.24'], capture_output=True, text=True)
        print(result.stdout)
        print(result.stderr)
        result = subprocess.run(['mpirun', '-np', str(nprocs),
        ↪  '--bind-to', 'socket', 'mbnexplorer', '-t', 'Test.task'],
        ↪  capture_output=True, text=True)
        print(result.stdout)
        print(result.stderr)
        if len(glob.glob('*.out'))>0:
            with open(glob.glob('*.out')[0]) as file:
                prev_completed = 'Have a nice day!' in file.read()
        print('Final equilibration completed')

set_run()
```